UNIVERSITAT DE BARCELONA

Modeling the atmospheric boundary layer in stably stratified conditions and over complex terrain areas: from mesoscale to LES

Mireia Udina Sistach

UNIVERSITAT DE BARCELONA

UNIVERSITAT DE BARCELONA
DEPARTAMENT D'ASTRONOMIA I METEOROLOGIA

Modeling the atmospheric boundary layer in stably stratified conditions and over complex terrain areas: from mesoscale to LES

Mireia Udina Sistach

PhD thesis

Programa de doctorat en Física

Supervisor:
Dra. Maria Rosa Soler Duffour

Barcelona, September 2015

Programa de Doctorat en Física
Línia de recerca en Meteorologia

Departament d'Astronomia i Meteorologia.
UNIVERSITAT DE BARCELONA

Modeling the atmospheric boundary layer in stably stratified conditions and over complex terrain areas: from mesoscale to LES

Memòria presentada per

Mireia Udina Sistach

per optar al grau de

Doctor en Física

Directora de la tesi:

Dra. Maria Rosa Soler Duffour

Tutora de la tesi:

Dra. Maria Rosa Soler Duffour

Barcelona, setembre de 2015

In every walk with nature one receives far more than he seeks.

John Muir

Acknowledgments-Agraïments

En primer lloc, gràcies Maria Rosa, per confiar en mi des del primer dia i permetre'm endinsar-me en el món fascinant de la *boundary layer*. Això ha estat com petites parts d'un trencaclosques que poc a poc s'han anat unint i ha anat agafant sentit. Gràcies per haver-me "enviat" als nombrosos congressos i donar-me la possibilitat poder conèixer els investigadors d'arreu en la matèria, què s'està fent i fer-me sentir part del tot. Saps que cada vegada que torno d'un congrés estic motivada i engrescada. Crec que he estat molt afortunada de tenir una directora de tesi com tu, sempre present, disposada i plantejant nous reptes, i alhora donant-me la suficient llibertat per créixer i ser autosuficient.

Thank you so much, Jielun Sun, for being a great host at NCAR and for allowing me learn from you. I will always remember the long discussions about the plots, which made me feel nervous but excited at the same time. You made me feel that what I was doing was important and, somehow, you made me develop the small scientist I have inside me. Many thanks also to Branko Kosović, great teacher of WRF-LES, scientist and better person. Thanks for attending my multiple questions about the code and being patient. I also thank many other friendly people at NCAR, especially from the MMM division.

Gràcies al professorat del Departament d'Astronomia i Meteorologia (DAM), especialment al Dr. Lorente per tenir sempre paraules simpàtiques i al Dr. Bech per ser tant proper. Gràcies també a gent del Servei Meteorològic de Catalunya: al Jordi Mercader pels bons consells i al Manu Bravo per ajudar-me en els inicis. També al Jordi Moré i a l'Abdel. I al Jordi Barcons per fructíferes converses. I al JR Miró pels moments compartits a La Cerdanya i per transmetre empenta. Espero que aquest sigui un inici de llarg temps de col·laboracions. A la Laura Trapero del CENMA, Andorra, perquè seguim treballant juntes i coincidint en molts congressos. I al Pau Casso per la predisposició a col·laborar. Por otro lado, gracias a Carlos Yagüe por trasmitir-me ánimos en mis inicios y también a Samuel Viana. Gràcies a la Secretaria del DAM: al JR per fer tots els tràmits més fàcils i de tant en tant filosofar una estona. I a la Montse i la Rosa per les gestions sempre a temps.

I ara toca donar les gràcies als amics i companys del DAM, als que hi són i a tots els que hi han estat durant aquests anys. Per aquí ha passat molta gent, i mirant enrere, cadascú ha aportat una certa singularitat i ha enriquit els moments viscuts. Primer, als companys de despatx amb qui hem passat més estones: la Miriam i el Pedro. A la Miriam per fer saltar rialles que sovint acaben en atacs de riure i tenir converses que fan més

amens els dies al DAM. Ens queda pendent una partida al Mario Car. Al Pedro, per ser un gran company de feina i millor persona. Estic segura que seguirem quedant per fer una "cervecita" de tant en tant. Al recent incorporat Bernat, tan de bo seguim treballant junts! A la Mateu per trobar en tu una bona confident, per la complicitat que tenim i per les grans estones al terrat. A la Yolanda, per ser un exemple a seguir i no tenir mai un "no" per resposta. Al Didac, sempre disposat a escoltar i tenir intenses converses i/o moments d'humor absurd. A l'Ossó, per les tertúlies d'actualitat i política i per les sortides en BTT, que bé que ho hem passat junts! Al Carrasco per sempre ser-hi als dinars. Al David pels bons moments compartits. A l'Àlex per l'empenta que encomanes. I als que queden una mica més lluny: a l'Adolfo per fer-me descobrir Sant Andreu i compartir bons moments, al Vicent pels "piti-time" i reflexions junts, a l'Aitor per fer-me riure i passar-ho sempre bé, i al Raúl per la formació ens els inicis. I als molts altres membres del DAM: Raül Marcos, Marco Turco, Maria, Montse i tots els "astros"!

Ja fora de l'àmbit de feina, m'agradaria donar les gràcies a la resta de gent que m'ha acompanyat en aquest camí. Gràcies nenes: Gemma, Maria, Bet, Pachi, Vicky, Marta, Joana, Marina. Sempre hi sou i saber sempre ens tindrem és el millor regal que ens podem fer. Quina sort de tenir-vos i com m'agrada poder compartir les vides! Gràcies ambientòlegs: Maria, Pep, Rosa, Métre, Collba, Alexis i als sobrevinguts Pepo, Pere, Marta i Judit. Ja són molts anys des que vam acabar la carrera i seguir-nos trobant i disfrutant de sobretaules és un gust. Gràcies també a la gent de Boulder: Maria, Mònica, Roger, Laia, Raquel, Marta, Jeannie, Pedro, Jose, i tots els que em deixo. Vau fer que els tres estius a Colorado fossin molt més que anar a treballar a l'NCAR.

A les cousins: Ire i Júlia. Sou imprescindibles i m'encanta que sigui així. A l'equipo, les Tapes, quina sort poder desfogar-me en els partits i post-partits de dimecres a hores intempestives. I a la resta de la family: a l'Albert, germà, que sempre hi ets, ho sé! Als avis que ja no hi són des de fa temps, especialment i a l'àvia que fa poc que va marxar, un petó! Als tiets, les tietes i tiet Udina i resta de cosins. Als cunyats i als sogres per la seva generositat.

Finalment, gràcies Pares. Vosaltres sou l'origen de tot, en la confiança que sempre m'heu donat i la possibilitat d'arribar fins aquí. Diuen que educar és molt difícil i crec que vosaltres ho heu sabut fer molt bé. Us estimo!

I gràcies Jordi. Amb tu sóc qui vull ser. Simplement, gràcies per fer-me feliç.

Resum

La capa límit atmosfèrica és la part més baixa de l'atmosfera terrestre on s'hi desenvolupa la vida humana. Es pot definir com la capa d'aire que està directament influenciada per la superfície terrestre i respon als seus forçaments en escales de temps d'una hora o menys. La capa límit en condicions d'estratificació estable i sobre terreny no homogeni esdevé un sistema molt complex amb múltiples interaccions dels processos físics que hi tenen lloc, en un ampli rang d'escales espacials i temporals. Durant la nit en condicions de cel clar o en qualsevol massa d'aire establement estratificada el flux és tèrmicament estable, sense o bé amb poca turbulència i on els moviments verticals tendeixen a ser inhibits. Malgrat això, sovint apareixen episodis de turbulència intermitent i d'ones de gravetat que modifiquen l'estructura dinàmica del flux a la capa límit estable. La turbulència generada en aquestes condicions és altament anisotròpica i amb remolins de molt petites dimensions, de manera que encara és més difícil representar el seu comportament en models teòrics de turbulència. A més a més, els moviments en condicions estables estan molt condicionats per la topografia subjacent i circumdant, generant vents catabàtics, corrents de densitat i vents de capa baixa, que a la vegada poden generar ones de gravetat i turbulència. Donada aquesta complexitat, aquesta tesi pretén contribuir a la millor comprensió d'alguns d'aquests processos i fenòmens que tenen lloc en la capa límit establement estratificada i en zones de terreny heterogeni.

Per a entendre i quantificar algunes de les incerteses que planteja l'atmosfera a la capa límit podem distingir tres procediments que estan molt relacionats entre sí: les descripcions teòriques, les campanyes experimentals i la simulació numèrica. D'una banda, la teoria constitueix la base del procés de comprensió i, sovint, utilitza dades observacionals de campanyes experimentals per a la formulació de relacions matemàtiques. No gaire lluny, els models numèrics permeten la comprensió més enllà de les dades experimentals, així com testejar les descripcions teòriques, a més de simular fenòmens que són molt difícils de mesurar. Principalment en aquesta tesi hem utilitzat, a més d'observacions, models numèrics per afrontar les incerteses que sorgeixen en la capa establement estratificada i en zones de terreny complex.

Aquests models numèrics de predicció del temps contenen les equacions primitives de l'atmosfera per descriure i pronosticar els moviments i propietats de l'atmosfera. Al llarg d'aquesta tesi s'ha utilitzat un dels models més coneguts arreu del món, el *Weather Research and Forecasting* (WRF), emprant dues aproximacions diferents: la mesoscala i el

large eddy simulation (LES). Mentre la metodologia utilitzant la mesoscala ens ha permès investigar els patrons de circulació en un ampli rang d'escales, l'aproximació LES ens ha servit per resoldre explícitament la turbulència i descriure la seva estructura. Des d'un altre punt de vista, la mesocala està basada en parametritzacions físiques necessàries per tancar el sistema d'equacions primitives de l'atmosfera que sovint donen lloc a resultats diferents, mentre que el LES és una bona eina per adreçar algunes de les formulacions incloses en les parametritzacions. En aquesta tesi s'han utilitzat ambdues metodologies per investigar alguns d'aquests aspectes.

Així doncs, amb els motius exposats anteriorment, el principal objectiu de la tesi que es presenta és:

Contribuir a la comprensió dels fenòmens que tenen lloc a la capa límit en condicions d'estratificació estable i sobre àrees de terreny complex i explorar les capacitats i les limitacions de la seva modelització numèrica.

La tesi es divideix en dues parts principals: un recull d'antecedents i teoria de la capa límit atmosfèrica i els fonaments de la modelització i la recopilació dels principals resultats obtinguts en la simulació numèrica de diferents processos físics a la capa límit.

La primera part inclou el **capítol 2** en què es descriu la teoria fonamental de la capa límit, fent especial èmfasi en la descripció de la capa límit estable i dels fenòmens sobre terreny complex: els corrents de densitat, ones de gravetat i ones de muntanya. El **capítol 3** introdueix les bases de la modelització de l'atmosfera, les diferents aproximacions a les equacions que governen el fluid atmosfèric i detalls del model WRF. Per últim, el **capítol 4** recull la teoria fonamental de la modelització a la capa límit i de la turbulència amb la descripció de les seves parametritzacions, principalment les utilitzades en el model WRF. També es tracten els reptes en el futur dels models numèrics a elevada resolució quan s'apliquen sobre terreny complex.

En la segona part s'inclouen tres capítols amb els principals resultats basats en articles publicats o en procés de publicació en revistes científiques indexades. En el **capítol 5**, fent ús del model WRF en l'aproximació de mesoscala, hem determinat l'origen d'una corrent de densitat que va donar lloc a ones de gravetat interna en la zona del *Centro de Investigaciones de la Baja Atmósfera* (CIBA). Hem vist que una massa d'aire amb origen de brisa marítima juntament amb els vents catabàtics originats a les cadenes muntanyoses del voltant són l'origen de la corrent de densitat que genera ones de gravetat al seu pas per l'àrea del CIBA. Les simulacions, a més, assenyalen que l'esquema de capa límit local d'ordre 1.5 reprodueix millor l'estructura de la corrent de densitat que l'esquema no local d'ordre 1.

El **capítol 6** investiga l'estructura vertical de la turbulència en condicions neutrals i estables fent ús del model WRF en l'aproximació LES (WRF-LES). En primer lloc, s'han validat els perfils de primer i segon ordre del WRF-LES amb un cas de referència

en condicions estables. Com a part principal, s'han investigat els règims d'intensitat de turbulència en funció de la velocitat del vent. Malgrat que el règim de turbulència dèbil no s'ha aconseguit simular, s'ha obtingut una relació semblant a les observacions en situació de forta turbulència, amb el creixement de la intensitat de turbulència en funció del vent tot i que, contrari a les observacions, a cada alçada la taxa de creixement varia. Les condicions de contorn del model en la superfície i al límit superior sembla que poden ser les causes de les discrepàncies entre les relacions obtingudes amb les simulacions i les observacions a la capa límit estable.

Finalment, el **capítol 7** inclou l'estudi de les ones de muntanya sobre la orografia complexa del Pirineu. S'ha simulat un cas d'ones atrapades a sotavent amb el model WRF en el mode mesoscalar, per tal d'avaluar la capacitat del model per a representar l'esdeveniment i la variació en els resultats en funció de les seves diferents opcions físiques i de configuració. Hem vist que és necessari baixar la grandària del pas de malla a 1 km per tal de reproduir les ones i la seva propagació. S'han detectat discrepàncies entre la longitud d'ona reproduïda pel model i l'observada amb els núvols lenticulars a partir d'imatges de satèl·lit. Finalment, els **capítols 8 i 9**, conclouen els principals resultats i el treball futur que es planteja derivat d'aquests. També es detallen les diferents línies de recerca que es preveu dur a terme.

Abstract

The atmospheric boundary layer in stably-stratified conditions and over non-homogeneous terrain becomes a complex system with many interactions of physical processes occurring in a wide range of different spatial and temporal scales. During clear sky night-time or in any stably-stratified conditions, flows are generally thermally stable, non-turbulent and vertical motions tend to be inhibited. However, intermittent turbulent events and gravity waves are usually present in the stable boundary layer (SBL), which can substantially modify the flow structure. The generated turbulence can be highly anisotropic and turbulent eddies can be of a very small size, which pose difficulties for the already existing turbulence theoretical models. In addition, the circulations in stable flows can be strongly driven by the underlying and surrounding topography, generating katabatic winds, density currents and low level jets, which in turn, trigger gravity waves and turbulence. Given the mentioned complexity, this thesis aims to contribute to a better comprehension of some of the processes and phenomena that occur in the SBL and over complex terrain areas.

In order to understand and quantify the unknown atmospheric processes one can distinguish three different procedures that are very well connected: theoretical descriptions, experimental campaigns and numerical modeling. The theory constitutes the base for the understanding process and usually utilizes observational data from experimental campaigns to formulate mathematical relationships. Not far, the numerical models allow us to further understand the experimental data, to test the theoretical relationships or to simulate processes which are very difficult to measure. In this thesis we have principally used numerical models to deal with the uncertainties that arise in stably-stratified flows and over heterogeneous terrain and to explore the model capabilities and limitations to resolve them.

These numerical weather prediction (NWP) models contain the primitive equations of the atmosphere to describe and forecast the flow motions and properties. In this thesis we have employed one of the worldwide known NWP model, the Weather Research and Forecasting (WRF) model, using two different approaches: the mesoscale approximation and the large eddy simulation (LES). While the mesoscale methodology has allowed us to investigate the flow circulation patterns in a wide range of scales, the LES approximation has enabled us to explicitly resolve the turbulence and describe its structure. From another perspective, the mesoscale approach is based on physical parameterizations necessary to close the primitive equations which usually lead to different results, whereas LES is a

proper tool to address some of these formulations to be included as parameterizations. In this thesis each methodology has been applied to investigate these different purposes.

Using the WRF model with the mesoscale approach we have determined the origin of a density current that generated internal gravity waves over the *Centro de Investigaciones de la Baja Atmósfera* (CIBA) site. We have seen that the long distance mesoscale sea-breeze circulation and the night-time katabatic flows originated in the surrounding complex topography were the origin of the density current which generated displacement in the air parcels and periodic oscillations. In terms of the gravity wave generation, simulations have revealed differences between local and non-local ABL schemes. The local approach has reproduced in a better way the sharp change in magnitudes with the current entrance and the gravity wave generation, although its arrival is anticipated in time.

In this thesis the vertical turbulence structure using the LES approximation of the WRF model has been investigated. As a previous step, we have first validated the WRF-LES model in the SBL with a reference case by a comparison of the first and second order moments profiles. Using different wind speed initial conditions we can reproduce neutrally and stably stratified flows. However, different from what is observed in the atmosphere, stably stratified flows are strongly coupled with the surface and turbulence is always maintained, event with strong temperature gradients. We have shown how the turbulence intensity increases sharply with the wind speed at each height above ground but the increase rate (slope) is not maintained, as we would have expected. It seems that the top domain potential temperature inversion affects the flow turbulence structure over the whole domain. We conclude that LES simulated flows cannot reproduce the low turbulence range of the hockey-stick turbulence pattern because they are influenced by the surface layer parameterization which strongly conditionates the obtained stably stratified flows.

Finally, we have studied topographically generated gravity waves over the Pyrenees and specifically simulated a trapped lee wave event using the mesoscale approximation with WRF. We have seen that the model is able to reproduce the gravity waves at the lee side of the mountain range with periodic oscillations in all magnitudes. We have seen that a 1-km horizontal resolution is necessary to capture the wave field. We have also shown that upstream conditions have to be well represented in order to capture the adequate wave characteristics. In addition, the simulated case study reveals that the valley circulations near the earth surface are highly modified by the presence of mountain waves aloft, with signals of rotor circulations and turbulent zones.

Contents

1 Introduction

1.1 Background and motivation

The Atmospheric Boundary Layer (ABL) or Planetary Boundary Layer (PBL) is the lower part of the earth atmosphere where the human life is developed. It can be defined as the bottom portion of the troposphere that is directly influenced by the earth surface and it responds to its forcings, such as frictional drag, solar heating, evapotranspiration and terrain induced flow modification with a time scale of one hour or less (Stull 1988). Different from the region above (the free atmosphere), the flows in the ABL are frequently turbulent and the vertical transport of momentum, heat and other scalar quantities (such as pollutants) dominates over the horizontal transport. The small scale (microscale) forcings with temporal and spatial scales located at the lower part of the spectrum, govern the ABL flows (Arya 2001). In addition to the small scale processes, the ABL is a very complex system with interaction of several scales of motion, ranging from large-scale weather events to mesoscale circulations and the mentioned fine-scale turbulence motions. For these reasons, dealing with atmospheric flows in the lower part of the atmosphere is not an easy task and many efforts are necessary for a comprehensive understanding of the involved physical processes.

The ABL has been widely studied analyzing observations obtained through fixed instrumentation sites (towers, surface sensors, etc) and experimental campaigns. Most of these campaigns and intensive measurements have been done in homogeneous, flat terrain. Having data in this *canonical* conditions is very useful to understand, describe and formulate many ABL processes; however, the real world is not flat and homogeneous and it includes many processes at different scales interacting together, which makes the ABL

a very complex system. A useful technique for studying the ABL including the circulation interaction between different scales, in different dimensions and temporality, are the numerical models. These models applied to the atmosphere are mathematical models that resolve the primitive non-linear differential equations of the atmosphere to describe and to forecast the atmospheric flow properties.

Since the beginning of the 21^{st} these numerical weather prediction (NWP) models have been extensively used by the atmospheric science research community. They have many capabilities and possibilities to be used, as they cover almost all the dimensions in space and in time. Global models are used to study global dynamic circulations and climate change scenarios. Within the mesoscale range, Mesoscale Meteorological Models (MMMs) are usually the NWP models used for operational forecasts for a delimited area of interest. Using the nesting capability of these models, forecasting the atmospheric flows and phenomena associated to different scales, from global to mesoscale and including microscale is technically possible. Among the existing MMMs, the Weather Research and Forecasting model (WRF) is one of the most used mesoscale models in the scientific and weather service community that allows the simulation of atmospheric flows in all these different scales.

As MMMs are relatively new, there are still many things to improve and to explore in them. Specifically, one of the great challenges is the correct parameterization of the physical processes that cannot be resolved by the dynamic core of the model. These physical processes are usually sub-grid, that is, their dimensions are below the grid model size. Regarding the ABL, the parameterization of the turbulence is well described by the daytime convective conditions, when turbulence is strong and there is a well-mixed layer. Nevertheless, during night-time, when the soil radiation balance is governed by the long wave emission term, both the surface and the air in contact above it cool, leading to the formation of the Stable Boundary Layer (SBL). Then turbulence is weak, intermittent or may be suppressed, and many uncertainties arise. Most importantly, certain phenomena that occur during night-time in the SBL, such as drainage winds (Soler et al. 2002), katabatic flows (Cuxart et al. 2007), low level jets (Conangla and Cuxart 2006; Cuxart 2008), gravity waves (Chimonas 2002; Adachi et al. 2004; Bastin and Drobinski 2005; Viana et al. 2010; Udina et al. 2013; Román-Cascón et al. 2015), some of them producing intermittent turbulence (Sun et al. 2002, 2004; Terradellas et al. 2005), and other submeso motions (Mahrt 2014), can substantially modify the ABL structure and circulation so the models have to represent them properly. In a similar way, many parameterizations of the ABL are designed for homogeneous and flat terrain but it is not clear how well they can describe phenomena that occur in heterogeneous complex terrain (mountainous areas), such as mountain-valley winds, gravity waves or lower turbulent zones. In particular, one of these complex terrain generated phenomena, mountain waves, have a great influence on the flow circulation and momentum transport (Hoinka 1984) and can be accompanied by clear-air turbulence (Clark et al. 2000), lee-wave rotor formation (Mobbs et al. 2005;

Darby and Poulos 2006; Vosper et al. 2006; Grubišic and Billings 2007; Sheridan et al. 2007; Doyle et al. 2009; Cohn et al. 2011), downslope winds (Mobbs et al. 2005; Klemp and Lilly 1975) and windstorms (Lilly 1978). This thesis aims to contribute to a better understanding of the ABL in the previous situations, when it is stably stratified and over complex terrain, using the WRF model, for both, helping the phenomena description and analyzing the model capability to reproduce them. Observational data has also been used, obtained from experimental campaigns, in order to study the phenomena at a local scale, while the model has allowed to study them through a mesoscale perspective.

From another point of view, NWP has evolved very fast in 15-20 years thanks to the growing computer capacity in such way that nowadays it is possible to run simulations from grid spacing of tens of km to grids of tens of meters, either parameterizing the turbulent fluxes (Seaman et al. 2012) or explicitly resolving the turbulence (Talbot et al. 2012). Conceptually, though, there is a limit of increasing the grid resolution in the mesoscale range, that is when the length scale of the turbulent eddies becomes of the order or larger than the grid size. When this limit is reached, the turbulence is not parameterized anymore and it has to be resolved by the model dynamics, what is called the Large Eddy Simulation (LES). These LES models are able to resolve explicitly the three dimensional turbulence in atmospheric flows (Moeng 1984; Mason and Derbyshire 1990; Nieuwstadt et al. 1993; Brown et al. 1994; Sullivan et al. 1994; Andren 1995; Kosović and Curry 2000; Saiki et al. 2000; Cuxart et al. 2000; Basu and Porté-Agel 2006; Jimenez and Cuxart 2005; Beare et al. 2006; Moeng et al. 2007; Huang and Bou-Zeid 2013). As the atmospheric processes will be better resolved with a smaller grid size and computer capacity will not be a limitation, the NWP is going towards using finer grid spacings, and therefore LES will be needed. For this reason LES technique has lately caught the interest of the ABL modelers, thus, in the near future the proper coupling between MMMs and LES seems to be the next step to achieve. In that sense, part of this thesis also aims to assess the WRF-LES model accurateness in simulating the turbulence structure, specially under stable conditions.

In all this context, this thesis aims to deal with the presented topics from a modeling perspective to assess the numerical model capabilities and limitations to reproduce certain physical processes observed in the ABL and to contribute to their better comprehension.

1.2 Objectives

As presented before, this thesis deals with processes and uncertainties that occur in the ABL when it is stably stratified and/or over complex terrain using numerical models and observational data. The main goal of this thesis is:

- **To contribute to a better knowledge of the processes that occur in the atmospheric boundary layer in stably-stratified conditions and over complex terrain areas and establish the capabilities and limitations of their numerical modeling.**

1.2.1 Specific objectives

The specific objectives dealt with are:

- To determine the origin of Internal Gravity Waves observed in the CIBA site using the WRF model.
- To investigate the ability of the WRF model to reproduce mesoscale phenomena: density currents and internal gravity waves.
- To explore the mesoscale horizontal and vertical structure of a density current that outbreaks at the CIBA site during eight consecutive late evenings.
- To validate WRF-LES in the stable boundary layer comparing the obtained profiles with a reference case.
- To examine the vertical structure of turbulence in neutral and stably stratified conditions with the WRF-LES model.
- To assess the WRF-LES simulation limitations in resolving the turbulence related to the boundary conditions.
- To study the predictability of the WRF model to capture a trapped lee wave event over a complex terrain area: the Pyrenees.
- To evaluate the influence of the PBL model physics, resolution and resolved topography on mountain waves characteristics, wavelength and amplitude.
- To explore the circulations near the earth surface below the mountain waves and the possible rotor formation areas.

1.3 Structure of the thesis

This thesis is divided into two main parts: (i) a theoretical background on the atmospheric boundary layer and its modeling fundamentals (ii) the achieved results of numerical model simulations of different physical processes in the ABL.

The first part contains three different chapters. **Chapter 2** includes the theoretical framework of the ABL, specifically dealing with the stable ABL and its features in complex terrain. **Chapter 3** introduces the fundamentals of modeling the atmospheric flows to understand their different possible approaches, the governing equations and a description of the mesoscale model used in this thesis. The last chapter of this first part, **chapter 4**, describes some of the key points of modeling the ABL, the parameterizations used in the WRF model, the large-eddy simulation approach and the issues when modeling over complex terrain.

The second part includes the results of the four peer reviewed articles (see Sect. 1.4) divided in three chapters. The first chapter, **chapter 5**, presents a case study of a density current and the associated gravity waves at the CIBA site using mesoscale modeling. The aim of the study is to understand the origin of the gravity waves observed from the CIBA tower measurements Viana et al. (2010) and determine the capability of the model to reproduce them. In addition, the event was observed to be frequently repeated; therefore, a sequence of eight density currents were also modeled and analyzed in detail. This chapter contains all the results published in Udina et al. (2013) and some in Soler et al. (2014).

Chapter 6 explores the vertical structure of turbulence in neutrally and stably stratified flows using the WRF-LES. More specifically, the main goal is to investigate the relationship between the turbulence strength and the wind speed found in Sun et al. (2012) with a resolving-turbulence model (WRF-LES). Previously, a validation of the WRF-LES model in the SBL is presented in comparison with a reference case (Beare et al. 2006).

The last chapter of results, **chapter 7**, looks into modeling atmospheric flows over complex terrain, specifically about the mountain wave phenomena over the Pyrenees area. A trapped lee wave event is analyzed through mesoscale modeling in order to study the wave pattern and distribution and the different model sensitivity to reproduce it. The predictability of this mountain wave event is addressed with the arising uncertainties.

Chapter 8 summarizes general conclusions with the main achievements obtained in this thesis and specific conclusions for each chapter of results. **Chapter 9** presents the future work that may come out of the obtained results and the planning of future perspectives.

1.4 Papers

The scientific articles published or in process of being published in peer-reviewed journals included in this thesis are:

- Paper 1: **Model simulation of gravity waves triggered by a density current**

  M. Udina, M.R. Soler, S. Viana, C. Yagüe

  2013. Quarterly Journal of the Royal Meteorological Society. 139 (672): 701-714.

- Paper 2: **Observational and Numerical Simulation Study of a Sequence of Eight Atmospheric Density Currents in Northern Spain**

  M.R. Soler, M. Udina, E. Ferreres

  2014. Boundary-Layer Meteorology. 153 (2): 195-216.

- Paper 3: **Exploring vertical turbulence structure in neutrally and stably stratified flows using Weather Research and Forecasting - Large-Eddy Simulation model (WRF-LES)**

  M. Udina, J. Sun, B. Kosović, M.R. Soler

  2015. Accepted in Boundary-Layer Meteorology Journal.

- Paper 4: **A modeling study of a trapped lee wave event over the Pyrenees**

  M. Udina, M.R. Soler, O. Sol

  2015. Submitted to Monthly Weather Review Journal.

Part I

The atmospheric boundary layer: background theory and modeling fundamentals

2

The Atmospheric Boundary Layer

Contents

In this chapter we introduce the general structure and classification of the ABL, a description of the turbulence and the specific features of the ABL over complex terrain, describing phenomena such as density currents, gravity waves and, specifically, mountain waves.

2.1 The ABL structure

The ABL is defined as the part of the troposphere that is directly influenced by the presence of the earth's surface, and responds to surface forcings with a timescale of about an hour or less (Stull 1988). The ABL can be explored over the sea or over land, and forcings are very different in both conditions. Over land, the ABL has a diurnal cycle and is mostly influenced by the local scales, because of the topography influence. In contrast,

over the sea the ABL is mainly driven by the synoptic scale processes or advected air masses and less influenced by the diurnal cycle.

Over land, for clear sky conditions, in high pressure regions and over homogeneous terrain, the structure and evolution of the ABL can be summarized with the popular scheme from Stull (1988) (adapted in Fig. 2.1). The vertical layers within the ABL can be classified in: the surface layer, the outer layer and the capping layer (or entrainment zone). Above the capping inversion there is the free atmosphere, where the effects of the earth's surface are not noticeable anymore. The surface layer is the very low region in contact with the surface (usually considered a 10% of the ABL) where the fluxes are nearly constant. The outer layer is the region above the surface layer and below the capping inversion which is formed by the Convective Boundary Layer (CBL) during daytime, or the Stable Boundary Layer (SBL) and the Residual Layer (RL) during night-time (both forming the nocturnal boundary layer, or NBL). The capping inversion is a layer of statically stable air that limits the boundary layer and the free atmosphere, acting as a lid to the rising thermals thus restraining the domain of turbulence (Stull 1988).

The ABL depth (also named PBL height) depends on the turbulent mixing that can be thermally- or mechanically-generated (see Sect. 2.2). During daytime the ABL is deep ($\approx$ 1-2 km) dominated by the amount of heating that induces the air convection, mixing and homogenization. During night-time, as there is no heating forcing from the sun, the thermal turbulence is suppressed. The ground emits long-wave radiation and cools off, and so does the air in contact with the surface, a temperature inversion is formed and air becomes statically stable. The PBL depth is, then, lowered to a few hundreds of meters.

The CBL is formed by a superadiabatic surface layer and an adiabatic mixed layer above. It is characterized by strong mixing and large eddies that distribute heat and water vapor, momentum or pollutants. It is formed during late morning and afternoon periods over land, from the surface to the entrainment zone (Arya 2001). The wind profile is sub-geostrophic and follows the logarithmic profile near the surface and is uniform above it (see profile in Fig. 2.1). The SBL, instead, is defined as a non-turbulent (or sporadic turbulent) layer with statically stable air that inhibits the vertical motions and turbulent eddies tend to be of smaller size than in CBL. As we said, it is formed at night due to the radiative cooling of the ground surface or by the advection of a warmer air over a cooler surface. The wind speed is weak or calm near the surface due to the surface friction and accelerates aloft, producing a low-level jet (LLJ) maximum (see profile in Fig. 2.1). The LLJ may be generated by inertial oscillation of wind or by the existence of some source of baroclinicity at low levels that can generate low-level circulations (Cuxart 2008). The SBL depth increases as the night progresses below the RL, which is a remaining layer of similar characteristics to the daytime CBL, that remains during night-time (see Fig. 2.1). The RL is neutrally stratified, i.e. an adiabatic layer but without convection, and with a vertically uniform potential temperature gradient ($\partial\theta/\partial z = 0$) and adiabatic cooling.

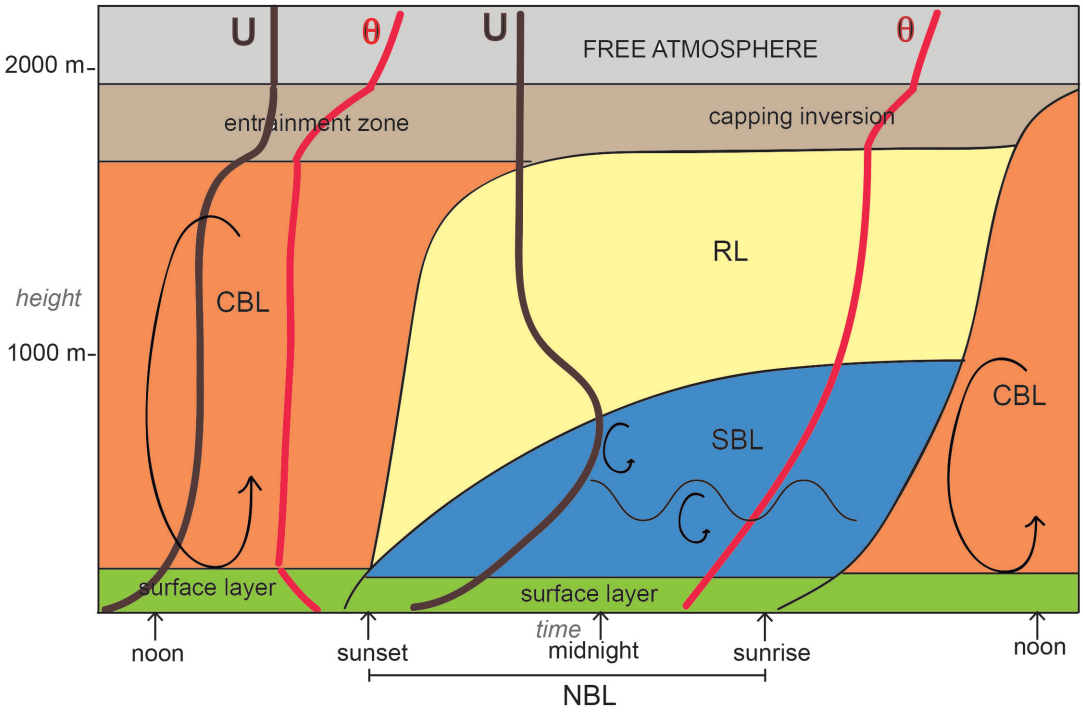

Figure 2.1: Evolution and structure of the daily ABL in high-pressure and clear-sky conditions, with the profiles of potential temperature (θ) and wind speed (U) for daytime and night-time conditions. Scheme adapted from Stull (1988).

This thesis mainly deals with the SBL or stably-stratified flows from a modeling perspective. Chapters 5 and 7 are related to phenomena that occur in stably-stratified flows over non-homogeneous terrain and how a mesoscale model is able to reproduce them. Chapter 6 focuses in the turbulence structure of stably stratified flows through LES modeling.

2.1.1 Classification of the SBL

Due to the complexity and the interaction of many factors in the SBL, it is much less understood than the CBL. Turbulence is suppressed or intermittent, then, pollutants can be confined or spread horizontally because the vertical motions are inhibited. In the SBL turbulence is anisotropic, which makes it difficult to describe through the Kolmogorov theory. In addition, in the SBL, underlying topography and local circulations become very important producing phenomena such as katabatic winds, density currents, low level jets, gravity waves, etc. that modify the ABL structure and interact in different scales. Turbulent eddies in the SBL are generated mechanically, by shear, and can be very small in strongly stratified environments.

In order to understand and quantify the processes in the SBL, several experimental campaigns have been carried out since the middle of the 20^{th} century. One of the first observational efforts was the Kansas experiment in 1968, designed to verify the scaling parameters in the surface layer in the SBL. In 1998 the first campaign in low to mid-latitudes took place in northern Spain, at the CIBA (Centro de Investigaciones de la Baja Atmosfera), named SABLES98 (Stable Atmospheric Boundary Layer Experiment in Spain-1998) (Cuxart et al. 2000). Soon after, the CASES99 (Cooperative Atmosphere-Surface Exchange Study - 1999) (Poulos et al. 2002) took place in a flat terrain area in Kansas (USA), which was one of the biggest campaigns designed to study the NBL phenomena, dealing with the understanding of turbulent events in the night-time, involving many measurements and participants. Later, again at the CIBA site, the SABLES2006 (Yagüe et al. 2007) field campaign was carried out during summer. Since 2006 the Meteor Crater Experiment (METCRAX) in Arizona has been conducted to determine the role that basin-scale seiches and internal waves play in transport and mixing in basin stable layers. More recently, in 2011, the BLLAST (Boundary-Layer Late Afternoon and Sunset Turbulence) (Lothon et al. 2014) took place in southern France, dealing with the transition from the CBL to SBL.

Since long ago, and still nowadays, a lot of efforts are put in improving the understanding and in theoretically describing the SBL, through observations and/or modeling. Around 1950s, Monin and Obukhov were the first that introduced the stability effects in the surface layer mixing description, what later lead to the Monin Obukhov Similarity theory (MOST). The MOST is a relationship that describes the vertical behavior of nondimensionalized mean flow and turbulence properties in the surface layer. In terms of turbulence, Mahrt (1998) classified the SBL into weakly stable, moderately stable and very stable regimes, depending on the variation of the sensible heat flux with the stability parameter (z/L), where z is the height above ground and L is the Obukhov length ($L = -\frac{\theta u_*^3}{kg\overline{w'\theta'}_s}$), where u_* is the friction velocity, k the Von Karman constant, g the acceleration of gravity, $\overline{w'\theta'}_s$ is the sensible heat flux at the surface. They established that for weaker stability, the heat flux decreases with decreasing z/L due to weaker temperature fluctuations. They also found that for weakly stable conditions the variances scale according to Monin-Obukhov similarity theory (more details in Sect. 4.3.4), but it was not the case for very stable conditions. More recently, Sun et al. (2012, 2015a) classified the turbulence regimes in the NBL from a different perspective. After analyzing the CASES99 dataset, they distinguished three different regimes of turbulence mixing from the surface up to 55 m, based on the relationship between the turbulence strength ($V_{TKE} = \sqrt{TKE}$), where TKE is the turbulent kinetic energy, and the wind speed (V) at each height ($V(z)$). Two main regimes are defined, separated by a threshold wind speed (V_s). The first regime is defined within wind speeds below V_s and is characterized by weak turbulence generated by shear over a finite $\delta z < z$. The second regime is a strong turbulence regime when $V > V_s$. Observations from Sun et al. (2012) suggest that the strong turbulence regime is

dominated by large coherent eddies that scale with z, implying that turbulence is generated by bulk shear (V/z, i.e., $\delta z = z$). They referred to the dramatic transition of the two regimes as the HOckey-Stick Transition (HOST) (Fig. 2.2). Occasionally. the turbulence strength is stronger than its shear generation at z with $V < V_s$, which may occur when turbulence is generated by large disturbing events above the ground, such as breaking waves or under low-level jets (LLJ), and this is defined as the third regime. Most importantly, their observations challenge the traditional turbulence parameterization based on Monin-Obukhov similarity theory (MOST), which relies on local vertical gradients.

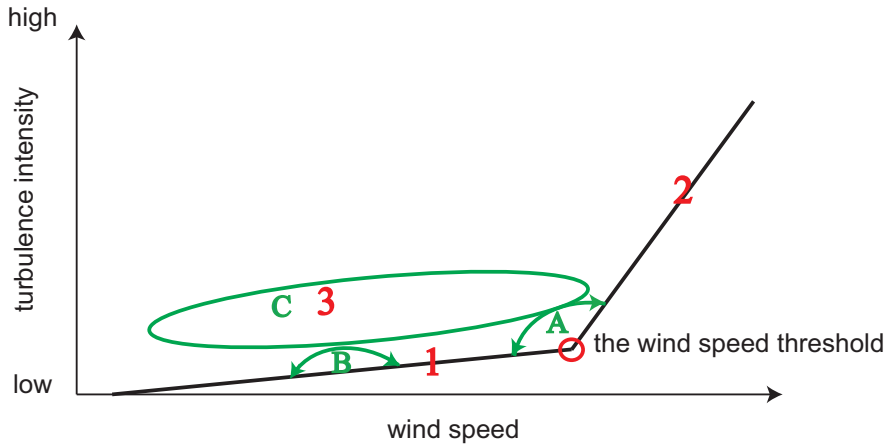

Figure 2.2: Figure 2 from Sun et al. (2012): Schematic of the three turbulence regimes (red numbers) and the three categories of turbulence intermittency (green letters) commonly observed during CASES-99 at each observation height. Turbulence in regime 1 is mainly generated by local instability. Turbulence in regime 2 is mainly generated by the bulk shear. Turbulence in regime 3 is mainly generated by top-down turbulent events. Source: Sun et al. (2012) ©American Meteorological Society. Used with permission.

Chapter 6 explores the vertical turbulence structure based on the regimes defined by Sun et al. (2012) within neutral and stable conditions through Large-eddy simulation modeling.

The aforementioned description of the ABL structure and classification applies to fair weather, clear sky and homogeneous terrain conditions. The real atmosphere, though, is much more complicated than that. In this thesis, we will not deal with precipitation, neither with cloudy ABLs which, of course, may interact with turbulence (Vilà-Guerau deArellano 2007) and modify the general patterns in the SBL. However, we will focus on the ABL over non-homogeneous terrain (Sect. 2.3).

2.2 Turbulence in the ABL

Turbulence is inherent in many natural processes in Earth. In fluid dynamics, *turbulence* can be defined as irregular fluctuations occurring in fluid motions. Following the American Meteorological Society (AMS) definition for turbulence in the atmosphere, it can also be defined as "random and continuously changing air motions that are superposed on the mean motion of air". Within the lower part of the troposphere, flows are frequently turbulent. Some common characteristics of turbulent flows are: rotational, three-dimensional, dissipative, unpredictable and where the inertial forces dominate over viscous forces. The Reynolds number (Re) is a parameter to determine whether a flow is laminar (non-turbulent) or turbulent. Re is defined as the ratio between the inertial forces and the viscous or friction forces:

$$Re = \frac{Ul}{\nu} \tag{2.1}$$

where U is the velocity, l the length scale and ν the kinematic viscosity, which is the dynamic viscosity divided by the density ($\nu = \mu/\rho$). Re is a good indicator of the flow type. A laminar flow has low Re number and therefore the viscous forces are dominant and the fluid motion is smooth and constant. A turbulent flow will have high values for Re, will be dominated by inertial forces and will tend to produce chaotic motions, eddies and instabilities. Generally, atmospheric flows are characterized by large ($Re \sim 10^7$ to 10^8), so the inertial forces dominate over the viscous forces.

Due to the randomness nature of the turbulence we use statistical methods for its description. Reynolds (1894) developed the Reynolds decomposition, a mathematical technique which separates the average $\overline{\phi}$ part (temporal or spatial) and the fluctuating ϕ' part (which varies very fast) of any quantity ϕ:

$$\phi = \overline{\phi} + \phi' \tag{2.2}$$

The average or mean part represents the effects of the mean flow properties and the perturbation part can represent either the wave effect or the turbulence effect that is superimposed on the mean flow (Stull 1988). To statistically describe the turbulence we use the variances and covariances. The variance ($\overline{\phi'^2} = \sigma_\phi^2$) represents the dispersion of data about its mean value and the covariance ($\overline{\phi'\psi'}$), the degree of common relationship between the two variables ϕ and ψ. A common nomenclature is to refer to mean $\overline{\phi}$ as the first-order moment, and the variance σ_ϕ^2 and the covariance ($\overline{\phi'\psi'}$) as the second-order moments. Third order moment, skewness, represents the upward (when positive) and downward (when negative) transport of the variance. A detailed formulation of these order moments is given in Sect. 4.4.1.

The origin of the turbulence in the ABL can be either mechanical (wind shear caused by friction with the surface, flow passing through an obstacle, etc), or thermal (convective mixing generated by solar surface heating). Within the ABL, turbulence can be continuous or intermittent, strong or weak. It is usually considered stationary, so its properties do

not vary with time and it is often considered homogeneous in the horizontal, but not in the vertical dimension. Turbulence is isotropic when its statistical properties do not vary with the coordinate system orientation; however, in the ABL it can be very anisotropic, for instance near the surface or in stably stratified environments. All fluids are turbulent unless they have a very low Reynolds number or very stable stratification (Wyngaard 2010).

A useful parameter to measure the turbulence intensity is the Turbulent Kinetic Energy (TKE). It includes the variances of the zonal, meridional and vertical wind components, u, v and w respectively, defined as:

$$TKE = \frac{1}{2}\left(\overline{u'^2} + \overline{v'^2} + \overline{w'^2}\right) = \frac{1}{2}\overline{u_i'^2} \tag{2.3}$$

The TKE is related to the transport of momentum, heat and moisture. The physical processes that generate turbulence can be described by the different terms of the TKE budget equation (see Sect. 3.2.2). The TKE has a diurnal cycle so it increases in the morning reaching its maximum in the afternoon and decay fast in the evening.

In terms of eddy sizes, production of turbulence is usually within the large eddy range (low frequencies or wavenumbers) and dissipation is greatest for smallest eddy sizes (high frequencies or wavenumbers). Dissipation can be described as the molecular destruction (viscous dissipation) of turbulent motions. This small-scale turbulence is, in turn, driven by the *cascade* of energy from the large eddies (Stull 1988). The middle portion between the large energy-containing eddies and small viscous eddies is called the inertial subrange (Fig. 2.3). In the *inertial subrange* there is an equilibrium between the energy containing eddies and the rate of dissipation such that $S \propto \epsilon^{2/3} k^{-5/3}$, where S is the spectral energy in a Fourier decomposition of a turbulent signal, ϵ is the viscous dissipation of the TKE and k is the wavenumber. This was shown by Kolmogorov (1941) establishing the -5/3 slope in the spectrum.

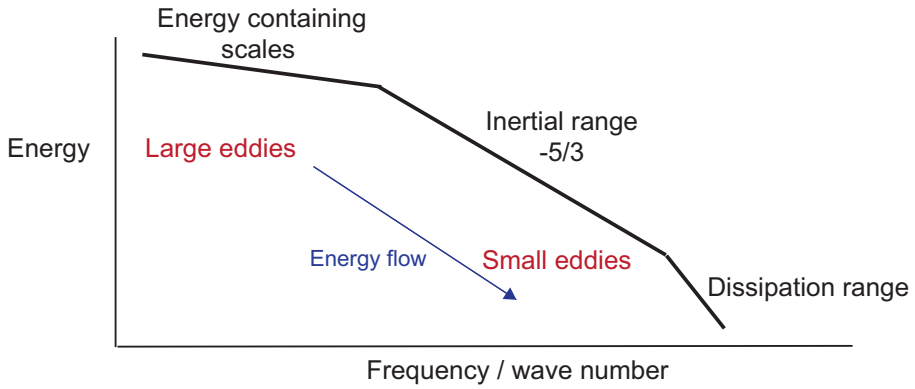

Figure 2.3: Turbulence spectrum scheme.

2.2.1 Turbulence analysis: Fourier and Wavelet transforms

In order to deeply study the turbulence we usually look at the size of the turbulent eddies. The traditional Reynolds decomposition where the mean values are separated from the turbulent part of the magnitude is a good approximation to describe the turbulence when the scales are well separated and there is a spectral gap between the large eddies and the small eddies, so the mean value is much larger than the fluctuating part, as in CBLs. However, when the scales of motions are not clearly defined and the gap is not present (as in SBL), other methods are needed (Terradellas et al. 2001).

The Fourier transform is one of these techniques and it is useful to analyze the different scales of motion in any data series. It is a function that decomposes a signal into sine and cosine waves of different amplitudes and frequencies, so we can obtain a two dimensional information about frequencies that are dominant within the signal, considered stationary, and their respective amplitude.

During the last decade of the 20^{th} century, another method was developed in order to deal with non-stationary signals which uses a fully scaleable window computed at different scales, the Wavelet transform (Torrence and Compo 1998; Terradellas et al. 2001). It is a mathematical tool that gives a time-frequency (or space-wavenumber) representation simultaneously, so for instance, in a time series, it gives the time evolution of the different frequencies that take part in the series (Terradellas et al. 2001). Then, it allows the analysis of time or distance series at very different scales, for instance, to distinguish between coherent structures (for example gravity waves) and small scale turbulence (Cuxart et al. 2002; Terradellas et al. 2005; Viana et al. 2010).

2.3 The ABL in complex terrain

Certain circulations and phenomena that occur within the ABL are caused by the presence of the topography, specifically, due to the interaction between the ambient winds and the terrain. Some examples are slope flows, katabatic winds, valley winds, drainage currents, low-level jets, etc. Due to the spatial extension of these systems they can be considered as orographic mesoscale phenomena. The presence of the terrain also induces wave motions in the atmosphere in a stably stratified environment, i.e. gravity waves and/or mountain waves. Sometimes, these mountain waves are associated with strong turbulence at low levels, the phenomenon known as rotor.

In this section we will focus on their effects on the ABL, specifically analyzing in detail two of these mesoscale systems: the density currents and gravity waves and, more specifically, the mountain waves.

2.3.1 Density currents

Density currents (also called gravity currents or buoyancy currents) are flows created by differences in the density of two adjacent fluids. They can be originated by large synoptic scale or mesoscale systems such as cold fronts, sea-breeze fronts, squalls, etc. They appear in a wide range of scales, from synoptic systems, mesoscale circulations or smaller scale local circulations. From the boundary-layer point of view, they are important because they produce a significant disturbance when they appear or they break out in a certain zone. They are a well-known source of turbulence and internal gravity wave activity (Simpson 1999). Among several origins of the density currents, we will detail, here, the sea-breeze and mountain slope winds.

The sea-breeze is a thermal circulation developed near the coastal zones produced by the different heating over water and land. As the heat capacity of water is larger than the heat capacity of the land surface, the land is warmer than the water during the day and cooler at night (Stull 1988). During the day, the resulting pressure gradient leads to a surface air movement from sea to land and a reverse circulation aloft. The sea-breeze intensity depends on the latitude, the time of the day and the land topography. In the mid-latitudes it is usually developed during spring and summer, when the temperature between water and land is larger (Soler et al. 2011). Sea-breezes can trigger cold air currents inland, generating mesoscale systems creating horizontal temperature gradients. They can initiate and help the development of katabatic flows and drainage currents and later generate internal gravity waves (Udina et al. 2013). Not so often, sea-breeze circulation can induce oscillations during day-time (Bastin and Drobinski 2005).

On the other hand, in mountainous terrain there are many circulations developed due to the presence of sloping terrain and thermal differences between day and night. Three different circulations can be distinguished, from a larger to a smaller scale:

- Plain-mountain winds during day-time and mountain-plain winds during night-time.
- Up-valley winds during day-time and down-valley winds during night-time.
- Anabatic flows during day-time and katabatic flows during night-time.

More specifically, katabatic or drainage winds are cold, dense, air flows moving downslope under the influence of gravity. The characteristic wind profile of the katabatic winds is a reduced wind speed near the ground due to surface friction, and a pronounced maxima at a certain height. Katabatic flows can be initiated by local surface cooling or by an earlier mesoscale system (Papadopoulos and Helmis 1999). In contrast, the anabatic winds are developed during day-time because the air over the slope is warmer and less dense than the air over the valley at the same level, so a horizontal pressure gradient is created which drives acceleration of the flow up the slope. As gravity does not accelerate the flow in this case, anabatic winds are usually less intense than katabatic winds.

Sometimes, katabatic winds are the origin of gravity currents affecting long distance areas (Adachi et al. 2004; Udina et al. 2013). When katabatic flows are very shallow or occur in small scales, they are also called nocturnal drainage flows. They can be originated in a gentle slope (Blumen et al. 1999; Cuxart et al. 2007) or in a shallow gully (Mahrt et al. 2001; Soler et al. 2002), and they can lead to mixing and intermittent turbulence. Katabatic winds and drainage currents have also been found to generated internal gravity waves (Chemel et al. 2009; Viana et al. 2010) and to interact with mountain waves (Poulos et al. 2000). Density currents are often a recurrent phenomenon that causes a disruption of the balanced flow during several days and repeated periods (Mayor 2011; Soler et al. 2014). Density currents have been often associated with intermittent turbulent episodes due to local thermal shear instabilities (Sun et al. 2002; Terradellas et al. 2005).

Both sea-breeze and mountain winds can be a source of gravity waves formation that modify the ABL structure.

2.3.2 Gravity waves

In terms of the Reynolds decomposition, waves can be defined as a fluctuation part of the air flow that would represent the wave effect superimposed on the mean wind (Stull 1988). Waves are very effective in transporting momentum and energy but transport little heat, moisture or other scalars (such as pollutants) (Stull 1988). They can be originated by the mean wind flowing over an obstacle (isolated peaks, mountain ranges), by a disruption of the balanced flow (density currents, downslope winds, density interfaces etc.), by vertical shear instability or between flows of different densities, among others. Gravity waves (GWs) are buoyancy perturbations only possible in stably stratified environments, initiated by the vertical displacement of the flow streamlines. As the atmosphere is always stably stratified over the PBL, gravity waves are everywhere in the atmosphere (Gossard and Hooke 1975). Within the PBL, gravity waves can be present during night-time, in stably stratified conditions. However, we cannot see the gravity waves, we can only see their effects on the atmosphere (Nappo 2002).

More specifically, internal gravity waves (IGW) are gravity waves formed in a fluid with continually varying density and have their maximum amplitude within the fluid (Markowski and Richardson 2011). In contrast, external gravity waves are those formed along the interface between two fluids of very different densities (as waves in the water surface). Here, by saying *gravity waves* we will be referring to *internal gravity waves*, as the atmosphere is a continuous fluid. In the IGW, the air parcels are lifted from its original equilibrium level by any disturbance which forces the elevation (mountain peak, disruption of air flow, etc.). After being risen, the air parcels become cooler and denser than the environment. When they reach the wave crest, the restoring force pushes back the parcels to its original equilibrium level and usually they overshoot it, then, the parcels become warmer and less dense than the environment and rise again. This oscillation mechanism can be maintained during minutes to hours until the frictional drag or turbulence dampens

it. The wave mechanism can also be seen as a continuous exchange between potential and kinetic energy, as the parcel initially gains potential energy and the restoring force generates a periodic energy exchange between potential and kinetic energy developing the wind speed oscillations (Sun et al. 2015c). In this type of waves potential temperature (θ) and vertical velocity (w) streamlines are 90° out of phase (Fig. 2.4), which indicates that buoyancy waves are effective in transporting momentum but they do not transport any heat.

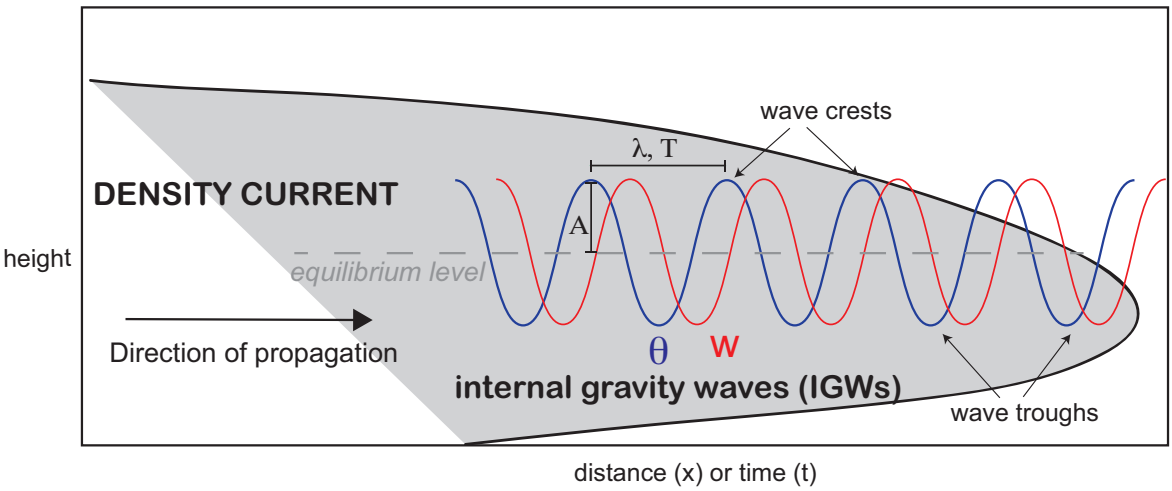

Figure 2.4: Density current and internal gravity waves (IGWs) scheme. Parcels are displaced from the equilibrium level and potential temperature (θ) and vertical velocity (w) fields oscillate with a certain period (T_f) or wavelength (λ), amplitude (A).

Regarding the general atmospheric circulation, GWs are important because they transport momentum horizontally and vertically, and may influence the momentum balance in the stratosphere. They are a source of turbulence production when they break, anywhere in the atmosphere. In addition, they can trigger convection and they can significantly affect the atmospheric mean horizontal flow, because vertical motions are much more significant with the presence of GWs. In the SBL gravity waves are significant because they transport momentum and energy at speeds that are different from the background wind (Sun et al. 2015b). More importantly, they can be a source of turbulence producing intermittent turbulence in the SBL. At the same time, the presence of the GWs in the SBL can modify the turbulence structure (Sun et al. 2015b).

On the other hand, another type of gravity waves can also be generated by instabilities and when stability is negligible, the so-called vorticity waves. In regions where strong shear exists across a density interface, they are called Kelvin-Helmholtz (KH) waves, for instance at the entrainment zone or in the top of a drainage current. Regions where KH waves are

developed can be critical levels, where the directional wind speed equals to the wave phase speed, and the deposition of horizontal momentum is likely to occur and waves break into turbulence (Nappo and Chimonas 1992; Dörnbrack and Nappo 1997).

Any oscillating surface displacement (y) as a function of position (x) and time (t) can be described by a solution of the form: $y(x,t) = Acos(kx - \omega t)$ where A is the amplitude, k is the wavenumber and ω is the angular frequency, so that $\omega = 2\pi f$, where f is the linear frequency. Thus, any oscillation can be characterized by their frequency or period of oscillation, their wavelength or wave number, their amplitude and their velocities (Fig. 2.4). The linear frequency (f) is the measurement of how many cycles happen in a certain amount of time and the period (T_f) is the amount of time between one cycle and it is the inverse of f, so $f = \frac{1}{T_f}$. In terms of spatial displacement, the wavelength (λ) can be defined as the distance between two wave crests and the wavenumber is the inverse of λ, then: $k = \frac{1}{\lambda}$. The amplitude (A) of a wave is the measurement of how big the wave is and it is measured as the height from the equilibrium level to the crest or the trough. The phase velocity is the velocity of the wave, defined as $c = f\lambda$, and it is the rate at which the phase of the wave propagates in space. For example, being fixed at the crest of the wave, it will appear to travel at the phase velocity. The group velocity (c_g) can be defined as the velocity at which the energy of a group of oscillations is propagated (Holton and Hakim 2012). In addition, the intrinsic wave frequency (f_i) can be defined as the frequency of oscillation measured by an observer or sensor that moves with the mean wind:

$$f = f_i + \frac{\overline{U}}{\lambda} \tag{2.4}$$

Then, for a standing (stationary) wave, such as a mountain wave, $f = 0$ so that the intrinsic frequency equals to the opposite wind effects ($f_i = -k\overline{U}$).

On the other hand, the Brunt Väisälä frequency (N) is defined as the frequency at which an air parcel will oscillate when displaced vertically within a statically stable environment:

$$N = \left(\frac{g}{\overline{\theta}} \frac{\partial \overline{\theta}}{\partial z} \right)^{\frac{1}{2}} \tag{2.5}$$

where g is the gravitational acceleration, θ is the potential temperature and z the altitude. N is used to measure the stability within a statically stable environment and so the ability of the environment to support the existence of IGWs. When the oscillations have a frequency smaller than N they are considered IGWs.

The IGWs have been studied through linear theory, observational campaigns and modeling studies. Many studies have dealt with the theory of the IGWs (Rottman and Einaudi 1993; Nappo 2002; Chimonas 2002). They have been observed in the NBL (Sun et al. 2004) in katabatic flows (Gryning et al. 1985; Bastin and Drobinski 2005) and within gravity currents or drainage flows (Adachi et al. 2004; Viana et al. 2010; Ferreres et al. 2013). However, the interaction between waves and turbulence in the SBL is still not

so well documented. Einaudi and Finnigan (1993) studied the wave-turbulence dynamics decomposing velocity, pressure and temperature fields into mean, wave and turbulent components. Later, Staquet (2004) demonstrated that mixing of breaking gravity waves is dominated by non-linear effects when the Froude number is of order 1 (see next subsection), whatever the flow conditions are. Other studies have focused on the turbulence generated by the mountain wave breaking (Epifanio and Qian 2008), what they attributed to shear production at the top edge of the lee-side shooting flow. Recently, Sun et al. (2015b) introduced a new thought explaining the relationship between the background bulk shear and the oscillations. After an air mass lifted by convergence (due to a cold current entrance, for instance), IGWs are generated and the wind speed is enhanced at the waves crest, producing large coherent eddies which transport heat and momentum and another type of oscillations can be generated, the turbulence-forced oscillations (TFOs). Sun et al. (2015b) concluded that both, IGWs and TFOs, lead to turbulent fluxes and mixing that change the mean airflow and the shape of the IGWs.

Chapter 5 presents a gravity wave event triggered by a density current through mesoscale modeling analyzing the flow structure and the origin of the wave generation.

Within gravity waves, in the next section we will give special attention to mountain waves, which are topographically generated IGWs.

2.3.3 Mountain waves

2.3.3.1 Background

Mountain waves are IGWs whose origin is the perturbation of the flow due to the interaction with a topographic obstacle. Mountain waves are usually stationary waves (also called standing waves), so their frequency for an external sensor is zero ($f = 0$), but their parcels move with an intrinsic frequency $-k\overline{U}$ for an observer moving with the main flow. They are usually developed above the ABL but they can impact the flow circulation and structure near the surface. When an air flow is able to overpass a topographic barrier, many phenomena can occur at downstream and above it. Among them, mountain waves are frequently generated, which can be vertically trapped or vertically propagating waves. Trapped waves can be manifested through consecutive lenticular cloud formation at the crests of the waves if there is enough moisture available (Fig. 2.5). Vertically propagating waves can form an altocumulus standing lenticular cloud. Cap clouds can also appear in the upwind side and rotor clouds below the wave crests. Mountain waves can be accompanied by clear-air turbulence (Clark et al. 2000) being a hazard to aviation. They can be a great opportunity, instead, for glider pilots to fly long distances downstream the mountain range. They are also associated with foehn events, specially if there is precipitation at the upwind side. Because they trigger momentum on the lee side of the mountain range,

violent downslope windstorms and sudden jumps in pressure called “hydraulic jumps” can be seen with the presence of mountain waves. Near the surface, mountain waves can be associated with lee-wave rotor formation or lower turbulence zones (Mobbs et al. 2005; Darby and Poulos 2006; Vosper et al. 2006; Grubišic and Billings 2007; Sheridan et al. 2007; Cohn et al. 2011), boundary layer separation, and/or downslope windstorms (Lilly 1978; Mobbs et al. 2005; Klemp and Lilly 1975).

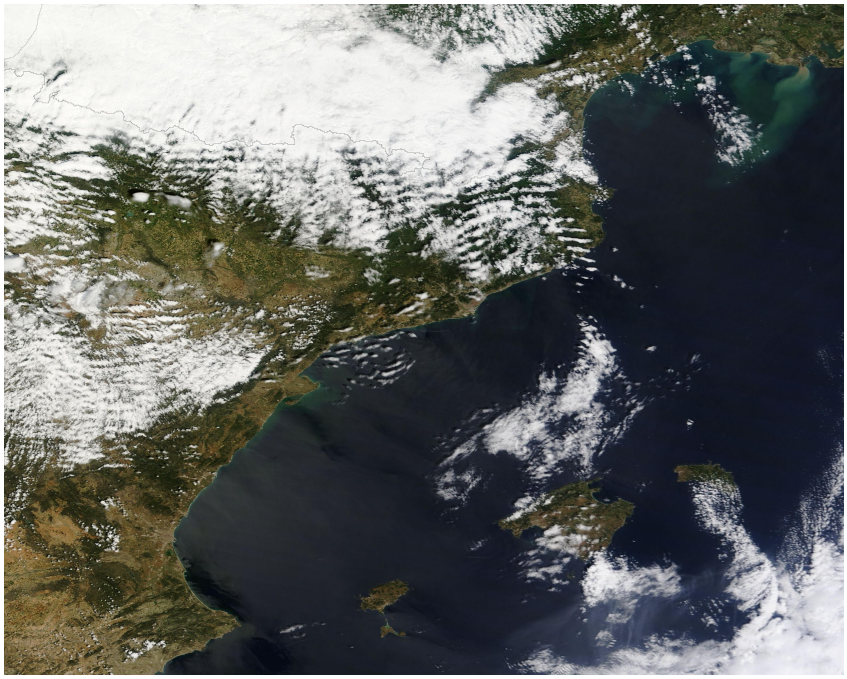

Figure 2.5: MODIS satellite image (22nd May 2013) with altocumulus lenticular clouds revealing trapped lee waves over the southern part of the Pyrenees.

Specifically, trapped lee waves (Fig. 2.6) can propagate long distances downstream of the terrain in the horizontal direction. They are manifested as oscillations in the main quantities such as wind components, potential temperature, water vapor, etc. In Fig. 2.6 the associated profile is indicated where a stable layer is present above the topographic crestline and wind increasing with height, the favorable conditions for trapped lee wave formation. In the vertical, they are usually evanescent with height, so the amplitude decreases with height. As shown in schematic Fig. 2.6, shear instabilities are generated near the wave crests. They can lead to rotor circulations that usually appear under the first wave crest, which may break into turbulence (Doyle et al. 2009; Cohn et al. 2011), and they can be accompanied by rotor clouds. They can also introduce momentum and energy at the top of the ABL and/or they can be absorbed by it (Jiang et al. 2006).

Several field experiments have been done to improve the understanding of the mountain wave generation and propagation. In 1982 the Alpine Experiment (ALPEX) field program addressed the problem of airflow over and around mountains in Europe, and how the

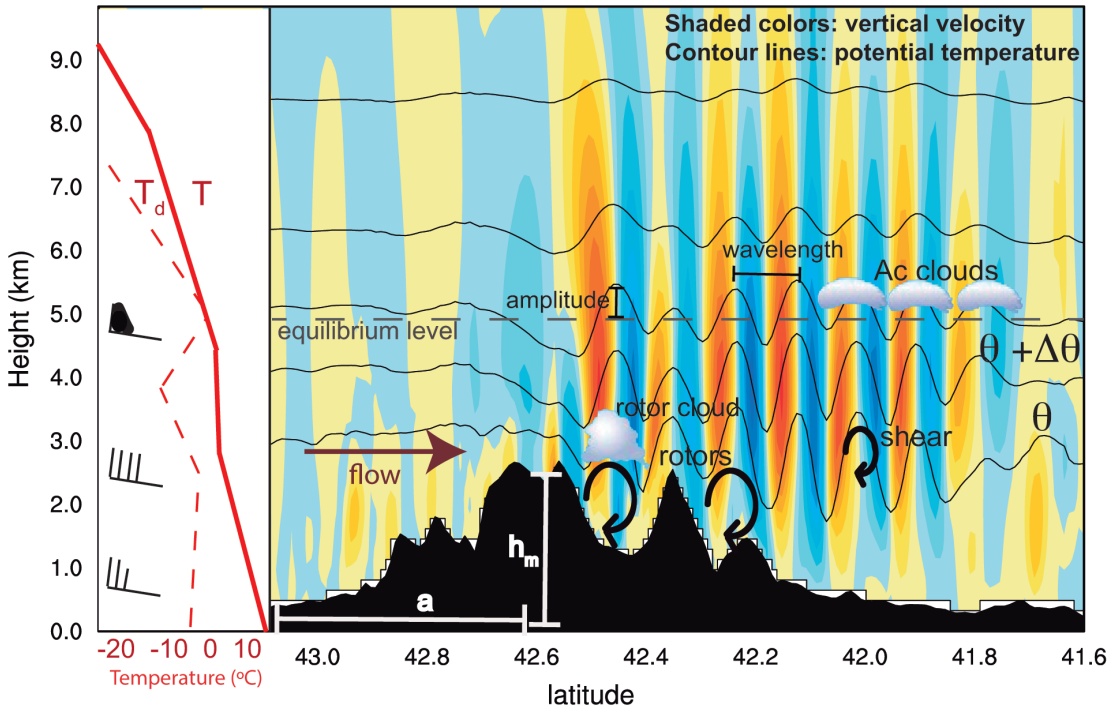

Figure 2.6: Phenomena associated with flows crossing a mountain range. Flow is coming from the left to the right and gravity waves are generated downstream of the mountain range. The underlying terrain is a realistic north-south cross section over the Pyrenees, where the mountain height can be approximated as h_m and a is the mountain half width. On the left side of the figure there is a possible sounding profile with air temperature (T), dew point temperature (T_d) and wind barbs.

resultant features of such airflow affect the global, regional, and local weather. From that campaign, Hoinka (1984) and Cox (1986) analyzed a mountain wave event. Later, in 1990, the first campaign over the Pyrenees, the Pyrenees Experiment (PYREX) (Bougeault et al. 1990, 1997), took place on its French side, with the objective of establishing the influence of the large mountain on the mesoscale flow and the effects on the momentum budget. They also found that mesoscale models performed reasonably well to resolve the flow over the mountainous terrain. Other relevant campaings have been: the Fronts and Atlantic Storm-Track Experiment (FASTEX) over Greenland (Doyle et al. 2005), the Mesoscale Alpine Experiment (MAP) over the Alps (Bougeault et al. 2001; Smith et al. 2007) and more recently the Sierra Rotor Project (SRP) and the Terrain-Induced Rotor Experiment (T-REX) (Grubišic et al. 2008) over the Sierra Nevada in the United States.

Mountain waves have also been studied through analytic solutions and numerical simulations, combining ideal and real simulations. Smith (1989) classified different flow regimes for hydrostatic flows over a mountain while Vosper (2004) investigated the upstream inversion effects on the lee waves and wave breaking establishing a diagnose model for a

two-dimensional (2D) flow. Also, Sheridan et al. (2007) explored the lee waves influence over the Pennines with ideal numerical modeling showing that a rapid decrease of the Scorer parameter (${l_s}^2$) can be the prerequisite for large-amplitude waves with effects near the surface. An intercomparison between mesoscale models for a wave breaking in the Boulder windstorm (Doyle et al. 2000) and for the T-REX mountain-wave simulations (Doyle et al. 2011) was done in a 2D mode. Their results revealed that differences among models were due to numerical techniques and they suggested the need of using three dimensional simulations. Doyle et al. (2005) showed a good representation of a wave breaking event with the COAMPS model that was also analyzed with linear theory and 2D simulations concluding that the diabatic effects can increase the wave amplitude. Moreover, vertical profiles upstream of the mountain range are determinant in the generated wave field downstream of it. Doyle and Smith (2003) found a trapped train of lee waves ducted from vertically propagating waves, consequence of diabatic processes associated with precipitation upstream of the Hohe Tauern crest. On the other hand, mountain-wave events have been simulated using real atmospheric conditions, combining the satellite water vapor imagery (Otkin and Greenwald 2008; Feltz et al. 2009) or using radar observations over Scandinavia (Kirkwood et al. 2010). Evidences of mountain waves have also been reported and simulated in the Andes mountain range region (Spiga et al. 2008), over the Basen nunatak in Antarctica (Valkonen et al. 2010) and in the upper troposphere-lower stratosphere (Plougonven et al. 2008; Mahalov et al. 2011).

2.3.3.2 Linear theory of mountain waves

Linear theory is able to give a comprehensive understanding of wave processes and their effects on the air flow. More details of the governing equations of atmospheric dynamics will be given in chapter 3; however, we will here advance the main expressions for gravity waves that can be described by the linear theory. First, linearizing the equations we ignore the terms with the perturbation variables. Then, for a two-dimensional hydrostatic steady flow, with the Boussinesq approximation, neglecting the coriolis force and viscosity and combining the momentum, thermodynamic and continuity equations we obtain the vertical velocity (w) equation (Holton and Hakim 2012), also called mountain wave equation or Taylor-Goldstein equation:

$$\frac{\partial^2 w}{\partial z^2} + \frac{\partial^2 w}{\partial x^2} + {l_s}^2 w = 0 \tag{2.6}$$

where ${l_s}^2$ is the Scorer parameter defined as:

$${l_s}^2 = \frac{N^2}{U^2} - \frac{1}{U}\frac{\partial^2 U}{\partial z^2} \tag{2.7}$$

and N is the Brunt Väisälä frequency and U the wind speed.

Analytic solutions for the equation 2.6 can be obtained for different underlying topography (sinusoidal terrain, isolated mountain), with different characteristics depending on

${l_s}^2$. A typical case of study is the isolated mountain with specific geometric topography shape called Witch of Agnesi (WOA) with a shape defined by:

$$z(x) = h_m \frac{a}{x^2 + a^2} \tag{2.8}$$

where h_m is the obstacle height, x is the distance from the ridge top and a is the obstacle half width.

An analytic solution for equation 2.6 of the WOA topography can be obtained, for the vertical velocity of a two-dimensional flow with no shear and constant stability. The solution basically distinguishes between two types of waves (Fig. 2.7):

- Evanescent or vertically trapped waves when $a << \frac{U}{N}$ (Fig. 2.7a)
- Vertically propagating waves when $a >> \frac{U}{N}$ (Fig. 2.7b)

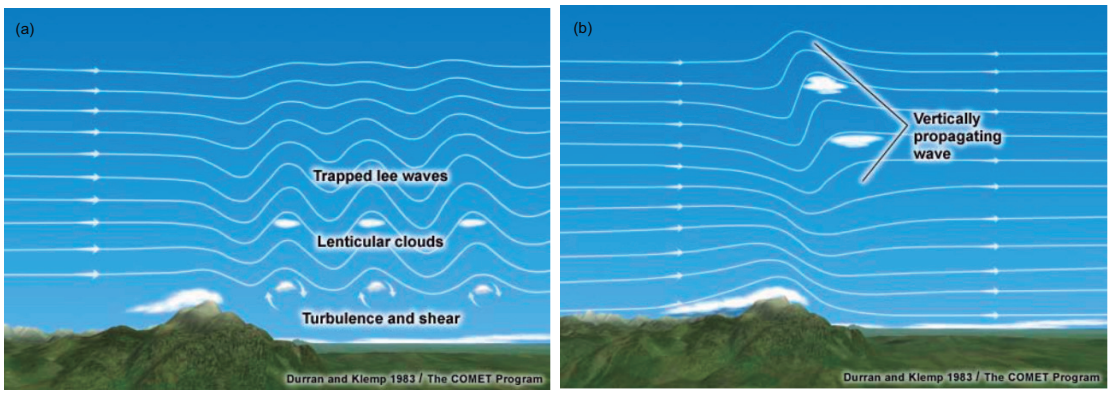

Figure 2.7: (a) Vertically trapped waves. (b) Vertically propagating waves. Source: The COMET Program / Durran and Klemp (1983).

Trapped lee waves are likely to occur when the Scorer parameter decreases rapidly with height Scorer (1949), which implies that the horizontal wind speed increases with height or that stability decreases with height. Then, a necessary condition for trapped lee waves is a certain difference between ${l_s}^2{}_L$ and ${l_s}^2{}_U$, the Scorer parameters in upper and lower layers respectively, that leads the wave to propagate vertically in the lower layer and decays exponentially with height at the upper layer (Durran 2003). As shown in Fig. 2.7a, there is no tilt in trapped lee waves, as the wave energy is reflected at the upper layer.

With analytic solutions, we can summarize three factors that determine the mountain wave formation and structure: the shape of the mountain (mountain height, mountain half width), the wind speed of the incident flow and the stability structure (θ profile, N, etc.). Depending on these three factors, gravity waves will (or will not) be generated downstream of the mountain range with more or less amplitude and wavelength, or they will propagate vertically or downstream. The Froude number (Fr) is a useful parameter to determine the ability of the flow to cross a mountain barrier. It is a non-dimensional number with the

ratio of inertial to gravitational forces on a flow, or it can be though as the ratio between kinetic energy (wind speed) and potential energy (stability times mountain height):

$$Fr = \frac{U}{Nh_m} \tag{2.9}$$

If Fr is greater than 1 ($Fr >> 1$) the flow crosses the mountain barrier and it can be approximated to the linear theory. When Fr is close to 1 ($Fr \approx 1$) the flow descends the mountain range and mountain waves are likely to be generated downwind of it. If Fr is smaller but close to 1 ($Fr \approx 0.4$) part of the air flow is able to cross the obstacle and part of it is blocked, then, flow is highly affected by nonlinearity, mountain waves are generated and flow splitting and wave breaking are likely to occur downstream of the mountain range. Instead, when Fr is much smaller than the unity ($Fr << 1$) the air parcels in the flow do not have enough energy to go through the topographic obstacle and the flow is blocked or surrounds the mountain.

Similar to the last classification but using the non-dimensional mountain height $\hat{h}= \frac{Nh_m}{U}$, which is the inverse of the Fr, Smith (1989) classified different flow regimes for hydrostatic flows over a mountain, while Vosper (2004) investigated the upstream inversion effects on the lee waves and wave breaking establishing a diagnose model for a two-dimensional flow.

As we said, linear theory explains the wave processes and their effects on the air flow reasonably well assuming that: the mountain height, h is much smaller than the flow depth, the perturbation of the wind is much smaller than the mean wind ($u' << \overline{u}$) and the inertial forces dominate over the gravitational forces, that is, $Fr >>> 1$. Unfortunately in the atmosphere it is quite frequent that $Fr \approx 1$ or $u' \approx \overline{u}$, therefore nonlinearity becomes important and the linear theory is not valid anymore. When non-linear interactions become important, waves are usually associated with turbulence. This turbulence can be generated by wave breaking or by wave interactions and can be intermittent in time and space.

On the other hand, when the linear theory reaches its limits, modeling the atmospheric flows can be a good tool to analyze non-hydrostatic flows and non-linear processes. Mesoscale or microscale models are able to include the three-dimensionality, parameterizing or resolving nonlinear terms and including the realistic underlying topography, thus, giving a better approach to the real flows over complex terrain (more details in Sect. 4.5).

2.3.3.3 Rotors

Rotors and lower-tropospheric turbulence are often associated with mountain waves. While mountain waves have usually a background laminar flow, near the surface the flow can be very turbulent. A rotor is a region of recirculating flow with horizontal vorticity oriented in parallel to the ridge crest. The strength of the rotor can be described by the TKE, which measures the turbulence intensity and also by the vorticity (ζ), which measures the tendency of the vector field to rotate:

$$\zeta = \bigtriangledown \times \mathbf{v} = \begin{vmatrix} i & j & k \\ \frac{\partial}{\partial x} & \frac{\partial}{\partial y} & \frac{\partial}{\partial z} \\ u & v & w \end{vmatrix} = \left(\frac{\partial w}{\partial y} - \frac{\partial v}{\partial z}\right) i - \left(\frac{\partial w}{\partial x} - \frac{\partial u}{\partial z}\right) j + \left(\frac{\partial v}{\partial x} - \frac{\partial u}{\partial y}\right) k \quad (2.10)$$

Then, for the planar surface $j - k$ the x component of the vorticity is: $\frac{\partial w}{\partial y} - \frac{\partial v}{\partial z}$. The rotor location can be determined when there is a rotor cloud formed near the top of the rotor circulation, under higher lenticular clouds. However, if there is not sufficient moisture available, the cloud will not be formed but the rotor circulation may exist. Hertenstein and Kuettner (2005) classified two types of rotors: (i) a first type associated with trapped lee waves usually confined below the first mountain wave crest, near the mountain base, containing moderate to strong turbulence. (ii) A second type with similar characteristics to a hydraulic jump, formed above the mountain top and further downstream of it, containing strong turbulence. The first type is more frequently observed than the second type.

There exist evidences of rotors and turbulence events at the lee of steep mountain ranges such as the Owens Valley in the Sierra Nevada, USA. Grubišic and Billings (2007) observed a lee-wave rotor event using wind profiler and radiosonde data, as well as numerical simulations. Later, within the T-REX campaign (Grubišic et al. 2008), Cohn et al. (2011) examined in detail the structure and evolution of mountain wave and rotor events using a network of three radar wind profilers. Among other results, they found subrotors in the vicinity of the wave crest and described the lower turbulence zone. Their results were in accordance with the previous work from Doyle and Durran (2007) and Doyle et al. (2009) which described rotor dynamics and subrotor vortices with observational and numerical simulations. Other rotor evidences have been found downwind of a mountain range in Falkland Islands in South Atlantic (Mobbs et al. 2005), in the lee of Pike's Peak near the Rocky Mountains in Colorado, USA (Darby and Poulos 2006), downwind the Pennines in northern England (Sheridan et al. 2007) or associated with the Adriatic bora windstorms (Gohm et al. 2008). In addition, many authors have analyzed the rotor dynamics and structure with analytical solutions and numerical simulations (Queney 1955; Doyle and Durran 2002; Jiang et al. 2007; Sheridan et al. 2007; Doyle and Durran 2007; Doyle et al. 2009). Moreover, the upstream conditions were also investigated focusing in temperature inversion location and the wind speed profile (Vosper 2004; Mobbs et al. 2005; Hertenstein and Kuettner 2005; Grubišic and Billings 2007; Smith and Skyllingstad 2009).

Chapter 7 contributes to a better knowledge of mountain waves studying the capability of the mesoscale model in order to correctly reproduce them. The influence of mountain waves near the surface and the presence of a rotor is also investigated.

3

Fundamentals of modeling the atmospheric flows

Contents

In this chapter the governing equations of the atmospheric flows are introduced, presenting different possible approximations. The system components and physic parameterizations of the Weather Research and Forecast model are also specified in this chapter.

3.1 The governing equations of the atmospheric flows

The general Navier-Stokes (NS) equations describe and forecast the flow motion by a set of nonlinear partial differential equations that can be applied to the movement of gases or liquids: atmosphere, ocean currents, water flow in pipes, etc. Each application requires the proper hypotheses and approximations.

The NS applied to the evolution of the atmosphere in the boundary layer are based on the Newton's second law and the conservation principles of mass and energy. The

formulation that applies to the boundary layer can be summarized with the following equations (from Stull (1988)), so the viscous effects here are considered. In this notation, the i indexes refer to the velocity vector components (u, v, w) while the j indexes refer to the generic component of distance coordinates (x, y, z).

The **conservation of momentum** (Newton's second law): Considering an incompressible flow, under the forces of: gravity, coriolis, pressure and viscosity:

$$\frac{\partial u_i}{\partial t} + u_j \frac{\partial u_i}{\partial x_j} = -\delta_{i3} g + f_c \epsilon_{ij3} u_j - \frac{1}{\rho} \frac{\partial p}{\partial x_i} + \nu \frac{\partial^2 u_i}{\partial x_j^2} \tag{3.1}$$

where δ_{i3} equals to 1 when $i = j$ and to 0 when $i \neq j$, g is the gravitational acceleration, $f_c = 2\omega sin\phi$ (ϕ being the latitude and ω the angular velocity of earth), ϵ_{ij3} is the unit tensor, ρ is the air density, p is the pressure and ν is the kinematic viscosity.

The **conservation of mass** (continuity equation):

$$\frac{\partial \rho}{\partial t} + \rho \frac{\partial u_j}{\partial x_j} = 0 \tag{3.2}$$

For an incompressible flow, where $(\partial\rho/\partial t)/\rho << \partial u_j/\partial x_j$, the continuity equation reduces to:

$$\frac{\partial u_j}{\partial x_j} = 0 \tag{3.3}$$

The **conservation of energy / thermodynamic energy equation** (first law of thermodynamics):

$$\frac{\partial \theta}{\partial t} + u_j \frac{\partial \theta}{\partial x_j} = \nu_\theta \frac{\partial^2 \theta}{\partial x_j^2} - \frac{1}{\rho C_p} \left(\frac{\partial R_n}{\partial x_j} \right) - \frac{L_p E}{\rho C_p} \tag{3.4}$$

where ν_θ is the kinematic viscosity for heat (also called the thermal diffusivity), C_p is the specific heat of air at constant pressure, R_n is the net radiation (gain or loss of heat), E represents the mass of water vapor per unit volume per unit time being created by a phase change from liquid or solid and L_p is the latent heat associated with the phase change of E.

In the boundary layer we also include the equation of state which describes the state of the gases in the boundary layer, and the conservation of moisture or water vapor:

The **equation of state** for ideal gases:

$$p = \rho R T_v \tag{3.5}$$

where ρ is the moist air density, R is the gas constant for dry air and T_v is the virtual absolute temperature.

The **conservation of water vapor**:

$$\frac{\partial q}{\partial t} + u_j \frac{\partial q}{\partial x_j} = \nu_q \frac{\partial^2 q}{\partial x_j^2} + \frac{S_q}{\rho} + \frac{E}{\rho} \tag{3.6}$$

assuming incompressibility, where q is the specific humidity of air, ν_q is the kinematic viscosity for humidity, S_q is the moisture source term and E represents the mass of water vapor (per unit volume per unit time) being created by a phase change from liquid or solid.

3.2 Different approximations to the governing equations of the atmospheric flows

Modeling the atmosphere means resolving the governing equations of the atmospheric flows (presented in section 3.1). One can distinguish two different numerical approaches to study the atmospheric flows: the Computational Fluid Dynamics (CFD) and the Mesoscale Meteorological Models (MMM) (also the Global Climate Models (GCMs) for larger scales). Basically, both approaches, CFDs and MMMs resolve the NS equations but they are designed for different purposes and different spatial and temporal length scales. CFD's are usually run within the microscales, including spatial scales below 3 km and time scales shorter than about 1 hour (Stull 1988), while MMM's are designed to cover the mesoscale, which implies horizontal scales from few kilometers to several hundred kilometers or so, and temporal scales from few hours to few days (Pielke Sr 2013).

3.2.1 Computational Fluid Dynamics

The CFD's are mostly used by the engineering community to resolve the turbulent flow equations for applications such as wind energy and engineering design. The CFD codes resolve the incompressible NS equations (equations 3.1, 3.3, 3.4) with slight variations depending on the modeled flow. The Boussinesq approximation is usually included, neglecting density variations but including them in the buoyancy term. Some CFD's may also include the pressure-poisson equation. There are three popular approaches within the CDF's:

1. Direct Numerical Simulation (DNS). Using this technique, the NS equations are resolved completely and all the turbulent motions and eddies as well. It requires high computational resources and it is very time-consuming. Nowadays the high-performance computing capabilities allow DNS on the order of 10^{10} to 10^{11} grid points, corresponding to Reynolds number of around 10^5. Therefore, DNS of atmospheric flows are still not doable with the present computational capabilities.

2. Large Eddy Simulation (LES). This technique is based on filtering the NS equations and resolving the large eddies, while the small eddies are modeled. The filter can be the grid size, so the eddies smaller than the grid size will be modeled by a sub-filter turbulence model. LES is less computationally demanding than DNS but it is still expensive. The obtained solutions are less accurate than DNS but more than RANS.

3. Reynolds-Averaged Navier-Stokes (RANS). The RANS solve the averaged NS equations, so only the mean flow is resolved and all the eddies are modeled. In other words, the effect of turbulence on the mean flow is modeled. The RANS models can be steady, so based on time-averaging, or unsteady (URANS) so ensemble-averaging is needed. All the RANS are the cheapest in terms of computer time consuming, although the obtained results are less accurate than LES or DNS. Technically speaking, MMM models can be classified as complex URANS models, as they are based on the Reynolds averaged NS equations and all the turbulence is parameterized.

3.2.2 Mesoscale Meteorological Models

The MMMs solve the Euler equations which are simplifications of the general NS equations for an inviscid flow (no viscosity term in equation 3.1). The MMMs resolve the fully compressible equations, as the domain height requires considering the compressibility effects. In addition to the conservation of momentum (equation 3.1), mass (equation 3.2) and energy (equation 3.4), the Euler equations include the gases state equation (equation 3.5), and the conservation of moisture (equation 3.6). The vertical coordinates are usually based on pressure and follow the terrain shape (sigma coordinates). The MMM equations are resolved in planar surfaces, therefore they need a coordinate system given by a map projection, such as Lambert conformal, Mercator and Polar stereographic.

Since MMMs do not resolve the turbulent motions, the governing equations are modified by the Reynolds decomposition and averaging (Stull 1988; Pielke Sr 2013) when they have to be used to resolve turbulent flows. Then averaging the equations and using the Boussinesq approximation, we obtain the following Reynolds-Averaged Navier-Stokes equations:

The **conservation of momentum**:

$$\frac{\partial \overline{u_i}}{\partial t} + \overline{u_j}\frac{\partial \overline{u_i}}{\partial x_j} = -\delta_{i3}g + f_c\epsilon_{ij3}\overline{u_j} - \frac{1}{\rho}\frac{\partial \overline{p}}{\partial x_i} + \nu\frac{\partial^2 \overline{u_i}}{\partial x_j^2} - \frac{\partial \overline{(u_i' u_j')}}{\partial x_j} \tag{3.7}$$

where a new turbulence term (the last term on the right hand side) is added to the basic conservation equation (Eq. 3.1), which represents the divergence of the turbulent momentum flux. It can be also seen as the influence of the Reynolds stress on the mean motions (Stull 1988).

The **conservation of mass** for the mean quantity (Eq. 3.8) and for the turbulent

fluctuations (Eq. 3.9):

$$\frac{\partial \overline{u_j}}{\partial x_j} = 0 \tag{3.8}$$

$$\frac{\partial u'_j}{\partial x_j} = 0 \tag{3.9}$$

The **conservation of energy or heat**:

$$\frac{\partial \overline{\theta}}{\partial t} + \overline{u_j}\frac{\partial \overline{\theta}}{\partial x_j} = \nu_\theta \frac{\partial^2 \overline{\theta}}{\partial x_j^2} - \frac{1}{\rho C_p}\left(\frac{\partial \overline{R_n}}{\partial x_j}\right) - \frac{L_p E}{\rho C_p} - \frac{\partial \overline{(u'_j \theta')}}{\partial x_j} \tag{3.10}$$

Again, the equation is similar to the basic heat conservation equation (Eq. 3.4) but with the inclusion of the turbulence (last term at the right hand side) that represents the divergence of the turbulent heat flux.

The **equation of estate**:

$$\overline{p} = \overline{\rho} R \overline{T_v} \tag{3.11}$$

The **conservation of water vapor**:

$$\frac{\partial \overline{q}}{\partial t} + \overline{u_j}\frac{\partial \overline{q}}{\partial x_j} = \nu_q \frac{\partial^2 \overline{q}}{\partial x_j^2} + \frac{S_q}{\rho} + \frac{E}{\rho} - \frac{\partial \overline{(u'_j q')}}{\partial x_j} \tag{3.12}$$

where the last term represents the divergence of the turbulent total moisture flux.

These turbulent flux terms appearing at the right hand side of the RANS equations (Eq. 3.7, 3.10, 3.12) arise due to the nonlinearity of the advection terms of the initial governing equations (Eq. 3.1, 3.4, 3.6) and they are unknown terms that have to be parameterized (the *closure problem*, see Sect. 4.2). In MMMs, the parameterization is usually handled by the planetary boundary layer (PBL) schemes, that represent the vertical turbulent contribution term, usually named as vertical diffusion, while the turbulence in horizontal dimensions is treated separately (more detailed in section 4.2). Some of the PBL schemes contain a prognostic equation for the TKE, represented as e, to describe the physical processes that generate turbulence, so using the summation notation $\overline{e} = 0.5\overline{u_i'^2}$, we can obtain:

The **TKE budget equation**:

$$\frac{\partial \overline{e}}{\partial t} + \overline{u_j}\frac{\partial \overline{e}}{\partial x_j} = +\delta_{i3}\frac{g}{\overline{\theta}_v}(\overline{u'_i \theta'_v}) - \overline{u'_i u'_j}\frac{\partial \overline{u_i}}{\partial x_j} - \frac{\partial (\overline{u'_j e})}{\partial x_j} - \frac{1}{\overline{\rho}}\frac{\partial (\overline{u'_i p'})}{\partial x_i} - \varepsilon \tag{3.13}$$

From the equation 3.13 we can see that the TKE storage and advection is a balance between the buoyant production (or consumption), the mechanical or shear production, the turbulent transport, its pressure redistribution and the dissipation of TKE.

The numerical resolution of the RANS equations is usually done using finite differences techniques. In order to resolve the equations, it is necessary to know the initial and boundary conditions. Mesoscale models usually take these initial and boundary conditions from larger domain, a global model, or reanalysis data. Different domains can be configured to cover different areas of interest using the nesting capability, as most of the MMMs allow the choice of different grid size resolution.

Most of the large scale models are hydrostatic, meaning that the pressure gradient is balanced by the downward weight of the atmosphere. Many mesoscale models are, instead, non-hydrostatic, specially when the grid size is reduced to a few kilometers. When the length scale of the resolved weather processes approximates to its vertical extension (sizes around 10 km or less) the hydrostatic assumption can be questioned. Models using non-hydrostatic approaches include an equation for the vertical motions. Examples of phenomena that include non-hydrostatic processes are: convective storms, gust fronts, convergence lines, gravity waves and turbulence.

Mesoscale modeling based on these MMM's is nowadays the main tool for the Numerical Weather prediction (NWP) for operative forecasts, wind energy applications, research purposes, etc. Several MMMs are currently used around the world such as ARPS, ALADIN, COAMPS, MM5, RAMS, UM (MetOffice) and WRF, among others.

3.3 The Weather Research and Forecast model

The WRF model is a state-of-art numerical weather prediction (NWP) simulation system developed by the National Center for Atmospheric Research (NCAR). The dynamic solver used in this study is the Advanced Research WRF (ARW). The ARW solver integrates the compressible non-hydrostatic equations in the flux form (Sect. 3.1). The map projections and the Coriolis terms are also included, as we are simulating real atmospheric flows. The WRF model can be used for a wide range of scales, from global to mesoscale scales and also resolving the microscales with large-eddy simulation.

The vertical coordinate in WRF is called eta coordinate system (η). It is a terrain-following, dry-hydrostatic pressure level configuration with a constant pressure at the top, originally proposed by Laprise (1992):

$$\eta = \frac{p - p_t}{p_s - p_t} \tag{3.14}$$

where p_t and p_s are the pressure values at the top and surface boundaries respectively. η varies from 1 at the surface to 0 at the upper boundary.

The sigma coordinates allow different spacing between levels along the vertical domain. Levels are usually concentrated close to the surface, so enhancing the vertical resolution near the ground and within the boundary layer, and they are stretched above it (Fig. 3.1a). Another advantage of the sigma coordinate system is that they do not interact with the ground and they have an easy implementation for the lower boundary condition.

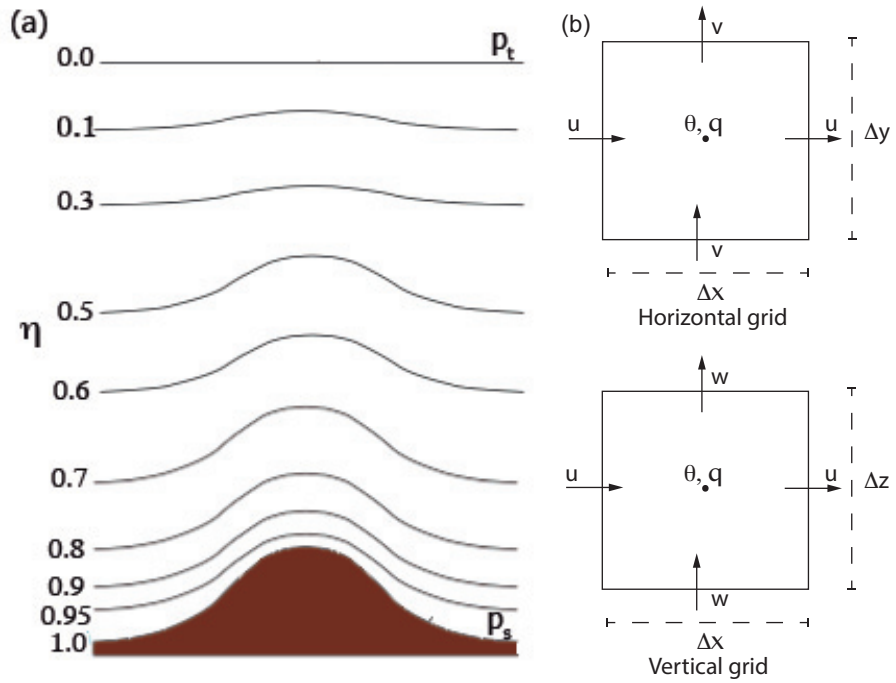

Figure 3.1: (a) Sigma levels representation; (b) Arakawa C grid with horizontal grid (up) and vertical grid (down) representation. Adapted from Skamarock et al. (2008).

Nevertheless, some limitations arise for high grid resolution and over complex terrain, with steep slopes, because of large differences in the horizontal pressure gradient (more details in Sect. 4.5).

The spatial discretization in WRF uses the staggered Arakawa C-grid type structure, which evaluates u-component at the center of the left and right grid faces and the v-component at the center of the upper and lower grid faces (Fig. 3.1b). Because of the nonlinearity of the advection terms, the spatial discretization can be done for different orders (from 2^{nd} to 6^{th}) which may introduce implicit diffusion (more in Sect. 4.3.5).

The temporal discretization in WRF is done using the third-order Runge-Kutta (RK3) time integration scheme (Wicker and Skamarock 2002) to separate the low-frequency modes. The time step has to be established so that the Courant-Friedrichs-Lewy (CFL) criteria is accomplished. It is a necessary condition for the convergence of the finite difference integration scheme relating the horizontal resolution (Δx) to the temporal resolution or time step (Δt) following the relation in Eq. 3.15:

$$CFL = \frac{u\Delta t}{\Delta x} \leq Cr_{max} \tag{3.15}$$

The maximum Courant number, Cr_{max}, should usually be less than 1, but it depends on the order of the spatial filtering. As a rule of thumb, it is calculated that the time step (in seconds) should be around 6 times the horizontal grid size (in km), so, $\Delta t \approx 6\Delta x$.

The acoustic modes are also integrated through a the acoustic time step ($\Delta\tau$), which is also constrained by a maximum number of the Courant number, including the sound speed (c_s), following the expression in Eq. 3.16:

$$Cr_{max} = \frac{c_s \Delta\tau}{\Delta x} \leq \frac{1}{\sqrt{2}} \tag{3.16}$$

Nevertheless, when the grid size is reduced to a few km there is another constraint for the time step derived also from the finite-difference discretization when the metric term from the coordinate transformation is considered: $M\frac{\Delta t}{\Delta x} < \beta$, where M is the physical diffusivity and β is a coefficient depending on the discretization (Arnold et al. 2012). Then Δt is not linear in Δx but it depends on Δx^2, and therefore, as the grid size decreases the time step has to be reduced proportionally to Δx^2. This is frequently the cause for the model integration failure in complex terrain areas, when the coordinate transformation causes metric terms to appear in the equations (Arnold et al. 2012) (more details are given in Sect. 4.5).

The WRF model includes two options for nesting and give lateral boundary conditions for small domains inside coarse domains: one-way and two-way nesting. In the one-way nesting methodology the information is transferred periodically from the coarse to the inner domain and the nested solution does not feedback to the outer domain. The two-way nesting approach includes feedback from the inner domain to the outer domain, so the transferred information is bidirectional. Both methodologies are widely used in MMMs but it is not clear which one performs better. Depending on the application and the involved scales, the choice of an adequate methodology can be justified. For easier implementation, one-way nesting is a good approach to see the net effect of the coarse domain over the inner domain.

3.3.1 WRF system components

The WRF model can run real-data or idealized simulations. Both schemes are shown in Figure 3.2. For the real-data cases there is a WRF Preprocessing System (WPS) that includes 3 programs to prepare the data for the *real.exe*. The *namelist.wps* has to be edited with the time and domain size information for the simulation set-up and then run:

- *geogrid.exe*: defines the model domains and interpolates the static geographical data to the domain.
- *ungrib.exe*: decodes the meteorological fields from the GRIB (GRIdded Binary) files of input data (from ECMWF, GFS, etc.)
- *metgrid.exe*: interpolates horizontally the meteorological fields extracted by ungrib to the model domain and grids. The output files are named for each domain as met_em.d0*.YYYY-MM-DD_hh:mm:ss, with the corresponding year (YYYY), month (MM), day (DD), hour (hh), minute (mm) and second (ss).

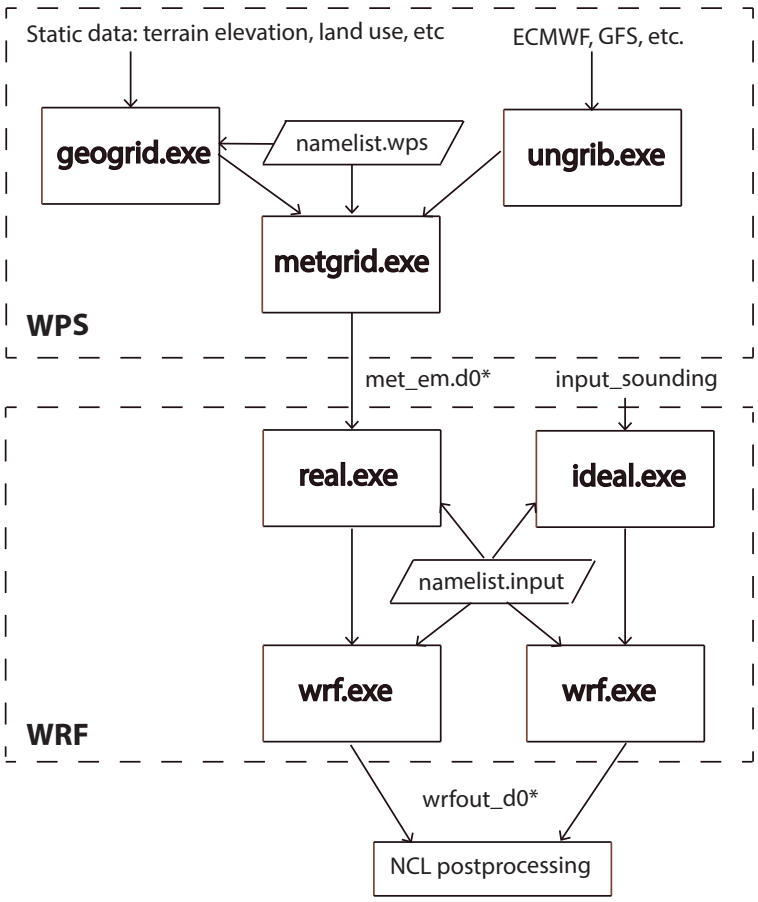

Figure 3.2: WRF execution scheme

Next, the *namelist.input* is edited with the set-up parameters: time, domains, physic parameterizations and dynamic options. Two programs are run:

- *real.exe*: prepares the initialization for a single time.
- *wrf.exe*: runs the WRF model.

Chapter 5 and 7 include results based on real-data simulations.

For ideal simulations there is no WPS but the initial conditions have to be set by an *input_sounding* which includes the initial profiles of temperature, wind components and humidity. After setting the *namelist.input*, two programs are run:

- *ideal.exe*: prepares the initialization for the run.
- *wrf.exe*: runs the WRF model.

Chapter 6 includes results based on ideal large-eddy simulations.

The output in both real and ideal simulations is a netCDF file with a name wrfout_d0*_YYYY-MM-DD_hh:mm:ss that is processed by the Ncar Command Language (NCL) for data treatment and visualization.

3.3.2 Physic parameterizations in WRF

Those processes smaller than the grid size have to be taken into account in bigger scale processes that are grid-resolved. This is done by the physic parameterizations, which statistically introduce the effects of the small scale processes in the resolved fields. The quantification of these sub-grid effects is usually determined with experimental campaigns and measurements. From the experimental results the parameterization process is based on finding a connection between a variable that describes the sub-grid process and a grid-resolved magnitude. This relationship is then written in a mathematical expression that can be introduced as a parameterization in the model.

The WRF model physic parameterizations include the microphysics, cumulus parameterizations, the atmospheric radiation physics, surface physics (including the surface layer and the land surface model) and the planetary boundary layer physics. Each physic parameterization contains several choices with schemes developed for different purposes and they are in constant development. Most of the parameterizations interact one with another, as shown in Fig. 3.3.

The microphysics (MP) parameterization describes the water vapor and precipitation processes within the clouds. Some of the parameterizations include the ice-phase and mixed-phase processes accounting for the vapor, cloud water or ice, and rain water or

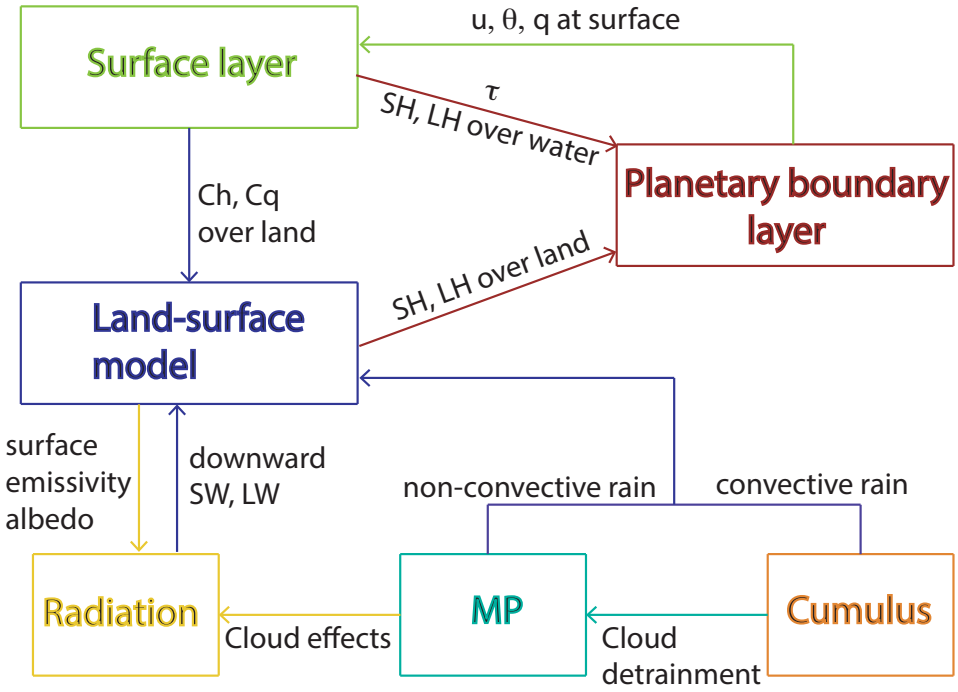

Figure 3.3: Interactions among physical parameterization schemes in WRF. Adapted from Dudhia (2011).

snow. This scheme provides information about the non-convective rain and introduces cloud effects to the radiation scheme Fig. 3.3. The cumulus parameterization provides the sub-grid effects of the convective and/or shallow clouds and convective rain. Theoretically, this parameterization is only valid for grid sizes greater than 10 km. Below grid sizes of $\approx$ 5 km the convective eddies can be resolved by the model itself.

The radiation physics scheme handles the heating due to radiative flux divergence and the surface radiative fluxes. The shortwave (SW) and the longwave (LW) radiation are treated separately to calculate the upward and downward fluxes. The information is transferred to the land-surface model which, in turn, provides the parameters of surface emissivity and albedo to the radiation scheme.

The surface layer physics scheme gives the momentum flux (τ) at the first level of the model for the PBL scheme, and the exchange coefficients for land-surface heat (C_h) and moisture (C_q) fluxes. Over land, the land-surface model calculates the heat (SH) and moisture (LH) fluxes from these exchange coefficients and from the radiation scheme (also from information from cumulus and microphysics scheme). Over the sea, the surface layer directly handles the heat (SH) and moisture (LH) fluxes computation. An extended explanation for the surface physics is given in section 4.3.4. The PBL physics parameterization handle the vertical turbulence. Since this thesis is focused on the ABL that is coupled with the surface, in the next chapter (chapter 4) we will describe in detail the last

two parameterizations: the PBL (and the turbulence treatment in WRF) and the surface layer parameterizations.

4

Modeling the atmospheric boundary layer

Contents

After introducing the theory of the ABL (Chapter 2) and the equations that govern the atmospheric flows (Chapter 3), here we present a chapter to understand the combination of both, that is, dealing with modeling the ABL.

4.1 Turbulence modeling

In the turbulence spectrum scheme (Fig. 4.1) we can see the different eddy sizes for a turbulent flow. Depending on the dimensions of the length of the turbulent eddies (l)

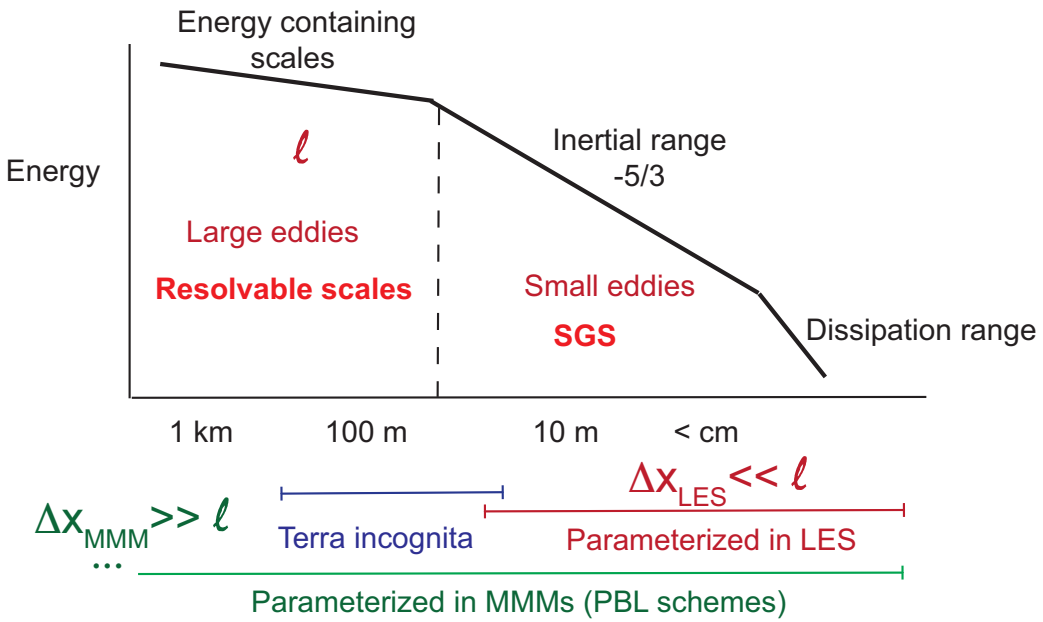

Figure 4.1: Turbulence spectrum and scales involved. Adapted from Moeng (2011).

and the grid size or spatial filter (Δx) we can also explain the different approaches to resolve a turbulent flow. It is shown how MMMs would parameterize all the turbulent motions through PBL schemes, while LES models calculate explicitly the large eddies that contain large amounts of energy and parameterize the small eddies with less energy. MMMs assume that l, the energy- and flux-containing turbulence, or the eddy size, is much smaller than the grid size, Δx. LES models, instead, expect that this l is larger than the spatial filter used in the equation of motion and the smaller eddies will be parameterized. This sub-grid scale (SGS) parameterization in LES is often based on the inertial-range theory that follows the Kolmogorov theory (Kolmogorov 1941), which assumes an energy cascade in the dissipation of the smallest eddies at a rate of -5/3 (see Sect. 2.2).

Wyngaard (2004) defined the term *Terra-incognita*, as the region in the spectrum where the scale of parameterized energetic eddies l is similar to the scale of the used spatial filter in the model Δx. This is a situation where neither the approximation of MMMs nor LES is not appropriate. Arnold et al. (2012) approximate the terra-incognita around the region where 100 m $\leq \Delta x \geq$ 300 m. However, MMMs can be questioned when using grid sizes of $\Delta x <$ 1 km. Reducing the grid size to hundreds of meters leads to the "double counting" issue i.e. the model is resolving and parameterizing the turbulence movements at the same time. However, it can be argued that PBL schemes would stabilize the PBL turbulent movements before the eddies are resolved. Nevertheless, fundamental explanation is needed to claim using the MMMs at higher resolution. In that sense, two conditions can be defined for using PBL schemes in grids of hundred-meter resolution in MMMs without problems. Firstly, ensuring a large ratio between horizontal and vertical

grid size ($\Delta x/\Delta z >> 1$), which would give sense to the hypothesis that vertical mixing dominates over horizontal mixing. Secondly, the scale of the eddies, l, should be much smaller than the Δx. This would occur, for instance, in stable boundary layers or nocturnal conditions, where eddies are small, but not in convective daytime ABLs where large eddies are dominating. Lately some studies have dealt with simulations using PBL schemes with grids around hundreds of meters. Seaman et al. (2012) used a grid resolution of $\Delta x = 444$ m for modeling nocturnal boundary layer with the WRF model, with a very fine vertical resolution so that $\Delta x >> \Delta z$. On the other hand, Horvath et al. (2012) performed mesoscale simulations with $\Delta x = 333$ and concluded that PBL traditional schemes may have issues in the range of the terra-incognita.

For unstable ABLs in grid resolutions of hundreds of meters, it is easy that $l >> \Delta x$, thus, resolving the turbulence in three dimensions using LES would be convenient. In general, the LES approach is valid when the grid ratio between the horizontal and vertical dimensions ($\Delta x/\Delta z$) is close to the unity (Lundquist et al. 2010). Both conditions, the energy containing and the grid ratio, are usually fulfilled for $\Delta x < 100$ m.

4.2 How to parameterize the ABL

Whether within the mesoscale or in the LES range, the sub-grid turbulence has to be parameterized. The number of unknown turbulent terms is larger than the number of equations, therefore, the description of the turbulence is not closed, what is called the *closure problem*. To be able to mathematically resolve the turbulent equations, the closure approximations are defined, using the *order closures*. There exist the zero order (no prognostic equations for the mean variables), first order (knowing the mean quantities and parameterizing second order moments), one-and-a-half order (having prognostic equations for some second order moments), second order (having prognostic equations for fluxes and variances and parameterizing the third order moments), and so on.

Traditionally, there exist two different schools of thought of turbulence closure: the local and non-local closure. The local closure is based on parameterizing the unknown quantities at one point with values or gradients of known quantities at the same point. The local closure can be applied in high order moments. The non-local closure obtains the unknown quantities from the mean known values at many points in space, so accounting for multiple eddies and advection processes. An example of the non-local closure is the transilient turbulence theory. It has been applied mostly to first-order closure (Stull 1988).

The first order closure retains the prognostic equations for the mean quantities (wind components, temperature, etc) and parameterizes the turbulent fluxes that appear in these equations using the *K-theory*, which approximates the fluxes of a variable ϕ to its gradients multiplied by an eddy diffusivity coefficient K, with a sub-index indicating the variable (K_ϕ in this case):

$$\overline{u_j'\phi'} = -K_\phi \frac{\partial \overline{\phi}}{\partial x_j} \tag{4.1}$$

The K-theory can be seen as an analogy with the molecular diffusion (Fick's law), where the flux tends to go from higher to lower concentrations with a magnitude proportional to the concentration gradient, but for larger scales in this case. The eddy diffusivity coefficient (K), also named eddy viscosity or eddy-transfer coefficient gives an idea of the effectiveness of the turbulence. It can be specified as a constant or can be parameterized as a function of other known quantities. The simple K-theory as in Eq. 4.1 is a local approximation.

The one-and-a-half order is often used for turbulence parameterizations. It is in between the first and the second order, therefore, the equations for the mean variables are known and some, but not all turbulent fluxes are resolved by prognostic equations. Usually, this 1.5 order closure includes a prognostic equation for the TKE.

4.3 ABL parameterizations in WRF model

In the WRF model, the PBL is the parametrization responsible of resolving the vertical turbulent fluxes not only within the ABL, but also in the free atmosphere, over the whole column of the atmosphere. While the vertical mixing is represented by these PBL schemes, the horizontal part is treated separately (see Sect. 4.3.5). The formulation of turbulence mixing and filtering in the WRF model aims to represent sub-grid turbulence processes that are not resolved by the grid itself.

Parameterizations of the ABL must include all vertical layers, the soil layer, the surface layer, the PBL layers and the PBL top, the interactions between them and with the free atmosphere through the entrainment processes (Fig. 4.2). Two PBL schemes from the WRF model are investigated here, the Yonsei University (YSU), a non-local closure scheme, and the Mellor-Yamada-Janjic (MYJ) scheme, a local closure scheme. Each scheme requires an specific surface layer scheme that computes momentum (τ), heat (SH) and moisture (LH) fluxes, and a land-surface model (LSM) scheme. Both give the lower boundary condition for the PBL schemes.

4.3.1 Non-local scheme: YSU

The Yonsei University (YSU) scheme (Hong et al. 2006) is a first order closure scheme (see Sect. 4.2). It is a non-local scheme based on non-local mixing (Fig. 4.2), which approximates the fluxes analyzing the mean profiles of turbulent mixing over the whole domain so it is more suitable to convective conditions. It is the next generation of the Medium Range Forecast Model (MRF) PBL (Hong and Pan 1996) which uses the countergradient terms to represent fluxes due to non-local gradients.

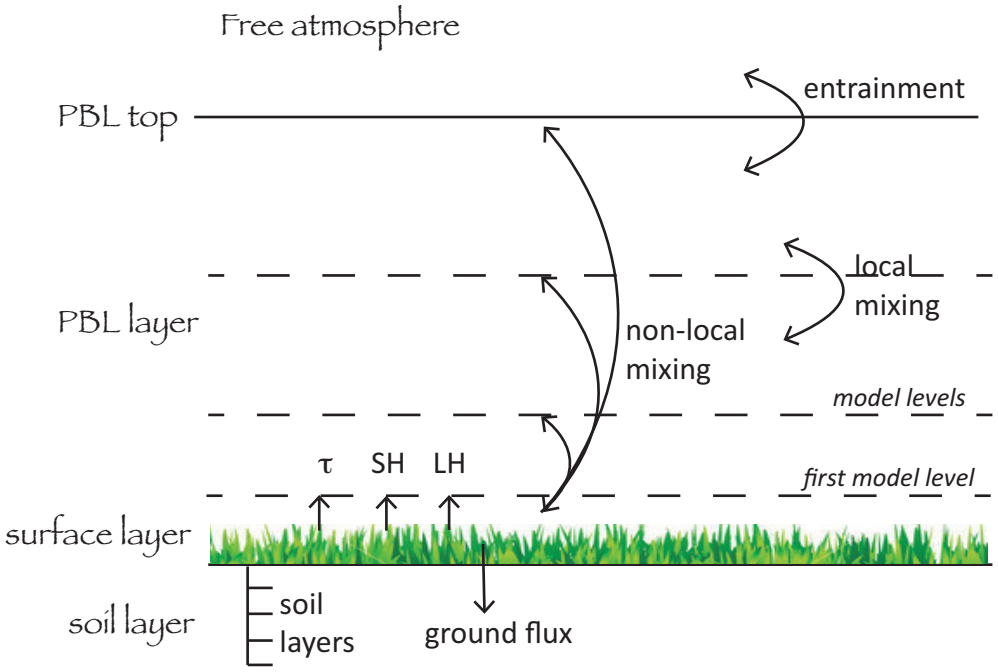

Figure 4.2: PBL processes in the WRF model. Adapted from Dudhia (2011).

The YSU scheme is based on a local K-profile but introduces a non-local gradient adjustment term (γ_ϕ) to incorporate the contribution of the large eddies and adds an explicit treatment of the entrainment processes at the top of the PBL with an asymptotic entrainment flux at the inversion layer proportional to the surface flux (last term of right-hand side in Eq. 4.2). According to Hong and Pan (1996), and following Deardorff (1972), Troen and Mahrt (1986) and Holtslag and Moeng (1991), the vertical turbulence contribution (last term in Eq. 3.7, 3.10 and 3.12) for any magnitude ϕ (u, v, θ, q) can be parameterized as:

$$\frac{\partial \overline{\phi}}{\partial t} = \frac{\partial}{\partial z}\left[K_\phi\left(\frac{\partial \overline{\phi}}{\partial z} - \gamma_\phi\right) - \overline{(w'\phi')}_h\left(\frac{z}{h}\right)^3\right] \tag{4.2}$$

where ϕ is any variable, K_ϕ is the eddy diffusivity coefficient, h is the height of the PBL, $\overline{(w'\phi')}_h$ is the flux at h (the inversion layer). When the boundary layer is stable there are no non-local terms (Eq. 4.2 without γ_ϕ and without term of right-hand side).

The eddy diffusivity for momentum (K_m) is calculated as (Hong et al. 2006):

$$K_m = \kappa \omega_s z\left(1 - \frac{z}{h}\right)^2 \tag{4.3}$$

where κ is the von Karman constant ($\kappa = 0.4$), z is the height from the surface and h is the PBL height and ω_s is the velocity scale, which is established with empirical functions (more details in Hong et al. (2006)).

The eddy diffusivity for heat (K_h) and moisture (K_e) is related with K_m through the Prandtl number (Pr):

$$K_{h,e} = \frac{K_m}{Pr} \tag{4.4}$$

In convective situations the PBL top (h) is established using the critical bulk Richardson number $Ri_{b,cr} = 0.25$, (while in MRF was 0.5) defined as:

$$h = Ri_{b,cr} \frac{\overline{\theta_{v1}}|\overline{U(h)}|^2}{g(\overline{\theta_v(h)} - \overline{\theta_s})} \tag{4.5}$$

where θ_{v1} is the virtual temperature at the lowest model level, $U(h)$ is the wind speed at h, $\theta_v(h)$ is the virtual potential temperature at h and θ_s is the appropriate temperature near the surface.

4.3.2 Local scheme - TKE closure schemes: MYJ

The Mellor-Yamada-Janjic (MYJ) scheme (Janjic 1990, 1996; Janjić 2002) is a 1.5 order scheme (2.5 turbulence level) with a prognostic equation for the TKE (Eq. 3.13). It is a local scheme so it estimates the turbulent fluxes at each grid point from the gradients or the mean values of the variables at that grid point.

It calculates the eddy diffusivity coefficients of any variable ϕ (K_ϕ) from the TKE (e) equation, based on a turbulence length scale (l) with a coeficient S_ϕ with the following relation:

$$K_\phi = l S_\phi \sqrt{\overline{e}} \tag{4.6}$$

The $\overline{e}$ production/dissipation equation is iteratively solved. From the TKE budget equation 3.13, for a one dimensional column (neglecting advection), neglecting subsidence and not considering horizontal homogeneity, the storage of the TKE is a balance between: the buoyancy (first term of right hand side), shear (second and third terms of right hand side) production or destruction, its turbulent transport (fourth term of the right hand side) and dissipation of energy (last term):

$$\frac{\partial \overline{e}}{\partial t} = \frac{g}{\theta_v}\overline{w'\theta'} - \overline{w'u'}\frac{\partial u}{\partial z} - \overline{w'v'}\frac{\partial v}{\partial z} - \frac{\partial}{\partial z}\overline{w'e'} - \varepsilon \tag{4.7}$$

where ε is molecular TKE dissipation, and each second order term is calculated using the K-theory defining K_m, K_e and K_h for momentum, TKE and heat fluxes respectively.

The turbulence length scale or mixing length (l) can be seen as a measure if the ability of turbulence to cause mixing. Their origin is from the Prandtl mixing-length theory where he said: "l may be considered as the diameter of the masses of fluid moving as a whole in each individual case". A common used form for l suggested by Blackadar (1962) is:

$$l = \frac{\lambda}{1 + \frac{\lambda}{\kappa z}} \tag{4.8}$$

where λ is the asymptotic length scale, which can chosen by the user, usually between 50-100 m or, as in MYJ, calculated as a function of PBL top (see Tastula et al. (2015)), κ is the Von Karman constant and $l \to kz$ near the surface. In the MYJ scheme l is preliminary calculated from the expression in 4.8 and later adjusted to satisfy further conditions.

Finally, the coefficients S_ϕ in Eq. 4.6 (where $\phi = m$ for momentum and h for heat), S_m and S_h, are computed from the nondimensional shear and stratification terms. More details can be found in Tastula et al. (2015).

On the other hand, the entrainment in the MYJ scheme is represented using the computed K_e from the prognostic $\overline{e}$ near the PBL top. The height of the PBL is established as the lower level where the TKE approximates to a minimum value of l.

Chapter 5 compares the performance of the WRF model using the YSU and MYJ parameterizations in resolving a density current circulation and the generation of gravity waves.

In chapter 7 simulations are run with both PBL schemes to validate the results against surface station data.

4.3.3 Free atmosphere mixing

In addition to handling the vertical turbulent mixing within the boundary layer, the PBL schemes in the WRF model also take care of the vertical turbulence that may be generated above the ABL, in the free atmosphere (when $z >$ PBL top), which is mostly stably-stratified. For the two different PBL schemes analyzed before (YSU and MYJ) the treatment of the mixing in the free atmosphere is different.

In the YSU scheme it is parameterized with the Richardson number following Louis (1979). For momentum, the calculation of the eddy diffusivity coefficient is:

$$K_m = l^2 f_m(Ri_g)\Big(\frac{\partial \overline{U}}{\partial z}\Big) \tag{4.9}$$

where the stability function for stably stratified atmosphere is (Hong et al. 2006):

$$f_m(Ri_g) = \frac{1}{(1 + 5Ri_g)^2} \tag{4.10}$$

and the gradient Richardson number (Ri_g) is:

$$Ri_g = \frac{g}{\overline{\theta_v}} \frac{\partial \overline{\theta_v}/\partial z}{(\partial \overline{U}/\partial z)^2} \tag{4.11}$$

where $\overline{U}$ is the wind speed and l, again, the length scale calculated such in equation 4.8 with a fixed asymptotic length scale.

For the MYJ scheme the vertical turbulence calculation in the free atmosphere is done as in the boundary layer, with the eddy diffusivity coefficients based on the TKE equation, as detailed in Sect. 4.3.2.

4.3.4 Surface layer and land surface model

The first vertical level of the model is considered to be within the surface layer in the model, defined as the layer where the fluxes are assumed constant and the shear turbulence dominates over the buoyant production. The surface layer computes the exchange coefficient for momentum (C_d) to calculate the momentum flux (τ) and the exchange coefficients for heat (C_h) and moisture (C_q) fluxes, necessary to calculate the heat (SH) and moisture (LH) fluxes (handled by the land-surface model to include radiation and precipitation forcings). The surface fluxes are calculated through the *drag law* (Stull 1988) as follows:

$$\tau = \rho u_*^2 = \rho C_d \overline{U_1^2} \tag{4.12}$$

$$SH = \rho c_p (\overline{w'\theta'})_s = \rho c_p C_h \overline{U_1}(\overline{\theta_1} - \overline{\theta_s}) \tag{4.13}$$

$$LH = \rho L_e (\overline{w'q'})_s = \rho L_e C_q \overline{U_1}(\overline{q_1} - \overline{q_s}) \tag{4.14}$$

where ρ is the air density, c_p the specific heat capacity of the dry air at a constant pressure and L_e is the latent heat of vaporization. $\overline{U}$ is the wind speed ($\sqrt{\overline{u}^2 + \overline{v}^2}$), $\overline{\theta}$ the potential temperature and $\overline{q}$ the specific humidity, where the subscript '1' designate the value at the lowest model-layer height (z_1) and 's' is the value at the surface. The friction velocity is defined as:

$$u_* = [(\overline{u'w'}_s^2) + (\overline{v'w'}_s^2)]^{\frac{1}{4}} \tag{4.15}$$

Using the relationship between the fluxes and their main gradients, Monin and Obukhov (1954) established the Monin-Obukhov similarity theory (MOST) to represent the buoyancy through the scaling length (L), with the stability parameter (z/L), where $L = \frac{-u_*^3 \theta_0}{kg(\overline{w'\theta'_0})_s}$. The local gradient Richardson number (R_i) can also be used to determine the stability. Then, the nondimensional gradients of velocity (Φ_m), temperature (Φ_h) and specific humidity (Φ_w) can be written as a function of z/L:

$$\frac{\kappa z}{u_*} \frac{\partial \overline{U}}{\partial z} = \Phi_m \left(\frac{z}{L}\right) \tag{4.16}$$

$$\frac{\kappa z}{\theta_*} \frac{\partial \overline{\theta}}{\partial z} = \Phi_h \left(\frac{z}{L}\right) \tag{4.17}$$

$$\frac{\kappa z}{q_*}\frac{\partial \overline{q}}{\partial z} = \Phi_w\left(\frac{z}{L}\right) \tag{4.18}$$

where the temperature scale $\theta_* = -\frac{(\overline{w'\theta'})_s}{u_*}$, and humidity scale $q_* = \frac{(\overline{w'q'})_s}{u_*}$.

Vertically integrating the nondimensional gradients Φ_m and Φ_h we obtain the stability functions ψ_m and ψ_h:

$$\psi_{m,h}\left(\frac{z}{L}\right) = \int_0^{z/L}[1 - \Phi_{h,m}(z/L)]\frac{d(z/L)}{z/L} \tag{4.19}$$

Combining equations 4.12 and 4.16 the exchange coefficient for momentum (C_d) can be expressed as:

$$C_d = \frac{\kappa^2}{\left[ln(\frac{z}{z_0}) - \psi_m(\frac{z}{L})\right]^2} \tag{4.20}$$

Similarly, combining equations 4.13 and 4.17 the exchange coefficient for heat (C_h) results in:

$$C_h = \frac{\kappa^2}{\left[ln(\frac{z}{z_0}) - \psi_m(\frac{z}{L})\right][\left[ln(\frac{z}{z_0}) - \psi_h(\frac{z}{L})\right]} \tag{4.21}$$

and combining equations 4.14 and 4.18 the exchange coefficient for moisture (C_q):

$$C_q = \frac{\kappa^2}{\left[ln(\frac{z}{z_0}) - \psi_m(\frac{z}{L})\right]\left[ln(\frac{\rho c_p \kappa u_* z}{c_s} + \frac{z}{z_l}) - \psi_h(\frac{z}{L})\right]} \tag{4.22}$$

where c_s is the effective heat transfer coefficient for non-turbulent processes.

The surface layer parameterization based on MOST in the WRF model consists of an iteration process (starting considering neutral conditions) where:

1. Calculate the stability parameters z/L
2. Establish an empirical stability function ψ for the corresponding z/L
3. Calculate the exchange coefficients through the expressions 4.20, 4.21 and 4.22

The surface layer coupled with the YSU and MRF schemes is the similarity theory based in MM5. It uses the functions from Paulson (1970), Dyer and Hicks (1970) and Webb (1970). The integrated similarity functions are calculated for different stability regimes (Zhang and Anthes 1982) as a function of the bulk Richardson number (Ri_b) (or z/L) defined in this case as:

$$Ri_b = \frac{g}{\overline{\theta_v}} z \frac{\overline{\theta_{v1}} - \overline{\theta_{vs}}}{\overline{U^2}} \tag{4.23}$$

The Ri_b delimits four different stability regimes: (i) the stable regime (when $Ri_b \geq 0.2$), (ii) the damped mechanical turbulence regime ($0 < Ri_b < 0.2$), (iii) the forced convection regime ($Ri_b = 0$) and (iv) the free convection ($Ri_b < 0$) (see Jiménez et al. (2012) for more details), with relationships including empirical constants from field experiments and further modifications (Jiménez et al. 2012).

The surface layer coupled with the MYJ scheme is the Eta similarity theory that is also based on MOST (Janjic 1996; Janjić 2002) and it includes viscous sub-layers over water (Janjic 1994) and over land Zilitinkevich (1995). Here, similarity stability functions of Paulson (1970) are used for the unstable surface layer with an applied correction from Beljaars (1995). For the stable surface layer the relationships from Holtslag and Beljaars (1988) are specified.

Once the exchange coefficients are calculated, the land-surface model (LSMs) gathers this information (Fig. 3.3) from the surface layer scheme, the radiation scheme (radiative forcing) and from the microphysics and convective schemes (precipitation forcing) and calculates the surface heat and moisture fluxes (Equations 4.13 and 4.14). The LSMs include the ground fluxes with the soil-layers information, including vegetation, canopy processes and the snow-cover.

4.3.5 Horizontal mixing

While the vertical turbulent fluxes are completely parameterized by the PBL schemes, the horizontal turbulence is considered partly or mostly resolved in the WRF model dynamics. However, some effects of the subgrid turbulent eddies are also included in the horizontal flow with the computation of horizontal turbulence (named as spatial diffusion) in the dynamical core. Then, the ARW solver in WRF has two different ways for treatment of horizontal turbulent mixing: the implicit and the explicit mixing. The implicit mixing is the artificial mixing introduced by the spatial filtering to account for the errors introduced when resolving the advection scheme by finite differences. Specifically, it is an implicit filter that damps the small-scale oscillations and increases the effective resolution of the model, so that in WRF the effective resolution can be estimated as $\approx 7\Delta x$ (Skamarock 2004). The explicit mixing or explicit diffusion can be specified in different spaces, on coordinate surfaces ($diff\_opt = 1$) or in physical space ($diff\_opt = 2$), or de-activated ($diff\_opt = 0$, for grid spacings larger than 10 km for example). For the calculation of the horizontal eddy diffusivities (K_h) there exist different options (using the namelist order km_opt): specifying constant values for K_h ($km\_opt = 0$) or using the Smagorinsky horizontal first order closure ($km\_opt = 4$) with the following expression Skamarock et al. (2008):

$$K_h = C_s^2 l^2 [0.25(D_{11} - D_{22})^2 + \overline{D_{12}^2}^{xy}]^{1/2} \tag{4.24}$$

where C_s is the Smagorinsky constant established as $C_s = 0.25$, l is the length scale

$l = (\Delta x \Delta y)^{0.5}$, D are the deformation terms of the stress tensor (τ_{ij}) due to the map scale factors (see Skamarock et al. (2008) for details). For scalar mixing K_h should be divided by the Prandtl number ($Pr = 1/3$) (Deardorff 1972).

If we run the WRF model in the LES mode (when the grid aspect ratio is similar in all dimensions), the 3D turbulence calculation is activated and the eddy diffusivities are calculated both for the horizontal (K_h) and the vertical (K_v) fluxes for the conserved variables, assuming that most part of the energy containing scales is resolved, and a small part is parameterized. Then, the PBL parameterization option is de-activated ($bl\_pbl\_physics = 0$). In this case, the eddy diffusivities can be calculated with a prognostic equation for TKE closure ($km\_opt = 2$) or with a 3D Smagorinsky scheme ($km\_opt = 3$) (more details can be found in Skamarock et al. (2008) and in next Sect. 4.4) .

4.4 Large-eddy simulation

According to Sect. 3.2, WRF-LES can be classified as a CFD that simulates the high-Reynolds number atmospheric flows integrating the NS equations including the earth's rotation and the buoyancy term (Boussinesq approximation) and parameterizing the viscous effects within the sub-grid. LES as a methodology for numerical simulation (Sect. 3.2.1) of high-Reynolds number turbulent flows was developed firstly on 1967 by Lilly (1967). Using Lilly's formulation Deardorff (1970a) succesfully carried out the first LES in a channel flow, and later for the atmospheric boundary layer (Deardorff 1970b). Nowadays, since the grid resolution can be increased and the computer power allows resolving the equations at these scales, the LES technique usage for resolving atmospheric flows is growing, catching the attention of atmospheric modelers.

For LES, the equations are filtered with a spatial filter, Δx, to resolve the energy-containing scales of the turbulent flow, l, assuming that $l >> \Delta x$. The energy below the cut-off scale is not resolved, i.e. the sub-grid scale (SGS) of turbulence has to be parameterized. As introduced in Sect. 4.1, the proper spatial filter or grid spacing for LES models depends on the sizes of the eddies that contain the energy, that will be larger for unstable conditions than for stable conditions. Looking at the turbulence spectrum (Fig. 4.1), LES would resolve the energy containing scales and partially the inertial range. LES also assumes that the resolved turbulence would be insensitive to the SGS model. So far, LES has been mostly applied to canonical boundary layer, i.e. flat terrain and horizontally homogeneous boundary layers, to study neutral, convective and stable flows. It has helped to increase the understanding of the flow structure and also the development of parameterizations for large-scale models. Nevertheless, LES of atmospheric flows has still many limitations, specially when the eddies are small and the SGS are not accurate. This situation is usually found near the *walls* (close to surface or near the top of the ABL) and for stably stratified flows.

In LES the NS equations are filtered for resolving large eddy motions in the atmospheric

boundary layer. Filtering the governing equations they can be formulated similar as Eq. 3.7, with the action of buoyancy (first term of the right hand side), coriolis (second term of the right hand side), pressure (third term of the right hand side) and the stress tensor including turbulence-viscosity effects (last term of the right hand side):

$$\frac{\partial \tilde{u_i}}{\partial t} + \frac{\partial (\tilde{u_i}\tilde{u_j})}{\partial x_j} = -\frac{g}{T_0}\tilde{\theta}\delta_{i3} - 2\epsilon_{ijk}\zeta_j\tilde{u_k} - \frac{\partial \Pi}{\partial x_i} - \frac{\partial \sigma_{ij}}{\partial x_j} \tag{4.25}$$

where ζ is the Earth's rotation and Π is the modified pressure. The $(\tilde{..})$ denotes a spatial filtering operation, using a filter of characteristic width similar to a length scale (Δ_f), which is of the order of the grid size ($\Delta_f/\Delta_x \approx 1$ or 2) (Basu and Porté-Agel 2006). The deviatoric or anisotropic SGS stress (σ_{ij}) is defined as:

$$\sigma_{ij} = \tau_{ij} - \frac{1}{3}\tau_{kk}\delta_{ij} \tag{4.26}$$

and the isotropic component of the SGS stress ($\frac{1}{3}\tau_{kk}\delta_{ij}$) is added to the pressure term through the modified pressure Π. The τ_{ij} is the total SGS stress defined as:

$$\tau_{ij} = (\tilde{u_i}\tilde{u_j})^r - \tilde{u_i^r}\tilde{u_j^r} = [(\tilde{u_i^r}\tilde{u_j^r})^r - \tilde{u_i^r}\tilde{u_j^r}] + (\tilde{u_i^r}\tilde{u_j^s} + \tilde{u_i^s}\tilde{u_j^r})^r + (\tilde{u_i^s}\tilde{u_j^s})^r \tag{4.27}$$

where the term in square brackets is the Leonard stress, the second term in the right hand side is the mixed term (Cross stress) and the third therm is the SGS Reynolds stress. The superscript r denotes the resolved part and the superscript s the subgrid fields (more details are given in (Kosović 1997)). The SGS stress and also the SGS heat flux (from filtering the conservation of energy equation) that arise from these equations are parameterized using a first order closure with eddy diffusivity approach. One of the most known is the Smagorinsky approach, based on a coefficient which can be constant or dynamic. In the next subsection there are more details about the SGS parameterizations.

LES has been successfully applied to study the ABL in different models since the Deardorff's work in the 70's. In the early 80's, Moeng (1984) used a new LES code to resolve the three-dimensional turbulence. Mason (1989), Schmidt and Schumann (1989) and Sullivan et al. (1994) performed LES simulations of neutral and CBL and other comparisons among LES codes (Nieuwstadt et al. 1993; Andren et al. 1994) were done, also focusing on sensitivities to SGS models. Later, many studies explored and developed new SGS models (Kosović 1997; Cuxart et al. 2000). As turbulence scale is reduced in stably stratified conditions, many LES have also been applied to study the SBL (Mason and Derbyshire 1990; Brown et al. 1994; Andren 1995; Kosović and Curry 2000; Saiki et al. 2000; Jimenez and Cuxart 2005; Beare et al. 2006; Huang and Bou-Zeid 2013). In particular, Beare et al. (2006) intercompared several LES models for the SBL as part of the Global Energy and Water Cycle Experiment Atmospheric Boundary Layer Study (GABLS) project, based on the BASE (Beaufort Sea Arctic Stratus Experiment) arctic observations, reproducing a clear air SBL driven by a cooling rate. In stable conditions, however, when the eddy size is very small, an accurate SGS model is needed to resolve the eddies smaller than the

grid size or the filter width. So far, a good representation of the (very) stable ABL with LES has not been achieved. In the last decade, some LES explored simulating flows over topography. (Chow et al. 2006) studied the flow in a steep valley in the context of the the Mesoscale Alpine Experiment (MAP) experiment. Golaz et al. (2009) validated an LES simulation over an island in Scotland, the Askervein Hill. Lately, Talbot et al. (2012) simulated the atmosphere over realistic terrain, comparing ideal and real simulations with the WRF model.

4.4.1 WRF-LES

The WRF model can be used for simulating high resolution flows with the LES approach, what is called WRF-LES. First published literature of WRF-LES not came out until the end of the first decade of the XXIst century (Moeng et al. 2007; Mirocha and Kosović 2010; Mirocha et al. 2013). A great advantage in comparison with other LES codes is that WRF-LES uses the nesting capability to provide the periodic boundary conditions and the possibility to directly couple LES domains from mesoscale simulations. WRF-LES nesting can be done with one-way interaction (Mirocha et al. 2013; Muñoz-Esparza et al. 2014) or two way interaction, as examined by Moeng et al. (2007).

The ideal mode of WRF-LES needs an initial profile (*input_sounding*) of potential temperature, humidity and wind components. The lateral boundary conditions are periodic from the coarse to the nested domain. The top boundary condition has to be set with a potential temperature inversion layer and a damping layer to absorb waves generated by numerical instabilities. The lower boundary condition is based on a MOST (see Sect 4.3.4), slightly modified, to calculate the momentum and heat fluxes at the first layer of the model. In WRF-LES, the surface heat flux can be prescribed with a fixed value or calculated through a cooling rate ($d\theta/dt$). From equation 4.13 the θ_s is caclulated for each time step (dt):

$$\theta_s(t) = TSK(t) - \frac{d\overline{\theta}}{dt}dt \tag{4.28}$$

where TSK represents the soil skin temperature, changing with time at each iteration. The implementation of a cooling rate in the surface layer through equation 4.28 was done to execute WRF-LES in a more realistic stable boundary layer and is activated in the *namelist.input* file through the option *isftemp = True*.

When using WRF-LES, the PBL parameterizations are turned off and the three-dimensional turbulence is activated (as we have seen in Sect. 4.3.5). Then, the eddy diffusivities are similarly calculated in horizontal and vertical directions, so similarly to Eq. 4.24 but for the three-dimensional resolved turbulence the computation of K_h and K_v in the WRF model (Skamarock et al. 2008) is given by:

$$K_{h,v} = C_s^2 l_{h,v}^2 max\Big[0, (D^2 - P_r^{-1}N^2)^{1/2}\Big], \tag{4.29}$$

where

$$D^2 = \frac{1}{2}\Big[D_{11}^2 + D_{22}^2 + D_{33}^2\Big] + \overline{(D_{12}^{xy})}^2 + \overline{(D_{23}^{x\eta})}^2 + \overline{(D_{12}^{y\eta})}^2 \tag{4.30}$$

and each D represents the deformation term of the stress tensor (τij) due to the map scale factors. Here, the horizontal length scale (l_h) and vertical length scale (l_v) are calculated in a different way depending on the grid dimensions. For isotropic grids ($\Delta x, \Delta y \approx \Delta z$), the length scales $l_{h,v} = (\Delta x \Delta y \Delta z)^{1/3}$ and $K_h = K_v$. For anisotropic grid (where $\Delta x, \Delta y > \Delta z$), the length scale $l_h = (\Delta x \Delta y)^{0.5}$ and $l_v = \Delta z$, and K_h and K_v are calculated using Eq. 4.29.

All the other physic parameterizations such as radiation schemes and cloud physics are deactivated. As the grid spacing is much smaller in LES than in mesoscale simulations, the total horizontal domain size is reduced as well, so a typical LES domain is around a few kilometers. Moeng et al. (2007) recommended nested domains (horizontally) larger than 5 times the PBL height. In the vertical, the domain is supposed to be around the PBL top, so depending on stability it can be from a few hundred meters (SBL) to 1 or 2 km (CBL). Also because of the reduced grid size, the time step is lowered, to prevent the CFL condition. For instance, for a 20 m grid simulation the time step was set down to 0.03 seconds.

Simulations are run during several hours so the flow reaches quasi-stationarity. The quasi-instantaneous results should be averaged spatially and/or temporally to obtain the first (mean), second (variances) and third (skewness) order statistics. Then, for a given variable $\phi(t, z, y, x)$ the 2 right most dimensions are one-dimensionalized in a new matrix to compute the spatial averages, so that, $\phi(t, z, m)$ where $m = y * x$. Then, the statistics are calculated with the following steps:

1. First order statistics, averages:

$$\overline{\phi}(t, z) = \frac{1}{m_{max}} \sum_{m=1}^{m_{max}} \phi(t, z, m) \tag{4.31}$$

2. Second order statistics, variances:

$$\overline{\phi'^2}(t, z) = \sigma_\phi^2(t, z) = \frac{1}{m_{max} - 1} \sum_{m=1}^{m_{max}} \big(\phi(t, z, m) - \overline{\phi}(t, z)\big)^2 \tag{4.32}$$

3. Third order statistics, skewness:

$$\overline{\phi'^3}(t, z) = \frac{1}{(m_{max} - 2)\sigma_\phi^3} \sum_{m=1}^{m_{max}} (\phi(t, z, m) - \overline{\phi}(t, z))^3 \tag{4.33}$$

where m_{max} is the number of points in x-direction and y-direction ($m = y * x$). Next, the variable is averaged in time to obtain vertical profiles of the resulting order moments.

4.4.1.1 Sub-grid scale models in WRF-LES

Mirocha and Kosović (2010) developed the SGS parameterization in WRF-LES through a subfilter turbulence stress model. Kirkil et al. (2012) also explored the accurateness of some dynamic SGS models in comparison with the constant coefficient Smagorinsky model (Smagorinsky 1963). Within the WRF-LES there are different SGS models that parameterize the sub-grid stresses. The standard SGS model in WRF is the simplest first-order closure Smagorinsky model that uses a linear eddy viscosity approach (Smagorinsky 1963; Lilly 1967). These scheme can include a prognostic equation for the SGS TKE, then, it is called a 1.5 TKE model (Lilly 1967). Both are based on an eddy-viscosity (ν_t) approach to formulate the deviatoric part of the SGS stress (σ_{ij}) which appeared in Eq. 4.25 (Kosović 1997):

$$\sigma_{ij} = \tau_{ij} - \frac{1}{3}\tau_{kk}\delta_{ij} = -2\nu_t S_{ij} \tag{4.34}$$

where S_{ij} represents the resolved strain rate tensor, $S_{ij} = \frac{1}{2}\left(\frac{\partial \tilde{u}_i}{\partial x_j} + \frac{\partial \tilde{u}_j}{\partial x_i}\right)$, and ν_t is the eddy viscosity.

The eddy viscosity, ν_t, can be formulated (i) as proportional to the strain rate stress, which is known as Smagorinsky model:

$$\nu_t = (C_s l)^2 (2 S_{ij} S_{ij})^{1/2} \tag{4.35}$$

where C_s is the Smagorinsky constant and l (Δ_f in Sect. 4.4) can be established as $l = (\Delta x \Delta y \Delta z)^{1/3}$, or (ii) similarly to the 1.5 TKE closure PBL schemes (Eq. 4.6), the eddy viscosity can be also approximated by the SGS TKE, e, (that requires resolving the prognostic equation for the sub-grid kinetic energy):

$$\nu_t = l C_e \sqrt{e} \tag{4.36}$$

where C_e is a modeling coefficient similar to C_s.

Many LES models use Smagorinsky-type models for SGS parameterization although it is known that they are too dissipative and cannot represent the local kinetic energy backscatter, i.e. the reverse energy transfer. They neither represent the anisotropy of the turbulence. Using dynamic Smagorinsky models would help to develop backscatter effects but not to resolve the anisotropy. In WRF-LES model there is another SGS model in addition to Smagorinsky, the Nonlinear Anisotropy Backscatter (NBA) model (Kosović 1997; Mirocha et al. 2010) which aims to resolve these limitations, accounting for the anisotropy and the energy backscatter of the SGS tensor.

Chapter 6 explores the vertical structure of turbulence using the WRF-LES model with the methodology described above and using the Smagorinsky SGS model.

4.4.2 Future: from mesoscale to LES

Thanks to the capacity of computers and CPUs, running operational forecasts with MMMs at high resolutions (grid sizes $\approx$ 1 km or less) is nowadays possible. One have to bear in mind, though, that when the turbulent energy scale is larger than the grid size, the mesoscale approach is not valid anymore. Then, the transition from mesoscale (MMM) to microscale (LES) is needed. Since the WRF model allows nesting LES domains within a mesoscale domain, it seems easy to simulate this transition. Indeed, it can be easy in terms of design and execution, although several limitations and considerations appear when jumping from mesoscale to LES approaches.

In LES, turbulence has to be initialized (spin-up) and has to be periodic. Periodicity can be set using one-way nesting coupling, so the information from the parent domain is transferred to the nested domain at each time step. The spin-up of turbulence in the inner domain is a more complicated issue. In the inlet boundaries the mesoscale domain does not provide enough turbulence for the LES domain, so turbulence has to be developed. Recently, Mirocha et al. (2014) added terrain perturbations to accelerate the turbulence, but it leads to errors in the mean variables in the LES domain. They also found that the different SGS physics between domains can lead to different results. Another limitation is the steep slopes that appear in the vertical levels when using fine grid sizes in complex terrain areas (more details in Sect. 4.5).

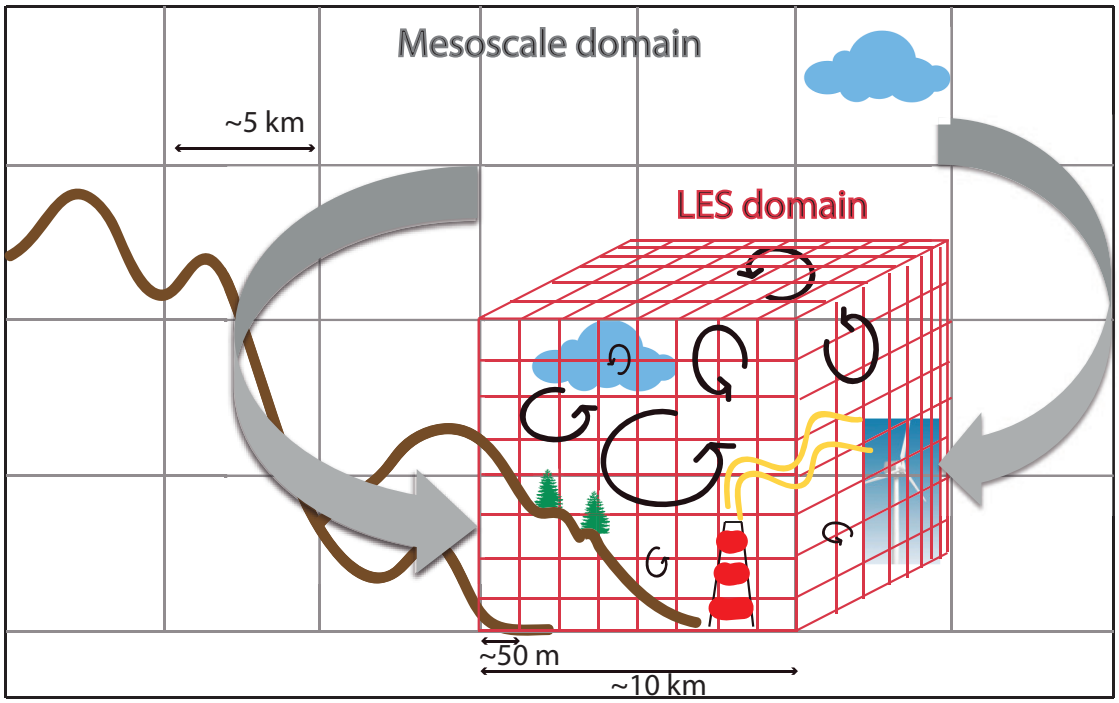

Figure 4.3: Transition from mesoscale to LES scales. Adapted from Moeng (2011).

In terms of modeling the ABL, nesting LES inside the mesoscale over realistic topography seems to be the logical next step to achieve. By doing that, all the scales present in the atmosphere will be resolved: from large scale advection and fronts to local circulations and even small turbulent features (Fig. 4.3). Therefore, future research is needed to address all the emerging issues when simulating flows from meso to microscales.

4.5 Modeling in complex terrain

Several field experiments have been done to improve the understanding of the flow over complex terrain (see Sect. 2.3.3.1). Among many other studies, they lead to NWP performance and model inter-comparisons over complex terrain. On the other hand, some efforts, but not many, have been put in modeling complex terrain with the LES approach. Some authors have simulated flows over real or ideal heterogeneous terrain using LES: for neutral turbulent flows (Brown et al. 2001), using the Askervein hill data (Chow and Street 2009; Golaz et al. 2009) or to study the wave breaking and rotor formation (Epifanio and Qian 2008; Smith and Skyllingstad 2009).

Simulating atmospheric flows over complex terrain is still a challenge. Mountainous terrain with abrupt slopes and deep valleys needs grid refinement to be well represented. At the same time, for good forecast of magnitudes (such as temperature, humidity or wind), a correct representation of the terrain is needed. This means reducing the horizontal grid resolution down to 1 km or less. It is, though, when some limitations and problems in models show up. In areas with abrupt terrain elevations (such as the Pyrenees in Fig. 4.4) coarse horizontal grid sizes are not able to capture the terrain shape (Fig. 4.4a and 4.4b). As the grid spacing is reduced, the topography is better represented (Fig. 4.4c).

From the mesoscale perspective, the flow features over complex terrain have to be included in the sub-grid parameterizations. For instance, the gravity wave drag parameterization for grid sizes greater than 10 km was found necessary (Kim and Arakawa 1995) over mountainous regions in order to represent an important sub-grid component of the momentum flux that affects the jet stream level. Jiménez et al. (2012) introduced a correction for the surface parameterization to account for the negative wind bias in the mountain hills and the positive wind bias near the plains.

On the other hand, when the grid size is reduced down to hundreds of meters, wether using mesoscale or LES approaches, other considerations arise. The smaller the grid spacing the more precision we will get in the topography elevation for each grid point. Therefore, magnitudes near the surface such as temperature, humidity and wind will be better resolved. However, the good representation of the topography leads to steep slopes that are a limitation for numerically resolving the equations with the terrain-following hydrostatic-pressure vertical coordinates. For terrain steeper than about 40 to 45° current levels of discretization reach their limit (Arnold et al. 2012) because of an incorrect calculation of the horizontal pressure gradient term. When that happens, smoothing of

the terrain is necessary. Another solution is changing the coordinate system to a cartesian height system which is called "Immersed Boundary Method" (IBM), which is currently in development (Lundquist et al. 2010). Moreover, all the parameterizations that assume horizontal homogeneity may be compromised when details of topography are resolved. An example is the MOST applicability for the surface layer. MOST assumes homogeneity and exchange of momentum through shear stress. In complex terrain the surface layer parameterizations should include heterogeneity and three-dimensional momentum calculation. In addition, when there is steep topography it would be also required to include the topographic shading and the cloud shading over the terrain, which adds many complexities to the radiation schemes. The previous discussion highlights that modeling in complex terrain is not an easy task. Further research is still needed in this field to address and resolve these issues.

Chapter 7 presents a modeling study of mountain wave event over a complex terrain area with the mesoscale approach of the WRF model.

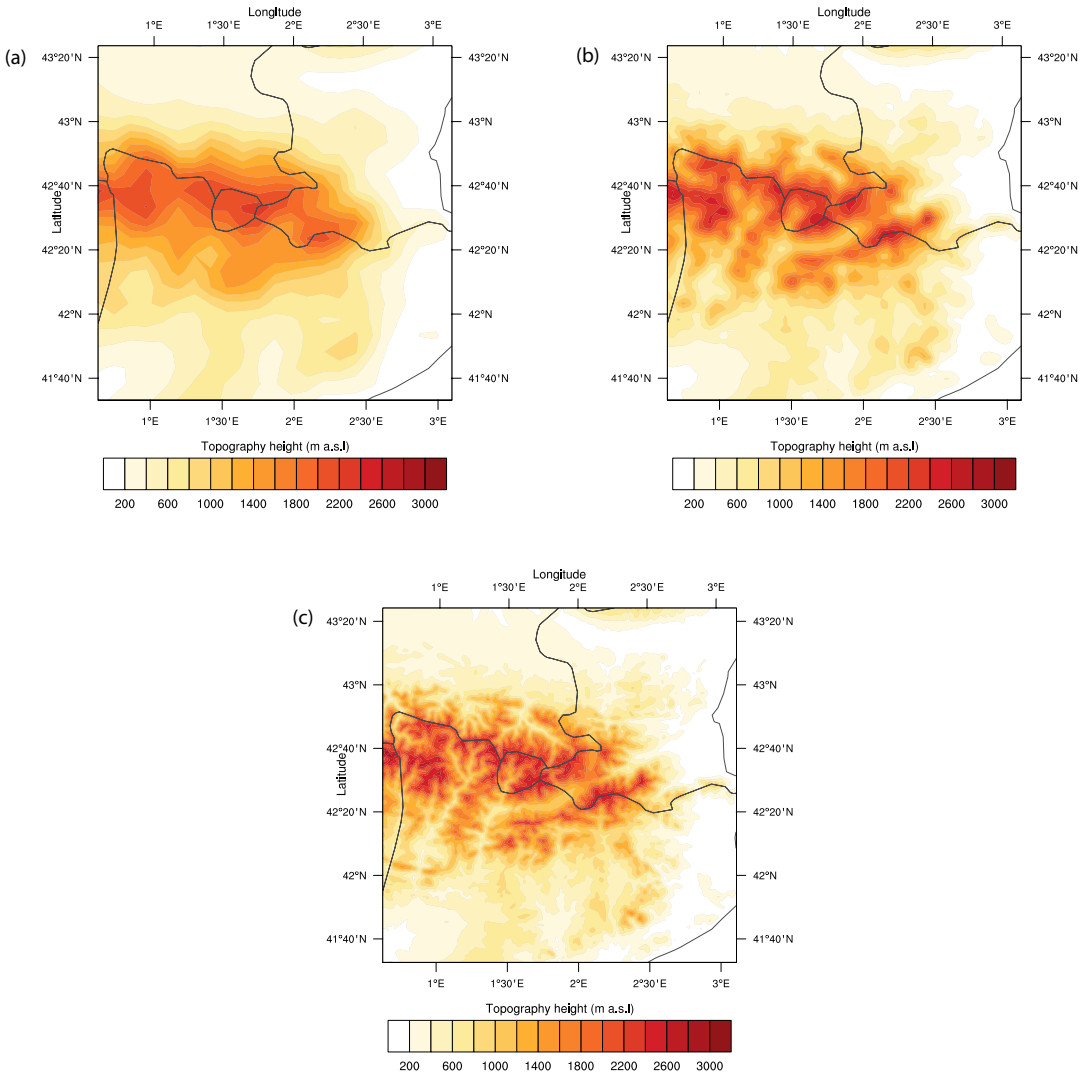

Figure 4.4: The Pyrenees topography represented by different horizontal grid resolutions: (a) Δx =9 km, (b) Δx =3 km, (c) Δx =1 km.

Part II

Simulation of physical processes in the ABL

5

Density currents and gravity waves at the CIBA site

Contents

This chapter presents a mesoscale model analysis of a density current arrival at the CIBA site which lead to the generation of gravity waves. The chapter is focussed on the analysis of a single event that occurred during the night from 22 to 23 June 2006, reported by Viana et al. (2010). In addition, a sequence of similar events observed consecutively during 8 days, from 3-10 July 2003, are simulated and analyzed as well. These results have been reported in Udina et al. (2013) and Soler et al. (2014):

- Udina, M.; Soler, M.R.; Viana, S.; Yagüe, C. 2013. **Model simulation of gravity waves triggered by a density current**. Quarterly Journal of the Royal Meteorological Society. 139 (672): 701-714.

- Soler, M.R.; Udina, M.; Ferreres, E. 2014, **Observational and Numerical Simulation Study of a Sequence of Eight Atmospheric Density Currents in Northern Spain**. Boundary-Layer Meteorology. 153 (2): 195-216.

5.1 Introduction

Gravity or density currents are flows created by differences in the density of two adjacent fluids (Adachi et al. 2004). They are important mesoscale phenomena often originated and driven by topographical features that influence local weather. They are manifested as cold air, close to the ground, that flows under the influence of gravity (Stull 1988), and they can arise from squalls, distant cold fronts, sea-breeze fronts or other atmospheric mesoscale disturbances (Simpson 1999). In addition, on relatively flat plains adjacent to mountain slopes, gravity currents may be initiated by katabatic flows coming off the mountains at night (Adachi et al. 2004). Papadopoulos and Helmis (1999) found that the origin of a katabatic flow at the foot of a slope can be both local cooling and the arrival of a density current that enhances shallow surface inversions and produces sharp falls in temperature as well as changes in wind direction. The development of the different regimes depends on the distribution of cooling along the slope, the stratification at the bottom of the slope and the ambient wind speed and direction (Mahrt et al. 2010).

In any case, the irruption of this flow with sudden variations in the abovementioned magnitudes may result in vertical displacement of air parcels from their equilibrium position, which has been shown to be a common source of IGWs (Chemel et al. 2009). These act as a modulator of the gravity current and may produce events of intermittent turbulence (Soler et al. 2002; Sun et al. 2002; Terradellas et al. 2005). IGWs are important atmospheric disturbances because they transport energy and momentum and they can be a source of turbulence. During breaking processes a transfer of momentum, heat and humidity is produced from the wave field to the main flow. The interaction between waves, turbulence and small-scale structures is complex in the boundary layer (Chimonas 1999; Viana et al. 2009, 2012).

Waves are usually manifested as fluctuations in pressure, wind and temperature fields (Nappo 2002). Many studies have dealt with the theory of IGWs (Rottman and Einaudi 1993; Chimonas 2002). Several authors have observed them in the NBL (Sun et al. 2004), in katabatic flows (Gryning et al. 1985; Bastin and Drobinski 2005) or within gravity currents (Adachi et al. 2004). Gravity waves can exist over a wide range of scales and periods. In the present study we deal with IGWs generated in the first few hundred meters of the NBL within a cold density current.

Experimental campaigns such as SABLES98 (Cuxart et al. 2000), CASES99 (Poulos et al. 2002) and SABLES2006 (Yagüe et al. 2007) have dealt with typical processes in the stable boundary layer. It was often observed that mesoscale circulations were the origin of different phenomena such as: intermittent turbulence, IGWs, low-level jets (LLJs) and drainage winds. Some of these events have been analyzed using the wavelet method and multi-resolution flux decomposition to study pressure perturbations related to IGWs (Cuxart et al. 2002; Terradellas et al. 2005; Viana et al. 2007, 2009, 2010).

As Conangla and Cuxart (2006) indicate, high-resolution mesoscale simulations are needed to better determine the origins of IGWs and turbulent processes. Little effort has been made to model gravity waves around the range of the meso-gamma scale. Thus, starting from an observational study of IGWs generated at the top of a drainage flow (Viana et al. 2010) during the SABLES2006 field campaign, here we aim to simulate the event through mesoscale meteorological modelling. Since we deal with mesoscale motions, mesoscale meteorological simulations are a good tool for representing thermal circulations over complex terrain, such as sea-breezes, drainage flows and LLJs. Mesoscale models can solve the atmospheric equations with quite detailed horizontal and vertical resolution; however, the turbulent diffusion processes are subgrid-scale and therefore they have to be parametrized in the models. Different ways of representing subgrid-scale vertical mixing processes lead to differences in the turbulent fluxes predicted by the boundary layer schemes (Alapaty et al. 1997).

The WRF model is widely used to study mesoscale phenomena. Mesoscale disturbances are one of the sources of small-scale phenomena that most influence circulation patterns and the transport of any quantity (energy, heat, momentum, humidity, etc.); it is therefore necessary for the model to capture them correctly. Recent evaluations and comparisons between different planetary boundary layer (PBL) schemes of the WRF model (Hu et al. 2010; Shin and Hong 2011; Jiménez et al. 2012) show good performance in diurnal cycles but more discrepancies at night. Nocturnal flow regime studies reveal that boundary layer fields are very sensitive to the boundary layer scheme used (Mölders and Kramm 2010). Here we examine the sensitivity of the model to two different PBL parametrizations: the Mellor-Yamada-Janjic (MYJ) scheme and the Yonsei University (YSU) scheme. In addition, fine horizontal resolution is used in the model (1 km), as recent studies Seaman et al. (2009); Stauffer et al. (2009) have stressed the importance of using high horizontal and vertical resolutions to capture stable boundary layer processes.

The WRF model has also been used to simulate convectively generated gravity waves (Lane and Knievel 2005), associated with an upper-level jet system (Lu et al. 2006) or in stable conditions over Base nunatak in Antarctica (Valkonen et al. 2010). Recently, Larsén et al. (2011) have used the WRF model to demonstrate the correspondence between the model and observed wind and temperature spectra, with and without the presence of gravity waves. Following on from previous studies, here we attempt to explore the capacity of WRF to: i) simulate the presence of an IGW at the top of a gravity current with 1 km resolution; ii) simulate the mesoscale flow structure that generated the gravity waves, as well as their origin; and iii) analyze the characteristics of the gravity wave generated by the gravity current, using the wavelet transform (Torrence and Compo 1998; Terradellas et al. 2001) applied to the WRF model data. The wavelet transform, as mentioned in Sect. 2.2.1, is a modern multiscale tool that permits the analysis of time series at very different scales in order to give the time evolution of the different frequencies that contribute in these time series (Terradellas et al. 2005). In this study the wavelet technique is applied to determine the characteristic parameters of the gravity waves from one minute model outputs of potential temperature.

5.2 Description of the CIBA site

The study area and model domains are centered on the Research Centre for the Lower Atmosphere (CIBA) situated at 41°49' N, 4°56'W, 840 m ASL: about 30 km north-west of the city of Valladolid, in the upper Duero basin of the Northern Spain, (San José et al. 1985). The area is surrounded by mountains, over 100 km away that rise to over 2500 m ASL: the Cantabrian Mountain Range to the north, the Central Mountain Range to the south and the Iberian Mountain Range to the east (Fig. 5.1a). CIBA sits on a small plateau known as Montes Torozos, which is an almost nearly flat area of 800 km2, 840 m ASL and approximately 50 m above the surrounding flat lands (Fig. 5.1b). The plateau has a gentle slope that accounts for a total increase in height of 30 m along 50 km from the north-east to the south-west, while the north-west and the south-east borders are slightly above the level of the inner plateau (Bravo et al. 2008). It is covered by grain crops and uniform vegetation with a roughness parameter of about 0.011 m (San José et al. 1985).

The area has been used for many atmospheric boundary layer experiments, such as SABLES98 and SABLES2006, whose objectives were to study the properties of the mid-latitude stable boundary layer and the typical features of the NBL such as: intermittent turbulence, slope flows, down-valley winds, LLJs and gravity waves (Cuxart et al. 2000; Terradellas et al. 2001; Conangla et al. 2008; Cuxart 2008; Bravo et al. 2008; Viana et al. 2007, 2009, 2012).

The laboratory's main facility is a 100-m mast equipped with fast-response sonic anemometers and a set of conventional sensors that measure wind speed and direction, air temperature and relative humidity at different heights (Table 5.1), as well as soil

Table 5.1: Main instrumentation installed on the 100-mast

Instrument	Heights (m)	Sampling rate (Hz)
Metek USA-1 sonic anemometers	3, 19.6, 96.6	20
Wind vanes	9.6, 34.6, 74.6, 98.6	5
Cup anemometers	2.3, 9.6, 34.6, 50.0, 74.6, 98.6	5
Platinum resistance thermometers	2.3, 10.5, 20.5, 35.5, 97.5	1
Microbarometers	20, 50, 100	2
Humidity sensors	10, 97	5

temperature and atmospheric pressure at the surface. In addition, six Paroscientific microbarometers were installed in 2006: three of them on the mast at 20, 50 and 100 m; and the remaining three at 1.5 m AGL on the vertices of a triangle of around 200 m to detect the IGWs (see Table 1 in Viana et al. (2010) for details). A Radio Acoustic Sounding System (RASS) sodar and tethered balloon soundings were used to collect additional data.

5.3 WRF configuration

The WRF model simulation configuration is detailed for the single event case study (22-23 June 2006) and for the eight consecutive density currents (3-10 July 2003).

5.3.1 WRF configuration for the single case study

Simulations were run with the WRF modelling system: a state-of-the-art mesoscale numerical weather prediction system, developed by a collaborative partnership in the USA. The version used was 3.1.1 and the dynamics solver used in this study was the Advanced Research WRF (ARW) designed for both research and operational applications (Skamarock et al. 2008). WRF is a fully-compressible non-hydrostatic model, with a terrain-following vertical coordinate; the horizontal and vertical grid staggering is of Arakawa C-grid type. It has many physics options to choose from for the parametrization of the microphysics, cumulus, surface layer, land surface, boundary layer and radiation physics.

The model configuration (Table 5.2) consists of four domains centred on the location of the CIBA meteorological tower, with horizontal resolutions of 27, 9, 3 and 1 km (Fig. 5.1). Domains 1 (27 km), 2 (9 km) and 3 (3 km) are run in two-way nesting from 0000 UTC 22 June to 0600 UTC 23 June 2006 with output files saved every hour. For these domains, the first 6 h are treated as spin-up and the next 24 h are used for evaluation. Domain 4 (154 x 100 1 km-cells) is nested from domain 3 in one-way nesting, with the study focusing on the night from 1800 UTC 22 June to 0600 UTC 23 June 2006. The reason for applying one-way nesting for the smaller domain is that in two-way nesting, all domains are run at the same time and interact fully. The inputs into a nest from the

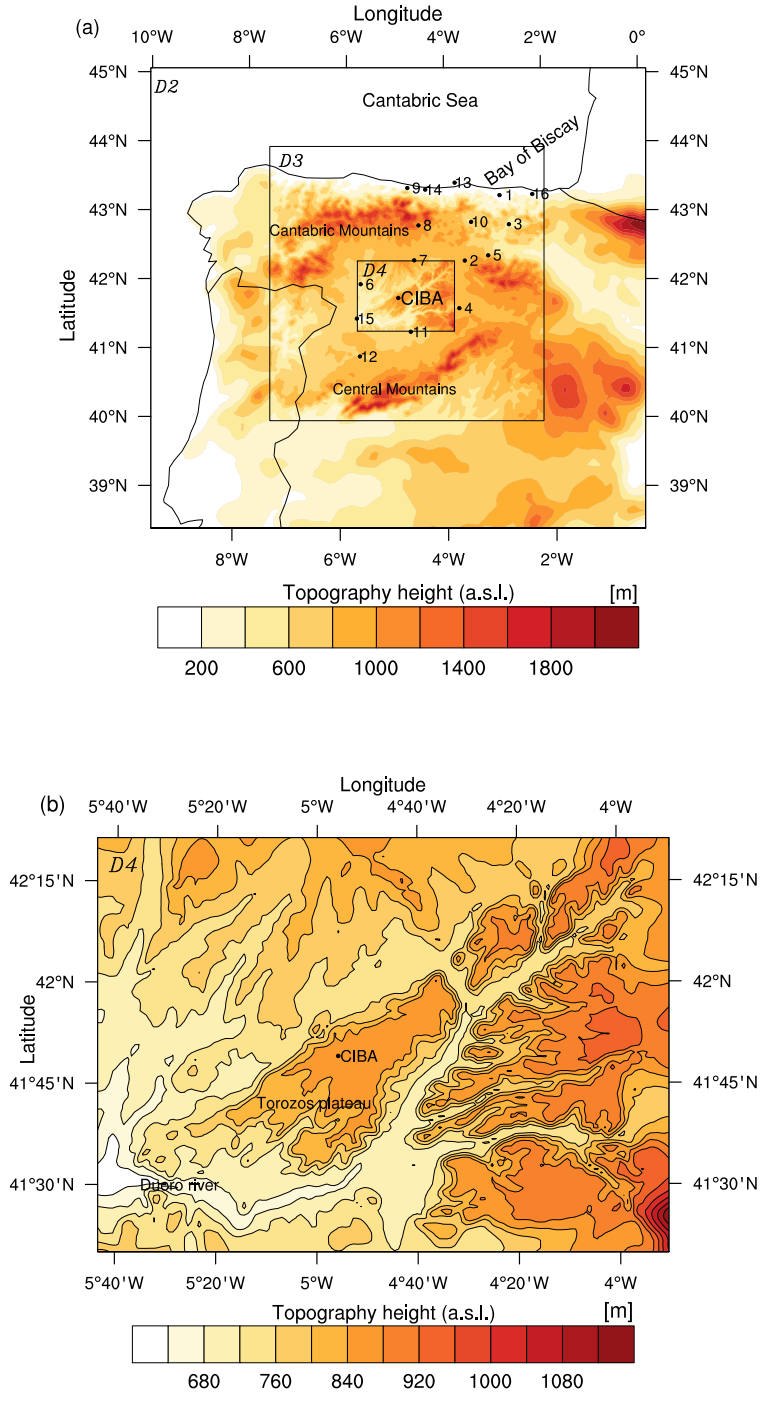

Figure 5.1: (a) Nested model domains D2, D3, D4 with 9-, 3- and 1-km resolutions respectively; geographical location of the CIBA site; topography and emplacement of 15 surface meteorological stations within the domain D3 numbered from 1 to 15. (b) Detailed topography of the inner domain D4 with 40-m terrain height contours.

coarse domains are introduced through its boundary, while feedback to the coarse mesh occurs over the whole of the nest interior, as its values are replaced by a combination of fine domain values. This procedure requires model outputs for the same time interval in all the domains, which makes it difficult to obtain model outputs with a higher frequency in the smaller domain (1 minute) for spectral analysis. Thus, domains 3 and 4 are run in one-way nesting, and the output files are saved at 12-minute and 1-minute time intervals for mean values and spectral analysis respectively. In general, two-way nesting is believed to work better because it allows smaller-scale features to feed back and influence features at the larger scale. However, detractors of two-way nesting claim that the method somehow "pollutes" results obtained in the outer domain (Soriano et al. 2002).

In this work, the study and the analysis are focused on domains 3 and 4 (Fig. 5.1) since their high resolution (3 and 1 km respectively) allow the details of the flow over the Duero basin and Montes Torozos plateau to be captured. In the vertical, 48 sigma levels are used from the ground up to 100 hPa for all the domains with the first level 6 m above the surface, and the first 20 levels all within the first 250 m. Initial and boundary conditions are taken from the National Centers for Environmental Prediction (NCEP), in particular from the Climate Forecast System Reanalysis (CFSR) which has a horizontal resolution of 0.5° and the boundary conditions are forced every 6 h.

The physics package includes the rapid radiative transfer model (RRTM) scheme for long-wave radiation (Mlawer et al. 1997), the Dudhia scheme for shortwave radiation (Dudhia 1989), the New Thompson microphysics scheme (Thompson et al. 2004), the Grell 3D cumulus scheme (Grell and Dévényi 2002) and the Noah Land Surface scheme (Chen and Dudhia 2001). With this physics package, two simulations are run using two different parametrizations of surface layer and PBL. The first one includes the MM5 similarity for surface layer and the YSU scheme (Hong et al. 2006) for PBL, whilst the second uses the Eta surface layer scheme and the MYJ for PBL (Janjic 1990, 1996; Janjić 2002).

The YSU PBL scheme is a first-order non-local scheme, with a counter-gradient term in the eddy-diffusion equation. The YSU scheme is modified in WRF version 3 (Hong 2010) from the Hong et al. (2006) formulation by using the exchange coefficient as a parabolic function of height in the mixed layer. In addition, the top of the stable boundary layer (SBL) is determined by the bulk Richardson number, R_B, increasing its critical value from zero to 0.25 over land, thereby enhancing mixing in the stable boundary layer (Hong and Kim 2008). The MYJ PBL scheme uses the 1.5-order (level 2.5) local turbulence closure model of Mellor and Yamada (1982) to represent turbulence above the surface layer.

The MYJ scheme determines eddy diffusion coefficients from prognostically calculated turbulent kinetic energy (TKE). Mellor and Yamada (1982) argue that the scheme is appropriate for all stable and slightly unstable flows, but that errors are likely to occur when the flow approaches the free-convection limit. Several studies have compared different PBL parametrizations in the WRF model (Nolan et al. 2009; Hu et al. 2010) showing that under stable conditions there is no PBL scheme that satisfactorily simulates the stable

Table 5.2: Model configuration options used for WRF simulations of 22-23 June 2006

	Domain 1	Domain 2	Domain 3	Domain 4
Horizontal grid	27 km	9 km	3 km	1 km
Dimensions (x, y, z)	65, 60, 48	88, 82, 48	139, 130, 48	154, 100, 48
Initial and boundary conditions	NCEP CFSR 0.5x0.5 every 6h			WRF domain D3
Simulated period	From 0000 UTC 2006-06-22			From 1800 UTC 2006-06-22
	to 0000 UTC 2006-06-24			to 0600 UTC 2006-06-23
Radiation	Dudhia scheme short wave radiation. RRTM long wave radiation			
Land surface	NOAH Land-Surface Model (4 subsoil layers)			
Microphysics	New Thompson et al. scheme			
Convection	Grell 3D scheme			
PBL and Surface layer Exp 1. YSU	Yonsei University scheme (YSU) for PBL; MM5 similarity sfc layer			
PBL and Surface layer Exp 2. MYJ	Mellor-Yamada-Janjic scheme (MYJ) for PBL; Eta sfc layer scheme			

boundary layer and upper inversion. However, local TKE closure schemes perform better than first-order approaches (Chiao 2006; Shin and Hong 2011).

Currently, each PBL parametrization is tied to particular surface-layer schemes in the WRF model. The MM5 surface layer scheme coupled to the YSU model uses the stability functions from Paulson (1970), Dyer and Hicks (1970), and Webb (1970) to compute surface exchange coefficients for heat, moisture, and momentum. Following Beljaars (1995), a convective velocity is used to enhance surface fluxes of heat and moisture. Thermal roughness parameterization included in the current version of this scheme is assumed the same as momentum roughness length. A Charnock relation relates roughness length to friction velocity over water. Following Zhang and Anthes (1982), there are four stability regimes. In contrast, the Eta surface layer scheme (Janjic 1996; Janjić 2002) coupled to the MYJ model is based on similarity theory (Monin and Obukhov 1954). The scheme includes parametrizations of a viscous sub-layer. Over water surfaces, the viscous sub-layer is parametrized explicitly following (Janjic 1994). Over land, the effects of the viscous sub-layer are taken into account through variable roughness height for temperature and humidity as proposed by Zilitinkevich (1995). The Beljaars (1995) correction is applied in order to avoid singularities in the case of free convection and vanishing wind speed (and consequently u_*). The surface fluxes are computed by an iterative method.

The role of surface-layer parametrizations in atmospheric numerical models is to calculate the surface exchange coefficients (C_d, C_h, C_q) to compute the sensible and latent heat fluxes and momentum flux, consistent with the flux-profile relationships. Furthermore, it provides the lower boundary condition for the vertical transport in PBL schemes. This implies that correct parametrization of land surface processes is very important if it is to provide crucial and reliable information on the daily evolution of the PBL. Much work analyzes the sensitivity of simulated variables to surface-layer parametrizations in order to assess the relative contributions of the surface-layer parametrizations to typical features of each PBL scheme. Shin and Hong (2011) shows that, in the surface layer, temperature and moisture are more strongly influenced by surface-layer formulations than by PBL mixing algorithms in both PBL convective and stable regimes, while wind speed depends on vertical diffusion formulations in the convective regime. Regarding PBL structures, surface-layer formulations only contribute to near-surface variability and then PBL mean properties, whereas the shapes of the profiles are determined by PBL mixing algorithms. However, there are still many sources of error in the surface-layer schemes which are not easy to isolate, although these errors can affect the performance of PBL parametrizations Shin and Hong (2011).

5.3.2 WRF configuration for the eight consecutive density currents

In the study of the sequence of eight density currents from 3 to 10 July 2003 we used a slightly different configuration of the WRF model (see Table 5.3). We used the version 3.3.1 and three domains centred on the location of the CIBA meteorological tower, with

horizontal resolutions of 9, 3 and 1 km (Fig. 5.1a). Here, domains 1 (9 km), 2 (3 km) and 3 (1 km) are run in two-way nesting from 0000 UTC 3 July to 1200 UTC 11 July 2003 and the first 12 h are treated as spin-up. Fields are saved every 5 min in this case. In the vertical, 48 sigma levels are used from the ground up to 100 hPa for all the domains with the first level 2 m above the surface, and the first 13 levels all within the first 100 m. Initial and boundary conditions are taken from the ERA-Interim analysis from the European Centre for Medium Range Weather Forecasts (ECMWF) in this case, with a horizontal resolution of 0.125° and the boundary conditions are forced every 6 h.

The physics package is similar to the one used for the simulations of the single event in 2006, except that we choose only one scheme for the PBL, the MYJ local scheme and the Eta-surface layer.

Table 5.3: Model configuration options used for WRF simulations of the eight density current sequence, from 3 to 10 July 2003

	Domain 1	Domain 2	Domain 3
Horizontal grid	9 km	3 km	1 km
Dimensions (x, y, z)	88, 82, 48	145, 145, 48	154, 112, 48
Initial and boundary conditions	ECMWF 0.125x0.125 ° every 6h		
Simulated period	0000 UTC 3 July 2003 - 1200 UTC 11 July 2003		
Radiation	Dudhia scheme for short wave radiation, RRTM for long wave radiation		
Land surface	NOAH Land-Surface Model (4 subsoil layers)		
Microphysics	New Thompson et al. scheme		
Convection	Grell 3D scheme		
PBL	Mellor-Yamada-Janjic scheme (MYJ)		
Surface layer	Eta surface layer scheme		

5.4 Outbreak of the density current

The single event study focuses on a single night during the SABLES2006 field campaign (Yagüe et al. 2007). As previously commented, the night of the case study is 22-23 June 2006 when the synoptic situation at the Iberian Peninsula was dominated by an area of high pressure with a weak horizontal pressure gradient. Under these conditions, a sudden shift in the wind has commonly been observed at the CIBA site (Yagüe et al. 2007). It usually occurs between several tens of minutes and a few hours after the establishment of the stable regime. During the night in this study, a rapid reorganisation of the dynamic and the mass fields occurred soon after sunset (which took place at 1958 UTC). The overview of the night using the values recorded at the different levels of the tower show a weak north-west wind during the late afternoon (Fig. 5.2a). The wind gradually turned

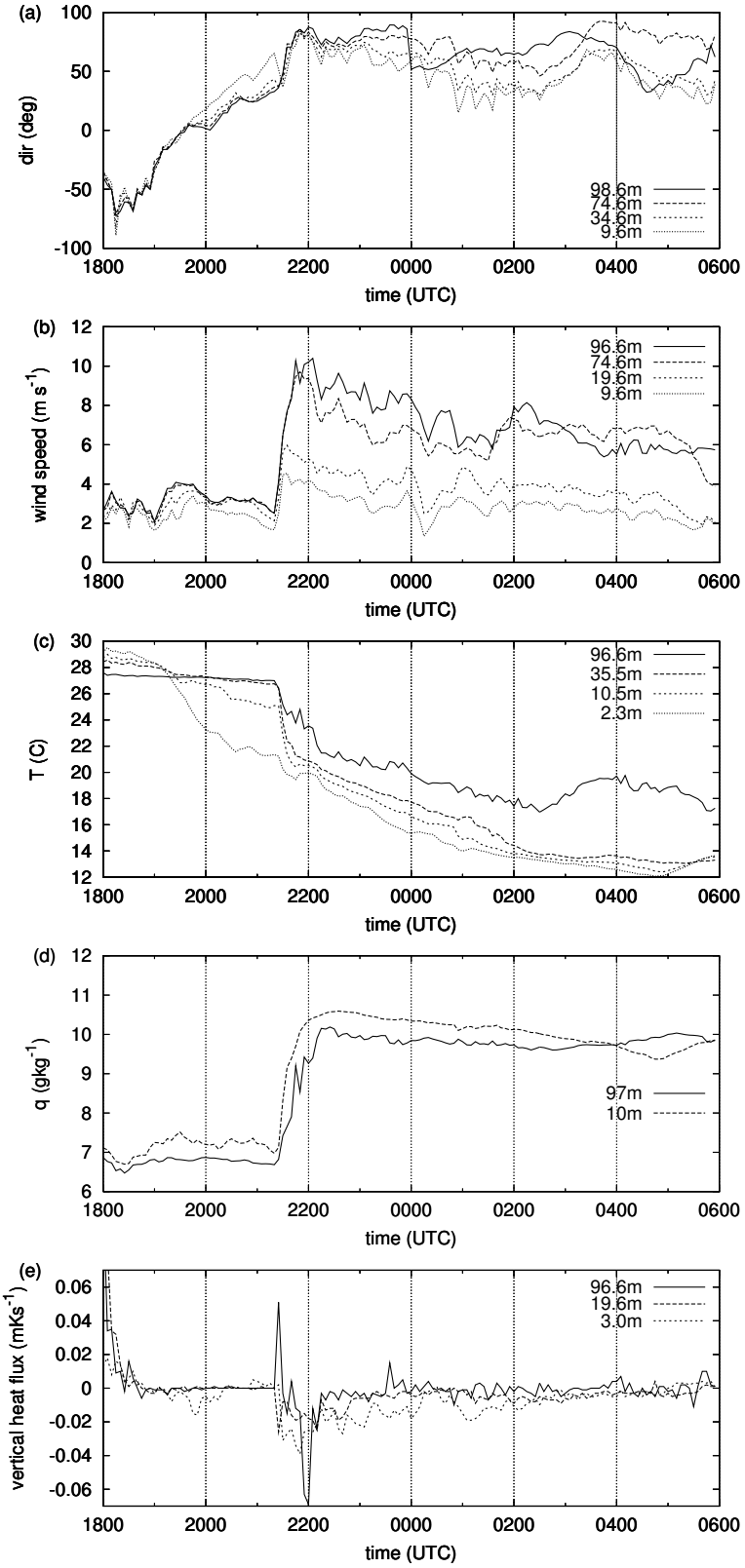

Figure 5.2: Wind direction (a), wind speed (b), temperature (c), specific humidity (d) and vertical heat flux (e) at different tower levels during the night of 22-23 June 2006 (all averaged over 5-minute periods).

north east from 1900 UTC to 2130 UTC, when there was a sudden intrusion by an eastern current of moderate speed (about 10 m s^{-1} at the highest level of the mast, around 98 m) (Fig. 5.2b). Surface radiative cooling favoured a temperature inversion of nearly 5°C between the surface and the top of the 100-m mast (Viana et al. 2010) before the passage of the density current, but the sudden change in wind velocity was accompanied by a rapid fall in temperature, especially at the upper levels (Fig. 5.2c), causing a reduction in the thermal inversion after the outbreak of the current at the lower levels. The specific humidity increased at all levels (Fig. 5.2d), suggesting the arrival of a cold and moist gravity current from the north-east whose origin could have been a diurnal sea-breeze coming from the Cantabrian Sea, as the WRF mesoscale simulations will evince in Sect. 5.7 where an analysis at the regional scale is done. At the top of the tower, upward vertical heat flux (calculated using the 5-minute Reynolds average) reveals the displacement of the parcels due to the arrival of the current, since the mean vertical velocity is positive (see Viana et al. (2010)), turning downward a few minutes later when the cold air surpasses the measuring level (Fig. 5.2e).

5.4.1 Eight consecutive density currents

After an exhaustive analysis of the CIBA database derived from the 2003 INTERCLE experiment (*Estudio y parametrización de los intercambios de calor, humedad y momento en la Capa Límite Estable*), we observe that the outbreak of the density current is not an isolated episode, as it is cyclically daily repeated during certain periods. Here, we analyze the observations made on eight consecutive nights (from 3 to 10 July 2003) to characterize the arrival of a sequence of density currents at the site. During this period, as in the event in June 2006, the synoptic situation over the Iberian Peninsula was dominated by an anticyclone with a weak horizontal pressure gradient. Under these conditions, the overviews of each night using data from different levels of the tower show similar evolution for all nights, as we can see in Fig. 5.3, which presents the time evolution at the CIBA tower for the eight consecutive nights, from 1800 UTC to 0600 UTC.

An early temperature inversion (Fig. 5.3a) develops close to the surface along with light north-westerly winds (Fig. 5.3b,c) just after sunset. However, this situation persists for only a short time, as approximately 1 h later, the wind speed increased abruptly at all levels but most markedly at the highest level of the tower, by nearly 10 m s-1 at 98.6 m (Fig. 5.3b) and the wind direction veered significantly towards a north-easterly direction (Fig. 5.3c). The surface temperature inversion was greatly affected as the sudden change in wind speed and wind direction was accompanied by a rapid fall in temperature, especially at the upper levels (Fig. 5.3a), which caused a weakening of the thermal inversion after the onset of the density current at the lower levels. These changes suggest the arrival of a cold gravity current from the north-east sector that displaced the air at these levels and pushed it upwards, as an updraft current, which is clearly noticeable in the vertical wind-speed measurements. In addition to these changes, the specific humidity increased

at all levels (Fig. 5.3d), suggesting the arrival of a cold and moist gravity current from the north-east whose origin could have been a diurnal sea breeze originating in the Bay of Biscay in the Cantabrian Sea. This suggestion is supported by the WRF mesoscale simulations presented in the regional scale analysis in the sections below. However, due

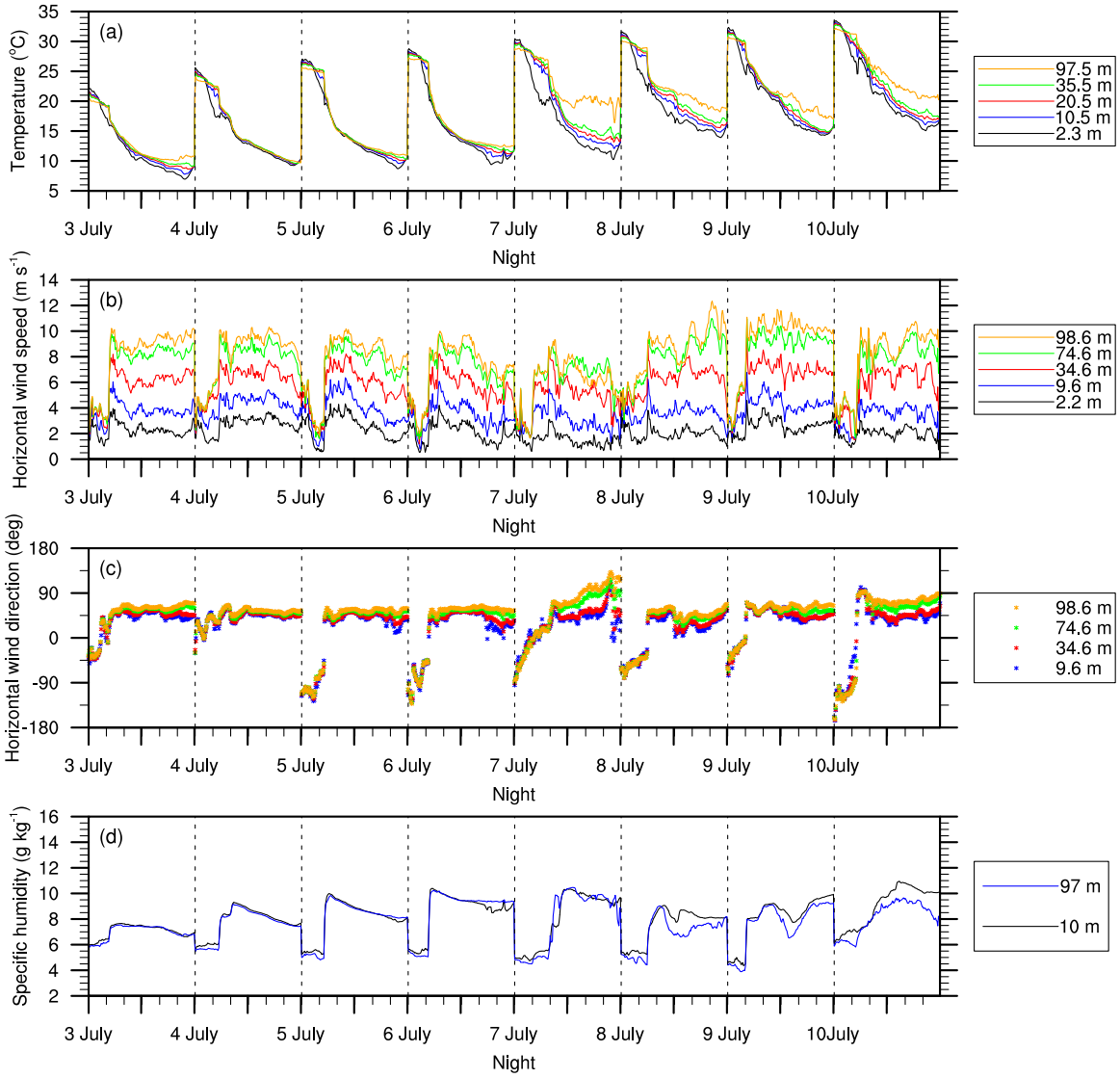

Figure 5.3: Time series for eight consecutive nights (3-10 July 2003) from 1800 UTC to 0600 UTC of: (a) air temperature; (b) wind speed; (c) wind direction, where wind direction values are switched from 000-360 to -180-000-180 with the negative values corresponding to the western quadrant; d) specific humidity measured at the different levels of CIBA tower (all averaged over a 5-min period)

to the complex topography of the area, this cold and moist flow is reorganized as a set of drainage flows that interact and become an organized north-easterly flow within the Duero basin (Bravo et al. 2008; Cuxart 2008; Martínez et al. 2010). As this coherent structure is also associated with local thermal and shear instabilities (Einaudi and Finnigan 1993; Sun et al. 2002), their effect can also be seen in the TKE and turbulent sensible heat-flux time history.

5.5 Model evaluation

5.5.1 Evaluation at the CIBA site for the single event

The model results from the D4 domain output corresponding to the two experiments (MYJ and YSU experiments) are checked against observations from tower measurements at CIBA site during 22-23 June 2006 night-time (from 1800 UTC to 0600 UTC) (Fig. 5.4).

Overall, the YSU experiment tends to match the observations better in time but it does not capture the sharp shifts (i.e., in wind speed or specific humidity), so the YSU scheme seems to be too diffusive. In contrast, the MYJ experiment gives a better picture of the changes in magnitude for nearly all the variables, but predicts the gravity current outbreak around 90 minutes earlier.

The temperature drop at 10 m and 97 m is well captured by the MYJ experiment but it is predicted around 90 minutes in advance, whilst the YSU experiment simulates the drop in temperature at the right time, but more gradual than actually occurs at low levels (Fig. 5.4a). At the upper levels, the YSU scheme captures the drop in temperature at 97 m well although the scheme underestimates the temperature after 2300 UTC (Fig. 5.4b). The observational fall in temperature matches a sudden increase in wind speed, especially around 100 m AGL, where it rises from 3 to 10 m s-1 (Fig. 5.4d). This is also captured by the MYJ scheme, which is able to forecast the increase in wind velocity but it is predicted earlier than it is actually observed, while the YSU scheme predicts the increase at 10 m but does not capture the sharp increase at 100 m (Fig. 5.4c and Fig. 5.4d). The shift in wind direction from north to east at all levels is captured quite well by the simulations, although they tend to overestimate the eastern component during the outbreak (Fig. 5.4e and Fig. 5.4f). Specific humidity rise is simulated by the MYJ scheme but is also ahead of observations while the YSU scheme forecasts it gradually, meaning that the cold flow has been stirred and has been losing its original properties during the preceding hours (Fig. 5.4g and Fig. 5.4h). With the change in wind speed and direction, strong shear at the surface layer is generated (Fig. 5.4i) and therefore high values of friction velocity (u_*) are measured, which are quite well captured by the MYJ scheme but also ahead of the observations. With the arrival of the density current, the YSU scheme forecasts an increase in u_*, but it prevails all night, therefore it simulates much stronger turbulence than is observed during the hours after the arrival of the current. This behaviour evinces that YSU introduces too much diffusivity as we will see in the next sections. Also with

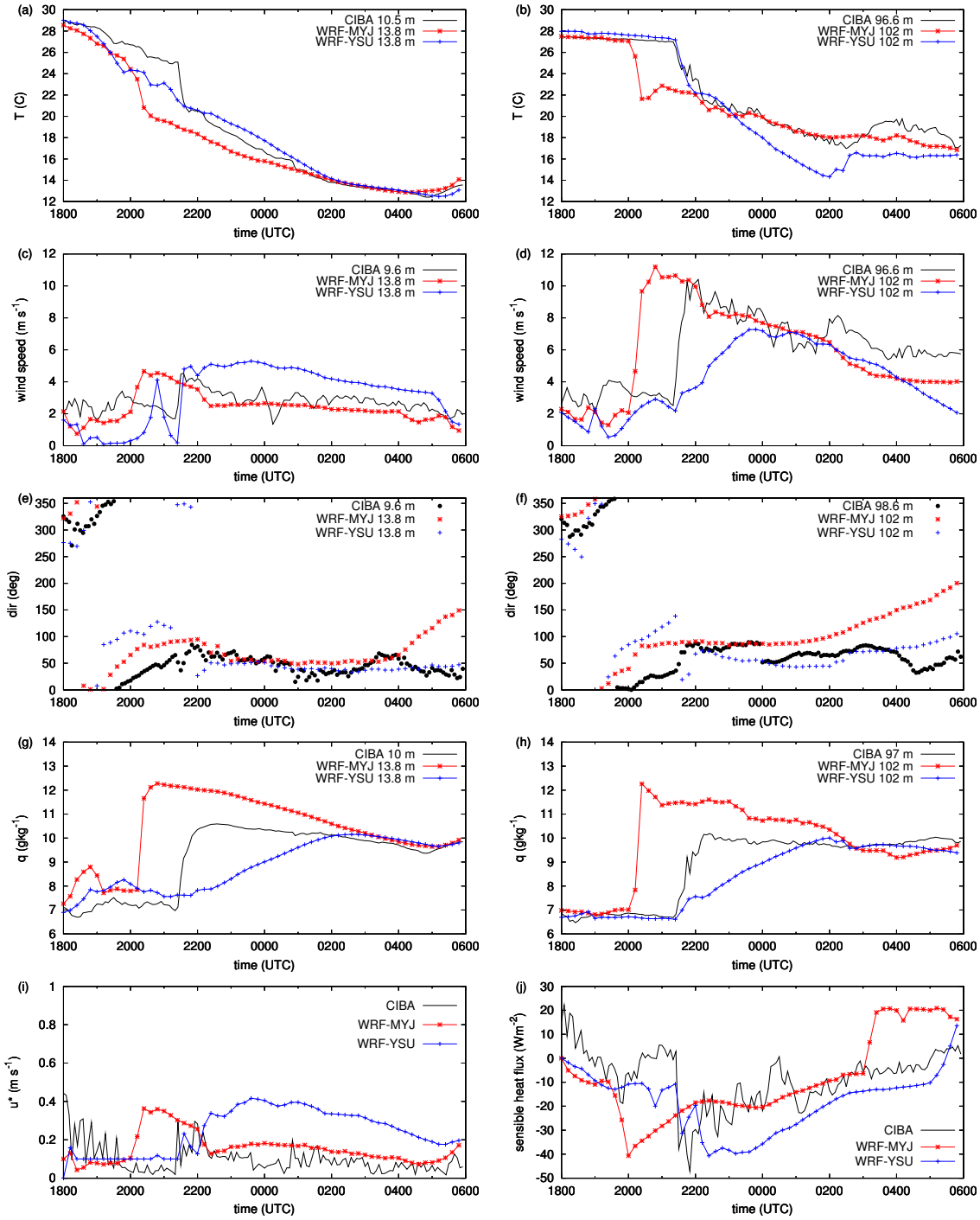

Figure 5.4: Comparison between time series measurements from CIBA tower and model simulations for 22-23 June 2006, using two model experiments (MYJ and YSU): temperature at 10 and 100 m (a) and (b) respectively; wind speed at 10 and 100 m (c) and (d) respectively; wind direction at 10 and 100 m (e) and (f) respectively; specific humidity at 10 and 100 m (g) and (h) respectively; friction velocity and heat flux evaluated at surface layer (i) and (j) respectively.

the onset of the density current, a negative sensible heat flux is established at the surface (Fig. 5.4j). TKE output is only calculated by the MYJ simulation as it is a 1.5 closure TKE scheme. Comparing the TKE simulation with the tower observations we can see that the model underestimates its value, even in daytime (not shown). In addition, during the transition from daytime to night-time, the model establishes values of TKE that are too low as well, therefore producing less turbulence forcing suitable conditions to anticipate nocturnal radiative cooling, the generation of katabatic flows over the slopes and the arrival of the density current.

5.5.2 Evaluation of eight consecutive density currents

The model evaluation is also done for the eight consecutive density currents observed in July 2003 (see Sect. 5.4.1). Daily comparisons of model results with observations for the whole period analyzed indicate that the correspondence of the model to the observations is similar every day. To summarize this information, in Fig. 5.5 we only present the comparison for the highest level of measurement, the level at which the arrival of the density current is most significant.

The results show that the model captures the onset of the density current with the corresponding abrupt temperature decrease (Fig. 5.5a), although its arrival, again, is predicted approximately 90 min early. The model also slightly underestimates maximum temperatures and overestimates minimum temperatures, mainly at the highest measurement level. For wind velocity (Fig. 5.5b), the model also predicts the arrival early, but is capable of predicting the sharp increase and maintains the high wind speeds at the higher levels of the tower, although the maximum value is overestimated. Moreover, the model captures the shift in wind direction from north-west to north-east at the arrival of the density current, but it also predicts the event too early (Fig. 5.5c). The model also catches the sharp increase in humidity at 97 m (Fig. 5.5d), but again it tends to predict it early. Overall, it overestimates the numerical values, mainly in the second part of the period where it overestimates the maximum values.

To evaluate the model performance quantitatively and globally over the simulated period, we have calculated several statistics taking 5-min model results and 5-min averaged Reynolds observations. The mean bias (MB) and the root-mean-square error (RMSE) were calculated for wind speed; whilst the mean bias and the mean absolute gross error (MAGE) were calculated for temperature, wind direction and specific humidity, according to Tesche et al. (2002). The values are summarized in Table 5.4. For temperature, overall MAGE is below the benchmark while MB indicates that the model tends to underestimate the temperature, mostly at medium and higher levels where the values are far from the benchmark. The statistics show that the model tends to underestimate wind speed, especially at the higher levels; although the values are slightly below or within the benchmark. Wind direction is not well predicted by the model; MAGE is far from the benchmark mainly at the lower levels whilst MB values are slightly below the benchmark. These

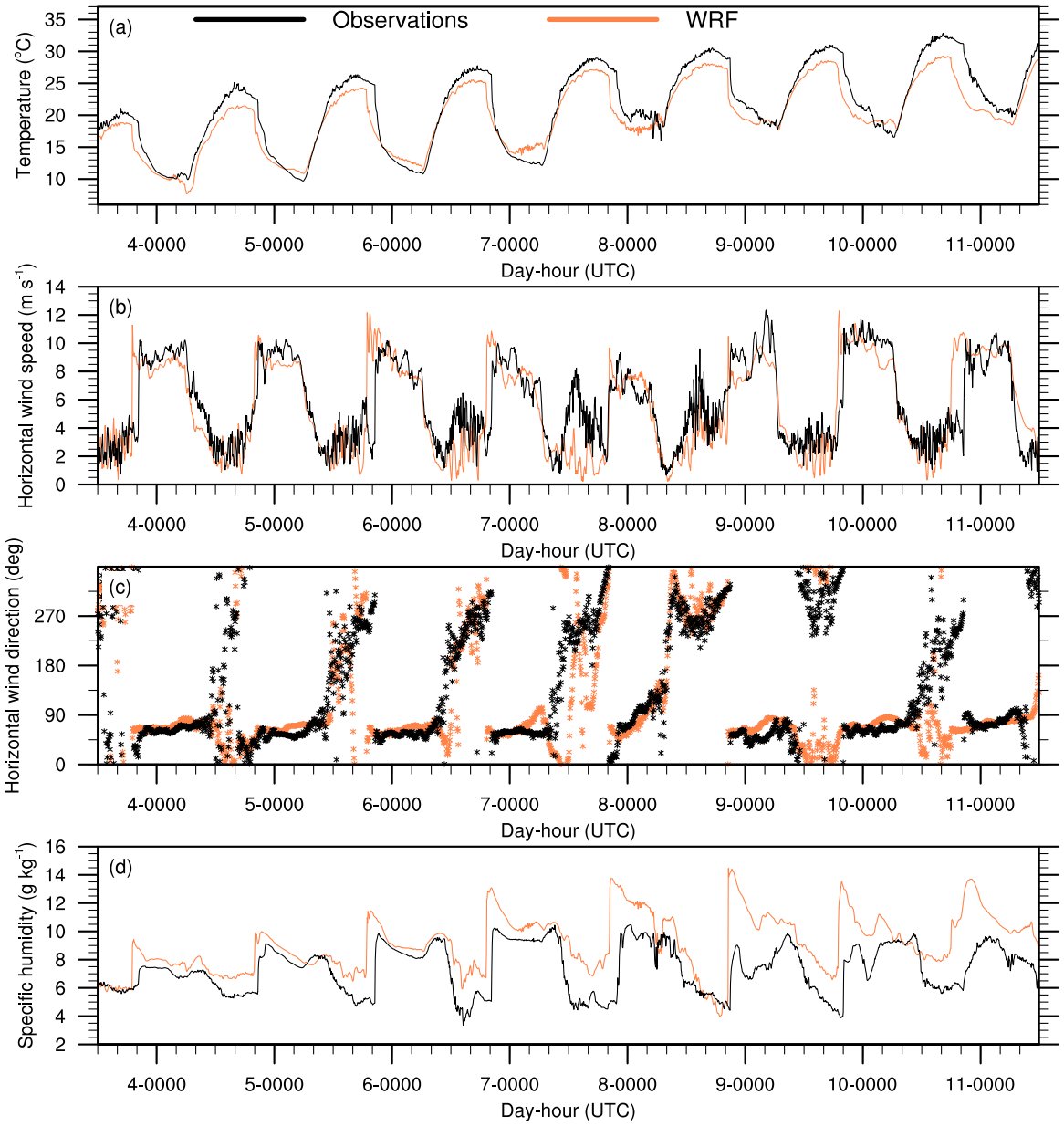

Figure 5.5: Comparison between time series of model simulation (5-min results) and measurements from the highest level of the CIBA tower for the period 3-10 July 2003; (a) air temperature, (b) wind speed, (c) wind direction and (d) specific humidity.

Table 5.4: Statistics for air surface temperature (temp), wind speed (wsp), wind direction (wdir) and specific humidity (q) based on CIBA tower values for the period 3-10 July 2003.

	Statistic	Benchmark	Levels				
			2.3m	10.5 m	20.5 m	35.5 m	97.5 m
Temp (K)	MAGE	< 2	1.43	1.50	1.50	1.53	1.87
	MB	$< \pm\ 0.5$	-0.46	-0.98	-1.12	-1.21	-1.46
			2.3 m	9.6m	34.6 m	74.6 m	98.6 m
wsp (m s^{-1})	RMSE	< 2	1.04	1.37	1.71	1.94	2.03
	MB	$< \pm\ 0.5$	-0.37	0.01	-0.45	-0.45	-0.34
wdir (deg)	MAGE	< 30		42.02	40.58	38.35	38.25
	MB	$< \pm\ 10$		-13.68	-13.78	-14.70	-15.26
			10 m	97 m			
q (g kg^{-1})	MAGE	< 2	1.68	1.84			
	MB	$< \pm\ 1$	1.62	1.79			

results agree with those of Jiménez et al. (2010); Jiménez and Dudhia (2012) who found that areas with more complex terrain show larger systematic differences in wind direction between model predictions and observations, and these differences depend on wind speed: the greater the wind speed, the smaller the differences in wind direction. Finally, specific humidity is quite well predicted by the model as MAGE is overall below the benchmark; MB is within the target values and, overall, the model tends to overestimate the specific humidity.

5.6 Vertical structure of the density current

To further evaluate the differences between observations and model outputs and to understand the differences between the two PBL schemes used, the vertical structure of the gravity current at the CIBA site for the 22-23 June 2006 event was analyzed. To this end, we compare time-height diagrams of wind speed and direction (Fig. 5.6a and Fig. 5.6b) and temperature (Fig. 5.7a and Fig. 5.7b) from model outputs at the CIBA site with the RASS-SODAR sodargrams of wind speed (Fig. 5.6c) and temperature (Fig. 5.7c). The sodargrams only reach a height of 200 m, while the model outputs allow us to complete the vertical structure further up (up to 500 m in the plots).

Before the outbreak, the MYJ scheme predicts light winds from the north-east and north-west, whilst after 2000 UTC, an eastern current about 300 m thick is established with an LLJ which has a peak wind speed of around 11 m s^{-1} at 100 m (Fig. 5.6a). As the night progresses, the wind direction turns from east to south above 200 m and the wind velocity decreases considerably. In the YSU scheme (Fig. 5.6b) the current arrives around 2130 UTC with a similar thickness as in the MYJ scheme, but more stirred and

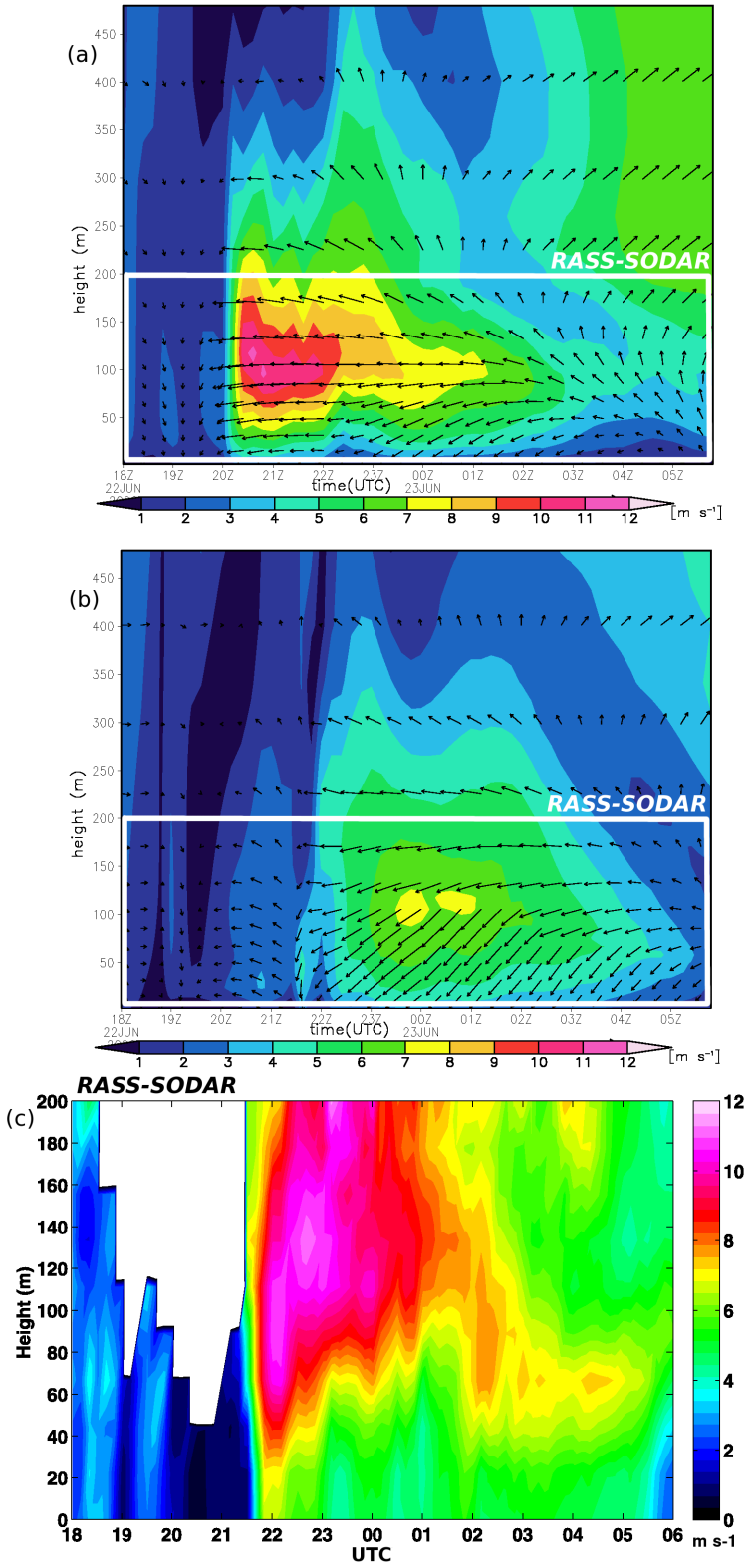

Figure 5.6: Time-height diagrams of wind speed (shaded) and horizontal wind direction (vector) in the MYJ (a) and YSU (b) schemes (12-minute averaged outputs) at the CIBA site; RASS-SODAR sodargram of wind speed (c) during the night of 22-23 June 2006 (10-minute averaged).

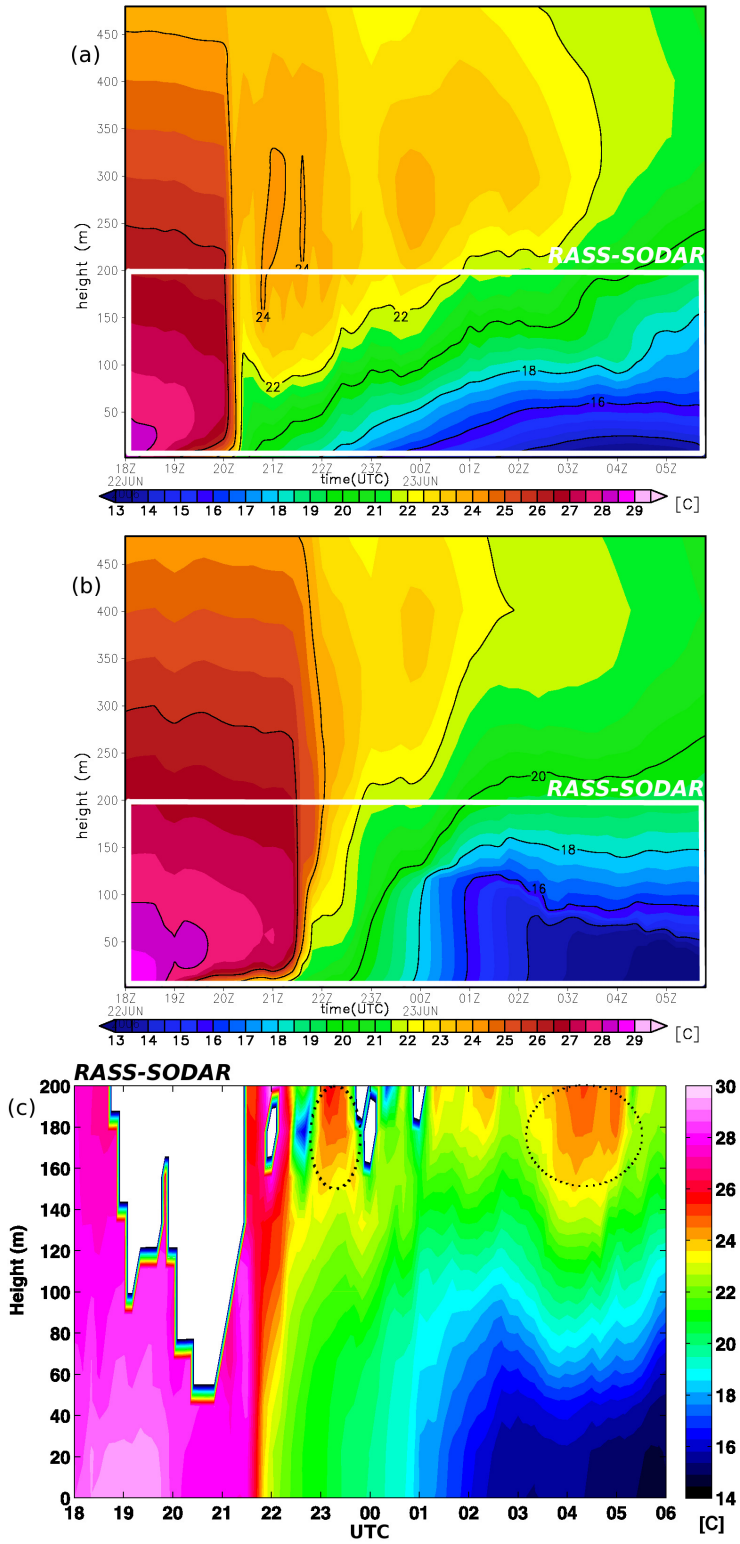

Figure 5.7: Time-height diagrams of absolute temperature in the MYJ (a) and YSU (b) schemes at the CIBA site (12-minute averaged outputs); RASS-SODAR sodargram of temperature (c) during the night of 22-23 June 2006 (10-minute averaged).

with lower wind speeds (7-8 m s^{-1}) which departs more from observations. With the outbreak of the density current, the thermal vertical structure forecast by both schemes (MYJ in Fig. 5.7a and YSU in Fig. 5.7b) changes completely, showing both schemes and the temperature sodargram a strong temperature inversion. The MYJ scheme confines the cold air in a thinner layer than the YSU or temperature sodargram do, thus enhancing vertical temperature gradients. This fact contributes to accelerating the air mass coming from the north-east over sloping terrain and could be the reason why MYJ forecasts the outbreak of the density current in advance. Although the YSU scheme is capable of forecasting the outbreak on time, it confines the cold air in a thicker layer because it enhances vertical mixing during night-time (as in Hu et al. (2010)). Also as shown in Fig. 5.7 and after the entrance of the density current, above the LLJ we can see a warm layer located at around 200 m high, since as the cold current advances it pushes the warm air upwards, similarly to the advance of a cold front. This warm layer is forecast by both schemes but its persistence is better simulated by MYJ in accordance with the RASS-SODAR data (see broken circles in Fig. 5.7c). This could also be evidence that YSU is too diffusive. In shorts, the comparison between the model outputs and the RASS-SODAR data in the first 200 m, shows that the MYJ scheme represents the wind structure of the density current better.

5.7 Mesoscale fields

5.7.1 Mesoscale evaluation for the single event

A mesoscale overview of the wind and temperature fields could be very useful for detailed study of the flow and the thermal circulation patterns that cannot be inferred from tower measurements at a specific site. However, before analysing the model outputs from domain D3, we will evaluate them with a comparative analysis against observations from 15 surface stations covering this third domain (see Fig. 5.1a). We use the third domain model (3-km grid) because it is centred on the CIBA site and covers the area in a radius of 250 km, including the nearest mountain ranges. The statistics are calculated hourly over a 24-hour period (from 0600 UTC 22 June to 0600 UTC 23 June 2006) dividing them into 2 periods: (i) transition from night-time to daytime and daytime (from 0600 UTC to 1700 UTC) and (ii) transition to night-time and night-time (from 1800 UTC to 0500 UTC) to take into account the daytime and night-time evolutions separately. Temperature at 2 m and both wind speed and direction at 10 m were chosen to calculate the following statistics: mean bias (MB) and root-mean-square error (RMSE) for wind speed; and mean bias and mean absolute gross error (MAGE) for temperature and wind direction (Tesche et al. 2002). Their values are summarised in Table 5.5.

Temperature and wind speed statistics are overall below the benchmarks, except for wind speed predicted by YSU during night-time, which means that this scheme does not match with the real data from surface stations. Wind direction is not well predicted by any

Table 5.5: Statistics for surface temperature, wind speed and wind direction, based on hourly values for 15 surface meteorological stations (see locations in Fig. 5.1a) from daytime (0600 UTC to 1700 UTC 2006-06-22) night-time (1800 UTC 2006-06-22 to 0600 UTC 2006-06-23), including the transition to night-time. The benchmarks for the statistics are proposed by Tesche et al. (2002) to validate meteorological simulations.

	Statistic	Benchmark	MYJ		YSU	
			Daytime	Night-time	Daytime	Night-time
Temperature	MAGE	< 2 K	1.201	1.740	1.144	1.263
(2 m)	MB		-0.101	-1.275	0.027	-0.504
Wind speed	RMSE	< 2 m s^{-1}	1.537	1.676	1.423	2.496
(10 m)	MB		1.072	1.071	0.686	1.803
Wind direction	MAGE	< 30 deg.	42.547	37.162	51.075	41.729
(10 m)	MB		37.162	6.625	10.400	0.917

of the schemes at the station points. The MAGE value for temperature is slightly higher for the MYJ scheme than for YSU, although both tend to underestimate temperature values as MB is negative. This trend is noticeable during night-time for the MYJ scheme, that underestimates the surface temperature at most of the surface stations. During night-time, wind speed and wind direction are better predicted by the MYJ scheme although both schemes overestimate wind speed values.

For a broader mesoscale overview, temperature and wind fields for the third domain are shown (Fig. 5.8). The analyzed model outputs correspond to the MYJ scheme, as it is the scheme that better captures the onset of the density current. At 1600 UTC, a cold moist mass of air from the Cantabrian Sea started moving south-westward far from the CIBA site (Fig. 5.8a). Over the following hours, the flow accelerated as it passed over the mountain ranges, arriving at the centre of the domain a few minutes after 2000 UTC (Fig. 5.8b). This occurred during the transition from day to night, with the beginning of the establishment of the NBL. From 1600 to 2000 UTC we can see how near-surface air temperature falls as the flow moves from north-east to south-west due to the movement of the density current itself but also affected by ground radiative cooling which enhances the movement of the current at the mountain slopes via the generation of a katabatic flow. At 100 m AGL, behaviour of the air mass is similar, reaching high wind speeds of around 10 m s^{-1} (Fig. 5.8c and d).

To further analyze the circulation pattern, we use the WRF outputs through a cross section in the north-east to south-west direction (see dotted lines in Figs. 5.8a, b, c, d). In Fig. 5.9a and Fig. 5.9b we can see, through the potential temperature cross section, a strong temperature inversion established within the density current in the north-east part of the domain, although a daytime regime still remains at the south-west part. The wind vector projected over the NE-SW axis is shown in Fig. 5.9c and Fig. 5.9d, which

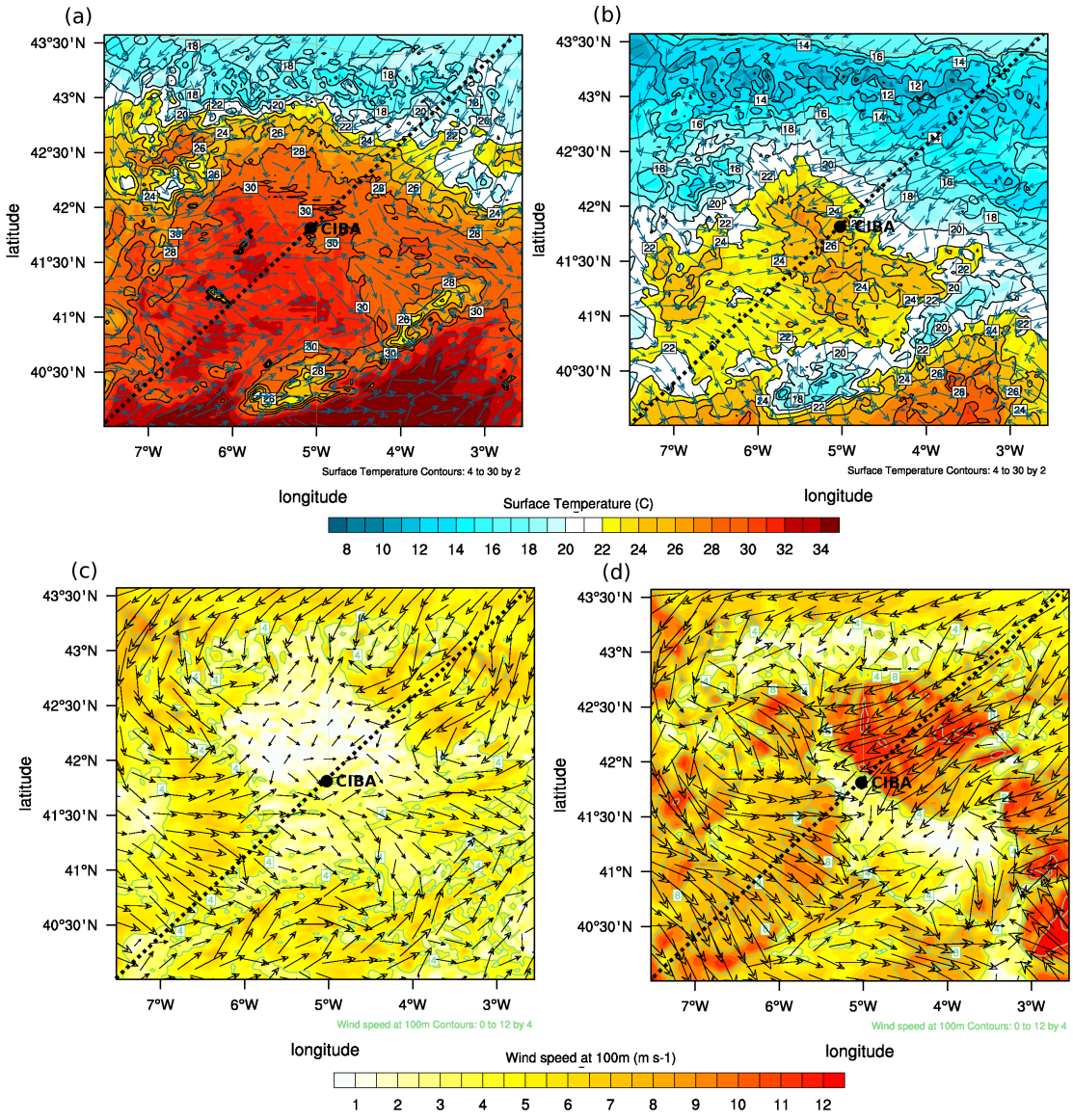

Figure 5.8: D3 MYJ model outputs of: (a) 2 m air temperature (shaded) and 10 m horizontal wind vectors at 1600 UTC; (b) idem at 2000 UTC; (c) horizontal wind speed at 100 m (shaded) and 100 m horizontal wind vectors at 1600 UTC; (b) idem at 2000 UTC.

correspond to 1600 and 2000 UTC respectively. Maximum wind speeds are found over sloping terrain leeward of the north-east mountain range at around 2000 UTC (Fig. 5.9d).

The flow reaching the CIBA site seems to have originated over the Cantabrian Sea, but it was strongly perturbed by topographical features when the air mass crossed the mountain range located in the north-east part of the third domain. Flows over sloping terrain were accelerated due to pressure and temperature gradients. So both the sea breeze entrance and the katabatic wind were the origin of the cold density current that moved fast as the air surface cooling established by the MYJ scheme is over-predicted by the model (as shown by surface station statistics). The topographical effects become even more decisive and the air mass from the north-east is accelerated even more in the model. This would also explain the anticipation of the event produced by the MYJ experiment. So this cold and moist gravity current moved fast, enhanced turbulence and produced waves over the Torozos plateau. Similarly, Sun et al. (2002) analyzed a wind surge and a temperature drop that revealed the passage of a density current associated with intermittent turbulence.

5.7.2 Mesoscale evaluation for the eight consecutive density currents

The statistics were calculated from hourly values for the whole period, from 3-10 July 2003. Temperature at 2 m, both wind speed and direction at 10 m, and specific humidity at 2 m were chosen to calculate the statistics. The values are summarized in Table 5.6. The statistics indicate that temperature, wind velocity and specific humidity are quite well predicted by the model as the corresponding statistics are overall slightly below or within the benchmarks, but in this case MB is positive, indicating that the model overestimates these variables. For wind direction, the statistics are worse, compared to those reported and discussed above.

Table 5.6: Statistics for surface temperature, wind speed and wind direction, based on surface stations values from 3-10 July 2003. The benchmarks for the statistics are proposed by Tesche et al. (2002) to validate meteorological simulations.

	Statistic	Benchmark	Values
Temperature (2 m) [K]	*MAGE*	< 2	1.9
	MB	$< \pm\ 0.5$	1.4
Wind speed (10 m) [m s^{-1}]	*RMSE*	<2	1.4
	MB	$< \pm\ 0.5$	0.31
Wind direction (10m) [deg]	*MAGE*	< 30	64.2
	MB	$< \pm\ 0.5$	12.8
Specific Humidity (2 m) [g kg^{-1}]	*MAGE*	< 2	1.59
	MB	$< \pm\ 1$	1.44

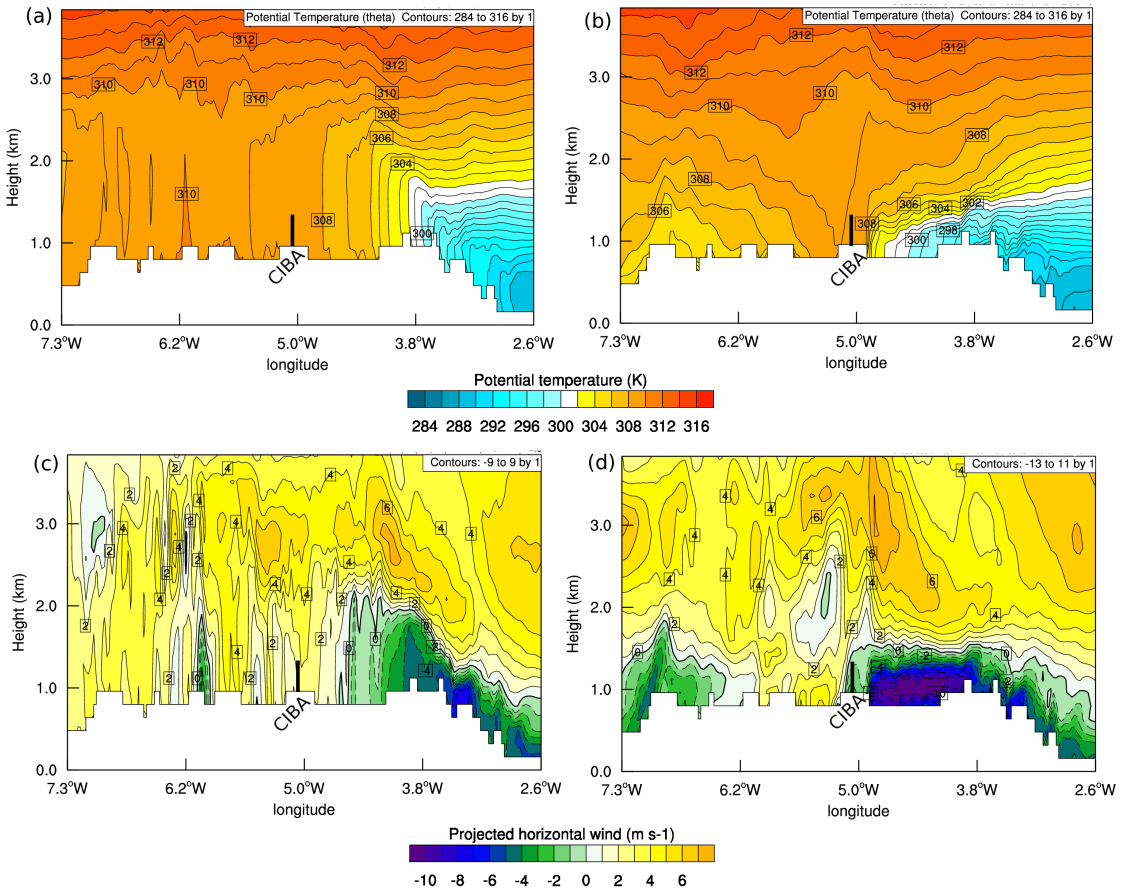

Figure 5.9: NE-SW (dashed line in Figure 7) vertical cross section of: potential temperature at 1600 UTC (a) and 2000 UTC (b), and horizontal wind parallel to the NE-SW cross section at 1600 UTC (c) and 2000 UTC (d).

5.8 Oscillation features

In Viana et al. (2010) wavelet transforms applied to the data from microbarometers revealed traces of IGWs in pressure records after the outbreak of the gravity current generating periodic pressure and temperature oscillations. In this section we test the capacity of the model to reproduce the oscillations generated after the arrival of the cold current. To this end, we analyzed one-minute model outputs at the CIBA site from the two WRF experiments (MYJ and YSU). Results from the MYJ experiment indicate the presence of oscillations in temperature and specific humidity between 130 m and 300 m AGL at the CIBA site (Fig. 5.10-left), and therefore they demonstrate that the WRF model using the MYJ scheme can reproduce the generation of gravity waves. They appear a few minutes after the onset of the density current as a consequence of the cold air intrusion, since the air parcels rise forming a warm layer and therefore a pressure disturbance is generated, as we can see in Figure 9a. A few minutes later, at the warm layer at the top of the current, periodic oscillations of temperature and humidity at different levels are simulated by the model, as seen in Fig. 5.10b and 5.10c (left column). Before the outbreak, above 130 m, temperature decreases with height, whilst after this event a thermal inversion is well established (Fig. 5.10b-left). In contrast, the specific humidity rises after the outbreak (Fig. 5.10c-left) and changes its profile structure. The well-mixed vertical structure before the outbreak is replaced by a decrease in the specific humidity with height after the onset of the current. Vertical velocity from the model output at 167 m increases suddenly to about 0.3 m s^{-1} and then falls to about -0.1 m s^{-1} in two minutes (not shown). This upward motion coincides with the large temperature fall and the large increase in specific humidity. At the time the current arrives, maximum values for the vertical velocity of around 0.7 m s^{-1} are seen at around 300 m AGL whilst in the YSU scheme the values are slightly lower, only reaching vertical velocities of 0.5 m s^{-1} at the same heights.

The disturbances are only detected by the model in the MYJ experiment whilst the YSU experiment (Fig. 5.10a, b and c, right column) did not reveal any monochromatic oscillating behaviour after the arrival of the density current. Although YSU is able to forecast the outbreak of the gravity current, the small fluctuations of pressure, temperature and humidity show that the scheme is not able to generate waves with sufficient intensity (Fig. 5.10-right). The reason is that YSU provides more night-time mixing than MYJ, as mentioned above.

In order to obtain information about wave parameters such as period, wavelength, phase velocity and direction, the wavelet method described by Terradellas et al. (2005), never before applied to simulated data, is applied to the model results of the MYJ experiment with a frequency of 0.0166 Hz corresponding to the one-minute output. This method provides the horizontal components (kx, ky) of the wavenumber vector, from the phase differences of the wavelet transforms from different time series of a given magnitude at different points in the ground or at a certain height. From kx and ky, the rest of the relevant wave parameters can be derived. In this case, the method is applied to potential

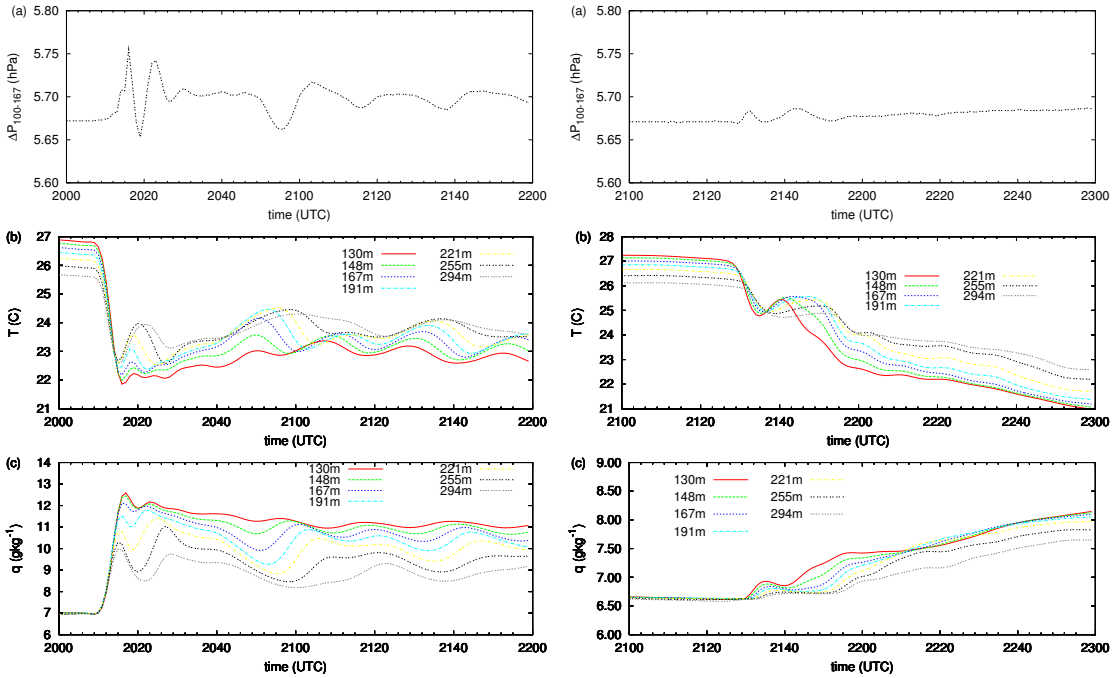

Figure 5.10: One-minute output time series from MYJ (left column) and YSU (right column) experiment of ΔP100-167 (a), temperature (b) and specific humidity (c) at different levels from 2000 to 2200 UTC at the CIBA site.

temperature data at 167 m AGL from three-point triangulation around the CIBA tower. Theoretical polarisation relationships (Gossard and Hooke 1975) between pressure, temperature and specific humidity over the tower are well accomplished by one-minute model outputs. That is why wavelet analysis has been applied to potential temperature rather than pressure. The theoretical polarisation relation is especially well fulfilled between temperature and specific humidity, so one-minute model outputs of potential temperature at 167 m AGL are chosen because they show the most monochromatic behaviour. The wavelet method establishes a wave period of around 20-22 minutes, a phase velocity about 6-9 m s^{-1}, a wavelength of around 8-10 km and a direction of 240-260° (coming from the NE and heading SW). These wave parameters are quite different from those found in Viana et al. (2010) where they showed evidence of gravity waves from temperature measurements around 100 m above the ground and from pressure time series in the layer between 50 and 100 m. The main parameters of these waves were derived from wavelet cross correlation of high resolution pressure time series recorded by a 200-m array of microbarometers with a frequency of 2 Hz deployed at surface level (recall that pressure is a non-local flow variable that can be affected by events taking place on the whole overlying atmospheric layer). They found a wave with a period of around 10 minutes, propagating roughly from the north (20°) with a phase velocity of 6.2 m s^{-1} and a wavelength of nearly 3.5 km, propagating mainly around 50-100 m above surface (as they could determine by a set of

microbarometers deployed along the 100-m mast). The estimated Brunt-Väisälä frequency during the event was N = 0.03 s^{-1} at 167 m AGL which is higher than the frequency of the wave (0.0052 s^{-1}), which indicates that the modelled wave was compatible with an IGW (Stull 1988; Sun et al. 2004). From these results, we can summarize that: i) the model generates the waves propagating at higher levels from where they were produced according to observations, but not at lower levels; ii) the oscillations generated by the density current in the model have some parameters that are different from those observed, since during its downward vertical propagation the modelled wave was damped and below 130 m the oscillation is almost imperceptible.

5.9 Summary and Conclusions

Starting from an observational study of IGWs generated by a density current during a single night (22-23 June 2006) (Viana et al. 2010), in this study we try to simulate the presence of IGWs generated by a density current using the WRF model. Furthermore, we analyze the flow structure that generated these gravity waves, and its origin. In addition several density current entrances have also been detected on eight consecutive days in July 2003 with similar features than the one in 2006 (Soler et al. 2014).

Our results show that WRF mesoscale meteorological modelling is an efficient tool for studying the origin and development of a density current and the generation of gravity waves. We show that the origin of the IGWs observed and modelled at the CIBA site was a cold air density current coming from the north-east, which was modulated by the topography of the area studied. Specifically, the flow originated in the Cantabrian Sea, several mountain slopes then cross through its trajectory, which were the main cause of its strong acceleration.

High-resolution (1-km) simulations are also useful in the sensitivity analysis of two boundary layer schemes (MYJ and YSU) that have been used extensively by the scientific community. A comparison of these schemes shows that the MYJ scheme simulation gives better results, as it better represents the main features of the density current measured by the tower instruments and by the RASS-SODAR, although the event is predicted to occur earlier than it is observed to occur. The study has also shown the capacity of this scheme to detect the oscillations in temperature and specific humidity generated by the arrival of the density current. However, although the YSU scheme captures the arrival of the current on time, it fails to correctly track its properties and predicts a less sharp change in magnitudes than is observed, because it provides more night-time mixing than MYJ. This is also why the YSU scheme does not reproduce the gravity waves due to the arrival of the cold current.

According to the model, with the intrusion of the cold air mass at the CIBA site, the ambient air is pushed upwards (the intrusion thus acts as a cold front) forming a warm layer above the maximum wind at the top of the density current where, a few minutes

later, disturbances in pressure, temperature and humidity occur at these levels. It is also shown that the area where the waves are generated coincides with the warm layer at the top of the current. The comparison between measurements and simulations reveals some other discrepancies, in addition to the time gap. Measurements of oscillations from the tower sensors show that the waves were produced mainly at around 100 m, while model simulation results show waves above this level. Furthermore, the wave parameters calculated from the measurements reveal waves with shorter periods and shorter wavelengths than those calculated from the model outputs. Thus, the model seems to reproduce waves in the warm layers, where vertical temperature gradients are smoother and less than those found at lower levels. Therefore, at lower levels, the simulated propagated wave may arrive as a damped and smoothed perturbation, so the predicted parameters may be different from those calculated from observations. Moreover, the 1 km resolution of the model could be too coarse to solve a wave of 3.5 km wavelength. Other reasons for the discrepancies may include the application of the wavelet technique to different variables which, moreover, were sampled with different frequencies.

To achieve conclusive results regarding the capacity of the models to simulate IGWs, it is necessary to perform further studies to clarify the importance of the model parametrizations, especially in surface layer and in the PBL.

6

Exploring vertical turbulence structure in neutrally and stably stratified flows using WRF-LES model

Contents

These results have already been accepted for publication in the peer-reviewed Boundary-Layer Meteorology journal corresponding to:

Udina, M.; Sun, J.; Kosovic, B.; Soler, M.R. 2015. **Exploring vertical turbulence structure in neutrally and stably stratified flows using Weather Research and Forecasting - Large-Eddy Simulation model (WRF-LES).** Boundary-Layer Meteorology.

6.1 Introduction

The atmospheric stable boundary layer (SBL) is commonly formed when the underlying ground is cooled by longwave radiation and turbulent mixing is weak (Stull 1988). In recent decades, several field campaigns were conducted to study the SBL such as SABLES98 (Stable Atmospheric Boundary-Layer Experiment in Spain 1998) (Cuxart et al. 2000), CASES-99 (Cooperative Atmosphere-Surface Exchange Study 1999) (Poulos et al. 2002), and SABLES2006 (Stable Atmospheric Boundary Layer Experiment in Spain) (Yagüe et al. 2007). Studies from these campaigns have improved the understanding of the SBL. However, the SBL turbulence parametrization in mesoscale models and also in the subgrid scale in large eddy simulation (LES) models is still poor, particularly under strong stable stratification associated with weak winds.

As we introduced in Sect. 2.1.1 in chapter 2, SBL has been divided into several regimes. Recently, Sun et al. (2012) (henceforth S12) investigated the month long nocturnal CASES-99 dataset over a 60-m layer and classified two main turbulence regimes for a given height above ground (z) in terms of the relationship between turbulence strength expressed in terms of the variances of wind components and horizontal wind speed (V). Sun et al. (2015a) and Sun et al. (2015b) (henceforth S15) referred to the dramatic transition between the two regimes in S12 as the HOckey-Stick Transition (HOST). The first regime is characterized by weak turbulence generated by shear over a finite $\delta z < z$ when V is less than its threshold value, V_s. The second regime is a strong turbulence regime when $V > V_s$. Their observations suggest that the strong turbulence regime is dominated by large coherent eddies that scale with z, implying that turbulence is generated by bulk shear (V/z, i.e., $\delta z = z$). Occasionally, the turbulence strength is stronger than its shear generation at z with $V < V_s$, which may occur when turbulence is generated by large disturbing events above the ground, such as breaking waves under low-level jets (LLJ) (see Figure 2 from S12).

S15 further investigated the HOST, and found that the temperature below z in the strong turbulence regime is nearly uniform in contrast to the strong temperature stratification in the weak turbulence regime. The results suggest that the strong large coherent eddies in the strong turbulence regime are responsible for mixing the layer to a vertically uniform state. Based on the concept of the turbulence energy consumption for turbulence kinetic energy and turbulence potential energy developed by Ostrovsky and Troitskaya (1987) and Zilitinkevich et al. (2007), S15 explained the observed HOST. S15 employed the budget equations for turbulent potential energy (TPE) and turbulent kinetic energy

(TKE), which together constitute the turbulent total energy (TTE = TKE + TPE), to explain the maintenance of turbulence by the velocity shear in any stratification. From this perspective, in the stably stratified atmosphere, a significant portion of the shear-generated turbulence energy is used to increase the TPE through heat transfer, thus, TKE weakly increases with V. In the nearly neutral atmosphere when $V > V_s$, temperature fluctuations in the form of TPE is reduced significantly as a result of the reduced heat transfer. Therefore, the shear-generated turbulence energy leads directly to the sharp increase of TKE with V. In other words, shear-generated turbulent mixing shapes the vertical temperature gradient, resulting the observed relationships between the turbulence strength and V.

The current study investigates the relationship between turbulence strength and V beyond the 60-m height layer used in S12 by using the LES mode of the Weather Research and Forecasting Model (WRF-ARW) (Skamarock et al. 2008), i.e., WRF-LES (Moeng et al. 2007; Mirocha et al. 2010). Previous WRF-LES studies have improved the sub-grid scale model (SGS) performance (Mirocha et al. 2010; Kirkil et al. 2012) by including the nonlinear backscatter and anisotropy (NBA) model (Kosović 1997). Other studies used LES nested in the WRF domain either in the two-way nesting (Moeng et al. 2007) or in the one-way nesting (Liu et al. 2011; Mirocha et al. 2013; Talbot et al. 2012; Muñoz-Esparza et al. 2014) but only in unstable atmosphere. One of the advantages of using the WRF-LES model is the ability to simulate the atmosphere over realistic terrain (Talbot et al. 2012). As the other LES models, the WRF-LES is designed to directly resolve the large eddies that dominate turbulent energy and parametrize the effect of small eddies with the SGS models. The WRF-LES provides a useful tool to investigate nonlinear dynamics of turbulence where it is suitable. Because turbulent eddies are much smaller in the SBL than in the convective boundary layer (CBL), simulating SBL requires a high-resolution grid with an accurate SGS model as well as high computational resources.

LES modeling has been used to study the SBL in the literature (Mason and Derbyshire 1990; Brown et al. 1994; Andren 1995; Kosović and Curry 2000; Saiki et al. 2000; Basu and Porté-Agel 2006; Jimenez and Cuxart 2005; Beare et al. 2006; Huang and Bou-Zeid 2013) obtaining continuous turbulent boundary layers. In particular, Beare et al. (2006) conducted an LES model intercomparison as part of the Global Energy and Water Cycle Experiment Atmospheric Boundary Layer Study (GABLS) project for the SBL driven by a fixed cooling rate, based on the BASE (Beaufort Sea Arctic Stratus Experiment) arctic observations. As a detailed analysis of WRF-LES performance in simulating SBLs has not been carried out, in this study we also present a validation of the first and second order profiles of WRF-LES against the LES models used in GABLS presented in Beare et al. (2006) (henceforth B06).

This chapter is structured as follows. The model description and methodology are described in Sect. 6.2. Then, a WRF-LES validation against the GABLS case is included in Sect. 6.3. In Sect. 6.4, we describe the general characteristics of the neutral and

stable LES simulations and their comparison for a range of initial geostrophic winds, as well as their higher order moments profiles. Dependence of turbulence strength and turbulent temperature fluctuations on V, their vertical variations and the structure of turbulent eddies are examined in Sect. 6.5. Comparison between observed and simulated relationships are discussed in Sect. 6.6 and, finally, the summary and conclusions are given in Sect. 6.7.

6.2 Methodology

The idealized LES simulations are carried out using the WRF-LES model version 3.4 (Moeng et al. 2007; Mirocha and Kosović 2010; Mirocha et al. 2013). A filter is applied for the resolved velocity field to obtain variables of large energetic eddies. The effect of small-scale turbulence on resolved fields is parameterized with a linear eddy viscosity approach, using a prognostic equation for TKE, what is called the 1.5-order TKE model (Mirocha et al. 2014), based on the Smagorinsky model (Smagorinsky 1963; Lilly 1967). Additional simulations are run using the NBA subgrid scheme, which includes nonlinear terms that account for the anisotropy and the energy backscatter of the sub-grid stress tensor, although their results are not presented in this study. A Coriolis parameter of $f = 0.0001$ s^{-1} ($\approx 45°N$) is applied. The fifth-order finite-differencing advection scheme is chosen for horizontal advection, the third order for vertical advection, and the third-order Runge-Kutta scheme for time integration.

The domain size is 1×1 km in the horizontal directions (x, y) and 600 m in the vertical (z), with 200 grid points in both x and y directions and 100 levels in z. The horizontal grid spacing ($\Delta x = \Delta y$) is 5 m and the vertical resolution (Δz) is 1.8 m in the first 20 levels and stretched above it (to 3.3 m at level 40 and to 10 m at level 80). A damping layer is added at the domain top to absorb waves generated by any perturbation. The lateral boundary conditions are periodic in the horizontal directions. The MOST bulk formula is used to calculate the momentum and heat fluxes at the surface, i.e., the surface momentum is estimated as a function of V, and the sensible heat flux is proportional to the difference between the surface skin temperature and the air temperature at the first grid level of 1.8 m. The underlying topography is homogeneous and flat in the whole horizontal domain. This configuration is used for two different groups of simulations with different initial conditions: (i) one simulation is to reproduce the stable boundary layer case for GABLS to validate the WRF-LES for the SBL and (ii) a group of simulations is designed to explore the vertical turbulence structure, which is labeled as EVTS, in neutral and stable conditions.

1. For the WRF-LES-GABLS case simulation the initial conditions are taken from the description of the LES arctic SBL case for GABLS in B06. The initial potential temperature (θ) is set to 265 K from the surface up to 100 m, then increasing at 0.01 K m^{-1} to domain top up to 268 K. The initial specific humidity (q) is set to

2 g kg^{-1} for the first 375 m above the ground and remains at 1 g kg^{-1} above 375 m. The gesotrophic wind components are $u_g = 8$ m s^{-1} and $v_g = 0$ m s^{-1}. The surface roughness length z_0 is set to 0.1 m and the surface boundary condition is a varying surface temperature with a cooling rate of 0.25 K h^{-1}. A 300-m damping layer is added at the domain top. As in GABLS, the reference potential temperature is established as $\theta_0 = 263.5$ K.

2. For the WRF-LES-EVTS simulations the initial θ is set to 290 K from the surface up to 175 m, to increase at 0.01 K m^{-1} between 175 m and 375 m, and to remain at 292 K above 375 m. The initial q is set to 10 g kg^{-1} for the first 175 m above the ground, decrease linearly to 4 g kg^{-1} from 175 m to 225 m, and remains at 4 g kg^{-1} above 225 m. Four values of geostrophic wind (V_g): 16.5, 13.75, 11 and 8.25 m s^{-1}, which are referred as A, B, C and D, respectively, are used to represent the imposed constant horizontal pressure gradients for driving the boundary layer (BL). The four constant initial wind components profiles are set to equal to V_g such that the resulting equilibrium flow is primarily along y-axis. As explained in Sect. 6.4, wind directions do not vary much due to the relatively strong mixing even for the stable simulations. The minimum V_g is chosen in this study such that turbulence near the surface can be resolved with the prescribed cooling rate without the run-away cooling problem (Derbyshire 1990; Jimenez and Cuxart 2005). The surface roughness length z_0 is set to 0.05 m, which is derived from the CASES-99 observations (Sun 2011), and to 0.5 m. The ground surface is set with two different surface thermal conditions: a constant surface temperature with zero surface heat flux corresponding to neutral condition, and a varying surface temperature with a cooling rate of 0.25 K h^{-1} (Table 6.1), which is the same used by B06. A 200-m damping layer is added at the domain top. The reference potential temperature is set to 300 K, as it is the default value in WRF. Then, a total of eight EVTS simulations are obtained, four for the neutral condition (A-neutral, B-neutral, C-neutral, D-neutral) and four for the SBL (A-stable, B-stable, C-stable, D-stable).

All simulations are run for 9 hours to allow the development of the boundary layer to reach a quasi-steady state. The outputs from the last simulated hour are taken to compute the statistics via the Reynolds spatial and temporal averaging in this study. For the statistics of first (mean), second (variances), and third (skewness) order moments, we first average them over the entire horizontal domain of 200 $\times$ 200 data points, and after we average them in 5-min intervals. Increasing intervals to 10-min does not change conclusions in the study. The first order magnitudes are the horizontal wind speed and potential temperature (θ) profiles. The second order variables include the momentum fluxes ($\overline{w'u'}$) and ($\overline{w'v'}$), the heat flux ($\overline{w'\theta'}$) and the variances of u (σ_u^2), v (σ_v^2) and w (σ_w^2), where u and v are the horizontal wind components and w is the vertical wind component, the overlines represent the space-time averages, and the primes represent the

perturbations from the space-time averages. We also calculate $TKE = [\frac{1}{2}(\sigma_u^2 + \sigma_v^2 + \sigma_w^2)]$. The total second order terms are calculated as the sum of the resolved and the subgrid parameterized components. The w skewness defined as $\overline{w'^3} = \frac{\sum_{i=1}^{N}(w_i - \overline{w})^3}{(N-2)\sigma_w^3}$ where N is the number of data points, is also computed.

Because part of the second (and higher) order moments are parameterized by the subgrid scales in the LES simulations, their uncertainty associated with various assumptions leads uncertainty in their simulated results when their subgrid components are larger than their resolved components, such as near the surface or when the atmosphere is really strongly stable.

6.3 WRF-LES validation in the SBL

In this section we present a comparison between WRF-LES and the models used in the GABLS case in B06 reproducing the arctic stable boundary layer case. The outputs with $\Delta x = 6.25$ m from the B06 models are chosen for the comparison, which is the closest resolution to the $\Delta x = 5$ m grid used in WRF-LES. The subgrid scale model used in the simulations is the Smagorinsky-based 1.5-order TKE model.

In general, the first order profiles fit well with those from the LES models used in B06. The horizontal wind speed profile (Fig. 6.1a) is close to the Universitat de les Illes Balears (UIB) model (Cuxart et al. 2000), with the super-geostrophic jet peak maximum at the lower height range of the models. The potential temperature profile (Fig. 6.1b) tends to be similar to the University of Hannover and Yonsei University (IMUK) model (Raasch and Schröter 2001) and close to the UIB model, with a lowered potential temperature inversion at the top of the SBL. The calculated BL depth (h) is around 147 m, which is, again, at the lower range of the B06 models values (between 150 and 200 m), so the WRF-LES boundary layer depth is slightly shallower. As in Kosović and Curry (2000), the h is calculated as the height where the momentum flux decreases to 5% of its surface value divided by 0.95. The momentum flux at the surface in the WRF-LES-GABLS case is 0.058 m^2 s^{-2}, corresponding to a friction velocity of 0.22 m s^{-1} which is at the lower end of the range of the B06 model values, meaning that WRF-LES is reproducing a lower turbulent mixing at the surface, which is consistent with the lower h. The heat flux at the surface is also smaller than the B06 models.

The obtained momentum flux ($\overline{w'u'}$) (Fig. 6.2a) and heat flux (Fig. 6.2b) profiles with WRF-LES are at the lower end of all the models used in the comparison in B06. The momentum flux profile is similar to the IMUK model near the surface merging with the other B06 models toward the top of the BL. Both profiles obtained with WRF-LES are similar to the ones obtained by Huang and Bou-Zeid (2013), reproducing the profiles in the lower end of the overall GABLS intercomparison. The vertical velocity variance (σ_w^2) (Fig. 6.2c) from the WRF-LES is well resolved, with a maximum at tens of meters above ground. The closest profile is the one corresponding to the UIB model. Fig. 6.2d shows

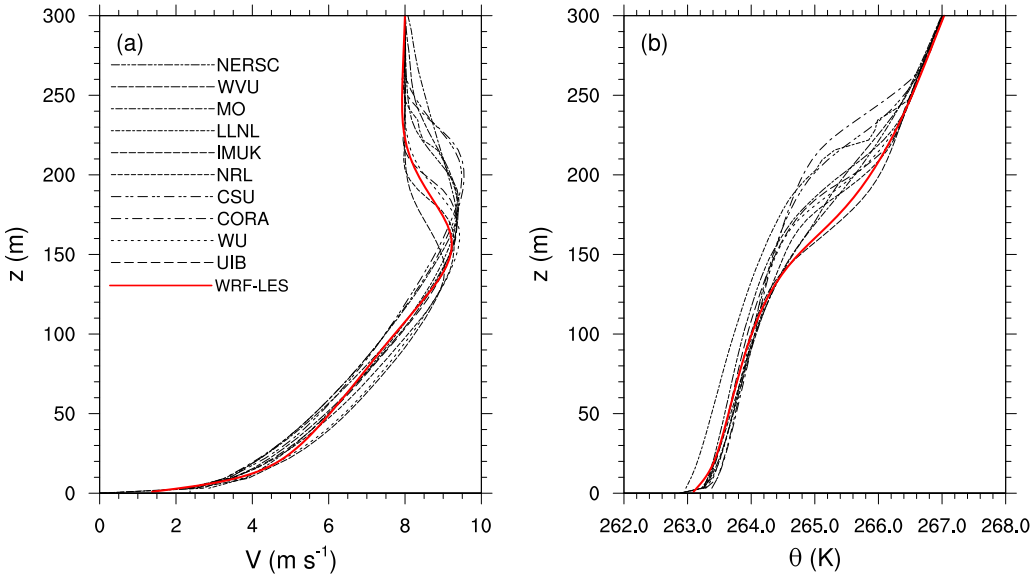

Figure 6.1: Vertical profiles of spatial and temporal averaged: (a) horizontal wind speed (V) and (b) potential temperature (θ). WRF-LES (red line) is compared against all the models used in the GABLS intercomparison in B06. Models from B06 correspond to the 6.25 m horizontal resolution.

that all the TKE is subgrid near the surface. This subgrid contribution to the total TKE decreases with height for all models and reaches to around a 10-15% above 30-40 m for WRF-LES. This value is lower than all the B06 models, which means that the TKE is better resolved above $\approx$ 30-40 m with the WRF-LES code than in the models used in B06.

With this result, we have presented the validation of the WRF-LES in the SBL for the first time. The comparison shows that WRF-LES is overall comparable with the LES models used in B06, reproducing the profiles within the values of the B06 models for a flow in the weakly SBL. The next sections aim to explore the details of the vertical flow structure obtained with the WRF-LES model in the stable and neutral environments.

6.4 Vertical variation of simulation results

The main characteristics of the WRF-LES-EVTS simulations with the four different geostrophic wind forcings (A, B, C, D) and the two surface conditions (neutral and stable) are given in Table 6.1, where the surface parameters such as the friction velocity ($u_* = [(\overline{u'w'})_s^2 + (\overline{v'w'})_s^2]^{\frac{1}{4}}$) and the surface heat flux ($H_s = \rho C_p(\overline{w'\theta'})_s$) (where s indicates the value at the surface) are included. The values of u_{*s} and H_s for the most stable case (D-stable) are similar to previous LES simulations of the stable boundary layer (Beare et al. 2006; Huang and Bou-Zeid 2013) corresponding to the continuously turbulent SBLs

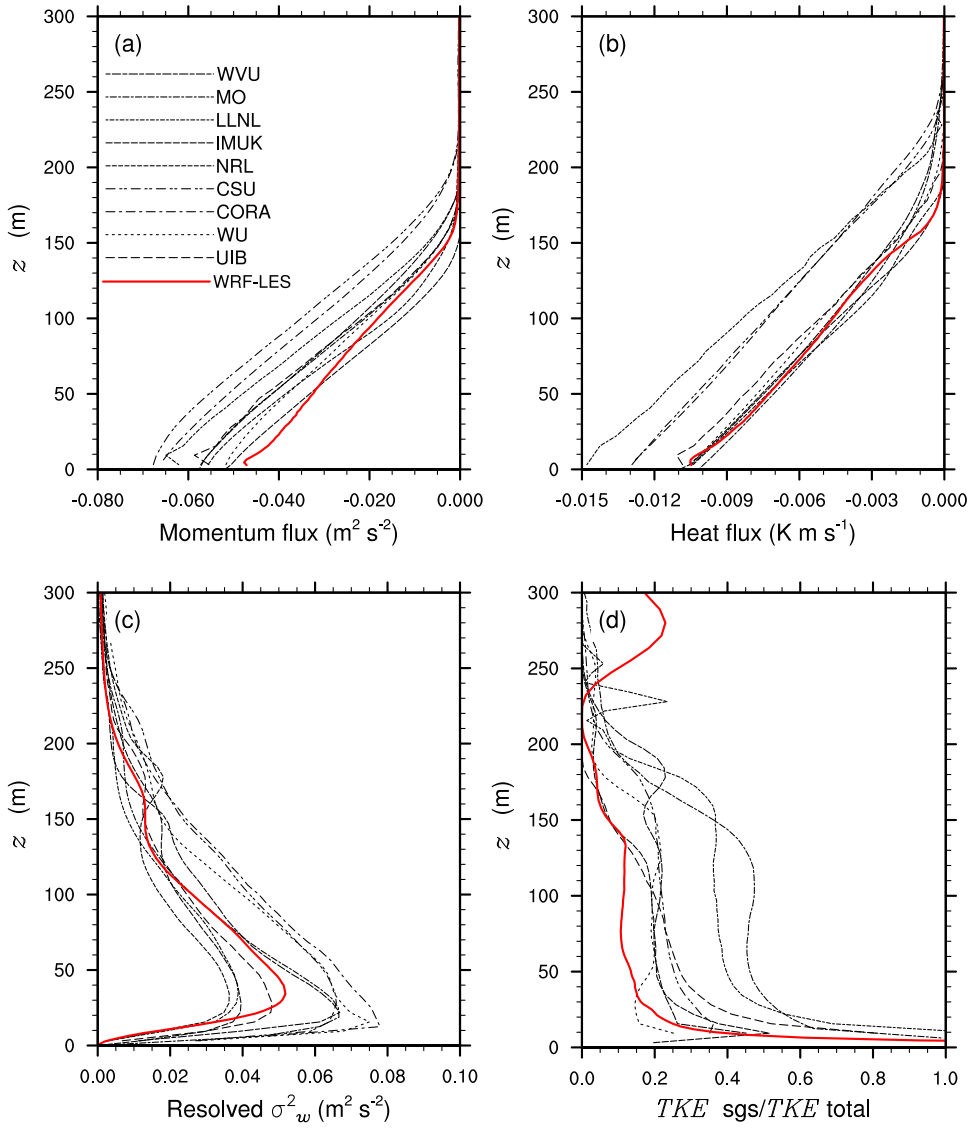

Figure 6.2: Vertical profiles of spatial and temporal averaged: (a) total momentum flux, (b) total heat flux, (c) resolved vertical velocity variance (σ_w^2) and (d) ratio between the subgrid (sgs) and the total TKE. WRF-LES (red line) is compared against all the models used in the GABLS intercomparison in B06. Models from B06 correspond to the 6.25 m horizontal resolution.

Table 6.1: Boundary layer characteristics of the WRF-LES-EVTS simulations.

Simulation	Cooling rate (K h^{-1})	V_g (m s^{-1})	h (m)	u_* (m s^{-1})	H_s (W m^{-2})
A-neutral	0	16.5	466.1	0.588	0
B-neutral	0	13.75	439.6	0.510	0
C-neutral	0	11	427.0	0.409	0
D-neutral	0	8.25	402.5	0.314	0
A-stable	0.25	16.5	402.1	0.501	-35.08
B-stable	0.25	13.75	336.3	0.404	-28.44
C-stable	0.25	11	240.4	0.316	-21.27
D-stable	0.25	8.25	169.3	0.220	-13.35

observed in CASES-99 (Van de Wiel et al. 2003).

The vertical structures of horizontal wind speed and potential temperature in the stable conditions (Fig. 6.3) agree with the SBL equilibrium model developed by Nieuwstadt (1985). As expected, the equilibrium V increases with z (Fig. 6.3a) and reaches to its maximum near the BL top (h), which is calculated as in Sect. 6.3. The h increases with V_g under both neutral and stable conditions (see Table 6.1 and horizontal lines in Fig. 6.3a). The next subsections describe the simulated vertical profiles for the neutral and stable cases, their comparison and the analysis of the higher order moments.

6.4.1 Neutral simulations

Because of the surface drag, the wind profile increases with height, z, for all simulations as a result of momentum transfer, and the horizontal wind speed at a given z increases with increasing V_g (Fig. 6.3a). Momentum fluxes decrease from the surface until the top of the BL due to the momentum sink at the surface (Fig. 6.4a). For the zero surface-cooling rate simulations (neutral), even though there is no heat added or removed from the surface, the turbulence generated by shear transports heat vertically from the initial vertical temperature inversion. Thus, after 9 hours into each simulation, the temperature profile reaches a constant value below h ($\approx$ 400 m) (Fig. 6.3b) and has increased about 1 K from the initial temperature profile (dotted black line in Fig. 6.3b). At the quasi-steady state, the heat introduced by the initial temperature inversion is homogenized through the turbulent mixing generated by shear in the whole BL so the sensible heat flux reduces to a small value (Fig. 6.4b).

6.4.2 Stable simulations

When the surface is cooled, heat is removed steadily at the surface and the initial constant θ is reduced at the surface. Turbulent mixing generated by shear adjacent to the surface

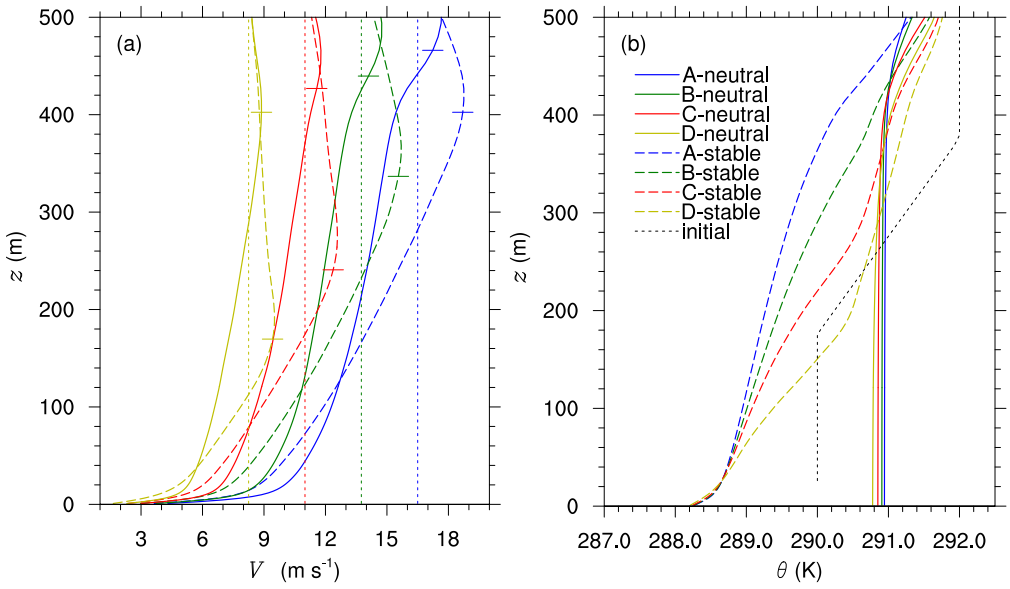

Figure 6.3: Vertical profiles of spatial and temporal averaged: (a) horizontal wind speed (V) and (b) potential temperature (θ). The 4 different geostrophic winds (A, B, C, D) are indicated by different colors, and the two surface conditions: with 0 heat flux (neutral) in solid lines and a cooling rate (stable) in dashed lines. The four thin dashed vertical lines in (a) correspond to the initial geostrophic wind for each wind regime. The small colored horizontal indicate the boundary layer top for each simulation (h).

transports cold air upward and warm air downward. Due to the decrease of the downward heat transfer with z (Fig. 6.4b), the SBL develops near the surface (Fig. 6.3b). Because the horizontal wind speed at a given z increases with increasing initial V_g (Fig. 6.3a) and the wind speed is linearly proportional to the sensible heat flux in the MOST bulk formula, the simulated surface sensible heat flux increases with increasing V_g at a given z (Fig. 6.4b).

The temperature near the surface does not vary significantly with increasing V_g (Fig. 6.3b), however, the increasing sensible heat flux with the increasing V_g extends the upward net transport of cold air in the vertical, leading to the increasing depth of the SBL with increasing V_g as shown in Fig. 6.3a and Table 6.1.

The simulated increase of the vertical sensible heat flux with increasing wind (Fig. 6.4b) maintains the positive temperature gradients without reaching a nearly neutral state. This behavior is different from the observation in S15 where strong turbulent mixing leads to a nearly constant vertical temperature gradient, when $V > V_s$ (details in Sect. 6.1) suggesting that molecular diffusion in the heat exchange at the cooling surface cannot keep up with the fast heat transport by turbulent mixing, leading to a nearly neutral boundary layer. In LES simulations the MOST bulk formula estimates the surface sensible

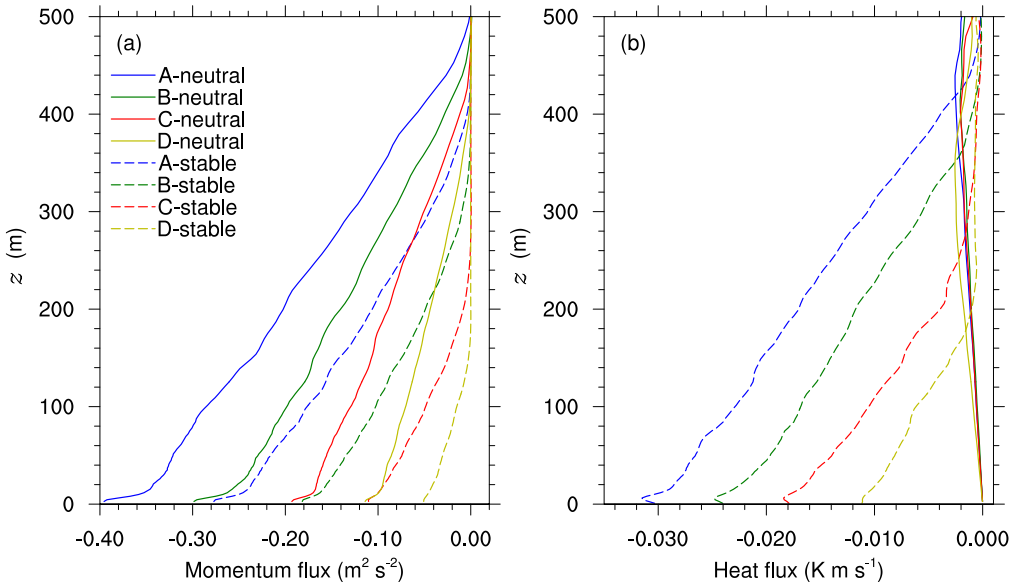

Figure 6.4: Vertical profiles of spatial and temporal averaged total fluxes (resolved + subgrid): (a) momentum fluxes and (b) heat fluxes. The 4 different geostrophic winds (A, B, C, D) are indicated by different colors, and the two surface conditions: with 0 heat flux (neutral) in solid lines and a cooling rate (stable) in dashed lines.

heat fluxes proportional to the horizontal wind speed and to the temperature difference between the aerodynamic temperature (T_a) (Sun and Mahrt 1995), and the the cooled surface skin temperature (T_s), which implicitly assumes a constant surface-air coupling by turbulent mixing, resulting in heat transfer much stronger than molecular diffusion. Thus, the MOST bulk formula applies T_s as the aerodynamic temperature, which is equivalent of assuming that surface molecular diffusion is the same as the turbulent mixing . This leads to an unrealistic thermal coupling, so the cold air from the surface can be transported further up by the strong shear associated with the strong V_g and vertical temperature gradients can be maintained even in strong wind conditions.

6.4.3 Comparison of wind profiles between simulated stable and neutral boundary layers

Comparison of V between the neutral and stable cases for a given V_g indicates that the increase rate of V with z is larger under the neutral condition than the stable one in the lower BL, which reverses in the upper BL (Fig. 6.3a). This vertical variation of V between the neutral and stable cases can also be explained by the turbulence energy variation in TKE and TPE. Because of the heat transfer associated with the surface cooling, part of the shear-generated turbulence energy is used for heat transfer, increasing TPE, which is dominated by temperature variances at the expense of the less significant increase of

TKE. While for the neutral case, the sensible heat flux approaches zero from the turbulent mixing of the initial vertical temperature gradient, shear-generated turbulent mixing leads to large TKE and momentum fluxes without being consumed to TPE. As a result, for the same V_g, the magnitude of the momentum flux at a given z is smaller for the stable case (Fig. 6.4a dashed lines) than for the neutral one (Fig. 6.4a solid lines). Consequently, for the same V_g, V is smaller for the stable case than for the neutral case in the lower BL. In contrast, in the upper BL, the large coherent eddies in the neutral simulations transport momentum in a deeper layer than in stable cases, which results in a stronger V in stable than in neutral case for a given V_g in the upper BL.

6.4.4 Higher order statistics profiles

As the momentum and heat flux profiles, the other second order variables σ_v^2, σ_w^2, and TKE for all the cases decrease gradually with z until they are nearly zero at the top of the BL, as both momentum and heat sinks are at the surface (Figs. 6.5a, c, and e). As in all previous LES studies (Andren 1995; Kosović and Curry 2000), the total horizontal wind variances (σ_v^2) have their maximum near the surface, which are higher in magnitude and located below the maximum of the vertical wind variance (σ_w^2). Because the simulated turbulent mixing is relatively strong in all the cases and the resulting equilibrium flow is nearly along the y-axis, the variances and momentum fluxes in the x directions, (σ_u^2) and ($\overline{u'w'}$) are smaller compared to the y direction magnitudes (σ_v^2) ($\overline{v'w'}$), and the wind direction rotation with z is also negligible for all the simulations.

The contributions of the subgrid components to the total (σ_v^2) and (σ_w^2) are maximum at the surface and decrease with z until the top inversion, where they increase again (Fig. 6.5b and 6.5d), as the subgrid parameterization affects the second and higher order variables when the size of dominant turbulent eddies is near the effective resolution. The subgrid contribution to the second order moments at the surface is almost 100% for σ_w^2, and about 40% for σ_v^2. As the WRF model completely resolves only eddies greater than $6-7\Delta x$ (Skamarock 2004), i.e. the effective resolution, the subgrid contribution dominates over the resolved part in these cases. Additional simulations were run changing from the 1.5-order TKE subgrid model to the NBA subgrid scheme to try to improve the unresolved variances. Unfortunately, using the NBA subgrid scheme lead to similar results in terms of the high order statistics profiles, i.e. the total variances are dominated by the subgrid part near the surface. Although Mirocha et al. (2010) demonstrated that the NBA model improved the TKE-based Smagorinsky model, our results did not reveal significant changes near the surface. Further research is needed.

In addition, the w skewness in Fig. 6.5f shows unrealistically negative values below 20 m. As the second order moments are not resolved but mostly parameterized through the subgrid scheme near the surface and according to the skewness sign change, in this study we will not consider heights below 20 m, which limits our investigation to the vertical domain between 20 m and h.

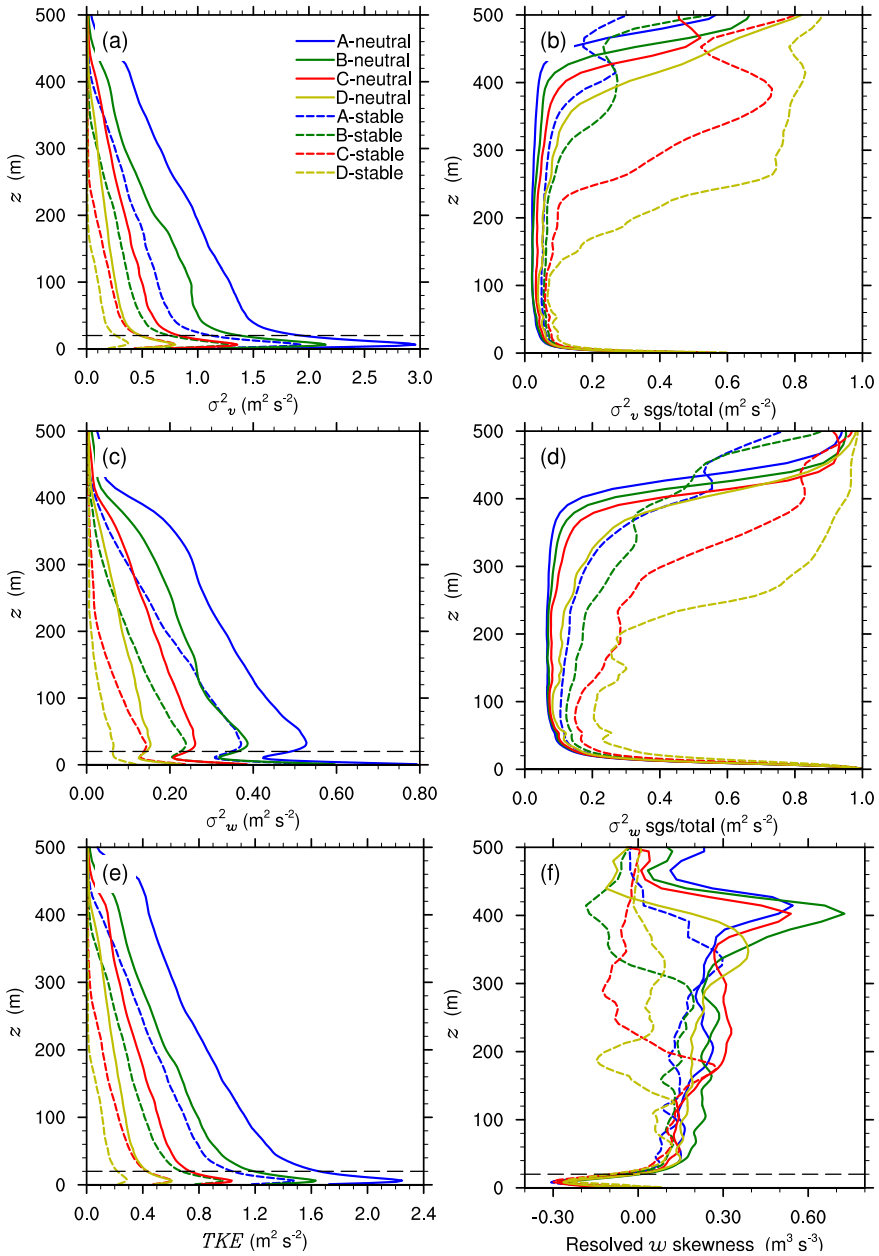

Figure 6.5: Vertical profiles of spatial and temporal averaged: (a) total horizontal wind speed variance (σ_v^2) (resolved + subgrid); (b) ratio between the subgrid (sgs) and the total horizontal wind speed variance; (c) total vertical wind speed variance (σ_w^2) (resolved + subgrid); (d) ratio between the subgrid (sgs) and the total vertical wind speed variance; (e) total turbulent kinetic energy (TKE) (resolved + subgrid); (f) vertical wind component skewness ($\overline{w'^3}$). The 4 different geostrophic winds (A, B, C, D) are indicated by different colors, and the two surface conditions: with 0 heat flux (neutral) in solid lines and a cooling rate (stable) in dashed lines. The thin black horizontal dashed line indicates the limiting height where resolved variances are larger than subgrid parts (also where skewness becomes positive).

6.5 Vertical variation of relationships between turbulent and mean variables

In this section we explore vertical variation of the relationship between turbulence strength and the horizontal wind speed from the WRF-LES-EVTS simulation results following the analysis of observed relationships presented in S12. The horizontal wind speed is defined as: $V = \sqrt{u^2 + v^2}$. As in S12, the turbulence strength can be expressed as the square root of the TKE, $V_{TKE} = [\frac{1}{2}(\sigma_u^2 + \sigma_v^2 + \sigma_w^2)]^{1/2} = \sqrt{TKE}$, or as the standard deviation of the vertical wind (σ_w) from 5-min data segments.

6.5.1 Turbulence relationships

The relationships between turbulence strength, V_{TKE}, and horizontal wind speed, V, and between σ_w and V in Fig. 6.6 are regressed from the WRF-LES-EVTS simulations of the last hour for the four V_g's under the neutral and the stable conditions (Fig. 6.6a and c) and with two roughnesses length parameters for neutral simulations (Fig. 6.6b and d). They are presented for four different heights of approximately 20m, 40m, 60m and 80m and compared with the observed relationship at 20 m from S12.

The simulated relationships for the stable and neutral cases all result in the linear increase of the turbulence strength (V_{TKE} or σ_w) with V at a given z, shifting to higher wind speeds as the height increases (Fig. 6.6). The reproduced pattern for both, neutral and stable, is similar to the strong turbulence - near neutral regime defined in S12, when $V > V_s$ (see gray line in Fig. 6.6), although the increase rate of V_{TKE} with V, i.e. the $V_{TKE} - V$ slope, from S12 is larger than the simulated one up to 60 m (Fig. 6.7).

The increase of σ_w is slower than the increase of V_{TKE} with V (Fig. 6.6c) and also shifts to higher wind speeds with z. This simulated slope is close to the observed in S12 in the simulated neutral, although still underestimated. Increasing the roughness length from $z_0 = 0.05$ m to $z_0 = 0.5$ m (Fig. 6.6b and d) does increase the slope as observed by Mahrt et al. (2013), but the slope for $z_0 = 0.5$ m is still smaller than the observed one at the same height. In any case, the simulation results confirm that the roughness length parameter adds uncertainty on the turbulence relationships.

As it is shown in Fig. 6.6a and Fig. 6.6c, the stable cases relationships reproduced by the model resemble the near-neutral regime (regime 2 in S12), located in the region of relatively strong wind speed, so the weak turbulence regime (regime 1 in S12) is not captured in our simulations. To further investigate the $V_{TKE} - V$ relationship for the stable case, we compare the simulated $\theta_*(z) = \overline{-w'\theta'}(z)/\overline{u_*(z)}$, which is strongly related to temperature fluctuations and TPE, as a function of V (Fig. 6.8a).

Comparison between the observed and the simulated θ_*-V relationships confirms that the simulated stable case is actually similar to regime 2 in S12, where θ_* decreases with V. As already mentioned in S15, the vertical temperature gradient is approximately

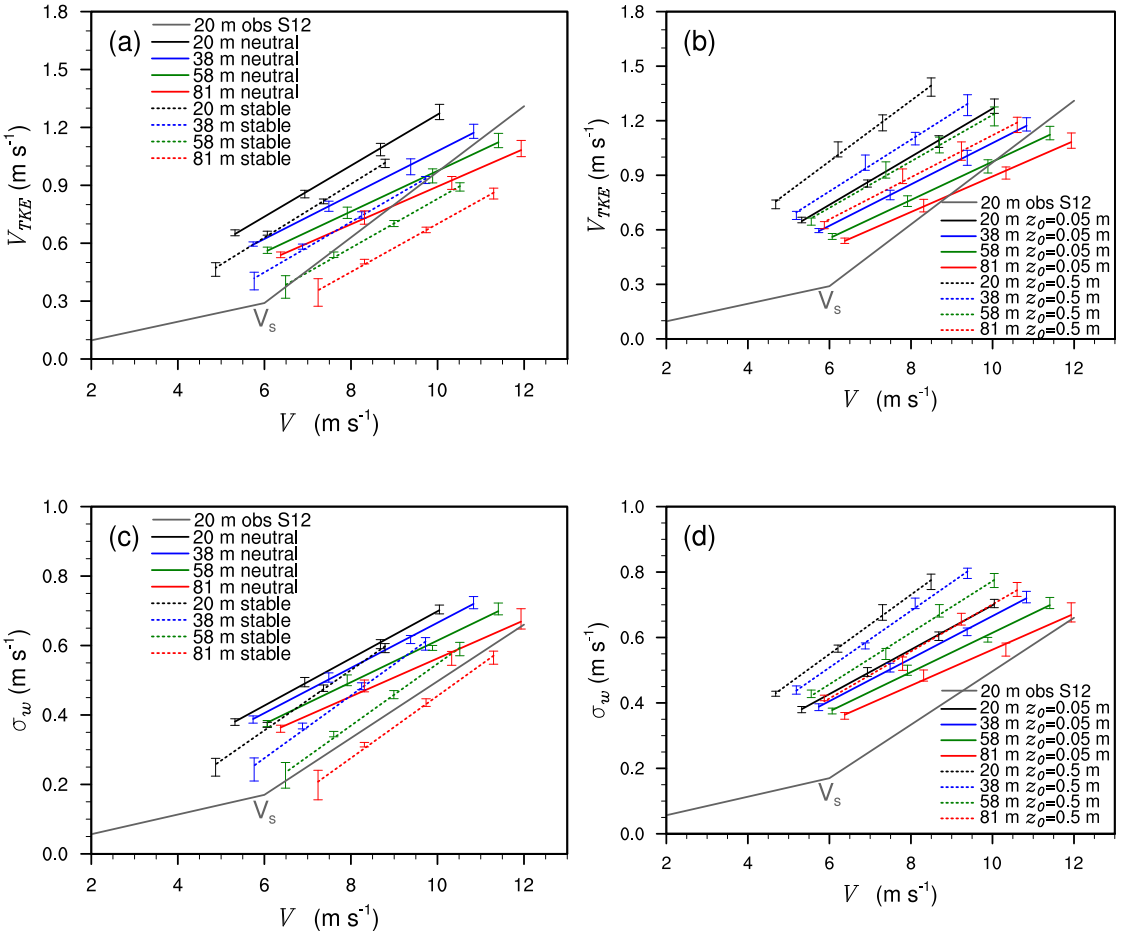

Figure 6.6: The relationships between: (a, b) the turbulence strength (V_{TKE}) and horizontal wind speed (V); (c, d) the standard deviation of the vertical velocity (σ_w) and V at various heights; (a, c) comparison for stable (dashed lines) and neutral (solid lines) cases with the surface roughness of $z_0 = 0.05$ m; (b, d) comparison of their relationships between $z_0 = 0.05$ m (solid lines) and $z_0 = 0.5$ m (dashed lines) for the neutral cases. The regression lines are calculated using 5-minute mean data from last hour of simulation with error bars corresponding to the standard deviation of each wind speed case. The solid gray line represents the relationships in observations from CASES99 at 20 m height obtained from S12 with the threshold wind speed (V_s) which delimits the weak turbulence regime ($V < V_s$) and the strong turbulence ($V > V_s$).

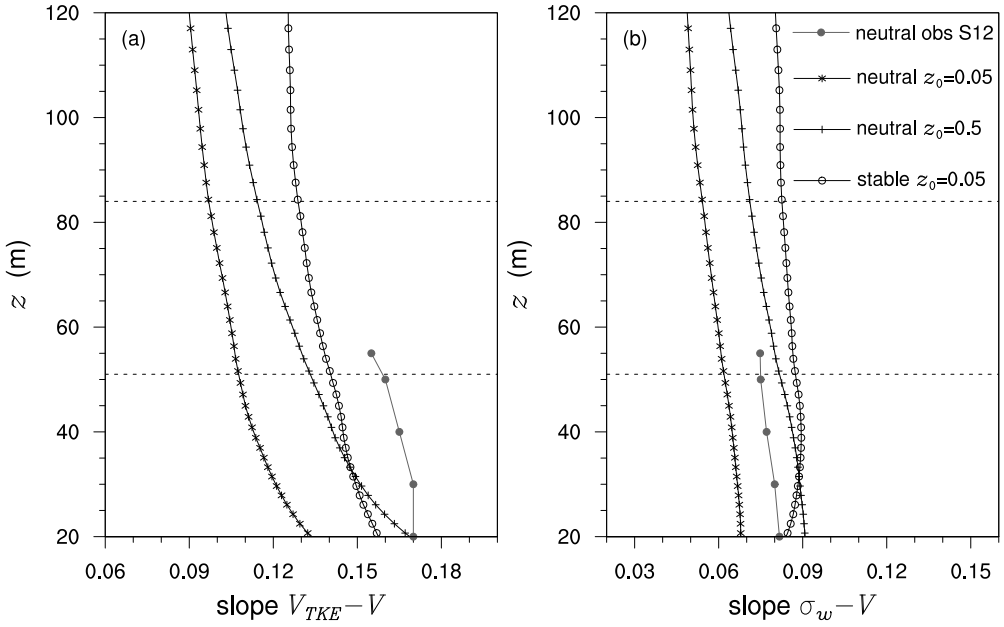

Figure 6.7: Regression line slope at each height (z) for the two neutral roughness length cases (z_0 = 0.5 and z_0 = 0.05 m), the stable case (z_0 = 0.05 m) and CASES99 observations of neutral atmosphere obtained from S12 (gray dotted line) in: (a) V_{TKE}- V relationship; (b) σ_w- V relationship.

homogeneous, so the shear-generated observed turbulent energy goes to TKE for $V > V_s$ and less amount goes to TPE. The relationship between V_{TKE} and $\partial\theta/\partial z$ in Fig. 6.8b suggests that large V_{TKE} is indeed related to small $\partial\theta/\partial z$. Therefore, although the temperature in the stable cases is not nearly uniform, the simulated stable cases have similar turbulence characteristics as the neutral regime defined in S12. In addition, as wind increases, the reduced energy usage for the temperature fluctuations leads to a sharp increase of V_{TKE} with V in stable case compared with the neutral case, that is, the slope is larger for stable than for neutral cases (Fig. 6.7). The different energy partition also explains this behavior, because as wind increases, more turbulent energy is in TKE form and less amount goes to TPE.

As explained in Sect. 6.4.1, the simulated stable stratification results from the unrealistic coupling by applying the surface skin temperature instead of the aerodynamic temperature in the MOST bulk formula. Thus, the simulated stable stratification cases do not represent the real stable atmosphere due to the unrealistic coupling between the surface and the air especially for strong V_g. Consequently we cannot simulate a realistic stable boundary layer, and, consequently, we do not observe the HOST from the LES

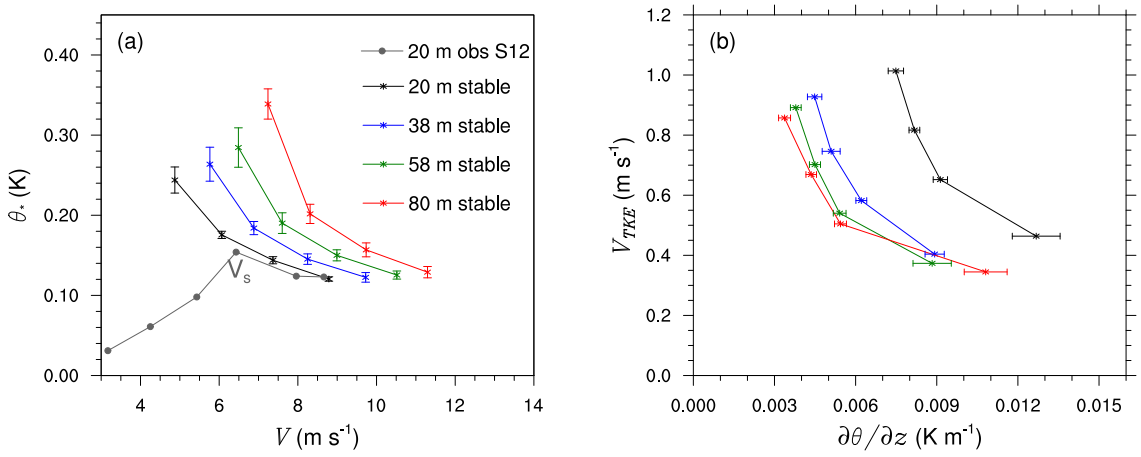

Figure 6.8: Relationship between: (a) θ_* and V; (b) V_{TKE} and $\partial\theta/\partial z$ at different heights above ground in stable simulations. Each marker indicates the averaged value for each wind speed simulation (A, B, C, D) with its corresponding standard deviation indicated with error bars. The dotted gray line represents the relationships in observations from CASES99 at 20 m height obtained from S12 with the threshold wind speed (V_s).

simulations. In addition, the run-away cooling issue mentioned in Sect. 2 also constrains the simulation of the SBL. Simulations in the weak wind range could not be run if the Derbyshire's criterion was not accomplished, that is, there is a maximum value for the heat flux which can be sustained for a fixed geostrophic wind. This is again due to the MOST bulk formula that assumes the skin temperature as the air temperature, leading to an excessive cooling near the surface which would not happen in the atmosphere, what is called the run-away cooling (Derbyshire 1990). In these conditions, there is too low mixing close to ground which leads to flow laminarization and turbulence in LES simulations cannot be resolved. Thus, we cannot simulate the weak wind, weak turbulence regime and we can neither simulate the transition between the stable regime associated with weak winds and the nearly neutral regime associated with strong winds with V, i.e. the HOST of V_{TKE}, as in S12.

Comparison between the vertical variations of the observed and the simulated slopes of the $V_{TKE} - V$ relationships for the neutral case indicates that the simulated slope steadily decreases with z while the observed one remains relatively constant with z. This decrease of the slope suggests the increasing influence of the stable stratification on the neutral $V_{TKE} - V$ relationship with z, which is further discussed in next Sect. 6.5.2.

6.5.2 Spectral analysis of resolved w

We examine the spectral peak of the resolved w as a function of the normalized wavenumber kz to examine the size of the dominant turbulent eddies at each z in comparison with

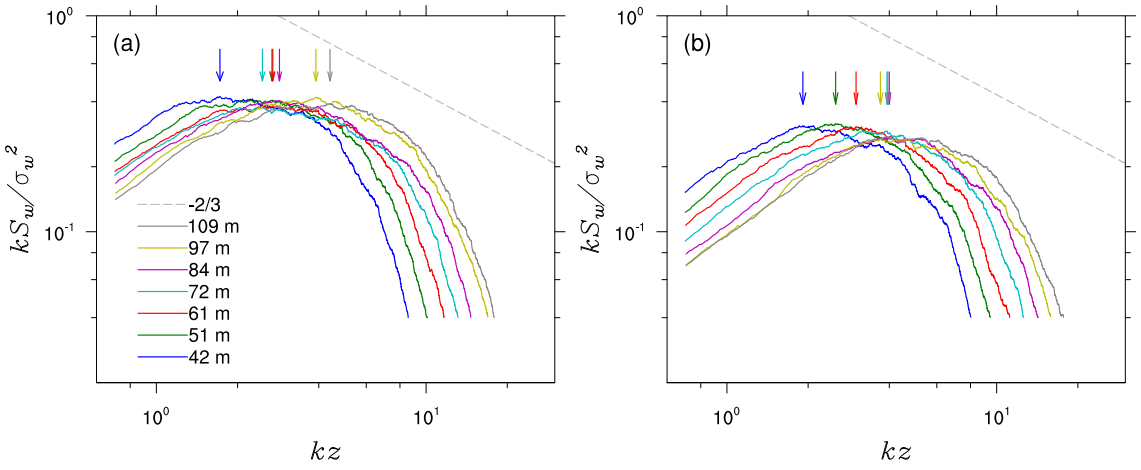

Figure 6.9: The power spectra of the vertical velocity kS_w normalized by the vertical wind component variance (σ_w^2) as a function of the wavenumber (k) normalized by the inverse of each height (z): (a) A-neutral simulation; (b) A-stable simulation. Each color represents a different height above ground. Dashed gray line indicates the theoretical spectra fall-off. Arrows indicate spectral peaks for each z.

the observed pattern in S12. The spectra here are calculated using the resolved w along the wind direction across the middle of the domain for A-neutral and A-stable at the heights shown in Fig. 6.9. The resulting spectra are averaged from those calculated at every 5 min during the last hour of the simulation.

On one hand, the contribution of the subgrid σ_w^2 to the total σ_w^2 is about 10 % in the layer between $\approx$ 40 m and h for A-neutral and A-stable (Fig. 6.5d), so we can investigate spectral peaks in this vertical domain for these two cases, where the resolved eddies dominate both σ_v^2 and σ_w^2 (Fig. 6.9). On the other hand, the w subgrid contribution is only significant at the high wavenumber end due to the increasing removal of the kinetic energy with increasing wavenumber through model filtering (Skamarock 2004), which is evident from the decrease of the spectra with kz faster than -2/3 marked in the grey lines in Fig. 6.9. Since we are only interested in spectral peaks low wavenumbers, we assume that the spectral error at the spectral peaks are negligible, thus the spectral correction proposed by Chow et al. (2005) is not performed here.

S12 found that the spectral peak of w in the nearly neutral atmosphere under strong winds occurs at fz/V, which does not vary with z. This result implies that the length scale of the dominant turbulent eddies scales with z. S15 further confirmed the contribution of the relatively large coherent eddies to turbulent mixing by investigating vertical coherences of vertical and horizontal wind components and temperature. In addition, S12 found that the w spectral peak at a given z shifts to high frequency compared to its neutral spectrum as the size of turbulent eddies decreases in the stable atmosphere. From our simulation

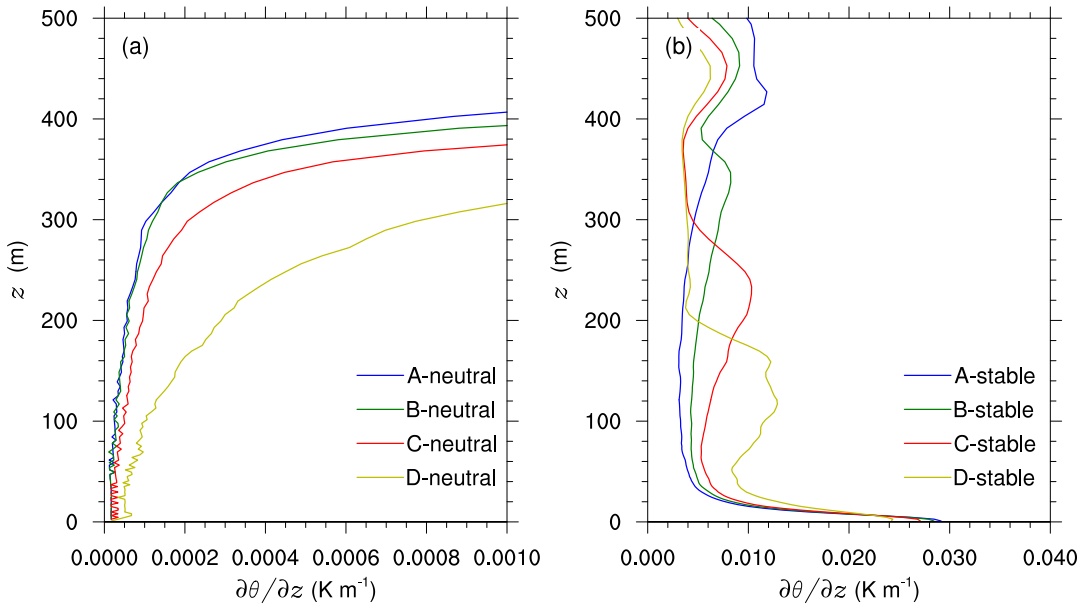

Figure 6.10: Vertical temperature gradient profiles of: (a) neutral and (b) stable cases. The 4 different geostrophic winds (A, B, C, D) are indicated by different colors.

results, we find that the simulated w spectral peaks shift toward higher kz for increasing z for both neutral and stable cases (Fig. 6.9). However, this shift for the neutral w is relatively small in the layer between 51 m and 84 m (Fig. 6.9a), suggesting that the air layer is more neutral in this layer compared to the rest of the BL layer, which is also confirmed by the smallest $\partial\theta/\partial z$ in the simulation layer in Fig. 6.10a, and the smallest contribution of the subgrid σ_w^2 to the total w in Fig. 6.5d. The relatively large shift toward high wavenumber above 84 m for the neutral case suggests the influence of the stable stratification above in reduction of the scale of turbulence eddies, which is in turn consistent with the steady decrease of the slope of the $V_{TKE} - V$ relationship with z in Sect. 6.5.1. We hypothesize that the initial temperature inversion located between 175 and 375 m (dashed gray line in Fig. 6.3b) may be the origin of this stable stratification influence. Further analysis of the vertical variation of $\partial\theta/\partial z$ for the neutral cases in Fig. 6.10a indicates that the vertical temperature gradient indeed increases with z for A-neutral especially above 200 m, the height where the temperature inversion was initially located. The vertical increase of the simulated $\partial\theta/\partial z$ for A-neutral implies that large coherent eddies generated by bulk shear reach even above the initial temperature inversion layer, resulting in the downward heat transfer and the increase of TPE from the shear-generated turbulence energy. As a result, the rate of the increasing TKE with V has to decrease with z, which, in turn, explains the decrease of the $V_{TKE} - V$ slope with z for the neutral case in Fig. 6.7a.

The spectral peak in the A-stable case of the resolved w shifts to higher kz or toward higher wavenumber k at the same z compared to the one in A-neutral (Fig. 6.9b). This is consistent with the observation in S12 under stable conditions due to the decreasing size of turbulent eddies in the stably stratified environment. Because of the surface cooling, the vertical stratification for the cooled surface with even the strongest V_g is much stronger than the initial inversion (Fig. 6.10b) so and the eddy size of the turbulent eddies decreases due to stability, as observed in S15.

6.6 Discussion

The simulated relationships between V_{TKE} and V (Fig. 6.6a) in neutral simulations is similar to the observed strong turbulence regime, i.e., near neutral regime defined in S12 and S15. The w spectral analysis also confirms the size of the dominant turbulent eddies scales with z under the nearly neutral conditions, which supports the idea of the important role of bulk shear, V/z, in turbulence generation in the nearly neutral atmosphere. The shift of the w spectral peak toward high wavenumber with increasing z above 84 m and the decrease of the slope of the $V_{TKE} - V$ relationship suggest that the initial top inversion temperature layer can influence the stratification down near the surface under strong turbulent mixing by large coherent eddies. The relatively small increase of $V_{TKE} - V$ with V for the simulated neutral cases compared to the observations, i.e. the underestimation of the slope (Fig. 6.7a), could be related to vertical variations of horizontal pressure gradients in the atmosphere while constant horizontal pressure gradients through V_g are used in the simulations. The baroclinicity may also play a role here in the atmospheric turbulent mixing, as discussed in Sun et al. (2013), so it needs to be further investigated. In addition, the influence of subsidence in the upper boundary condition may have to be taken into account (Mirocha and Kosović 2010).

The simulated relationships between V_{TKE} and V (Fig. 6.6a) and between θ_* and V (Fig. 6.8a) for the stable cases suggest that they also resemble the observed nearly neutral $V_{TKE} - V$ relationship even through the simulated $\partial\theta/\partial z$ is much larger than the observed one in the nearly neutral regime. This dilemma is due the unrealistic formation of the stable stratification from the unrealistic thermal coupling at the surface described by using the skin temperature in the MOST bulk formula to estimate the surface heat flux, while in the observed real atmosphere the strong turbulent mixing reduces the vertical temperature gradients. This result highlights the critical role of the heat transfer at the surface in establishing the stable boundary layer. As pointed by S15, when wind is weak, the shear-generated turbulent mixing transfers the cold air accumulated near the surface upward through molecular diffusion and the cold air near the surface results from the heat transfer. The heat transfer process vertically redistributes the cold air from a thin layer to a thicker layer, which enhances the stable stratification in the layer above the thin cold layer until turbulent mixing is so strong that the cold air is spread vertically

quickly through turbulent mixing, leading a nearly neutral stratification. Thus, the vertical temperature gradient is determined by the shear-generated turbulent mixing associated with V, implying that the temperature difference used in the MOST bulk formula has to be the aerodynamic temperature difference resulted from turbulent mixing. In the simulations, using the temperature difference between the skin temperature and the air temperature at the lowest grid point, the heat flux is estimated without considering the contribution of turbulent mixing in the temperature difference. Since molecular diffusion is a much slow process compared to turbulent mixing, we conclude that the heat transfer at the earth-air interface is different from the turbulent heat transfer in the atmosphere and needs to be reconsidered.

On the other hand, because of the subgrid part of the second order moments dominates below 20 m height, we have only investigated the vertical structure of the turbulence above this height. The unresolved turbulence near the surface may influence the turbulence relationships not only below this height but also above it. In that sense, further investigation to address the role of different subgrid schemes is needed, although different subgrid schemes may affect the simulations quantitatively but not qualitatively.

6.7 Summary and conclusions

The WRF-LES modeling system has been used to study the vertical structure of turbulence in the boundary layer. As WRF-LES has never been explored in the SBL, we first validated the results against the reference weakly stable case of GABLS. The comparison shows a good fit of the WRF-LES profiles with the LES models used in Beare et al. (2006), specifically among the models that produce shallower boundary layer heights and lower values of momentum and heat fluxes.

A group of LES simulations in neutral and stable conditions is carried out to study vertical variations of the HOST. A detailed analysis of the profiles of horizontal wind speed and potential temperature with the different contribution of the heat and momentum transport and the turbulence energy variation between TKE and TPE is presented in neutral and stable simulations. Due to the MOST bulk formula used in the surface layer in LES simulations, the sensible heat flux increases with the increasing geostrophic wind and maintains the positive temperature gradients near the surface even under strong winds because of the unrealistic thermal coupling. In contrast, observations from CASES-99 showed that wind speeds above a certain threshold lead to nearly zero vertical temperature gradients. Therefore, the simulated stable atmosphere shows very different characteristics than the observed, which may be also an issue for other LES studies.

Based on the turbulence relationships between the turbulence strength and the horizontal wind speed the neutral simulations are similar to the the strong, i.e., near neutral, turbulence regime defined in S12 where the large eddies and bulk shear are the dominating mechanism of turbulence generation. We also show that the roughness length parameter

influences the rate of the V_{TKE}-V relationship, i.e. the slope. In addition, this slope is slightly underestimated in the simulations, which could be attributed to the lack of baroclinicity in our simulations. We find that the w spectra peak shift to higher wavenumbers and the increasing temperature gradient with height for the different geostrophic winds, suggesting that the upper temperature inversion layer influences the turbulence structure in the neutral cases, as part of the shear-generated turbulence is in TPE form instead of TKE. This also leads to the vertical variation in the slope of V_{TKE}-V relationship.

The turbulence relationships and the θ_*-V pattern for the stable cases also resemble the near neutral turbulence regime, although the temperature gradients are positive and not uniform. Indeed, the surface layer parameterization based on MOST always maintains cold air transfer, even under strong horizontal wind speeds. In addition, this excessive cooling near the ground leads to the run-away cooling problem when the wind is weak, therefore, we cannot simulate the weak turbulence regime (regime 1 in S12) in the HOST pattern with our LES simulations. Using the air temperature instead of the skin temperature in the MOST bulk formula for estimating the heat fluxes would help to represent a realistic turbulent heat transfer and the temperature gradients, which, in turn, would solve these issues.

In summary, the investigation here further suggests the importance of the surface layer parameterization and the need of an adequate representation of the different heat transfer mechanisms at the surface and in the atmosphere in order to achieve realistic stable boundary layers. The upper LES boundary condition is also highlighted as an important factor for the turbulence structure.

7

A modeling study of a trapped lee wave event over the Pyrenees

Contents

These results have been submitted for publication to the peer-reviewed journal *Monthly Weather Review*.

7.1 Introduction

Mountain waves are topographically generated gravity waves, or buoyancy oscillations produced in a stably stratified flow by the disturbance of an air current that encounters an obstacle. Mountain waves impact the atmosphere circulation from the surface to the stratosphere and even mesosphere, in a wide range of different scales. They can be accompanied by clear-air turbulence (Clark et al. 2000), lee-wave rotor formation (Mobbs et al. 2005; Darby and Poulos 2006; Vosper et al. 2006; Grubišic and Billings 2007; Sheridan et al. 2007; Cohn et al. 2011), downslope winds (Mobbs et al. 2005; Klemp and Lilly 1975) and windstorms (Lilly 1978), modifying the surface wind and precipitation intensity as well.

Linear theory has been applied for the understanding of the mountain wave dynamics (Smith 1979). Analytical solutions for a given topography can distinguish between the trapped lee waves and the vertically propagating waves. Trapped lee waves are frequently manifested as lee-wave clouds in satellite imagery and they occur when the Scorer parameter (l^2) decreases with height (Scorer 1949) or when l^2 changes abruptly with height due to a potential temperature inversion. Although linear theory is useful to predict the wave processes, nonlinearity becomes important when the Froude number (Fr) is closer or less than the unity. Then, mountain waves are accompanied by flow reversal near the ground, blocking or breaking the mountain wave. In these situations, when the linear theory cannot be applied, data obtained from observational field campaigns and from the numerical weather prediction (NWP) models becomes fundamental for the understanding of the dynamics of the mountain waves and the associated phenomena.

Several field experiments and numerical simulations have been done during de last decades over complex terrain (extensively described in Sect. 2.3.3, chapter 2). However, there are still many uncertainties to resolve, specially to understand the numerical models performance in resolving mountain waves and their phenomena associated. More specifically, many uncertainties exist over the Pyrenees mountain range, which is an important mountain barrier that influence and modify the atmospheric flows that cross over it. As it is a nearly two dimensional ridge oriented west-east, the northern (southern) flows over the Pyrenees encounter a barrier and they have to overpass it, so they become disturbed at its south (north) side. This disturbances (gravity waves, mountain waves) are able to transport momentum and energy farther downstream or farther up in the vertical. They may also be a hazard for commercial flight routes, which are many in this area of Europe. In addition, they are of interest for glider pilots, that sometimes take profit of them to fly long distances. Mountain waves can also influence the circulations near the surface, within the the boundary layer (BL). In particular, trapped lee waves can introduce momentum and energy at its top, they can be absorbed by the BL (Jiang et al. 2006) or they can lead to rotor circulations within the BL and may break into turbulence (Doyle et al. 2009; Cohn et al. 2011).

Despite its significance, the Pyrenees have not been focus of study since long time ago.

The most remarkable studies in that are were the ALPEX in the 80s and the PYREX in the 90s (more details were given in Sect. 2.3.3.1). Both of them, though, did not deal with mountain waves from the modeling perspective. Since mountain waves are present in many areas, mesoscale models need to correctly represent the flow after crossing a mountain barrier, to adequately resolve the atmospheric circulations. Specifically, in the Pyrenees area, mountain wave events are repeated during winter season, therefore, there is a necessity for resolving the phenomena accurately. Furthermore, as the lee wave structure determines BL circulations and rotor formation within the BL, a correct representation of the wavelength and the wave amplitude is needed for capturing the lower troposphere turbulent zones. In this section we simulate a trapped lee wave event over the southern side of the Pyrenees to explore the capability of the model to reproduce it.

Firstly, the site characteristics with an analysis of the mountain wave occurrence and model setup is detailed in section 2. Next, the case-study description with the available observations and the model verification is given in section 3. Section 4 focusses on mountain wave characteristics simulated by the model in its different configurations, the wavelength and amplitude wave analysis and the valley circulations and some rotor signals seen near the surface. Finally, a summary and conclusions are given in section 5.

Mainly, the study aims to determine the WRF model ability to reproduce a mountain wave event and the impact on circulations near the surface. Firstly, the site characteristics with an analysis of the mountain wave occurrence and model setup is detailed. Next, the case-study description with the available observations and the model verification are given. The main results show the mountain wave characteristics simulated by the model in its different configurations, the wavelength and amplitude wave analysis and the valley circulations and some rotor signals seen near the surface.

7.2 Site characteristics and mountain wave occurrence

The Pyrenees is a mountain range in southwest Europe standing at the border between France and Spain. The size of the mountain range is about 400 km long (west-east) and 100 km wide (south-north) (Bougeault et al. 1997) (Fig. 7.1a). The average elevation gradually increases from west to the central part where the highest summits are found, with the highest point in the Peak Aneto (3404 m). In the Eastern part, where we focus our study, the mean elevation is remarkably uniform with a crestline around 3000 m (Fig. 7.1b).

In this study we will consider the mountain wave formation at the south part of the Oriental Pyrenees, when northerly flows influence the downwind side corresponding to Catalonia, Spain. Ideally, for northern flow perpendicular to the mountain range, the given topography (h_m = 2000 m) within a stable environment (N = 0.01 s^{-1}) gives a Froude number $Fr = \frac{U}{Nh}$ from 0.5 (for U = 10 m s^{-1}) to 1 (for U = 20 m s^{-1}). Within this range of values the flow is affected by nonlinearity, thus, flow spliting and wave

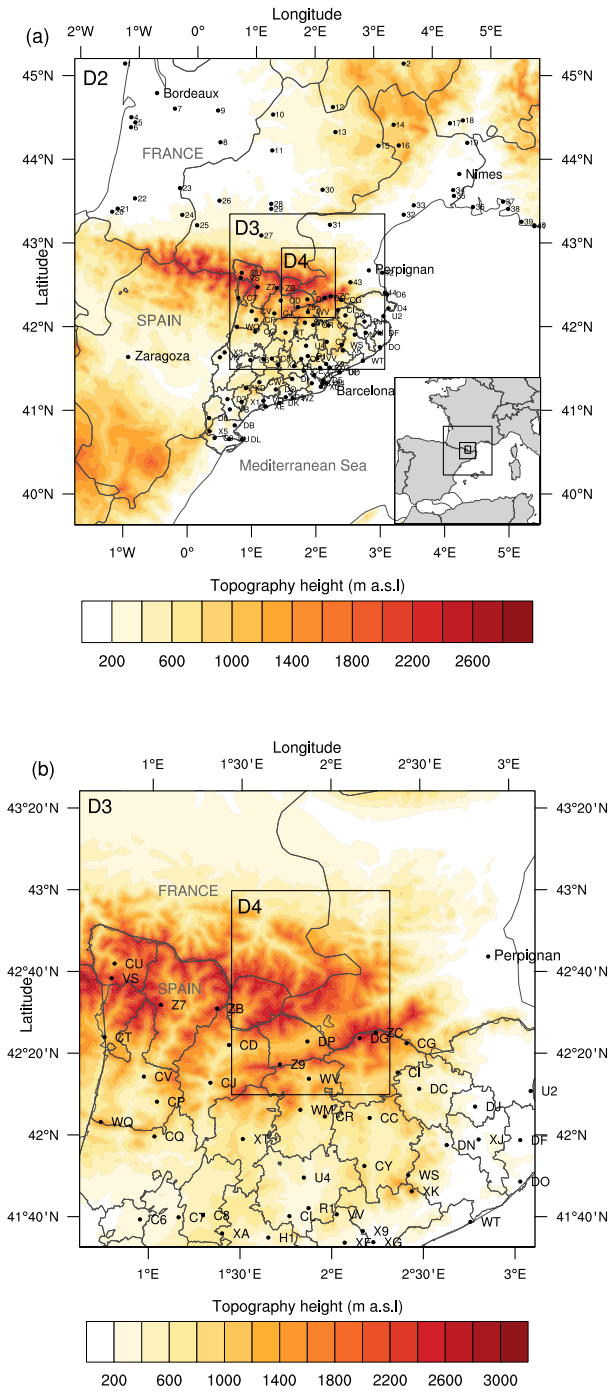

Figure 7.1: (a) WRF model 3 km-grid domain (D2) configuration, terrain elevation and location of the 1 km-grid domain (D3) and 500 m-grid domain (D4). Numbers indicate the surface stations from the Synop database and letters correspond to surface stations from the Catalan Meteorological Service. In the bottom right of the figure there is the location of the three domains. (b) WRF model 1 km-grid domain (D3) terrain elevation and surface stations location and inner 500 m-grid domain (D4).

breaking can occur downstream of the mountain range. According to Smith (1989) and Vosper (2004), mountain waves and lee waves will be produced with this characteristic values, with more chances to be accompanied by wave breaking when the incident wind is lesser.

In order to identify and characterize the presence of mountain waves in the Pyrenees we have used atmospheric soundings and high resolution satellite imagery from Moderate Resolution Imaging Spectroradiometer (MODIS) of 1 km resolution. We have analyzed seven years, from 2008 to 2014, of atmospheric soundings launched in Barcelona (see location in Fig. 7.1a) twice a day. In order to select the days with possible mountain waves formation, specifically trapped lee waves, we have imposed the following conditions: (i) a temperature inversion ($\Delta T/\Delta z \geq 0$) in any layer between 1 and 6 km, (ii) northerly winds between 315° and 45° and (iii) wind speed greater than 10 m s^{-1} in the selected layers. The first condition ensures the presence of a temperature inversion which delimits a region above where the air is statically stable and waves can be developed. The second condition imposes a northern wind component, perpendicular to the orientation of the Pyrenees. The wind speed condition ensures that part of the flow will be able to cross the mountain barrier.

The soundings analysis (Table 7.1) reveal that winter is the most likely season for mountain trapped wave formation. On average, 52 days per year are found during the 7 years analyzed (2008-2014), which represents a 15% of days per year for mountain wave occurrence. During winter season (December, January and February) 25% of days have good conditions for wave development and March is also a probable month, with a large number of days of occurrence, depending on the year. Although there is no direct way to verify the presence of gravity waves during these periods, we use the satellite imagery to detect the wave occurrence with Altoculumus (*Ac*) lenticular cloud formation. A review of the MODIS satellite imagery during the selected days in winter among 3 years (2012-2014) revealed a variety of situations, some cases with the presence of *Ac* but others with clear sky conditions or low level clouds. If bands of *Ac* clouds are formed, the presence of a lee wave train is confirmed, however, waves can be also developed without cloud formation when there is no enough moisture available in the atmosphere. In addition, many detected days with the presence of *Ac* from MODIS occurred during late spring and early autumn, probably because there is enough moisture availability to reach the condensation level and the cloud formation. From the several days selected from the sounding analysis and matching with the presence of *Ac*, in this study we analyze the specific event occurred on 13 September 2012, when the satellites MODIS and METEOSAT revealed a *Ac* cloud train formation at the south part of the Pyrenees (Fig. 7.3).

Table 7.1: Number of days in a month with favorable conditions for mountain waves formation during 7 year analysis (2008-2014) of soundings launched in Barcelona.

Mon	2008	2009	2010	2011	2012	2013	2014	%
Jan	6	4	7	6	12	11	6	24.0
Feb	1	12	7	7	11	11	5	27.6
Mar	10	10	5	2	7	2	10	21.2
Apr	7	2	3	2	1	2	1	8.6
May	0	6	8	2	3	3	4	12.0
Jun	3	2	3	2	3	6	1	9.5
Jul	0	1	8	5	3	2	4	10.6
Aug	1	0	6	1	1	5	2	7.4
Sep	3	2	1	4	5	2	2	9.0
Oct	1	12	0	4	6	2	1	12.0
Nov	6	8	7	2	2	10	2	17.6
Des	8	7	6	14	9	3	10	26.3
Tot	46	66	61	51	63	59	48	
%/y	12.6	18.1	16.7	14.0	17.3	16.2	13.2	

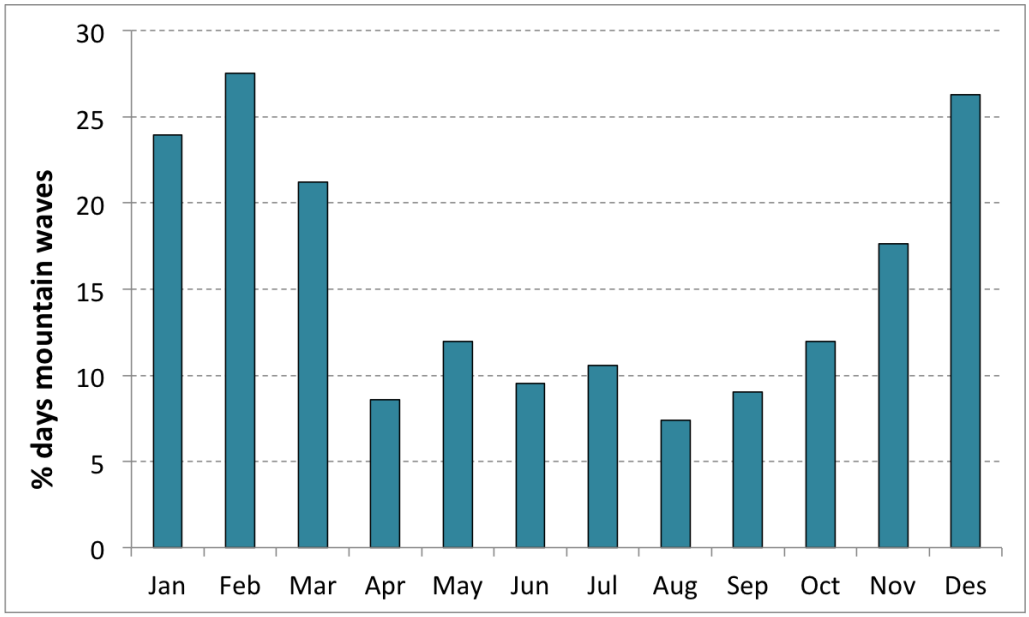

Figure 7.2: Percentage of days a month with favorable conditions for mountain waves formation according to 7-year atmospheric sounding analysis launched in Barcelona.

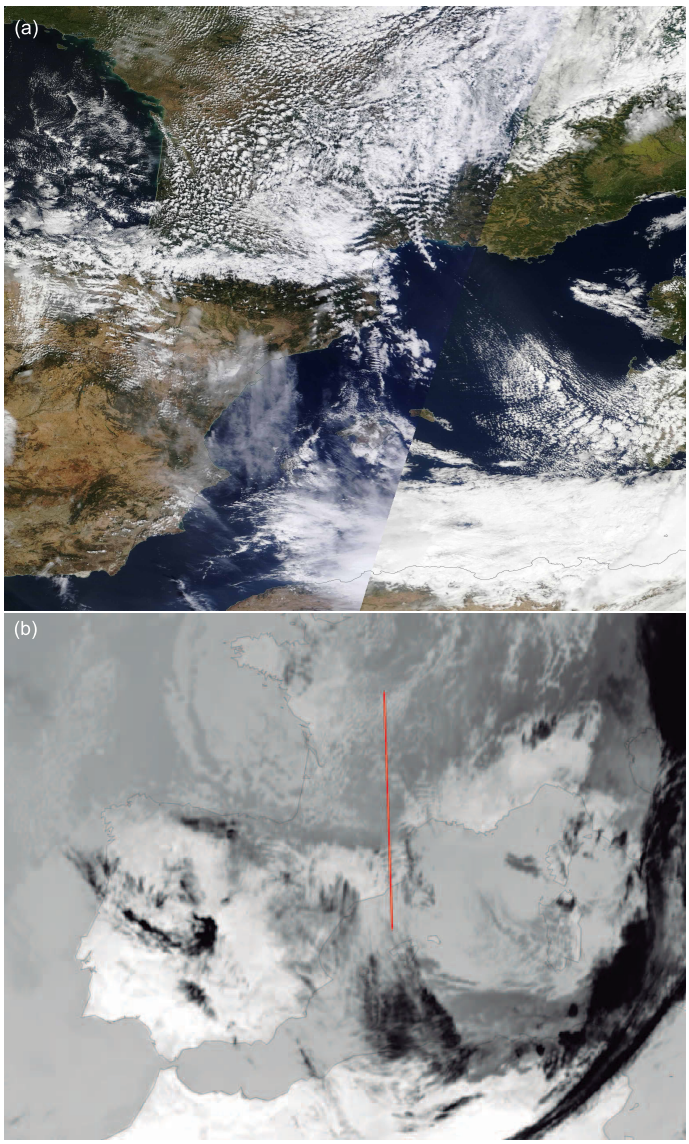

Figure 7.3: (a) MODIS visible satellite image of 13 September 2012 at 1130 UTC; (b) METEOSAT Brightness Temperature (TB) at 11 UTC corresponding to infrared channel 9, with the cross section (red line) corresponding to the wavelet analysis in Fig. 7.8.

7.3 Model setup and model experiments

In this study we use the version 3.4.1 of the numerical WRF model that is a state-of-art mesoscale model developed by the National Center for Atmospheric Research (NCAR). WRF is a fully compressible non-hydrostatic model, with a terrain-following vertical coordinate and with horizontal and vertical grid staggering of Arakawa C-grid type. We use four one-way nested domains of 9-km, 3-km, 1-km and 0.5-km horizontal resolutions ($\Delta x = \Delta y$) and 200 x 200 grid points in the three first domains (Fig. 7.1a), centered at (42.48°N, 1.867°E), near the Das (DP) station (Fig. 7.1b). The 31 vertical sigma pressure levels are non-uniform from the surface up to 100 hPa top pressure, with the first level around 25 m, increasing every 100 m near the surface and increasing 300 m at 2 km height. The WRF simulations are run from the 12 September 2012 at 0000 UTC to 14 September 2012 at 0000 UTC, leting the first 24 hour as a spin-up time. The initialization of the simulations is done with the ERA-Interim reanalysis from the European Centre for Medium-Range Weather Forecasts (ECMWF) interpolated at 0.125 in the horizontal, and 36 levels in the vertical up to 1 hPa. The basic simulation (*base*) uses the YSU planetary boundary layer (PBL) scheme, a non-local scheme which performs good during daytime in unstable conditions (Shin and Hong 2011; Udina et al. 2013). The surface layer for the YSU scheme uses the Monin-Obukhov similarity theory (Zhang and Anthes 1982). Other physic parameterizations used in this study include the rapid radiative transfer model (RRTM) scheme for long-wave radiation (Mlawer et al. 1997), the Dudhia scheme for short-wave radiation (Dudhia 1989), the new Thompson microphysics scheme (Thompson et al. 2004), the Noah land surface scheme Chen and Dudhia (2001) and the Kain-Fritsch for cumulus (Kain 2004), this last one only activated for the 9 and 3 km grid domains.

A set of simulations (Table 7.2) is performed to study the sensitivity of the variables and the mountain waves features to physic options and model configuration. We have studied the resolution effects by evaluating the model outputs obtained from the horizontal grids of the D2 (*baseD*2) and D3 (*base*) domains of 3 and 1 km respectively, and increasing the vertical resolution from 31 to 45 levels ($z45$). Different boundary layer physics are explored using the MYJ Janjic (1990, 1996); Janjić (2002) (MYJ) that is a local scheme and MYNN schemes Nakanishi and Niino (2006) ($MYNN$), which is a non-local scheme as YSU. Additional tests are done using the surface scheme for complex topography from Jiménez and Dudhia (2012) that corrects the positive wind bias near the plains and valleys and the negative wind speed biases in the mountains and hills (*twind*). On the other hand, the 3km grid resolved terrain is introduced in the 1 km simulation to see the influence of the unresolved topography ($topo3km$).

Table 7.2: Overview and acronyms of the model simulation configurations.

Simulation	Horizontal grid	Vertical levels	PBL	Topography
base	1 km	31	YSU	1 km
baseD2	3 km	31	YSU	3 km
z45	1 km	45	YSU	1 km
MYJ	1 km	31	MYJ	1 km
MYNN	1 km	31	MYNN	1 km
*twind**	1 km	31	YSU	1 km
topo3km	1 km	31	YSU	3 km

*Using *topowind* = 1 option from WRF (Jiménez et al. 2012)

7.4 Case study description and model validation

In this study the case study of the 13 September 2012 is chosen as a representative day of trapped lee wave formation that summarizes the main characteristics of the phenomena and the model performance. The synoptic situation was determined by the Azores high (1025 hPa) over the Atlantic Ocean and a shallow low pressure system over Italy and Baltic Sea. Both lead to a northerly flow over the Pyrenees.

The visible satellite image from MODIS valid for 13 September 2012 at 1130 UTC indicates a broad region of clouds upstream of the Pyrenees and bands of consecutive *Ac* lenticular clouds downstream of them (Fig. 7.3a), over the Catalan area, probably formed at the wave crests after the air parcels displacement from their equilibrium level. These type of clouds reveal a stable layer in the atmosphere where waves are trapped and can travel a long distance from the mountain range, i.e. trapped lee waves. They can also be distinguished in the METEOSAT satellite infrared Brightness Temperature (BT) image from channel 9 at 1100 UTC (Fig. 7.3b), although the 3 km grid resolution is not enough to observe the details as in the MODIS product.

In the following subsections we explore measurements from atmospheric soundings, wind profiler and the surface stations, comparing them with the corresponding WRF model outputs.

7.4.1 Atmospheric soundings

Figure 7.4 shows vertical profiles obtained from the atmospheric soundings launched the 13 September 2012 at 1200 UTC (solid line), and the WRF *base* simulation results (dashed line) at the same time. Two different locations are presented, downwind of the Pyrenees (Barcelona) (Fig. 7.4-top), and upwind of them (Nimes) (Fig. 7.4-bottom) which slightly

shifted eastward from the area of interest (see location in Fig.7.1a). Air and potential temperature vertical profiles reveal a two-layer structure divided by an inversion layer around 2 km (Fig. 7.4a,b and Fig. 7.4g,h) where high values of Brunt Väisälä frequency (N^2) are seen as well (Fig. 7.4f). The layer between the surface and 2 km is neutrally stratified corresponding to the boundary layer developed during daytime and the layer above 2 km is stably stratified at the upwind site (Fig. 7.4g). In general, the simulation results adjust quite well with the atmospheric soundings. The model simulation tends to smooth the temperature inversion although the two layer structure can be distinguished. A drying near the 2 km discontinuity is present in both sites (Fig. 7.4d) and 7.4j), but a moist layer is maintained aloft in the downwind site, which may be favorable for the lenticular cloud formation. The wind direction is maintained from the north above 1000 m for both locations (not shown), so perpendicular to the mountain range. The wind speed increases with height in both locations until the 2 km layer (Fig. 7.4c,i), but decreases above in Nimes (Fig. 7.4i). Other upwind locations near the Pyrenees (Bordeaux sounding) show a stronger shear with wind speeds increasing with height (from 15 m s^{-1} at 2 km height to around 30 m s^{-1} at 4 km), which reveals favorable conditions for trapped lee wave formation (Ray 1986). The simplified Scorer parameter at the upwind site, defined as $l^2 = N^2/U^2$ where U is the wind speed, slightly decreases with height above 4 km (Fig. 7.4k), which is also consistent with the possibility of trapped lee wave formation (Scorer 1949).

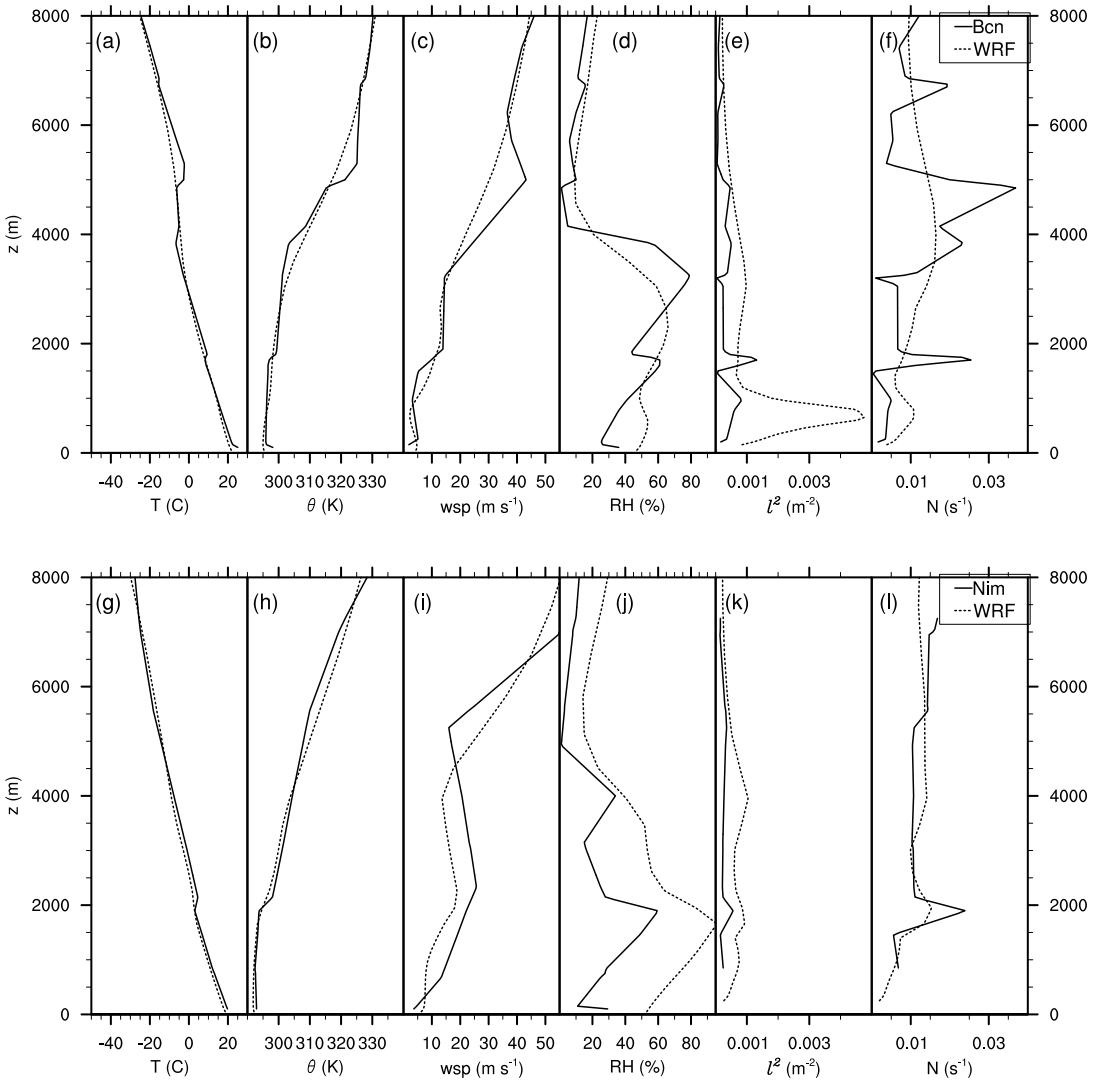

Figure 7.4: Vertical profile comparison between radiosoundings (solid line) and WRF model outputs (dashed line) in Barcelona (Bcn) at the top and Nimes (Nim) at the bottom at 1200 UTC including: (a, g) air temperature (T), (b, h) potential temperature (θ), (c, i) horizontal wind speed (wsp), (d, j) relative humidity (RH), (e, k) the simplified Scorer parameter (l^2) and (f, l) Brunt Väisälä frequency (N).

7.4.2 Upstream wind profiler

In order to evaluate the three wind components model performance we use the observations from the Ultra High Frequency (UHF) wind profiler radar located in Perpignan (42.73°N, 2.87°E) (see location in Fig. 7.1b), that are available from the HYdrological cicle in Mediterranean EXperiment (HYMEX) for the studied period. Although Perpignan is displaced east from the Pyrenees, it gives us an idea of the wind speed profile and evolution in the upstream part of the flow. The vertical wind component and the horizontal wind speed profiles up to 5 km are compared with the simulation through time-height plots from 0000 UTC 13 September 2012 until 2300 UTC 13 September 2012 (Fig. 7.5) which allow us to validate the upstream conditions in the simulation. Fig. 7.5a shows vertical upwdrafts before 0900 UTC until 1200 UTC that are captured by the simulation although not continuously maintained and less strong in intensity (Fig. 7.5b). The visible MODIS image at 1130 UTC shows lenticular clouds upwind the Pyrenees (Fig. 7.3), probably generated by a long distance mountain range such as The Alps. At that time, the UHF reveals positive vertical velocities of $\approx$ 2 m s^{-1}, enough for the vertical displacement of the parcels and the cloud formation at the wave crests. Although mountain waves are stationary, a time oscillating behavior is seen in the measured wind profiler vertical velocity in Perpignan during the following hours. Regarding the horizontal wind, a strong wind current is established around 1100 UTC at heights between 1 and 3 km (Fig. 7.5c), when the lenticular clouds are also seen in the satellite images. The changes in horizontal wind speed are generally well reproduced by the model but the magnitude is overall underestimated, around 3 or 4 m s^{-1} (Fig. 7.5d).

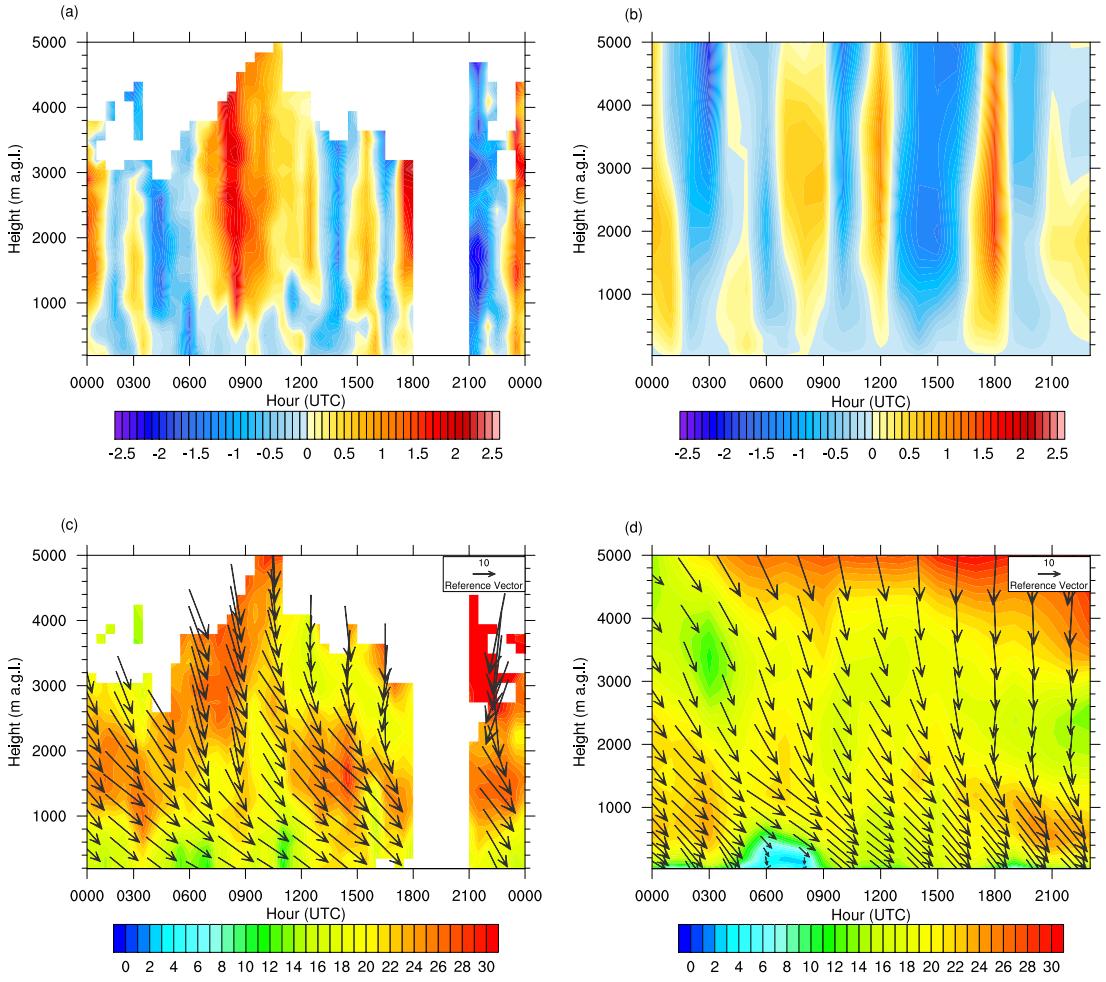

Figure 7.5: Time-height plots comparison between the UHF wind profiler in Perpignan (left) and the WRF model outputs (right) at the same location from 13 September 2012 at 0000 UTC until 13 September 2012 at 2300 UTC corresponding to: (i) vertical wind component of the UHF (a) and the WRF model (b); (ii) horizontal wind component (shaded) and horizontal wind vector (vector) of the UHF (c) and the WRF model (d). The white space indicates regions where there is missing or erroneous data from the UHF wind profiler.

7.4.3 Surface stations

The simulated 24 hour outputs of 2 m temperature and 10 m wind speed are validated with surface stations measurements for the different model configurations (Table 7.2) and summarized with statistics (Table 7.3). The upwind surface stations data are obtained from the Synop measurements and are compared with the D2 (3-km grid) domain model outputs, as D3 does not include enough upwind area (see Fig. 7.1). The downwind surface stations are taken from the Catalan Meteorological Service and compared with the 1 km domain. As shown in table 7.3, all model options have a negative bias in temperature, with the better metrics of correlation and bias for the $z45$ case, upwind the Pyrenees. At the downwind side, the best correlation is for the *base* case that uses the YSU scheme for the PBL and the smallest bias is obtained with the $z45$ configuration. The 10 m wind speed is generally overestimated by the model at the downwind side, as a positive bias is obtained in all model setups. In contrast, it is generally underestimated at the upwind side of the Pyrenees for all the experiments using 3-km model outputs, comparing with the surface stations data obtained from the Synop measurements. The standard deviation of the WRF is larger than the one from the observed wind speed at the downwind side, meaning that the model tends to exaggerate the wind variability (not shown). The smallest errors in wind speed are obtained by the *twind* simulation 1 km domain, which reduces the positive bias significantly. Thus, applying the surface parameterization proposed by Jiménez et al. (2012) leads to a better representation of the horizontal wind speed near the surface in this complex terrain area.

Table 7.3: Statistics for observed and simulated 2 m surface temperature (left column) and 10 m wind speed (right column) for the 24-hour period from 0000 to 2300 UTC, 13 September 2012. The calculated statistics correspond to the correlation coeficient (CC) and mean bias (MB) between the upwind surface stations from the Synop database and the 3 km simulation experiments (top) and the downwind surface stations from the Catalan Meteorological Service (meteo.cat) and the 1 km simulation experiments (bottom). The highlighted values in bold are the best statistic value for each variable and section.

Upwind 3 km-grid domain				
	2 m temperature		10 m wind speed	
Simulation	CC	MB	CC	MB
base	0.695	-1.448	0.516	-0.806
$z45$	**0.698**	**-1.426**	0.522	-0.755
MYJ	0.683	-1.634	**0.568**	**-0.297**
$MYNN$	0.675	-1.952	0.505	-0.869
twind	0.694	-1.582	0.460	-1.667
*topo*3*km*	0.695	-1.448	0.516	-0.807
Downwind 1 km-grid domain				
	2 m temperature		10 m wind speed	
Simulation	CC	MB	CC	MB
base	**0.943**	-0.853	0.434	2.052
*baseD*2	0.931	-1.018	0.364	2.063
$z45$	0.940	**-0.791**	0.399	2.423
MYJ	0.941	-0.956	0.433	2.847
$MYNN$	0.930	-1.216	0.405	2.061
twind	0.935	-1.188	**0.460**	**0.808**
*topo*3*km*	0.927	-1.041	0.364	2.260

7.5 Simulation of mountain waves

7.5.1 Mountain wave characteristics

The relative humidity and vertical wind horizontal plane views (Fig. 7.6) from the WRF model manifest a high-amplitude wave train formation over northern Catalonia, after crossing the Pyrenees mountain range, at 1200 UTC. Vertical velocities exceed 6 m s^{-1} at around 4 km above sea level (a.s.l.) (Fig. 7.6b) with ascent-descent couplets after crossing the first crestline and farther downstream where a second crestline is also present. According to the model, the mountain waves remain stationary during a few hours and are extended even farther downstream, with the maximum intensity between 1000 UTC

and 1600 UTC.

Vertical cross section through the middle of the domain following the solid line in Fig 7.6b, reveal the vertical extension of the wave field, strongly developed from 2 to 6 km height and smoothed above (Fig. 7.7). The horizontal wind is perturbed after crossing the crestline with an opposite phase with the potential temperature (Fig. 7.7a-top), which follows the linear theory (Gossard and Hooke 1975) and the buoyancy generated gravity waves structure, similar to Sun et al. (2015b) but above the PBL. Flow deceleration is seen underneath the wave crest down to the ground, in the valley area (more in Sect. 7.5.3). Since the wind speed increases with the height (Scorer 1949), the Scorer parameter decreases with height, thus, the vertical structure of the atmosphere is favorable for a trapped lee wave train formation. In addition, the amplitude of the waves is evanescent with height above 6 km. In the horizontal, the lee waves are extended downstream and attenuated by the boundary layer (Jiang et al. 2006) or dissipated further downstream. The isolines of water vapor mixing ratio are in phase with the isentropes (not shown), so clouds are likely to be formed in the end of each updraft.

The wavelet function applied to the model output spatial transects allow us to investigate the wavelength and the spatial location of the generated waves. The Morlet function is used as a mother wavelet. Wavelet plots show the power spectrum of the magnitude in color, the latitude in the x-axis and the number of grid points ($ngrid$) in the y-axis. The corresponding wavelength (λ) is calculated as the product of the number of grid points and the horizontal grid size ($\lambda = ngrid * \Delta x$), thus, $\lambda = ngrid$ in the 1-km grid simulations. The power spectrum is calculated in each vertical level, then averaged between levels from 3 km to 6 km, in the region where the waves are fully developed.

The power spectrum from both, the potential temperature (Fig. 7.7-bottom) and the vertical velocity (Fig. 7.9a-bottom) transects shows a strong signal around $\lambda = 12$ km in a broad region leeward of the mountain, after crossing the second crestline. In theory, the simulated wavelength from potential temperature fields can be compared with the observed wavelength derived from the lenticular clouds from the satellite images, because a cloud is likely to be formed at each wave crest. The separation distance between clouds is also calculated using the wavelet power spectrum (Fig. 7.8) obtained from the wavelet function applied to the BT field from the METEOSAT satellite along a fixed longitude (red line in Fig.7.3b). As the METEOSAT satellite has a 3 km grid resolution, the observed signal given by the power spectrum is between $ngrid = 6 - 7$ (around 42°N) which corresponds to a wavelength $\lambda = 18 - 21$ km (see white mark in Fig. 7.8). Looking at the MODIS image (Fig. 7.3) we can approximate a similar distance interval between the lenticular clouds. Therefore, the calculated wavelength of $\lambda = 18 - 21$ km obtained from the satellite imagery is larger than the $\lambda = 12$ km found in the model. Our first hypothesis is that these differences between the wavelength derived from the satellite images and the wavelength obtained from the simulation can be due to the imposed upstream conditions. As we have seen from measurements in Sect. 7.4 the model is generally underestimating the horizontal

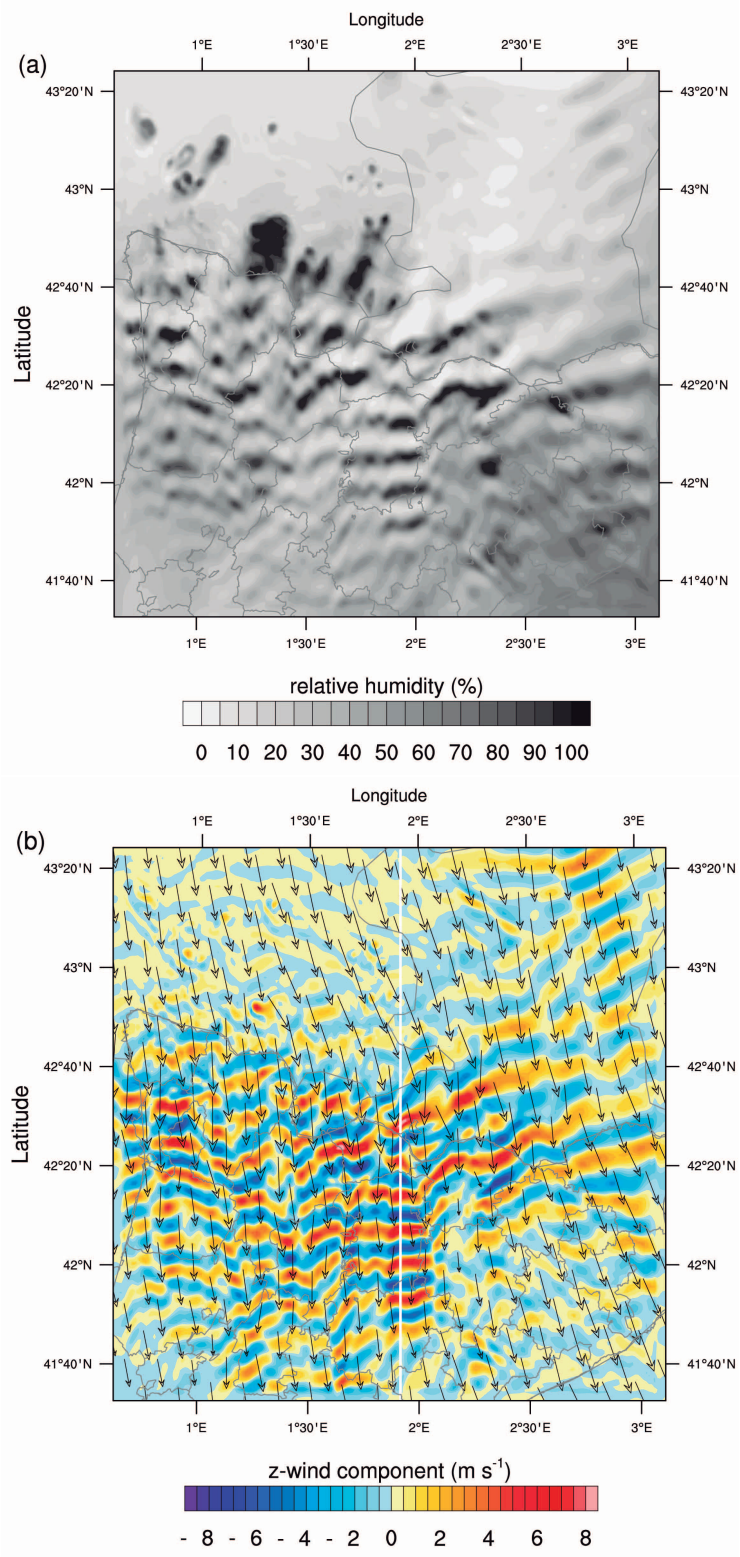

Figure 7.6: Horizontal plane views of the *base* simulations of: (a) relative humidity and (b) vertical wind component (shaded) and horizontal wind vector (vector), at 3500 m above sea level at 1200 UTC 13 September 2012. The white line in (b) corresponds to the cross section location in Fig. 7.7.

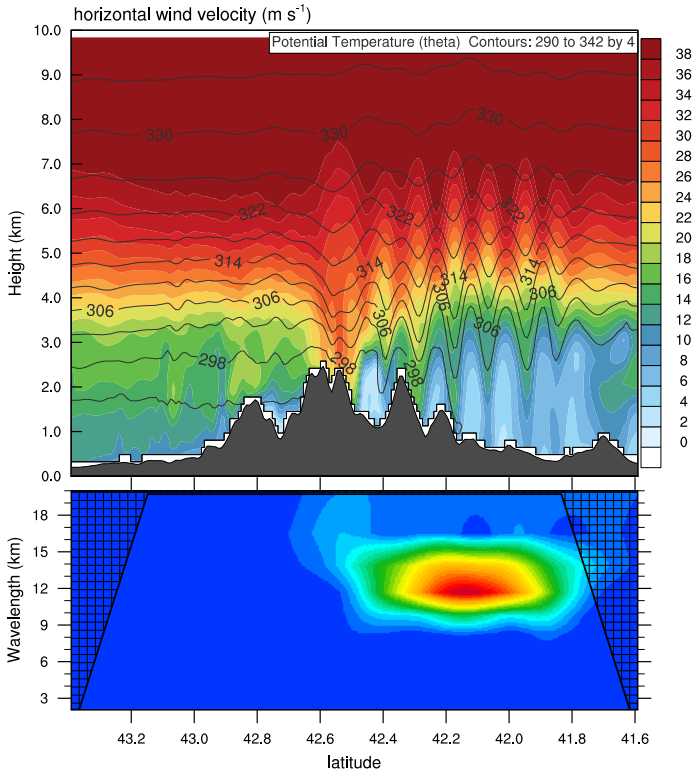

Figure 7.7: Cross sections for the *base* simulation of horizontal wind speed (shaded) and potential temperature (contour lines)at 1200 UTC 13 September 2012. The cross section corresponds to the black line drawn in Figure 7.6). In the bottom there are the averaged power spectrum between z=3 km and z=6 km of the horizontal wind speed.

wind speed, according to the wind profiler and the surface stations located at the northern side of the Pyrenees. Following the lee-wave linear theory, increasing the wind speed leads to a longer wavelength, thus, the underestimation of the wind speed intensity upstream the mountain range can be the reason for the model underestimation of the wave wavelength. On the other hand, we also hypothesize that the lenticular clouds may not be present in all the wave crests and so the estimated wavelength from the lenticular clouds is larger than the one of the wave itself. As we have no other measurements than satellite images to verify the characteristics of the mountain waves, we cannot verify this hypothesis.

In order to explore influence of the model configuration parameters in the resolved wave field and wave characteristics, the next subsection shows the results of the mountain wave patterns using different model options.

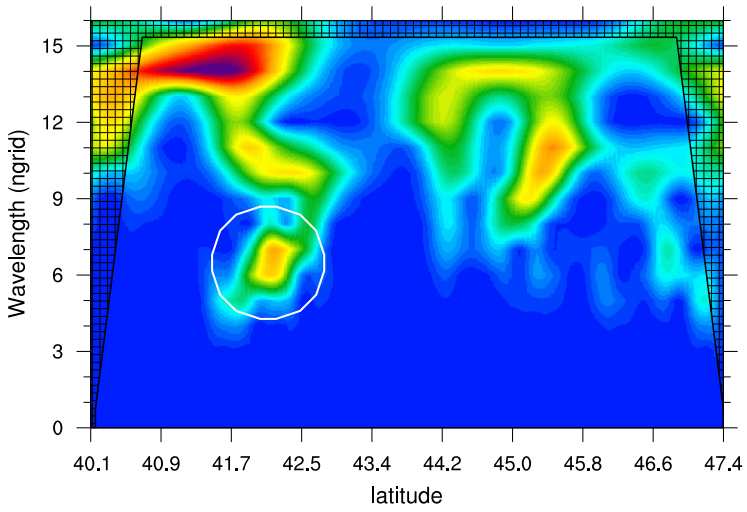

Figure 7.8: Wavelet power spectrum of the METEOSAT Brightness Temperature (BT) from infrared channel 9 image at 1100 UTC along a north-south transect at the fixed longitude 2.2°E corresponding to red line in Fig. 7.3b. The white circle indicates the region over the Pyrenees.

7.5.2 Sensitivity to model options

Using the set of simulations detailed in section 7.2, we explore the sensitivity of the waves characteristics in model outputs to different model configuration such as: vertical resolution, PBL schemes, resolved topography and horizontal resolution. The analysis is done with the vertical velocity (w) and potential temperature (θ) fields (Fig. 7.9) through the same cross section as in Fig. 7.7. The PBL height is also represented through the cross section in order to analyze the wave influence to the PBL top shape. In table 7.4 the main parameters of the waves for each experiment are summarized. The wavelength is determined by the wavelet analysis for the vertical velocity transect between 3 and 6 km (included at the bottom of each simulation experiment). The wave amplitude in the vertical dimension is calculated as the maximum value of half altitude difference between the first wave through and crest along the transect for each simulation.

In the all 1-km resolution simulation experiments (Fig. 7.9 a, b, c, d, e) the vertical wind cross section shows ascent-descent couplets and potential temperature isentropes oscillations after crossing the Pyrenees mountain range, forming a wave train extended more than 100 km downstream. Gravity waves are stationary and as we should expect from linear theory, θ is in phase 90° with w.

In the *base* simulation (Fig. 7.9a) the dominating wavelength is $\lambda = 12$ km, coherent with the wavelet analysis from the θ transects in Fig. 7.7. The maximum wave amplitude over the transect is found around 4 km altitude with values around 727 m with vertical

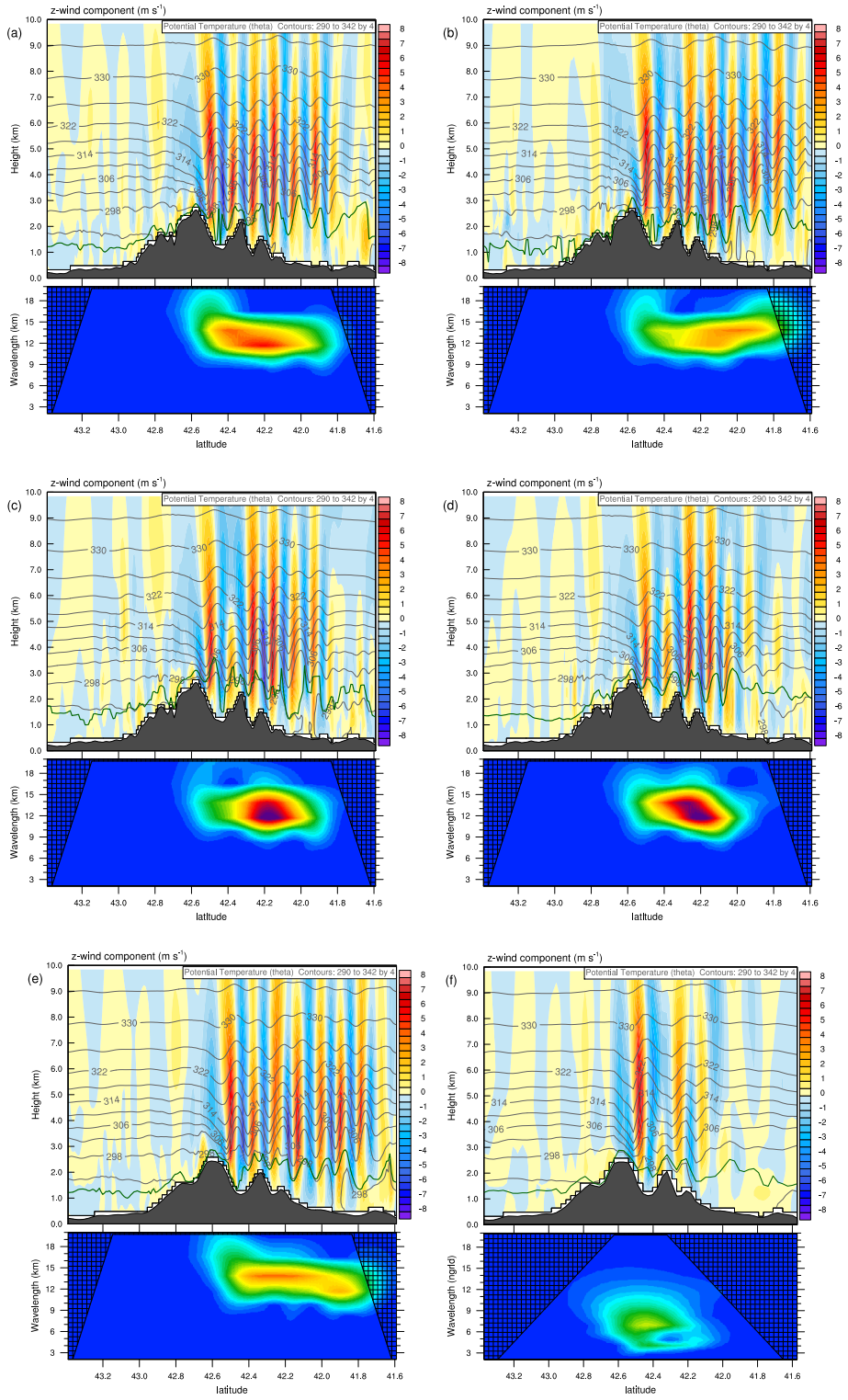

Figure 7.9: Cross sections of the vertical wind component (shaded), potential temperature (contour lines) at 1200 UTC 13 September 2012 following the white line in Fig. 7.6 for: (a) YSU, (b) $z45$, (c) MYJ, (d) $MYNN$, (e) $topo3km$ and (f) $baseD2$ simulations, with its corresponding averaged power spectrum at the bottom part, as in Fig. 7.7.

Table 7.4: Wave parameters among model experiments

Simulation	Wavelength	Amplitude
satellite	18-21 km	-
base	12 km	727 m
baseD2	12-21 km	404 m
z45	14 km	718 m
MYJ	12-13 km	808 m
MYNN	12-13 km	646 m
topo3km	14 km	646 m

velocities around 6 m s^{-1}. These magnitudes are similar than previous observed events in the area, such in Hoinka (1984). The PBL height represented with a green line in Fig. 7.9a follows the wave ascent and descend couplets after crossing the mountain barrier, at a height similar to the crestline. Increasing the vertical resolution from 31 to 45 levels (Fig. 7.9b-top) does not change the wave field significantly, neither the wavelength (Fig. 7.9a-bottom) or the amplitude of the generated waves, compared to the *base* case (Fig. 7.7a-bottom). However, the refinement in the vertical levels seems to make the waves field less dissipative so the wave train is propagated further downstream. Regarding the PBL schemes, replacing the YSU PBL scheme to MYJ (Fig. 7.9b) and MYNN (Fig. 7.9c) do not affect the wavelength or the amplitude of the generated waves, compared to the *base* case (Fig. 7.9a-bottom), with a maximum signal around $\lambda \approx 12$ km again. However, the PBL height is slightly different among the experiments. In MYJ case it is more irregular and does not follow the wave shape as clear as in YSU and $MYNN$ above the downstream plane. The YSU is a non-local scheme that calculates the PBL height in convective situations using the Richardson number criteria, based on the potential temperature gradients and wind speed, then, the PBL top follows the isentropes of the wave train. The MYNN, also a non-local scheme, behaves similar than YSU. Instead, the height of the PBL in the local MYJ scheme is determined as the lower level where the turbulent kinetic energy approximates to a minimum value of the length scale, therefore, less dependent on the potential temperature. Detailed differenced in the small valley between the two crestlines (lat = 42.5°) are described in next Sect. 7.5.3.

Fig. 7.9e corresponds to the replaced topography case ($topo3km$), where the *base* simulation uses the terrain height of the 3 km-resolution (D2), meaning that the terrain elevation is smoothed and less detailed than in the *base* case. We can see that the less well resolved terrain does not significantly affect the generated wave pattern downstream of the mountain range, but it shows a sligthly larger wavelength ($\lambda \approx 14km$). Indeed, the second crestline is smoothed in $topo3km$, and it is not interferring the generated first crestline wave (Stiperski and Grubišic 2011), which can be the reason for the larger λ.

The last shown experiment is the *baseD*2 case corresponding to the coarser resolution 3-km outputs (Fig. 7.9f). In this case, the vertical velocity cross section reveals smoother updraft and downdrafts, less intense in magnitude, smaller in amplitude but also in its extension downstream. An important updraft after the first range is captured. The wavelet signal is seen between 4 and 7 grid so between $\lambda = 12 - 21$ km ($\lambda = ngrid * 3$), thus a larger wavelength than the other experiments (Fig. 7.9f-bottom). Although the updraft after the first crestline is reproduced, no clear mountain waves are reproduced in this case, as the 3-km horizontal resolution may be too coarse to resolve the mountain waves in this case.

7.5.3 Valley circulations and rotor signals

Trapped lee waves can be associated with rotors and turbulent zones usually developed under the wave crests (Doyle and Durran 2002; Vosper 2004; Hertenstein and Kuettner 2005). Here, we investigate the presence of these rotor structure in "La Cerdanya" valley, a 10 km wide valley oriented from south-west to north-east, which base is around 1100 m a.s.l and the surrounding peaks elevate up to 3000 m (Fig. 7.10a). Looking in detail to the first wave crest (Fig. 7.10b), we can see two maximum updrafts with a maximum overpassing vertical velocities of around 8 m s^{-1} located over the northern downslope at "La Cerdanya" valley, after the higher mountain crestline that the northern flow encounters. One is located aligned with the "Carlit" mountain peak, which is one of the highest in the French area, with 2909 m of elevation and the other maximum is aligned with the Puigpedros peak of 2915 m. A similar location of the maximum updraft of the first wave crest is also seen in other simulated mountain wave episodes, so we find it interesting to explore a possible wave-rotor system in this area similar to the on reported from the T-REX experiment in Cohn et al. (2011).

A valley cross section (Fig. 7.11) is plotted to illustrate the circulations over the valley after the strong updraft aligned with the "Carlit" mountain peak, for three different PBL experiments: *base* using YSU, MYJ and $MYNN$. The cross section corresponds to the black line in Fig. 7.10b. As it is a narrow valley, we use the 500 m-grid domain (D4) to capture the topography details and be able to better resolve the flow circulations. From north (left) to south (right) after the downdraft over the slope, a strong updraft occurs before the wave crest followed by a downdraft over the center of the valley for all PBL experiments (Fig. 7.11a,b,c). The maximum vertical wind is located between 3 and 4 km a.s.l. but strong updraft starts near the surface. We can also see that the PBL height (green dots in Fig. 7.11a,b,c) is highly influenced by the wave shape, following the potential temperature isolines with the wave updrafts and downdraft over the valley, mostly for YSU and $MYNN$ experiments. For MYJ the PBL depth is more variable as more dependent on the TKE (as already mentioned in Sect. 7.5.2). The horizontal wind speed is weak and variable over the valley, below the first wave crest while it is very strong above it (Fig. 7.11d,e,f), therefore, a strong shear is seen in the intersection. In all experiments,

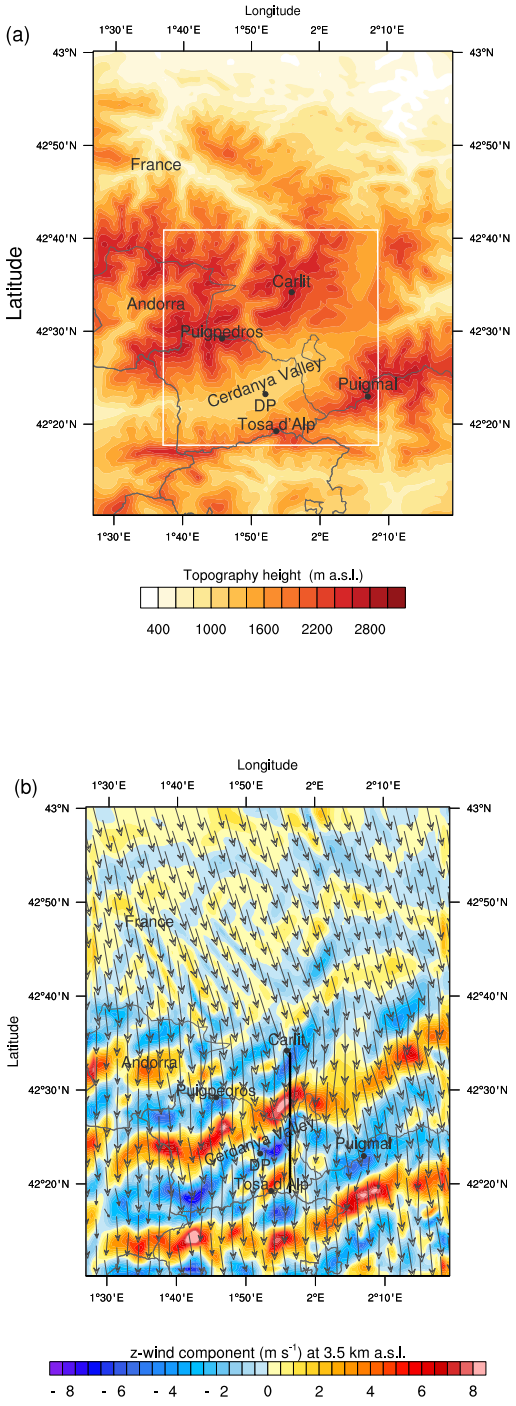

Figure 7.10: Horizontal plane views of domain 500 m-grid domain (D4) corresponding to *base* simulation with: (a) terrain elevation and location of the main mountain peaks and geographic references (Carlit, 2909 m; Puigpedros, 2900 m, Puigmal). DP indicates the surface meteorological station of "Das". The white line indicates the domain plotted in Fig. 7.12; (b) vertical velocity (shaded) and wind vectors (vectors) at 3.5 km a.s.l at 1300 UTC, 13 September 2012. Black line corresponds to the cross sections across La Cerdanya valley plotted in Fig. 7.11.

the y-wind vectors suggests a recirculation zone from the valley surface up to 1 or 1.5 km above. In addition, the x component of the horizontal vorticity ($\eta = \frac{\partial w}{\partial y} - \frac{\partial v}{\partial z}$) has large positive values along the upstream edge of the lee wave (Fig. 7.11g,h,i), similar to the experiments from Doyle and Durran (2007). From the MYJ and $MYNN$ experiments we can see different location of the turbulent kinetic energy (TKE) maximums. In both cases strong turbulence is located at the upstream edge of the first wave, where the maximum vorticity was also seen. In MYJ there is also a maximum TKE at the center of the valley, close to the surface (Fig. 7.11h), while in $MYNN$ the TKE maximums occur below the two small crests at elevated heights (Fig. 7.11i).

In all cross sections the wind vectors near the plain, below the wave crest suggest a recirculating wind zone. Despite the signals of wind reversal are found near the surface, the wind is weak and variable in these valley areas within the first hundreds of meters above ground (Fig. 7.12a). Thus, there are some signals but no clear wave-rotor system (Cohn et al. 2011) can be distinguished in our 3D real simulation experiments because wind is flowing from other directions near the surface rather than the dominating north-south. Thus, it is possible that three-dimensional wind may break the ideal 2D rotor structure, which on one hand, would reduce the generated turbulence, but on the other hand can generate turbulent zones which can be significant as well. In any case, the small subrotors along the ascending branch of the mountain lee wave seen by Doyle et al. (2009) and Cohn et al. (2011) are not reproduced in our model simulations, probably because a finer horizontal and vertical resolution is needed. On the other hand, different PBL scheme parameterizations lead to similar patterns near the surface in terms of wind and temperature structure, however, parameterized turbulent kinetic energy is differently distributed.

From this case study and after analyzing several northern wind events we can hypothesize the detailed circulations over The "Cerdanya Valley" when it is influenced by northern flows and mountain waves. The strongest wave updrafts occur at the lee side of the highest mountain peaks of "Carlit" and "Puigpedros". Aligned with them, over the valley area winds are weak and variable, which indicate possible areas where rotors may be formed (Fig. 7.12b). In any case, to proof this conceptual model about the valley circulations, measurements of vertical profiles of the main magnitudes would be needed around the area.

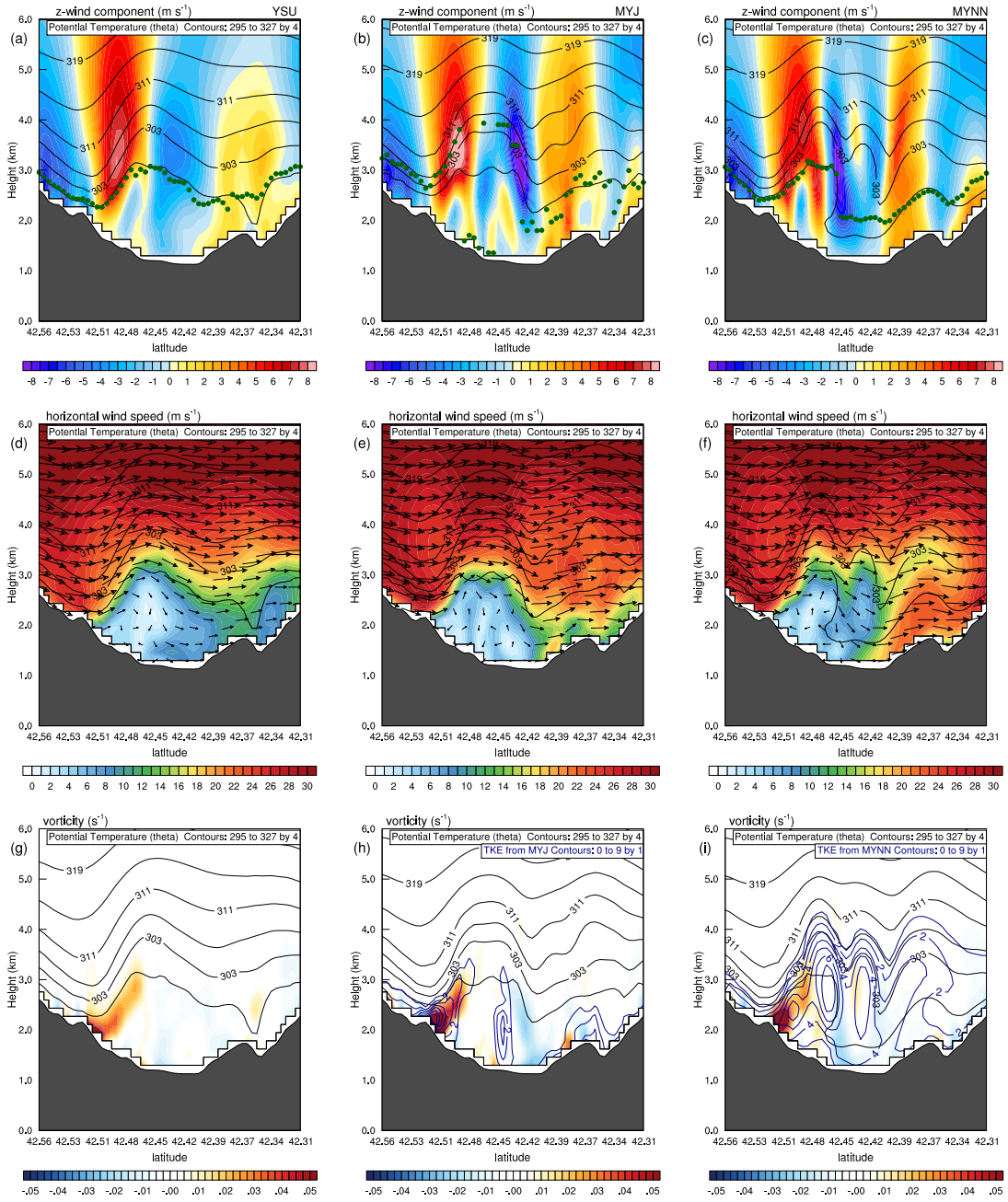

Figure 7.11: Valley cross section (see line in Fig. 7.10) at 1300 UTC, 13 September 2012 for (a,d, g) *base* case, (b, e, h) MYJ and (c, f, i) $MYNN$ configurations of: (a,b,c) vertical wind component (dashed), potential temperature (contour lines) and PBL height (green dots); (d,e,f) horizontal wind speed (shaded), potential temperature (contour lines) and y-wind component (vector) (g,h,i) x-component of horizontal vorticity (shaded) and potential temperature (contour lines). For (h) MYJ and (i) $MYNN$ experiments the TKE prognostic variable is also plotted.

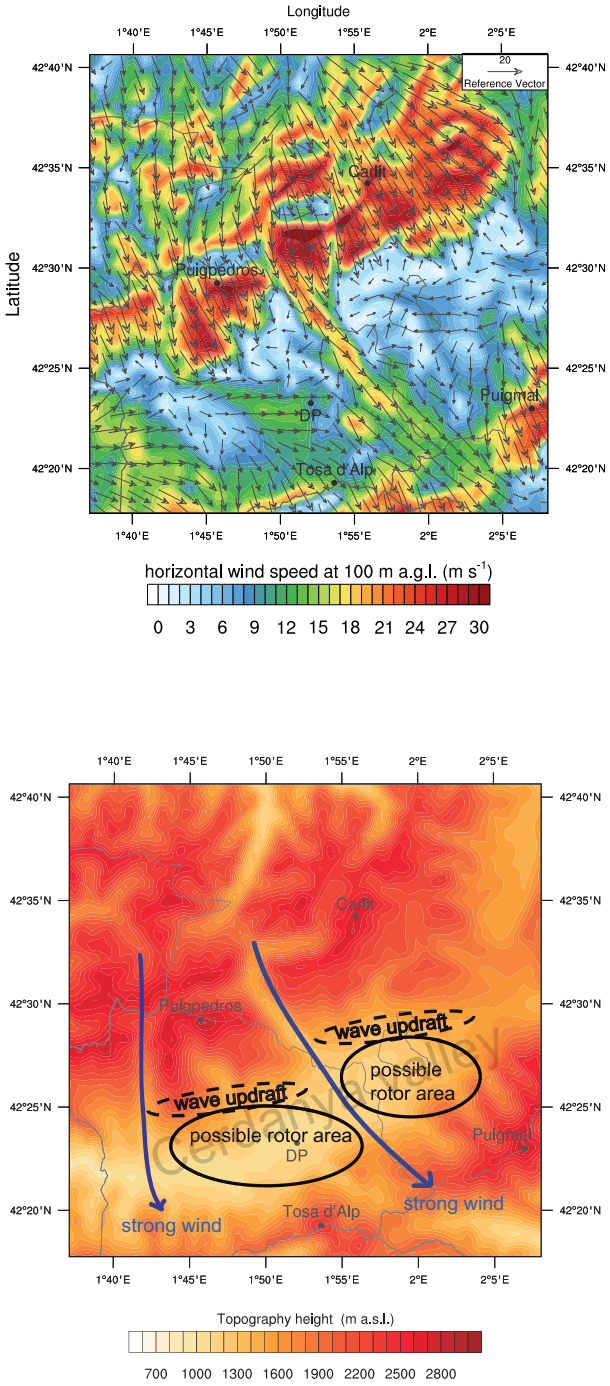

Figure 7.12: Valley circulations near the surface: (a) horizontal wind speed at 100 m above ground level (a.g.l.); b) detailed valley topography and conceptual model of valley circulations with the possible areas of rotor formation.

7.6 Conclusions

In this chapter we have documented a trapped lee mountain wave event over the Pyrenees through mesoscale simulations with the WRF model. Model results show trapped lee waves illustrated by wind, potential temperature and humidity fields after crossing the mountain range extended farther downstream. The mountain wave vertical extension reaches from the mountain top (around 3 km) up to the middle and upper troposphere, although the amplitude of the waves is strong up to 6 km and smoothed above.

According to the closest sounding in Barcelona, one out of four days a year in winter have the appropriate conditions for trapped wave formation south of the Pyrenees and winter is the most favorable season. However, lenticular clouds are not always present, as they develop only when there is enough humidity in the atmopshere. The specific event occurred on the 13 September 2012 is described in detail although other selected episodes were also simulated and analyzed. In this case, the satellite images from MODIS and the METEOSAT brightness temperature field revealed lenticular cloud formation over the southern part of the Pyrenees.

The predictability of the WRF model in reproducing a trapped lee wave event has been analyzed with a series of simulations varying the basic configuration and the physic options. From the different model experiments for the case study we can conclude that the horizontal grid resolution is more determining than the resolved topography or the vertical grid resolution for the mountain wave generation at the studied scales. Three PBL parameterizations (YSU, MYJ and MYNN) have been tested and results show little differences in the generated wave train characteristics but some in the PBL height top shape and in the circulations over the valley, specially for location of turbulent zones.

A 24-hour model experiment verification is also included. The surface stations validation revealed that 2 m temperature is well correlated but underestimated at the upwind and downwind side of the Pyrenees. The best model configurations for the temperature forecast are the *base* and the $z45$ cases for the 1-km horizontal grid spacing, both with the YSU PBL parameterization. The 10 m wind speed model verification reveals an underestimation at the upwind side using the surface stations, confirmed also by the UHF wind profiler data, and an overestimation at the downwind side. A poor wind correlation is found among all model experiments although the bias is improved in the 1-km horizontal grid *twind* simulation.

The obtained mountain waves with 3D real simulations have a shorter wavelength than the one derived from the satellite images. We hypothesize that the reason for the different wavelength could be the underestimation of the wind speed profiles upstream of the mountain range, as the model comparison of UHF wind profiler and the 10-m wind speed surface stations of the Pyrenees revealed an underestimation of the horizontal wind speed at the upwind site. On the other hand, we also suggest that the lenticular clouds may not be formed in all wave crests, which would also explain the wavelength discrepancy, although we do not have enough measurements to proof this statement.

The presence of a rotor has also been investigated over "La Cerdanya" valley, where the first wave updraft is usually located above a region of weak and variable wind near the surface where turbulence may be generated. Results suggest that flows over the plain are influenced by the presence of the updraft aloft, but no clear rotor structure is captured using 500 m grid resolution. Hence, further investigation is still needed to understand the turbulent zones within the rotors associated with mountain waves and its interaction with the boundary layer. For this purpose, besides vertical atmospheric measurements, increasing the horizontal and vertical resolution in numerical modeling seems to be necessary. Large-eddy simulation modeling can be adequate for this future research.

7.7 Future work

This study represents a first step work for a further investigation of the phenomena associated with lee mountain waves, such as: downslope windstorms, lee wave rotor formation and boundary layer separation. We have firstly explored the model capability of capturing topographically generated gravity waves and the different issues that arise from the model configuration. The rotor investigation at 1 km and 500 m shows that we need finer resolution to capture the small structures, and possibly the use of LES. From the analyzed event, we can also conclude that a further validation of the model vertical profiles of the main magnitudes is needed over the complex terrain area. In that sense, a future project will be developed over "La Cerdanya valley" which will combine measurements and modeling tools to understand the mountain wave effects near the surface.

8 Conclusions

A modeling study of different ABL processes has been done, dealing with mesoscale circulations, gravity waves and exploring the turbulence structure, in the SBL and over complex terrain. As a general conclusion, we have seen that mesoscale models are a useful tool to understand the physical processes that occur in atmospheric flows, their origin and their three dimensional structure, which helps to interpret time-series observations obtained in a single point. In addition, atmospheric models allow to investigate phenomena which are very difficult to analyze through measurements, such as mountain waves, which can trigger momentum and energy transport or can be a source of turbulence if they break. On the other hand, we have also used the modeling tools in the LES mode to resolve the turbulence and explore its structure. We have seen that LES is strongly affected by its upper and lower boundary conditions, and this statement has to be taken into account when simulating microscale flow properties.

Using mesoscale modeling, we have found that the origin of the observed gravity waves over the CIBA site was an organized mesoscale circulation, a cold air density current whose origin was a long distance sea-breeze in combination with katabatic flows formed in the surrounding mountain ranges, which accelerated the air mass. The arrival of the density current over the CIBA site produced the air parcels displacement which oscillate within the density current and generate internal gravity waves. We have shown that two PBL schemes in the WRF model produce different evolution of the density current and differences in oscillation structure as well. In particular, the local, 1.5 order scheme seems to perform the generation of IGWs better than the non-local, first order scheme for this type of stable stratified flows, although they are accelerated in exaggeration. However,

the IGWs generated by the model are slightly different from the observed, and the model seems to damp the oscillations at levels where they are observed. We have also showed the periodicity of such density current entrance during 8 consecutive days, at a similar time of day and with similar characteristics.

On the other hand, using the WRF model in the large eddy simulation mode we have explored the vertical variation of turbulence in neutral and stable conditions. Firstly, a reference case modeled with WRF-LES showed a good match with other LES models for the GABLS case in the stable boundary layer. Moreover, we designed a group of simulations with different wind speeds in neutral and stable conditions to analyze the turbulence intensity and its vertical variation. The simulations captured the near neutral regime but are not able to reproduce the very stable regime (weak turbulence) because the surface boundary condition (using MOST) maintains excessive cooling near the ground driven by a fast heat transfer by turbulent mixing instead of the slow molecular diffusion. Indeed, MOST assumes the skin temperature as the air temperature which a very different simulated stable boundary layer than the observed from CASES-99, as the positive temperature gradients are maintained near the surface even under strong winds because of the unrealistic thermal coupling. In addition, using all the simulation data, we can illustrate how turbulence intensity increases sharply with the wind speed at each height above ground but, unlike in observations from CASES99, the rate of increase (slope) is not maintained. The decrease in the size of the dominant turbulent eddies with increasing stratification (in the captured strong turbulent case) is attributed to the upper boundary condition influence, which also leads to the vertical variation of the turbulence relationships. We summarize that LES simulated flows are strongly influenced by the upper and lower boundary conditions. We also conclude that the surface layer parameterization needs to adequately represent the different heat transfer mechanisms for a realistic stable boundary layer representation.

In the last chapter of the thesis we have dealt with mountain waves over the Pyrenees. Despite them being a frequent phenomena in winter, very few research has been done studying the model ability to reproduce it and their influence within the boundary layer circulations or turbulence generation. Mesoscale simulations have shown to reproduce the main trapped lee wave pattern with periodic oscillations in all magnitudes, such as potential temperature, horizontal and vertical wind speed and vertical velocity. To study the WRF model performance in such event, we have explored different model configurations. Vertical resolution and different physical parameterization of the PBL, show small changes in the spatial and temporal wave train characteristics. The horizontal resolution, instead, seems to be more determinant, as 3-km horizontal grid is not enough to resolve the wave propagation. On the other hand, 1-km horizontal resolution outputs reproduce a wave field with shorter wavelengths than those derived from the satellite images. A possible reason is the underestimation of the horizontal wind speed of the incident flow in

the model, which may lead to underestimation of the wavelength. Regarding the effects of the mountain waves near the surface, simulations capture large bulence activity under the first mountain wave crest within the "La Cerdanya" valley although a detailed rotor structure cannot be captured with mesoscale simulations. We conclude that future work could be addressed to couple LES simulations in order to resolve the rotor and subrotor structures below the mountain waves.

9

Future work and future perspectives

This thesis gathers the main achievements of 5 years of research activity. To me, it is just a starting point to go on to different work streams of research. The acquired theoretical knowledge and the comprehension of the usage of modeling tools, specially with the WRF model, is essential for dealing with future perspectives.

A first work stream will be oriented to further use of modeling tools in complex terrain areas. More specifically it will be focused on the Catalan Pyrenees and in the "La Cerdanya" valley, a 20 km wide valley which is a very singular area strongly influenced by the mountain waves and rotor formation in the boundary layer in the presence of northern flows and also where cold pools and strongly stratified conditions are developed. In fact, the study presented in chapter 7 was done as a preliminary study to further study the mountain wave influence within the boundary layer and the phenomena which may be associated with it such as: strong wind gusts, downslope windstorms, lee wave rotor formation and boundary layer separation. More specifically, a future goal will be to address the rotor and sub-rotor structures associated with lee mountain waves which would lead to turbulence generation. For this purpose we will use observational data and simulations. Specific details of future work plan in the complex terrain area are given in the following points:

1. **Data analysis in complex terrain area: disrupted and non-disrupted conditions**

   Firstly, we will analyze observational data from the instruments deployed in "La Cerdanya" valley such as: a surface station, a Surface Energy Budget station and a boundary-layer temperature and wind profiler (WindRASS Scintec). The deploy-

ment of an ultra-high frequency (UHF) radar might be also possible, from where we will obtain wind velocity profiles up to 5-6 km. From these measurements we will be able to detect mountain wave events and associated phenomena, such as rotor circulations, boundary layer separation and turbulent zones (strongly perturbed conditions). On the other hand, we will also analyze the vertical structure of the boundary layer in non-perturbed conditions to further investigate the HOckey-Stick Transition (HOST) between the two turbulence regimes in complex terrain area. Our aim is also to explore the vertical extension of the HOST turbulent regime pattern and how the different scale interactions can be understood in it.

2. **Mesoscale simulations to analyze flow structure and scale interaction**

   In order to understand the physical processes, circulations and interactions which lead to the rotor formation and turbulence generation, real mesoscale simulations with the WRF model will be run. In this case, horizontal resolution will be increased to hundreds of meters, in order to adequately resolve the topography elevation and the vertical profiles of temperature, humidity, wind speed and wind direction. Special treatment for steep terrain will be necessary, either with smoothing functions or with a different coordinate system (Immersed Boundary Method) where vertical levels do not follow the terrain shape anymore. Mesoscale simulations will be validated with observations available, focussing on turbulent events and vertical turbulent structure in the boundary layer.

3. **LES simulations to analyze rotor structure and upstream flow properties**

   Small-scale simulations will be also carried out with the WRF model in the LES mode in order to explore the turbulence structure of the rotors and sub-rotor at the lee side of the mountain, over the valley, related with mountain waves generated aloft. Three-dimensional flow over idealized but near-realistic terrain will be carried out for different wind speed and stability regimes. A variety of upstream conditions will be investigated to explore their consequences on the lee side of the mountain. Horizontal pressure gradient reversal, or boundary layer separation will be also explored. In addition, a long-term goal will be to couple mesoscale with LES simulations through one-way nesting, which would allow to include a wide range of scales present in the atmosphere and, probably, better resolve the turbulent structures developed in the boundary layer.

4. **Improving surface layer parameterization in WRF model**

   From the results obtained in chapter 6, another work line is to improve the surface layer parameterization in the WRF model. Indeed, we have proved that strongly-stratified conditions cannot be represented using traditional MOST, as the flow is strongly coupled with the surface while, in reality, decoupling is more likely to occur. In that sense, the HOST approach (turbulence regimes transition) implementation

in the WRF surface layer may be possible. It would be done through a threshold wind speed function which would delimit the weak turbulent regime with local shear generated turbulence from the strong turbulent regime dominated by bulk shear turbulence generation. Furthermore, there is also a need to investigate baroclinic effects on the HOST turbulence pattern, forcing vertical variation of the horizontal wind speed.

Bibliography

Adachi A, Clark W, Hartten L, Gage K, Kobayashi T (2004) An observational study of a shallow gravity current triggered by katabatic flow. In: Annales Geophysicae, Copernicus GmbH, vol 22, pp 3937–3950

Alapaty K, Pleim JE, Raman S, Niyogi DS, Byun DW (1997) Simulation of atmospheric boundary layer processes using local-and nonlocal-closure schemes. Journal of Applied Meteorology 36(3):214–233

Andren A (1995) The structure of stably stratified atmospheric boundary layers: A large-eddy simulation study. Q J R Meteorol Soc 121(525):961–985

Andren A, Brown AR, Mason PJ, Graf J, Schumann U, Moeng CH, Nieuwstadt FTM (1994) Large-eddy simulation of a neutrally stratified boundary layer: A comparison of four computer codes. Q J R Meteorol Soc 120(520):1457–1484

Arnold D, Morton D, Schicker I, Seibert P, Rotach M, Horvath K, Dudhia J, Satomura T, Müller M, Zängl G, et al. (2012) High Resolution Modelling in Complex Terrain. Report on the HiRCoT 2012 Workshop, Vienna, 21–23 February 2012

Arya PS (2001) Introduction to micrometeorology, vol 79. Academic press

Bastin S, Drobinski P (2005) Temperature and wind velocity oscillations along a gentle slope during sea-breeze events. Boundary-Layer Meteorol 114(3):573–594

Basu S, Porté-Agel F (2006) Large-eddy simulation of stably stratified atmospheric boundary layer turbulence: a scale-dependent dynamic modeling approach. J Atmos Sci 63:2074—-2091

Beare RJ, Macvean MK, Holtslag AA, Cuxart J, Esau I, Golaz JC, Jimenez MA, Khairoutdinov M, Kosovic B, Lewellen D, et al. (2006) An intercomparison of large-eddy simulations of the stable boundary layer. Boundary-Layer Meteorol 118(2):247–272

Beljaars A (1995) The parametrization of surface fluxes in large-scale models under free convection. Q J R Meteorol Soc 121(522):255–270

Blackadar AK (1962) The vertical distribution of wind and turbulent exchange in a neutral atmosphere. Journal of Geophysical Research 67(8):3095–3102

Blumen W, Grossman R, Piper M (1999) Analysis of heat budget, dissipation and frontogenesis in a shallow density current. Boundary-Layer Meteorol 91(2):281–306

Bougeault P, Jansa Clar A, Benech B, Carissimo B, Pelon J, Richard E (1990) Momentum budget over the Pyrénées: The PYREX experiment. Bull Am Meteorol Soc 71:806–818

Bougeault P, Benech B, Bessemoulin P, Carissimo B, Clar AJ, Pelon J, Petitdidier M, Richard E (1997) PYREX: A summary of findings. Bull Am Meteorol Soc 78(4):637–650

Bougeault P, Binder P, Buzzi A, Dirks R, Kuettner J, Houze R, Smith R, Steinacker R, Volkert H (2001) The MAP special observing period. Bull Am Meteorol Soc 82(3):433–462

Bravo M, Mira T, Soler M, Cuxart J (2008) Intercomparison and evaluation of MM5 and Meso-NH mesoscale models in the stable boundary layer. Boundary-Layer Meteorol 128(1):77–101

Brown A, Derbyshire S, Mason P (1994) Large-eddy simulation of stable atmospheric boundary layers with a revised stochastic subgrid model. Q J R Meteorol Soc 120(520):1485–1512

Brown A, Hobson J, Wood N (2001) Large-eddy simulation of neutral turbulent flow over rough sinusoidal ridges. Boundary-Layer Meteorol 98(3):411–441

Chemel C, Staquet C, Largeron Y (2009) Generation of internal gravity waves by a katabatic wind in an idealized alpine valley. Meteorology and Atmospheric Physics 103(1-4):187–194

Chen F, Dudhia J (2001) Coupling an advanced land surface-hydrology model with the Penn State-NCAR MM5 modeling system. Part I: Model implementation and sensitivity. Mon Weather Rev 129(4):569–585

Chiao S (2006) Performance of planetary boundary layer schemes in the WRF model. In: 25th US Army Science Conference, Orlando, Florida, 27-30 November

Chimonas G (1999) Steps, waves and turbulence in the stably stratified planetary boundary layer. Boundary-Layer Meteorol 90(3):397–421

Chimonas G (2002) On internal gravity waves associated with the stable boundary layer. Boundary-Layer Meteorol 102(1):139–155

Chow FK, Street RL (2009) Evaluation of turbulence closure models for large-eddy simulation over complex terrain: flow over Askervein Hill. J Appl Meteorol Clim 48(5):1050–1065

Chow FK, Street RL, Xue M, Ferziger JH (2005) Explicit filtering and reconstruction turbulence modeling for large-eddy simulation of neutral boundary layer flow. J Atmos Sci 62(7):2058–2077

Chow FK, Weigel AP, Street RL, Rotach MW, Xue M (2006) High-resolution large-eddy simulations of flow in a steep Alpine valley. Part I: Methodology, verification, and sensitivity experiments. J Appl Meteorol Clim 45(1):63–86

Clark TL, Hall WD, Kerr RM, Middleton D, Radke L, Ralph FM, Neiman PJ, Levinson D (2000) Origins of aircraft-damaging clear-air turbulence during the 9 December 1992 Colorado downslope windstorm: Numerical simulations and comparison with observations. J Atmos Sci 57(8):1105–1131

Cohn SA, Grubišic V, Brown WO (2011) Wind profiler observations of mountain waves and rotors during T-REX. J Appl Meteorol Clim

Conangla L, Cuxart J (2006) On the turbulence in the upper part of the low-level jet: an experimental and numerical study. Boundary-Layer Meteorol 118(2):379–400

Conangla L, Cuxart J, Soler M (2008) Characterisation of the nocturnal boundary layer at a site in northern Spain. Boundary-Layer Meteorol 128(2):255–276

Cox KW (1986) Analysis of the Pyrenees lee wave event of 23 March 1982. Mon Weather Rev 114(6):1146–1166

Cuxart J (2008) Nocturnal basin low-level jets: an integrated study. Acta Geophysica 56(1):100–113

Cuxart J, Bougeault P, Redelsperger JL (2000) A turbulence scheme allowing for mesoscale and large-eddy simulations. Q J R Meteorol Soc 126(562):1–30

Cuxart J, Morales G, Terradellas E, Yagüe C (2002) Study of coherent structures and estimation of the pressure transport terms for the nocturnal stable boundary layer. Boundary-Layer Meteorol 105(2):305–328

Cuxart J, Jiménez M, Martínez D (2007) Nocturnal meso-beta basin and katabatic flows on a midlatitude island. Mon Weather Rev 135(3):918–932

Darby LS, Poulos GS (2006) The evolution of lee-wave-rotor activity in the lee of Pike's Peak under the influence of a cold frontal passage: Implications for aircraft safety. Mon Weather Rev 134(10):2857–2876

Deardorff JW (1970a) A numerical study of three-dimensional turbulent channel flow at large Reynolds numbers. J Fluid Mech 41(02):453–480

Deardorff JW (1970b) A three-dimensional numerical investigation of the idealized planetary boundary layer. Geophysical and Astrophysical Fluid Dynamics 1(3-4):377–410

Deardorff JW (1972) Numerical investigation of neutral and unstable planetary boundary layers. J Atmos Sci 29(1):91–115

Derbyshire SH (1990) Nieuwstadt's stable boundary layer revisited. Q J R Meteorol Soc 116(491):127–158

Dörnbrack A, Nappo CJ (1997) A note on the application of linear wave theory at a critical level. Boundary-Layer Meteorol 82(3):399–416

Doyle J, Durran D, Chen C, Colle B, Georgelin M, Grubisic V, Hsu W, Huang C, Landau D, Lin Y, et al. (2000) An intercomparison of model-predicted wave breaking for the 11 January 1972 Boulder windstorm. Mon Weather Rev 128(3):901–914

Doyle JD, Durran DR (2002) The dynamics of mountain-wave-induced rotors. J Atmos Sci 59(2):186–201

Doyle JD, Durran DR (2007) Rotor and subrotor dynamics in the lee of three-dimensional terrain. J Atmos Sci 64(12):4202–4221

Doyle JD, Smith RB (2003) Mountain waves over the Hohe Tauern: Influence of upstream diabatic effects. Q J R Meteorol Soc 129(588):799–823

Doyle JD, Shapiro MA, Jiang Q, Bartels DL (2005) Large-amplitude mountain wave breaking over Greenland. J Atmos Sci 62(9):3106–3126

Doyle JD, Grubišic V, Brown WO, De Wekker SF, Dörnbrack A, Jiang Q, Mayor SD, Weissmann M (2009) Observations and numerical simulations of subrotor vortices during T-REX. J Atmos Sci 66(5):1229–1249

Doyle JD, Gaberšek S, Jiang Q, Bernardet L, Brown JM, Dörnbrack A, Filaus E, Grubišic V, Kirshbaum DJ, Knoth O, et al. (2011) An intercomparison of T-REX mountain-wave simulations and implications for mesoscale predictability. Mon Weather Rev 139(9):2811–2831

Dudhia J (1989) Numerical study of convection observed during the winter monsoon experiment using a mesoscale two-dimensional model. J Atmos Sci 46(20):3077–3107

Dudhia J (2011) WRF Physics. WRF User's tutorial

Durran DR (2003) Lee waves and mountain waves. The Encyclopedia of the Atmospheric Sciences

Durran DR, Klemp JB (1983) A compressible model for the simulation of moist mountain waves. Mon Weather Rev 111(12):2341–2361

Dyer A, Hicks B (1970) Flux-gradient relationships in the constant flux layer. Q J R Meteorol Soc 96(410):715–721

Einaudi F, Finnigan J (1993) Wave-turbulence dynamics in the stably stratified boundary layer. J Atmos Sci 50(13)

Epifanio CC, Qian T (2008) Wave-turbulence interactions in a breaking mountain wave. J Atmos Sci 65(10):3139–3158

Feltz W, Bedka K, Otkin J, Greenwald T, Ackerman S (2009) Understanding satellite-observed mountain-wave signatures using high-resolution numerical model data. Weather and Forecasting 24(1):76–86

Ferreres E, Soler M, Terradellas E (2013) Analysis of turbulent exchange and coherent structures in the stable atmospheric boundary layer based on tower observations. Dynamics of Atmospheres and Oceans 64:62–78

Gohm A, Mayr GJ, Fix A, Giez A (2008) On the onset of bora and the formation of rotors and jumps near a mountain gap. Q J R Meteorol Soc 134(630):21–46

Golaz JC, Doyle JD, Wang S (2009) One-Way Nested Large-Eddy Simulation over the Askervein Hill. Journal of Advances in Modeling Earth Systems 1(3)

Gossard EE, Hooke WH (1975) Waves in the atmosphere: Atmospheric infrasound and gravity waves-Their generation and propagation. Atmospheric Science 2

Grell GA, Dévényi D (2002) A generalized approach to parameterizing convection combining ensemble and data assimilation techniques. Geophysical Research Letters 29(14):38–1

Grubišic V, Billings BJ (2007) The intense lee-wave rotor event of Sierra Rotors IOP 8. J Atmos Sci 64(12):4178–4201

Grubišic V, Doyle JD, Kuettner J, Dirks R, Cohn SA, Pan LL, Mobbs S, Smith RB, Whiteman CD, Czyzyk S, et al. (2008) The Terrain-Induced Rotor Experiment: A field campaign overview including observational highlights. Bull Am Meteorol Soc 89(10):1513–1533

Gryning SE, Mahrt L, Larsen S (1985) Oscillating nocturnal slope flow in a coastal valley. Tellus A 37(2):196–203

Hertenstein RF, Kuettner JP (2005) Rotor types associated with steep lee topography: Influence of the wind profile. Tellus A 57(2):117–135

Hoinka KP (1984) Observations of a mountain-wave event over the Pyrenees. Tellus A 36(4)

Holton JR, Hakim GJ (2012) An introduction to dynamic meteorology, vol 88. Academic press

Holtslag A, Beljaars ACM (1988) Surface flux parameterization schemes: Developments and experiences at KNMI. KNMI

Holtslag A, Moeng CH (1991) Eddy diffusivity and countergradient transport in the convective atmospheric boundary layer. J Atmos Sci 48(14):1690–1698

Hong J (2010) Note on turbulence statistics in z-less stratification. Asia-Pacific J Atmos Sci 46(1):113–117

Hong SY, Kim SW (2008) Stable boundary layer mixing in a vertical diffusion scheme. In: 18th Symposium on Boundary Layers and Turbulence B, vol 16

Hong SY, Pan HL (1996) Nonlocal boundary layer vertical diffusion in a medium-range forecast model. Mon Weather Rev 124(10):2322–2339

Hong SY, Noh Y, Dudhia J (2006) A new vertical diffusion package with an explicit treatment of entrainment processes. Mon Weather Rev 134(9):2318–2341

Horvath K, Koracin D, Vellore R, Jiang J, Belu R (2012) Sub-kilometer dynamical downscaling of near-surface winds in complex terrain using WRF and MM5 mesoscale models. Journal of Geophysical Research: Atmospheres (1984–2012) 117(D11)

Hu XM, Nielsen-Gammon JW, Zhang F (2010) Evaluation of three planetary boundary layer schemes in the WRF model. J Appl Meteorol Clim 49(9):1831–1844

Huang J, Bou-Zeid E (2013) Turbulence and vertical fluxes in the stable atmospheric boundary layer. Part I: A large-eddy simulation study. J Atmos Sci 70(6):1513–1527

Janjic Z (1996) The surface layer parameterization in the NCEP Eta Model. WORLD METEOROLOGICAL ORGANIZATION-PUBLICATIONS-WMO TD pp 4–16

Janjic ZI (1990) The step-mountain coordinate: Physical package. Mon Weather Rev 118(7):1429–1443

Janjic ZI (1994) The step-mountain eta coordinate model: Further developments of the convection, viscous sublayer, and turbulence closure schemes. Mon Weather Rev 122(5):927–945

Janjić ZI (2002) Nonsingular implementation of the Mellor–Yamada level 2.5 scheme in the NCEP Meso model. NCEP office note 437:61

Jiang Q, Doyle JD, Smith RB (2006) Interaction between trapped waves and boundary layers. J Atmos Sci 63(2):617–633

Jiang Q, Doyle JD, Wang S, Smith RB (2007) On boundary layer separation in the lee of mesoscale topography. J Atmos Sci 64(2):401–420

Jimenez MA, Cuxart J (2005) Large-eddy simulations of the stable boundary layer using the standard Kolmogorov theory: Range of applicability. Boundary-Layer Meteorol 115(2):241–261

Jiménez PA, Dudhia J (2012) Improving the representation of resolved and unresolved topographic effects on surface wind in the WRF model. J Appl Meteorol Clim 51(2):300–316

Jiménez PA, González-Rouco JF, García-Bustamante E, Navarro J, Montávez JP, de Arellano JVG, Dudhia J, Muñoz-Roldan A (2010) Surface wind regionalization over complex terrain: Evaluation and analysis of a high-resolution WRF simulation. J Appl Meteorol Clim 49(2):268–287

Jiménez PA, Dudhia J, González-Rouco JF, Navarro J, Montávez JP, García-Bustamante E (2012) A revised scheme for the WRF surface layer formulation. Mon Weather Rev 140(3):898–918

Kain JS (2004) The Kain-Fritsch convective parameterization: an update. Journal of Applied Meteorology 43(1):170–181

Kim YJ, Arakawa A (1995) Improvement of orographic gravity wave parameterization using a mesoscale gravity wave model. J Atmos Sci 52(11):1875–1902

Kirkil G, Mirocha J, Bou-Zeid E, Chow FK, Kosovic B (2012) Implementation and Evaluation of Dynamic Subfilter-Scale Stress Models for Large-Eddy Simulation Using WRF. Mon Weather Rev 140(1):266–284

Kirkwood S, Mihalikova M, Rao T, Satheesan K (2010) Turbulence associated with mountain waves over Northern Scandinavia–a case study using the ESRAD VHF radar and the WRF mesoscale model. Atmos Chem Phys 10:3583–3599

Klemp J, Lilly D (1975) The dynamics of wave-induced downslope winds. J Atmos Sci 32:320–339

Kolmogorov AN (1941) Dissipation of energy in locally isotropic turbulence. In: Dokl. Akad. Nauk SSSR, vol 32, pp 16–18

Kosović B (1997) Subgrid-scale modelling for the large-eddy simulation of high-Reynolds-number boundary layers. J Fluid Mech 336(1):151–182

Kosović B, Curry JA (2000) A large eddy simulation study of a quasi-steady, stably stratified atmospheric boundary layer. J Atmos Sci 57(8):1052–1068

Lane TP, Knievel JC (2005) Some effects of model resolution on simulated gravity waves generated by deep, mesoscale convection. J Atmos Sci 62(9):3408–3419

Laprise R (1992) The Euler equations of motion with hydrostatic pressure as an independent variable. Mon Weather Rev 120(1):197–207

Larsén XG, Larsen S, Badger M (2011) A case-study of mesoscale spectra of wind and temperature, observed and simulated. Q J R Meteorol Soc 137(654):264–274

Lilly DK (1967) The representation of small scale turbulence in numerical simulation experiments. Proceedings of the IBM Scientific Computing Symposium on Environmental Sciences 320-1951:195–210

Lilly DK (1978) A severe downslope windstorm and aircraft turbulence event induced by a mountain wave. J Atmos Sci 35(1):59–77

Liu Y, Warner T, Liu Y, Vincent C, Wu W, Mahoney B, Swerdlin S, Parks K, Boehnert J (2011) Simultaneous nested modeling from the synoptic scale to the LES scale for wind energy applications. J Wind Eng Ind Aerodyn 99(4):308–319

Lothon M, Lohou F, Pino D, Couvreux F, Pardyjak E, Reuder J, Vilà-Guerau de Arellano J, Durand P, Hartogensis O, Legain D, et al. (2014) The BLLAST field experiment: Boundary-Layer Late Afternoon and Sunset Turbulence. Atmospheric Chemistry and Physics Discussions 14(7):10,789–10,852

Louis JF (1979) A parametric model of vertical eddy fluxes in the atmosphere. Boundary-Layer Meteorol 17(2):187–202

Lu C, Hall W, Koch S (2006) Highresolution numerical simulations of gravity waveinduced turbulence in association with an upperlevel jet system. In: Preprints, 12th Conf. on Aviation, Range, and Aerospace Meteorology, Atlanta, GA, Amer. Meteor. Soc

Lundquist KA, Chow FK, Lundquist JK (2010) An immersed boundary method for the Weather Research and Forecasting model. Mon Weather Rev 138(3):796–817

Mahalov A, Moustaoui M, Grubišić V (2011) A numerical study of mountain waves in the upper troposphere and lower stratosphere. Atmospheric Chemistry and Physics 11(11):5123–5139

Mahrt L (1998) Nocturnal boundary-layer regimes. Boundary-Layer Meteorol 88(2):255–278

Mahrt L (2014) Stably Stratified Atmospheric Boundary Layers. Annual Review of Fluid Mechanics 46:23–45

Mahrt L, Vickers D, Nakamura R, Soler M, Sun J, Burns S, Lenschow D (2001) Shallow drainage flows. Boundary-Layer Meteorol 101(2):243–260

Mahrt L, Richardson S, Seaman N, Stauffer D (2010) Non-stationary drainage flows and motions in the cold pool. Tellus A 62(5):698–705

Mahrt L, Thomas C, Richardson S, Seaman N, Stauffer D, Zeeman M (2013) Non-stationary generation of weak turbulence for very stable and weak-wind conditions. Boundary-Layer Meteorol 147(2):179–199

Markowski P, Richardson Y (2011) Mesoscale meteorology in midlatitudes, vol 2. John Wiley & Sons

Martínez D, Jiménez M, Cuxart J, Mahrt L (2010) Heterogeneous nocturnal cooling in a large basin under very stable conditions. Boundary-Layer Meteorol 137(1):97–113

Mason P (1989) Large-eddy simulation of the convective atmospheric boundary layer. J Atmos Sci 46(11):1492–1516

Mason P, Derbyshire S (1990) Large-eddy simulation of the stably-stratified atmospheric boundary layer. Boundary-Layer Meteorol 53(1-2):117–162

Mayor SD (2011) Observations of Seven Atmospheric Density Current Fronts in Dixon, California. Mon Weather Rev 139(5):1338–1351

Mellor GL, Yamada T (1982) Development of a turbulence closure model for geophysical fluid problems. Reviews of Geophysics 20(4):851–875

Mirocha JD, Kosović B (2010) A large-eddy simulation study of the influence of subsidence on the stably stratified atmospheric boundary layer. Boundary-Layer Meteorol 134(1):1–21

Mirocha JD, Lundquist J, Kosovic B (2010) Implementation of a nonlinear subfilter turbulence stress model for large-eddy simulation in the Advanced Research WRF model. Mon Weather Rev 138(11):4212–4228

Mirocha JD, Kirkil G, Bou-Zeid E, Katopodes Chow F, Kosovic B (2013) Transition and Equilibration of Neutral Atmospheric Boundary Layer Flow in One-Way Nested Large-Eddy Simulations Using the Weather Research and Forecasting Model. Mon Weather Rev (2012)

Mirocha JD, Kosović B, Kirkil G (2014) Resolved turbulence characteristics in large-eddy simulations nested within mesoscale simulations using the weather research and forecasting model. Mon Weather Rev 142(2):806–831

Mlawer EJ, Taubman SJ, Brown PD, Iacono MJ, Clough SA (1997) Radiative transfer for inhomogeneous atmospheres: RRTM, a validated correlated-k model for the longwave. Journal of geophysical research 102(D14):16,663–16

Mobbs S, Vosper S, Sheridan P, Cardoso R, Burton R, Arnold S, Hill M, Horlacher V, Gadian A (2005) Observations of downslope winds and rotors in the Falkland Islands. Q J R Meteorol Soc 131(605):329–351

Moeng C (2011) Large-eddy Simulation of turbulence in the PBL. In: 12th WRF User's Workshop

Moeng C, Dudhia J, Klemp J, Sullivan P (2007) Examining two-way grid nesting for large eddy simulation of the PBL using the WRF model. Mon Weather Rev 135(6):2295–2311

Moeng CH (1984) A large-eddy-simulation model for the study of planetary boundary-layer turbulence. J Atmos Sci 41(13):2052–2062

Mölders N, Kramm G (2010) A case study on wintertime inversions in Interior Alaska with WRF. Atmospheric Research 95(2):314–332

Monin A, Obukhov A (1954) Basic laws of turbulent mixing in the surface layer of the atmosphere. Contrib Geophys Inst Acad Sci USSR 151:163–187

Muñoz-Esparza D, Kosović B, García-Sánchez C, van Beeck J (2014) Nesting Turbulence in an Offshore Convective Boundary Layer Using Large-Eddy Simulations. Boundary-Layer Meteorol 151(3):453–478

Nakanishi M, Niino H (2006) An improved Mellor–Yamada level-3 model: Its numerical stability and application to a regional prediction of advection fog. Boundary-Layer Meteorol 119(2):397–407

Nappo CJ (2002) An introduction to atmospheric gravity waves. Academic Press, San Diego

Nappo CJ, Chimonas G (1992) Wave exchange between the ground surface and a boundary-layer critical level. J Atmos Sci 49(13):1075–1091

Nieuwstadt F (1985) A model for the stationary, stable boundary layer. Turbulence and diffusion in stable environments pp 149–179

Nieuwstadt F, Mason PJ, Moeng C, Schumann U (1993) Large-eddy simulation of the convective boundary layer: A comparison of four computer codes. In: Turbulent Shear Flows 8, Springer, pp 343–367

Nolan DS, Zhang JA, Stern DP (2009) Evaluation of planetary boundary layer parameterizations in tropical cyclones by comparison of in situ observations and high-resolution simulations of Hurricane Isabel (2003). Part I: Initialization, maximum winds, and the outer-core boundary layer. Mon Weather Rev 137(11):3651–3674

Ostrovsky L, Troitskaya YI (1987) A model of turbulent transfer and dynamics of turbulence in a stratified shear-flow. IZVESTIYA AKADEMII NAUK SSSR FIZIKA ATMOSFERY I OKEANA 23(10):1031–1040

Otkin JA, Greenwald TJ (2008) Comparison of WRF model-simulated and MODIS-derived cloud data. Mon Weather Rev 136(6)

Papadopoulos K, Helmis C (1999) Evening and morning transition of katabatic flows. Boundary-Layer Meteorol 92(2):195–227

Paulson CA (1970) The mathematical representation of wind speed and temperature profiles in the unstable atmospheric surface layer. Journal of Applied Meteorology 9(6):857–861

Pielke Sr RA (2013) Mesoscale meteorological modeling, vol 98. Academic press

Plougonven R, Hertzog A, Teitelbaum H (2008) Observations and simulations of a large-amplitude mountain wave breaking over the Antarctic Peninsula. Journal of Geophysical Research 113(D16):D16,113

Poulos GS, Bossert JE, McKee TB, Pielke RA (2000) The interaction of katabatic flow and mountain waves. Part I: Observations and idealized simulations. J Atmos Sci 57(12):1919–1936

Poulos GS, Blumen W, Fritts DC, Lundquist JK, Sun J, Burns SP, Nappo C, Banta R, Newsom R, Cuxart J, et al. (2002) CASES-99: A comprehensive investigation of the stable nocturnal boundary layer. Bull Am Meteorol Soc 83(4):555–581

Queney P (1955) Rotor Phenomena in the Lee of Mountains1. Tellus 7(3):367–371

Raasch S, Schröter M (2001) PALM–a large-eddy simulation model performing on massively parallel computers. Meteorologische Zeitschrift 10(5):363–372

Ray PS (1986) Mesoscale meteorology and forecasting. American Meteorological Society

Reynolds O (1894) On the dynamical theory of incompressible viscous fluids and the determination of the criterion. Proceedings of the Royal Society of London 56(336-339):40–45

Román-Cascón C, Yagüe C, Mahrt L, Sastre M, Steeneveld G, Pardyjak E, van de Boer A, Hartogensis O (2015) Interactions among drainage flows, gravity waves and turbulence: a BLLAST case study. Atmospheric Chemistry and Physics Discussions 15(8):12,821–12,865

Rottman JW, Einaudi F (1993) Solitary waves in the atmosphere. J Atmos Sci 50:2116–2136

Saiki EM, Moeng CH, Sullivan PP (2000) Large-eddy simulation of the stably stratified planetary boundary layer. Boundary-Layer Meteorol 95(1):1–30

San José R, Casanova J, Viloria RE, Casanova J (1985) Evaluation of the turbulent parameters of the unstable surface boundary layer outside Businger's range. Atmospheric Environment (1967) 19(10):1555–1561

Schmidt H, Schumann U (1989) Coherent structure of the convective boundary layer derived from large-eddy simulations. J Fluid Mech 200:511–562

Scorer R (1949) Theory of waves in the lee of mountains. Q J R Meteorol Soc 75(323):41–56

Seaman N, Gaudet B, Zielonka J, Stauffer D (2009) Sensitivity of vertical structure in the stable boundary layer to variations of the WRF model's Mellor–Yamada–Janjic turbulence scheme.'. Boulder, 23e27 June p 7

Seaman NL, Gaudet BJ, Stauffer DR, Mahrt L, Richardson SJ, Zielonka JR, Wyngaard JC (2012) Numerical Prediction of Submesoscale Flow in the Nocturnal Stable Boundary Layer over Complex Terrain. Mon Weather Rev 140(3)

Sheridan PF, Horlacher V, Rooney GG, Hignett P, Mobbs SD, Vosper SB (2007) Influence of lee waves on the near-surface flow downwind of the Pennines. Q J R Meteorol Soc 133(627):1353–1369, DOI 10.1002/qj.110

Shin HH, Hong SY (2011) Intercomparison of planetary boundary-layer parametrizations in the WRF model for a single day from CASES-99. Boundary-Layer Meteorol 139(2):261–281

Simpson JE (1999) Gravity currents: In the environment and the laboratory. Cambridge University Press

Skamarock WC (2004) Evaluating mesoscale NWP models using kinetic energy spectra. Mon Weather Rev 132(12):3019–3032

Skamarock WC, Klemp J, Dudhia J, Gill D, Barker D, Wang W, Powers J (2008) A description of the Advanced Research WRF Version 3. NCAR Tech Notes-475+ STR. National Center for Atmospheric Research (NCAR)

Smagorinsky J (1963) General circulation experiments with the primitive equations: I. the basic experiment*. Mon Weather Rev 91(3):99–164

Smith CM, Skyllingstad ED (2009) Investigation of upstream boundary layer influence on mountain wave breaking and lee wave rotors using a large-eddy simulation. J Atmos Sci 66(10):3147–3164

Smith RB (1979) The influence of mountains on the atmosphere. Advances in geophysics 21:87–230

Smith RB (1989) Hydrostatic airflow over mountains. Advances in Geophysics 31:1–41

Smith RB, Doyle JD, Jiang Q, Smith SA (2007) Alpine gravity waves: Lessons from MAP regarding mountain wave generation and breaking. Q J R Meteorol Soc 133(625):917–936

Soler M, Infante C, Buenestado P, Mahrt L (2002) Observations of nocturnal drainage flow in a shallow gully. Boundary-Layer Meteorol 105(2):253–273

Soler M, Arasa R, Merino M, Olid M, Ortega S (2011) Modelling local sea-breeze flow and associated dispersion patterns over a coastal area in north-east Spain: a case study. Boundary-Layer Meteorol 140(1):37–56

Soler M, Udina M, Ferreres E (2014) Observational and Numerical Simulation Study of a Sequence of Eight Atmospheric Density Currents in Northern Spain. Boundary-Layer Meteorol 153(2):195–216

Soriano C, Jorba O, Baldasano JM (2002) One-way nesting versus two-way nesting: does it really make a difference? In: Air Pollution Modeling and its Application XV, Springer, pp 177–185

Spiga A, Teitelbaum H, Zeitlin V (2008) Identification of the sources of inertia-gravity waves in the Andes Cordillera region. In: Annales Geophysicae, Copernicus GmbH, vol 26, pp 2551–2568

Staquet C (2004) Gravity and inertia-gravity internal waves: breaking processes and induced mixing. Surveys in geophysics 25(3-4):281–314

Stauffer DR, Gaudet B, Seaman N, Wyngaard J, Mahrt L, Richardson S (2009) Sub-kilometer numerical predictions in the nocturnal stable boundary layer. Paper 18B 4

Stiperski I, Grubišic V (2011) Trapped lee wave interference in the presence of surface friction. J Atmos Sci 68(4):918–936

Stull RB (1988) An introduction to boundary layer meteorology. Kluwer Academic Publishers

Sullivan PP, McWilliams JC, Moeng CH (1994) A subgrid-scale model for large-eddy simulation of planetary boundary-layer flows. Boundary-Layer Meteorol 71(3):247–276

Sun J (2011) Vertical variations of mixing lengths under neutral and stable conditions during CASES-99. J Appl Meteorol Clim 50(10):2030–2041

Sun J, Mahrt L (1995) Determination of surface fluxes from the surface radiative temperature. J Atmos Sci 52:1096–1106

Sun J, Burns SP, Lenschow DH, Banta R, Newsom R, Coulter R, Frasier S, Ince T, Nappo C, Cuxart J, et al. (2002) Intermittent turbulence associated with a density current passage in the stable boundary layer. Boundary-Layer Meteorol 105(2):199–219

Sun J, Lenschow DH, Burns SP, Banta RM, Newsom RK, Coulter R, Frasier S, Ince T, Nappo C, Balsley BB, et al. (2004) Atmospheric disturbances that generate intermittent turbulence in nocturnal boundary layers. Boundary-Layer Meteorol 110(2):255–279

Sun J, Mahrt L, Banta RM, Pichugina YL (2012) Turbulence regimes and turbulence intermittency in the stable boundary layer during CASES-99. J Atmos Sci 69(1):338–351

Sun J, Lenschow DH, Mahrt L, Nappo C (2013) The Relationships among Wind, Horizontal Pressure Gradient, and Turbulent Momentum Transport during CASES-99. J Atmos Sci 70(11)

Sun J, Lenschow DH, LeMone MA, Mahrt L (2015a) The role of large-coherent-eddy transport in the atmospheric surface layer based on CASES-99 observations. Submitted to Boundary-Layer Meteorol

Sun J, Mahrt L, Nappo C, Lenschow DH (2015b) Wind and Temperature Oscillations Generated by Wave-Turbulence Interactions in the Stably Stratified Boundary Layer. J Atmos Sci 72(2014):1484–1503

Sun J, Nappo C, Mahrt L, Belušić D, Grisogono B, Stauffer DR, Pulido M, Staquet C, Jiang Q, Pouquet A, et al. (2015c) Review of wave-turbulence interactions in the stable atmospheric boundary layer. Reviews of Geophysics 53

Talbot C, Bou-Zeid E, Smith J (2012) Nested Mesoscale Large-Eddy Simulations with WRF: Performance in Real Test Cases. J Hydrometeorol 13(5):1421–1441

Tastula EM, Galperin B, Dudhia J, LeMone MA, Sukoriansky S, Vihma T (2015) Methodical assessment of the differences between the QNSE and MYJ PBL schemes for stable conditions. Q J R Meteorol Soc

Terradellas E, Morales G, Cuxart J, Yagüe C (2001) Wavelet methods: application to the study of the stable atmospheric boundary layer under non-stationary conditions. Dynamics of atmospheres and oceans 34(2):225–244

Terradellas E, Soler M, Ferreres E, Bravo M (2005) Analysis of oscillations in the stable atmospheric boundary layer using wavelet methods. Boundary-Layer Meteorol 114(3):489–518

Tesche T, McNally D, Tremback C (2002) Operational evaluation of the MM5 meteorological model over the continental United States: Protocol for annual and episodic evaluation. Submitted to USEPA as part of Task Order 4TCG-68027015(July 2002)

Thompson G, Rasmussen RM, Manning K (2004) Explicit forecasts of winter precipitation using an improved bulk microphysics scheme. Part I: Description and sensitivity analysis. Mon Weather Rev 132(2):519–542

Torrence C, Compo GP (1998) A practical guide to wavelet analysis. Bull Am Meteorol Soc 79(1):61–78

Troen I, Mahrt L (1986) A simple model of the atmospheric boundary layer; sensitivity to surface evaporation. Boundary-Layer Meteorol 37(1-2):129–148

Udina M, Soler MR, Viana S, Yagüe C (2013) Model simulation of gravity waves triggered by a density current. Q J R Meteorol Soc 139(672):701–714, DOI 10.1002/qj.2004, URL http://dx.doi.org/10.1002/qj.2004

Valkonen T, Vihma T, Kirkwood S, Johansson MM (2010) Fine-scale model simulation of gravity waves generated by Basen nunatak in Antarctica. Tellus A 62(3):319–332

Viana S, Yagüe C, Maqueda G, Morales G (2007) Study of the surface pressure fluctuations generated by waves and turbulence in the nocturnal boundary layer during SABLES2006 field campaign. Física de la Tierra (19):55–71

Viana S, Yagüe C, Maqueda G (2009) Propagation and effects of a mesoscale gravity wave over a weakly-stratified nocturnal boundary layer during the SABLES2006 field campaign. Boundary-Layer Meteorol 133(2):165–188

Viana S, Terradellas E, Yagüe C (2010) Analysis of gravity waves generated at the top of a drainage flow. J Atmos Sci 67(12):3949–3966

Viana S, Yagüe C, Maqueda G (2012) Vertical structure of the stable boundary layer detected by RASS-SODAR and in-situ measurements in SABLES 2006 field campaign. Acta Geophysica 60(5):1261–1286

Vilà-Guerau deArellano J (2007) Role of nocturnal turbulence and advection in the formation of shallow cumulus over land. Quarterly Journal of the Royal Meteorological Society 133(628):1615–1627

Vosper S (2004) Inversion effects on mountain lee waves. Q J R Meteorol Soc 130(600):1723–1748

Vosper S, Sheridan P, Brown A (2006) Flow separation and rotor formation beneath two-dimensional trapped lee waves. Q J R Meteorol Soc 132(620):2415–2438

Webb EK (1970) Profile relationships: The log-linear range, and extension to strong stability. Q J R Meteorol Soc 96(407):67–90

Wicker LJ, Skamarock WC (2002) Time-splitting methods for elastic models using forward time schemes. Mon Weather Rev 130(8):2088–2097

Van de Wiel B, Moene A, Hartogensis O, De Bruin H, Holtslag A (2003) Intermittent turbulence in the stable boundary layer over land. Part III: A classification for observations during CASES-99. J Atmos Sci 60(20):2509–2522

Wyngaard JC (2004) Toward numerical modeling in the "Terra Incognita". J Atmos Sci 61(14):1816–1826

Wyngaard JC (2010) Turbulence in the Atmosphere. Cambridge University Press

Yagüe C, Viana S, Maqueda G, Lazcano MF, Morales G, Rees JM (2007) A study on the nocturnal atmospheric boundary layer: SABLES2006. Física de la Tierra (19):37–53

Zhang D, Anthes RA (1982) A high-resolution model of the planetary boundary layer- Sensitivity tests and comparisons with SESAME-79 data. Journal of Applied Meteorology 21(11):1594–1609

Zilitinkevich S (1995) Non-local turbulent transport pollution dispersion aspects of coherent structure of convective flows. Air Pollution III, Air pollution theory and simulation (H Power, N Moussiopoulos, CA Brebbia, eds) Computational Mechanics Publ, Southampton, Boston 1:53–60

Zilitinkevich S, Elperin T, Kleeorin N, Rogachevskii I (2007) Energy-and flux-budget (EFB) turbulence closure model for stably stratified flows. Part I: steady-state, homogeneous regimes. Boundary-Layer Meteorol 125(2):167–191

List of Figures

List of Tables

A

Acronyms and abreviatons

ABL	Atmospheric Boundary Layer
AMS	American Meteorological Society
ARW	Advanced Research WRF
BL	Boundary Layer
CBL	Convective Boundary Layer
CIBA	*Centro de Investigaciones de la Baja Atmósfera*
CFD	Computational Fluid Dynamics
CFL	Courant-Friedrichs-Lewy
CFSR	Climate Forecast System Reanalysis
DNS	Direct Numerical Simulation
GW	Gravity Wave
HOST	HOckey Stick Transition Theory
IBM	Inmersed Boundary Method
IGW	Internal Gravity Waves
KH	Kelvin-Helmholtz
LES	Large Eddy Simulation
LLJ	Low Level Jet
LSM	Land Surface Model
LW	Long Wave
MMM	Mesoscale Meteorological Model

MRF	Medium Range Forecast
MYJ	Mellor Yamada Janjic PBL scheme
MOST	Monin Obukhov Similarity Theory
MYNN	Mellor-Yamada Nakanishi-Niino
MP	MicroPhysics
NBA	Nonlinear Anisotropy Backscatter
NBL	Nocturnal Boundary Layer
NCAR	National Center for Atmospheric Research
NCEP	National Centers for Environmental Prediction
NCL	Ncar Command Language
NWP	Numerical Weather Prediction
NS	Navier Stokes
PBL	Planetary Boundary Layer
RANS	Reynolds Averaged Navier Stokes
RL	Residual Layer
RRTM	Rapid Radiative Transfer Model
SBL	Stable Boundary Layer
SGS	Sub-grid scale
SW	Short Wave
TFO	Turbulence-Forced Oscillations
TPE	Turbulent Potential Energy
TKE	Turbulent Kinetic Energy
UHF	Ultra High Frequency
URANS	Unsteady RANS
WRF	Weather Research and Forecasting
WOA	Witch of Agnesi
YSU	Yonsei University PBL scheme

B

Notation and constants

R	Gas constant for dry air ($287 JK^{-1}kg^{-1}$)
g	Aceleration due to gravity
ρ	Air density
Re	Reynolds number
l	Mixing length, length scale
l_s^2	Scorer parameter
l_{sU}^2	Scorer parameter in the upper layers
l_{sL}^2	Scorer parameter in the lower layers
N	Brunt Väisälä frequency
θ	Potential temperature
θ_v	Virtual potential temperature
x	Cartesian coordinate towards east
y	Cartesian coordinate towards north
z	Cartesian coordinate up
u	Eastward moving Cartesian wind component
v	Northward moving Cartesian wind component
w	Upward moving Cartesian wind component, vertical velocity
f	Frequency
λ	Wavelength
k	Wavenumber
T_f	Period
A	Amplitude

Fr	Froude number
U	Horizontal wind speed
u_i	Represents u, v, w for i $= 1, 2, 3$ respectively
u_j	Refers to the generic components of distance coordinates x, y, z
h_m	Mountain height
ζ	Vorticity
LH	Latent heat flux
SH	Sensible heat flux
p	Pressure
ν	Kinematic viscosity
ν_θ	Kinematic viscosity for heat
ν_q	Kinematic viscosity for humidity
C_p	Specific heat of air at constant pressure
R_n	Net radiation
E	Mass of water vapor being created by a phase change from liquid or solid
L_p	Latent heat associated with the phase change of E
T	Air temperature
T_v	Air virtual temperature
q	Water vapor, Specific humidity
S_q	Specific humidity sources
e	Turbulent kinetic energy (TKE)
ϵ	Dissipation of TKE
η	Sigma coordinate
Cr	Courant number